

39083



National Library of Canada

Bibliothèque nationale du Canada

CANADIAN THESIS
ON MICROFILM

THÈSES CANADIENNES
SUR MICROFILME

NAME OF AUTHOR/NOM DE L'AUTEUR John William Rowson

TITLE OF THESIS/TITRE DE LA THÈSE Radioisotopic X-ray Analysis of Canadian Uranium Ores

UNIVERSITY/UNIVERSITÉ University of Regina

DEGREE FOR WHICH THESIS WAS PRESENTED/GRADÉ POUR LEQUEL CETTE THÈSE FUT PRÉSENTÉE Doctor of Philosophy in Chemistry

YEAR THIS DEGREE CONFERRED/ANNÉE D'OBTENTION DE CE DEGRÉ 1979

NAME OF SUPERVISOR/NOM DU DIRECTEUR DE THÈSE S. Hontzeas

Permission is hereby granted to the NATIONAL LIBRARY OF CANADA to microfilm this thesis and to lend or sell copies of the film.

L'autorisation est, par la présente, accordée à la BIBLIOTHÈQUE NATIONALE DU CANADA de microfilmer cette thèse et de prêter ou de vendre des exemplaires du film.

The author reserves other publication rights, and neither the thesis nor extensive extracts from it may be printed or otherwise reproduced without the author's written permission.

L'auteur se réserve les autres droits de publication, ni la thèse ni de longs extraits de celle-ci ne doivent être imprimés ou autrement reproduits sans l'autorisation écrite de l'auteur.

DATED/DATE January 12, 1979 SIGNED/SIGNÉ [Signature]

PERMANENT ADDRESS/RÉSIDENCE FIXÉE _____



National Library of Canada

Cataloguing Branch
Canadian Theses Division

Ottawa Canada
K1A 0N4

Bibliothèque nationale du Canada

Direction du catalogage
Division des thèses canadiennes

NOTICE

AVIS

The quality of this microfiche is heavily dependent upon the quality of the original thesis submitted for microfilming. Every effort has been made to ensure the highest quality of reproduction possible.

La qualité de cette microfiche dépend grandement de la qualité de la thèse soumise au microfilmage. Nous avons tout fait pour assurer une qualité supérieure de reproduction.

If pages are missing, contact the university which granted the degree.

Si il manque des pages, veuillez communiquer avec l'université qui a conféré le grade.

~~Some pages may have indistinct print especially if the original pages were typed with a poor typewriter ribbon or if the university sent us a poor photocopy.~~

La qualité d'impression de certaines pages peut laisser à désirer, surtout si les pages originales ont été dactylographiées à l'aide d'un ruban usé ou si l'université nous a fait parvenir une photocopie de mauvaise qualité.

Previously copyrighted materials (journal articles, published tests, etc.) are not filmed.

Les documents qui font déjà l'objet d'un droit d'auteur (articles de revue, examens publiés, etc.) ne sont pas microfilmés.

Reproduction in full or in part of this film is governed by the Canadian Copyright Act, R.S.C. 1970, c. C-30. Please read the authorization forms which accompany this thesis.

La reproduction, même partielle, de ce microfilm est soumise à la Loi canadienne sur le droit d'auteur, SRC 1970, c. C-30. Veuillez prendre connaissance des formules d'autorisation qui accompagnent cette thèse.

**THIS DISSERTATION
HAS BEEN MICROFILMED
EXACTLY AS RECEIVED**

**LA THÈSE A ÉTÉ
MICROFILMÉE TELLE QUE
NOUS L'AVONS REÇUE**

RADIOISOTOPIC X-RAY ANALYSIS OF CANADIAN URANIUM ORES

A Thesis

Submitted to the Faculty of Graduate Studies

In Partial Fulfilment of the Requirements

For the Degree of

Doctor of Philosophy

in Chemistry

Faculty of Science

University of Regina

by

John William Rowson

October, 1978

John William Rowson 1979

UNIVERSITY OF REGINA

FACULTY OF GRADUATE STUDIES AND RESEARCH

CERTIFICATION OF THESIS WORK

We, the undersigned, certify that ... John William Rowson

.....
candidate for the Degree of Doctor of Philosophy in Chemistry
has presented a thesis on the subject Radioisotopic X-ray Analysis
of Canadian Uranium Ores

.....
that the thesis is acceptable in form and content, and that the student
demonstrated a satisfactory knowledge of the field covered by the thesis
in an oral examination held on January 12, 1979.

External Examiner

J. Yaff
.....
Vice-Principal (Administration) McGill University

Internal Examiners

A. J. ...
H. ...
David ...
J. ...
...

UNIVERSITY OF REGINA

PERMISSION TO USE POSTGRADUATE THESES

Title of Thesis Radioisotopic X-ray Analysis of Canadian Uranium
 Ores

Name of Author John William Rowson

Faculty Faculty of Science

Degree Doctor of Philosophy in Chemistry

In presenting this thesis in partial fulfillment of the requirements for a postgraduate degree from the University of Regina, I agree that the Libraries of this University shall make it freely available for inspection. I further agree that permission for extensive copying of this thesis for scholarly purposes may be granted by the professor or professors who supervised my thesis work, or in their absence, by the Head of the Department or the Dean of the Faculty in which my thesis work was done. It is understood that any copying or publication or use of this thesis or parts thereof for financial gain shall not be allowed without my written permission. It is also understood that due recognition shall be given to me and to the University of Regina in any scholarly use which may be made of any material in my thesis.

Signature..... *J. W. Rowson*

Date..... January 12, 1979

/am

2/22/78
 100 cc.

UNIVERSITY OF REGINA

Faculty of Graduate Studies and Research

SUMMARY OF THE THESIS

Submitted in Partial Satisfaction
of the Requirements for the

DEGREE OF DOCTOR OF PHILOSOPHY

in

CHEMISTRY

by

JOHN WILLIAM ROWSON

B.Sc. University of Western Ontario

FACULTY OF SCIENCE

January 1979

Committee in Charge

W. D. Chandler (Department Head)

K. I. Ellison

S. Hontela (Supervisor)

D. W. Linton

I. H. Greenberg

C. W. Blachford (Dean of Graduate Studies and Research)

External Examiner

I. Yaffe (Vice President Administration)

McGill University

Montreal, Quebec

THESIS

RADIOISOTOPIC X-RAY ANALYSIS OF CANADIAN URANIUM ORES

Uranium ores from various locations in Canada were analyzed for uranium by X ray and γ ray energy spectroscopy. By selecting appropriate radioisotopes, techniques were developed to determine uranium by observing X rays from the K, L and M shells respectively. Together the procedures are suitable for a wide range of uranium concentrations in geological material and the results appear to be free from matrix enhancement and absorption effects. In addition, the γ emissions from uranium were used to determine the uranium isotope ratio.

The uranium K shell fluorescence was induced by a 10 mCi ^{60}Co point source which was mounted on a one dimensional goniometer. This instrument was designed with adjustable scatter angle primary and secondary collimation settings. The optimum geometrical conditions for analysis of uranium using partially thick powdered ore samples were found. Assumptions were drawn for innate geological specimens which led to the direct calculation of the matrix and thickness factors. This was accomplished by simultaneously and experimentally measuring the Compton scattering and transmitted peak intensities. These factors are then used to modify the $\text{U K}\alpha_1$ peak intensity so that no comparative standards are required to maintain accuracy. As such, the technique is a prime candidate for application to on-stream industrial analysis.

A source target excitation assembly was designed for the quantitative determination of uranium in thick samples of uranium bearing ores using L shell fluorescence. An annular source of ^{60}Co of about 50 mCi strength supplied the primary radiation. A molybdenum target was chosen to utilize the $\text{Mo K}\alpha$ secondary radiation in order to selectively excite only the uranium L_{III} subshell. A technique using the fluorescence to Compton scattering intensity ratio to provide adequate compensation for absorption and enhancement effects is described. Application of the technique gave a

calibration curve which is linear in concentration of uranium for four orders of magnitude. This technique may also be well suited to industrial on stream analysis.

The principle motivation for investigating uranium analysis using $M\alpha$ shell fluorescence is that this approach can potentially detect smaller quantities of uranium than can either $K\alpha$ or L shell excitation. Accordingly, a radioisotopic excitation system has been specifically designed to analyze small quantities of uranium precipitate. An annular source of ^{137}Cs approximately 10 mCi in strength supplied the excitation radiation. Uranium was separated from the geological material using a phase transfer catalyst. Thin specimens of uranium precipitate were prepared by electrodeposition onto a stainless steel cathode. La was added to the electrolyte and co-deposited with uranium. It was found that the $\text{La } L\alpha$ peak intensity could be employed as an internal standard to correct the $\text{U } M\alpha$ β peak intensity for thickness effects. The use of lanthanum also markedly improved the consistency of electrodeposition yields. The technique was applied to several low grade ores from major uranium mineral locations of Canada. The procedure is sensitive enough to analyze uranium at naturally found environmental concentrations.

And finally, the ^{235}U - ^{238}U isotope ratio has been determined on thin samples of uranium chemical precipitates. The ^{235}U and ^{238}U contents were analyzed by measuring the intensities of the 0.186 MeV ^{235}U and 0.0925 MeV ^{238}U doublet γ rays respectively. Interferences normally encountered by using the latter peak were removed by approximating the spectrum in the region of the ^{238}U doublet by a series of Cauchy functions. Intensity ratios varied linearly with isotope ratios for at least three orders of magnitude. For industrial quality yellow cake, the technique appears to be independent of sample thickness.

BIOGRAPHICAL

o JOHN WILLIAM ROWSON

- | | | |
|------|------|--|
| 1968 | | Honours Secondary Graduation Diploma
Kapuskasing District High School Kapuska
sing Ontario |
| 1971 | | Bachelor of Science University of Western
Ontario London Ontario |
| 1971 | 1974 | Laboratory Technologist Eldorado Nuclear
Limited, Eldorado Saskatchewan |
| 1975 | 1978 | Graduate student University of Regina
Regina, Saskatchewan
Saskatchewan Research Council Scholarship |
| 1978 | | Analytical Research Chemist Eldorado
Nuclear Limited Eldorado Saskatchewan |

ABSTRACT

Uranium ores from various locations in Canada were analyzed for uranium by X-ray and γ -ray energy spectroscopy. By selecting appropriate radioisotopes, techniques were developed to determine uranium by observing X-rays from the K, L and M shells respectively. Together the procedures are suitable for a wide range of uranium concentrations in geological material and the results appear to be free from matrix enhancement and absorption effects. In addition, the γ -emissions from uranium were used to determine the uranium isotope ratio.

The uranium K shell fluorescence was induced by a 10 mCi ^{57}Co point source which was mounted on a one dimensional goniometer. This instrument was designed with adjustable scatter angle, primary and secondary collimation settings. The optimum geometrical conditions for analysis of uranium using partially thick powdered ore samples were found. Assumptions were drawn for innate geological specimens which led to the direct calculation of the matrix and thickness factors. This was accomplished by simultaneously and experimentally measuring the Compton scattering and transmitted peak intensities. These factors are then used to modify the $\text{U K}\alpha_1$ peak intensity so that no comparative standards are required to maintain accuracy. As such, the technique is a prime candidate for application to on-stream industrial analysis.

A source-target excitation assembly was designed for the quantitative determination of uranium in thick samples of uranium bearing ores using L shell fluorescence. An annular source of ^{241}Am , of about 50 mCi strength, supplied the primary radiation. A molybdenum target was chosen

to utilize the Mo K α secondary radiation in order to selectively excite only the uranium L_{III} subshell. A technique, using the fluorescence to Compton scattering intensity ratio to provide adequate compensation for absorption and enhancement effects, is described. Application of the technique gave a calibration curve which is linear in concentration of uranium for four orders of magnitude. This technique may also be well suited to industrial on-stream analysis.

The principle motivation for investigating uranium analysis using M_V shell fluorescence is that this approach can potentially detect smaller quantities of uranium than can either K or L shell excitation. Accordingly, a radioisotopic excitation system has been specifically designed to analyze small quantities of uranium precipitate. An annular source of ⁵⁵Fe, approximately 10 mCi in strength, supplied the excitation radiation. Uranium was separated from the geological material using a phase transfer catalyst. Thin specimens of uranium precipitate were prepared by electrodeposition onto a stainless steel cathode. La³⁺ was added to the electrolyte and co-deposited with uranium. It was found that the La La peak intensity could be employed as an internal standard to correct the U M α , β peak intensity for thickness effects. The use of lanthanum also markedly improved the consistency of electrodeposition yields. The technique was applied to several low grade ores from major uranium mineral locations of Canada. The procedure is sensitive enough to analyze uranium at naturally found environmental concentrations.

And finally, the ²³⁵U/²³⁸U isotope ratio has been determined on thin samples of uranium chemical precipitates. The ²³⁵U and ²³⁸U contents were analyzed by measuring the intensities of the 0.186 MeV ²³⁵U and

0.0925 MeV ^{234}Th doublet γ -rays, respectively. Interferences normally encountered by using the latter peak were removed by approximating the spectrum in the region of the ^{234}Th doublet by a series of Cauchy functions. Intensity ratios varied linearly with isotope ratios for at least three orders of magnitude. For industrial quality yellow cake, the technique appears to be independent of sample thickness.

ACKNOWLEDGEMENTS

The author wishes to express his appreciation for the constant support and enthusiasm given by Dr. S.A. Hontzeas for the research undertaken in this thesis.

The author wishes to acknowledge the participation of the following industrial and governmental organizations through their provision of uranium bearing ore samples. Eldorado Nuclear Ltd., Mining Division, Gulf Minerals Canada Ltd., Amok Ltee., Uranerz Exploration Ltd., and the Elliot Lake Laboratory of the Canada Centre for Mineral and Energy Technology of the Department of Energy, Mines and Resources.

The author wishes to thank the following individuals for their valuable assistance in this work. Mr. H.H. Wirch, Laboratory Supervisor, Eldorado Nuclear Ltd., Mining Division, Dr. A.W. Ashbrook, Manager, Eldorado Nuclear Ltd., Research and Development Division (both for chemically standardizing the ore samples obtained) and Dr. H. Kreek, Programme Consultant, University of Regina (for helpful advice on computing problems).

The author wishes to express gratitude to the Saskatchewan Research Council for scholarships awarded him covering the period from August 1975 to August 1978 and to the National Research Council for grants given to Dr. S.A. Hontzeas permitting the purchase of the analyzing equipment.

TABLE OF CONTENTS

ABSTRACT	(ii)
ACKNOWLEDGEMENTS	(v)
LIST OF FIGURES AND ILLUSTRATIONS	(viii)
LIST OF TABLES	(xii)
1. INTRODUCTION	1
2. BACKGROUND FUNDAMENTALS	5
2.1. Attenuation of electromagnetic radiation by matter	5
2.2. Scattering	6
2.2.1. Rayleigh scattering	7
2.2.2. Compton scattering	12
2.3. The photoelectric effect	17
2.4. Atomic structure and X-ray spectra	21
2.4.1. The Auger effect	27
2.4.2. Fluorescent yield	28
2.5. Quantitative X-ray analysis	30
2.6. Quantitative γ -ray analysis	38
3. EXPERIMENTAL WORK	43
3.1. Preliminary considerations	43
3.2. Experimental facilities	55
3.3. The K X-ray experiment	59
3.3.1. Introduction	59
3.3.2. K X-ray experimental	63
3.4. The L X-ray experiment	74
3.4.1. Introduction	74
3.4.2. L X-ray experimental	76
3.5. The M X-ray experiment	80
3.5.1. Introduction	80
3.5.2. M X-ray experimental	83
3.6. The γ -spectroscopy experiment	93
3.6.1. Introduction	93
3.6.2. γ -spectroscopy experimental	99
4. RESULTS AND DISCUSSION	106
4.1. Precision analysis of experimental facilities	106
4.2. K X-ray results and discussion	109
4.2.1. Determination of optimum goniometer settings	109
4.2.2. Scattering intensity measurements	123
4.2.3. Sample thickness measurement	126

4.2.4.	Matrix compensation	128
4.2.5.	γ -ray spectrometer energy calibration	134
4.2.6.	Data and data analysis	134
4.2.7.	Specimen precision evaluation	160
4.3.	L X-ray results and discussion	163
4.3.1.	X-ray spectrometer energy calibration	163
4.3.2.	Matrix compensation	163
4.3.3.	Compton scattering intensity measurements	169
4.3.4.	Data and data analysis	170
4.3.5.	Comparison of fluorimetric and X-ray analyses	179
4.3.6.	Specimen precision analysis	181
4.4.	M X-ray results and discussion	184
4.4.1.	Energy calibration of the X-ray spectrometer	184
4.4.2.	Matrix element effects	186
4.4.3.	Optimum electrodeposition time determination	188
4.4.4.	Data and data analysis	193
4.4.5.	Uranium separation procedure	199
4.4.6.	Uranium analysis of low grade ores	201
4.4.7.	Specimen precision determination	204
4.5.	γ -spectroscopy results and discussion	211
4.5.1.	Energy calibration of the γ -ray spectrometer	211
4.5.2.	Spectral unfolding using Cauchy functions	213
4.5.3.	Evaluation of specimen thickness effects	224
4.5.4.	Data and data analysis	229
4.5.5.	Isotope ratio analysis of high grade uranium ores	234
4.5.6.	Determination of specimen errors for the γ -ray experiment	236
4.5.7.	Determination of the spectral unfolding error	239
5.	CONCLUSIONS AND CONTRIBUTIONS TO KNOWLEDGE	245
5.1.	The K X-ray experiment	245
5.2.	The L X-ray experiment	247
5.3.	The M X-ray experiment	249
5.4.	The γ -ray spectroscopy experiment	250
	REFERENCES	252
	APPENDIX A	256
	APPENDIX B	265
	APPENDIX C	274
	APPENDIX D	304
	APPENDIX E	312
	APPENDIX F	316
	APPENDIX G	321
	APPENDIX H	331

LIST OF FIGURES AND ILLUSTRATIONS

Number	Title	Page
1	Rayleigh scattering cross section as a function of incident photon energy for uranium and silicon	9
2	Rayleigh scattering cross section as a function of atomic number (Z) for 100 keV incident photons	10
3	Variation of Rayleigh scattering cross section with scatter angle for 80 keV photons impinging upon oxygen	11
4	Compton scattering cross section as a function of incident photon energy for uranium and silicon	14
5	Nearly linear correlation of Compton scattering cross section with atomic number (Z) for 100 keV incident photons	15
6	Typical correlation of relative Compton scattering cross section with scatter angle for 10 and 150 keV photons	16
7	Photoelectric cross section as a function of energy for uranium and silicon	19
8	Photoelectric cross section as a function of atomic number for 100 keV incident photons	20
9	Simplified model of the atom illustrating the origin of the principle X-ray lines	22
10	Illustration of the K, L and M fluorescent yield dependence on atomic number	29
11	General source, sample and detector geometry employed for X-ray analysis	31
12	Relative contribution of each attenuation mechanism to the total absorption cross section versus photon energy for both uranium and silicon atoms	46
13	Block diagram illustrating the major electronic components of the analyzing systems	56
14	Schematic diagram of the general source, sample and detector geometry as employed for the K X-ray experiment	64
15	Overall view of the K X-ray apparatus showing: the source, sample and detector geometry; the secondary collimation and scatter angle adjustment features	66

Number	Title	Page
16	Rear view of the K X-ray apparatus illustrating the source insertion location and the primary collimation adjustment feature	67
17	Front view of the K X-ray apparatus showing the installation of the bismuth target used to measure the transmitted radiation intensity	69
18	A schematic representation of the source, target, sample and detector geometry employed for the L X-ray apparatus	77
19	Exploded view of the combined electrodeposition cell and cathode construction	84
20	Drawing illustrating the construction of the rotating platinum anode	85
21	Radioisotopic source, sample and detector configuration as employed in the M X-ray experiment	86
22	Outline of total procedure adopted to analyze uranium in low grade ores or soils	89
23	Radium decay series	94
24	Actinium decay series	95
25	Simplified version of the decay schemes of ^{238}U , ^{234}Th , $^{234\text{m}}\text{Pa}$ and ^{234}Pa	97
26	Sample preparation and placement geometry used in the γ -spectroscopy experiment	104
27	Background spectrum recorded with scatter angle set at 25°	110
28	Background spectrum recorded with scatter angle set at 70°	111
29	Background spectrum recorded with scatter angle set at 130°	112
30	Relationship between average background intensity under each K shell spectral line observed and scatter angle	119
31	Variation of ^{57}Co Rayleigh scattering peak to uranium peak background intensity ratio with secondary collimation. The scatter angle is fixed at 130°	122

Number	Title	Page
32	Correlation between specimen thickness and the net specimen Compton scattering intensity	130
33	Photon energy calibration curve for the K X-ray experiment	135
34	The K X-ray spectrum from a uranium bearing ore containing 1.21% U_3O_8	136
35	Correlation between initial U $K\alpha_1$ intensity data and uranium concentration	154
36	Correlation of $U K\alpha_1$ intensity data as corrected by the matrix and thickness factors with uranium concentration	155
37	Photon energy calibration for the L X-ray experiment	164
38	Spectrum as observed with the L X-ray apparatus from a uranium bearing ore containing 0.038 % U_3O_8	171
39	Spectrum as observed with the L X-ray apparatus from a uranium bearing ore containing 1.21 % U_3O_8	172
40	Spectrum as observed with the L X-ray apparatus from a uranium bearing ore containing 9.95 % U_3O_8	173
41	Variation of U $L\alpha$ to Mo $K\alpha$ Compton intensity ratio with uranium concentration	176
42	Variation of U $L\alpha$ and Mo $K\alpha$ Compton peak intensities with uranium concentration	177
43	Photon energy calibration curve for the M X-ray experiment	185
44	Effect of electrodeposition time on the quantity of uranium deposited	190
45	Variation of electrolyte pH at 25° C with electro-deposition time	191
46	Spectrum as obtained with the M X-ray apparatus from 1.81×10^{-7} moles UO_2^{2+} electrodeposited on a stainless steel planchet	194
47	The observed intensities of the uranium $M\alpha, \beta$ and the lanthanum $L\alpha$ peaks versus moles of UO_2^{2+} electrodeposited	196

Number	Title	Page
48	Variation of uranium $M_{\alpha, \beta}$ to lanthanum L_{α} corrected intensity ratio with moles of UO_2^{2+} electrodeposited	198
49	Calibration curve prepared for analyzing low grade uranium ores or soils with the M X-ray apparatus	203
50	Photon energy calibration curve for the γ -spectroscopy experiment	212
51a	Gamma spectrum of a 0.027% ^{235}U standard	218
51b	Unfolding detail of figure 51a near 0.0925 MeV showing the ^{234}Th doublet	219
52a	Gamma spectrum of a 1.44% ^{235}U standard	220
52b	Unfolding detail of figure 52a	221
53a	Gamma spectrum observed from a 15.39% ^{235}U standard	222
53b	Unfolding detail of figure 53a	223
54	Attenuation of the ^{234}Th and ^{235}U γ -rays at various thicknesses of yellow cake	227
55	Linear correlation between the 0.0925 MeV ^{234}Th and the ^{235}U γ -ray intensities over a wide range of sample thicknesses	228
56	Narrow range calibration curve encompassing the natural uranium abundance	232
57	Log plot containing all the standards from 0.027% to 24.29% ^{235}U	233

LIST OF TABLES

Number	Title	Page
1	Quantum numbers	23
2	Inner core atomic energy levels	24
3	Commonly observed X-ray spectra lines	26
4	Some X-ray excitation parameters for uranium	50
5	Silicon absorption characteristics of some major uranium lines	50
6	Radionuclides used to standardize the energy calibrator	57
7	Reference sources used to calibrate the γ -spectrometer for the K X-ray experiment	71
8	Instrumental settings used for the K X-ray experimental work	72
9	Instrumental settings used for the L X-ray experimental work	79
10	Instrumental settings used for the M X-ray experimental work	92
11	Emissions from the ^{235}U reference source used to calibrate the γ -spectrometer	100
12	Instrumental settings used for the γ -spectroscopy work	101
13	Background intensities, with secondary collimation set at 5 cm	114
14	Background intensities with secondary collimation set at 12.5 cm	115
15	Background intensities with secondary collimation set at 20 cm	116
16	Background intensities with secondary collimation set at 27.5 cm	117
17	Background intensities with secondary collimation set at 35 cm	118
18	Variation of ^{57}Co Rayleigh scattering peak to uranium peak background intensity ratio with secondary collimation. Scatter angle is fixed at 130°	121

Number	Title	Page
19	Background data calculations required for determining the net specimen scattering intensity from the observed scattering intensity	124
20	Data illustrating the linear relationship between actual sample mass (g) and the net Compton scattering intensity	127
21	Data showing the correlation between net Compton scattering intensity and specimen thickness m (g/cm ²)	129
22	Calculation of mass absorption coefficients for an average uranium bearing granite	132
23	Calculation of net specimen scattering intensities from observed scattering intensities for Beaverlodge Lake ores	138
24	Calculation of net specimen scattering intensities from observed scattering intensities for Rabbit Lake ores	140
25	Calculation of net specimen scattering intensities from observed scattering intensities for Key Lake ores	141
26	Calculation of net specimen scattering intensities from observed scattering intensities for Elliot Lake ores	142
27	Initial data observed from Beaverlodge Lake ores required to evaluate the matrix and thickness factors	143
28	Initial data observed from Rabbit Lake ores required to evaluate the matrix and thickness factors	145
29	Initial data observed from Key Lake ores required to evaluate the matrix and thickness factors	146
30	Initial data observed from Elliot Lake ores required to evaluate the matrix and thickness factors	147
31	Determination of the matrix and thickness factors for Beaverlodge Lake ores	149
32	Determination of the matrix and thickness factors for Rabbit Lake ores	151
33	Determination of the matrix and thickness factors for Key Lake ores	152
34	Determination of the matrix and thickness factors for Elliot Lake ores	153

Number	Title	Page
35	Quantitative improvements in the linear curve fit for all of the ore types analyzed	157
36	Quantitative improvements in the linear curve fit for each of the ore types analyzed	158
37	Precision data used to determine the specimen error for the K X-ray experiment	161
38	Precision data used to determine the specimen loading error for the K X-ray experiment	162
39	Calculation of mass absorption coefficients for an average uranium bearing granite	167
40	Initial data measured from the L X-ray spectra of several uranium ores	174
41	Net peak intensities evaluated from experimentally measured intensities	178
42	Comparison of X-ray and fluorimetric analyses data	180
43	Precision data used to evaluate the L X-ray experiment specimen error	182
44	Precision data used to evaluate the L X-ray experiment specimen loading error	183
45	Calculation of mass absorption coefficients for an average uranium bearing granite	187
46	Data recorded for optimum electrodeposition time determination	189
47	Intensity data measured from M X-ray spectra taken of thin electrodeposited uranium specimens	195
48	Data for the U M X-ray analysis of several low grade ores	202
49	Precision data used to determine the specimen error for the M X-ray experiment	205
50	Data accumulated to evaluate the specimen loading error for the M X-ray experiment	206
51	Data recorded to determine the specimen preparation error using La^{3+} for the M X-ray experiment	208

Number	Title	Page
52	Data recorded to determine the specimen preparation error without La^{3+} for the M X-ray experiment	209
53	Application of the F ratio test for equality of variance resulting from specimen errors within the M X-ray experiment	210
54	Spectral interference encountered in measuring the ^{234}Th doublet intensity	214
55	Unfolded peak energies	216
56	Unfolded relative peak heights	217
57	Data used to evaluate the effect of specimen thickness on the $^{235}\text{U}/^{234}\text{Th}$ peak intensity ratio for yellow cake (approximately $\text{Na}_2\text{U}_2\text{O}_7$)	225
58	Data used to evaluate the effect of specimen thickness on the $^{235}\text{U}/^{234}\text{Th}$ peak intensity ratio for pure black oxide (U_3O_8)	226
59	Data observed from wide range uranium isotope standards	230
60	Data observed from narrow range isotope standards	231
61	$^{235}\text{U}/^{238}\text{U}$ ratios from some Canadian ores	235
62	Data used to determine the specimen error in the γ -ray spectroscopy experiment	
63	Data used to determine the specimen loading error in the γ -ray spectroscopy experiment	238
64	Precision data collected to determine the spectral unfolding error at 0.027% $^{235}\text{U}_3\text{O}_8$	240
65	Precision data collected to determine the spectral unfolding error at 1.44% $^{235}\text{U}_3\text{O}_8$	241
66	Precision data collected to determine the spectral unfolding error at 15.39% $^{235}\text{U}_3\text{O}_8$	242
67	Unfolding precision summary for the three concentration ranges	243

1. INTRODUCTION

In recent years, computerized process control has received widespread application in industrial circuits. During this period the cost of central processing units and input-output equipment has decreased substantially. Real-time operating computer systems oriented toward the requirements of industrial process control have been developed. Operation of such systems results in reduced costs and optimized product yields through improved efficiencies. Installation of this technology has generally been limited to industries of a secondary manufacturing nature, where initial input parameters which dictate the required processing, were accurately known. An early example may be cited from the automotive industry. In this case, a particular automobile is customer ordered from a possible wide range of models and options. These initial parameters are fed into the central processing unit to effectively control the production of the unit, i.e. the proper components arrive at the correct time to the appropriate location in the assembly line for fabrication of the final product. Later applications of computer processing can be found in situations where the input parameters are directly supplied by an in situ analysis of some form. Often, straightforward measurements of pH, temperature, flow rates or %transmittance etc., are all that is required to initiate computerized process control in many industrial streams such as those encountered in the chemical industries. Overall, the primary industries have benefitted relatively little by these advancements in computer hardware capability, because the initial input parameters cannot be defined with sufficient rapidity and/or accuracy.

However, in Canada the primary metallurgical extraction industries are currently moving towards adapting such techniques to their process streams.

Naturally, the analytical technique employed to determine the concentration of the metal extracted in a particular process is an essential factor toward the successful operation of a computerized process control system. It should possess the capability to determine the desired metal content, in situ, for specimen forms consisting of solids, solutions and slurries. No analytical method can deal with as wide a variety of specimen forms as X-ray spectroscopy. In addition to performing a nondestructive analysis, this method has sufficient sensitivity, speed, precision and accuracy to meet the desired requirements in most cases. Output data can be readily interfaced with the computing system to effect process control. Hence installations of such systems to-date in the metallurgical extraction industry have incorporated some form of X-ray analysis.

As in all instrumental analytical methods, the X-ray techniques are comparative ones and suitable standards of accurately known composition are required for calibration. The standards must have, as nearly as possible, the same chemical composition as the samples in both X-ray and other optical spectrochemical analyses. However, in the X-ray spectroscopy case, standards must also have the same physical form as the samples: solid metal can be analyzed only with solid standards, powders packed in cells only with similarly packed powder standards, solutions only with solutions etc. Moreover, solid standards must have the same surface texture as the samples and powders the same particle size dis-

tribution and packing density. These effects are particularly inconvenient when the substance must be analyzed in a number of physical forms. The limiting factor in the installation of computerized process control systems in the primary metallurgical extraction industry is that the necessary input parameters cannot be supplied with sufficient accuracy. This is directly attributable to these disadvantages.

With specific reference to the operation of a uranium extraction and concentration plant, much can be done to alleviate the above problems. An understanding of the attenuation of electromagnetic radiation as it traverses matter is essential. On the atomic scale, photons interact with atoms comprising the sample medium through several mechanisms. Each mechanism is responsible for the emission of characteristic and detectable radiation. Photon encounters are distinctly and substantially different with uranium atoms than they are for atoms in which uranium is normally associated with in a natural geological sample. This fact may be taken advantage of to mitigate the encumbrances limiting the accuracy of on-stream industrial analyses as applied to the primary uranium extraction industrial process.

Since uranium nuclei are unstable, the possibility exists of performing isotope analyses by γ -ray spectroscopy. These methods are also well suited for adoption to on-stream activity measurements. γ -ray techniques however, are comparative methods as well and are subject to the same restrictions (although generally not to the same extent) regarding standards for calibration as experienced for the X-ray case. The discovery, in 1972, of a naturally occurring fission reactor at Oklo, Gabon has initiated a search for similar phenomena in other parts of the

world. Certain uranium mineral zones of northern Saskatchewan have been cited as logical locations for such a reactor. At present, uranium concentration mills of northern Saskatchewan do not conduct uranium isotope analyses, principally due to the lack of a suitable technique. However, the chances of identifying a past nuclear disturbance would be greatly enhanced if isotope analyses could be routinely performed at the uranium extraction plant location.

As such, there are two major objectives of this thesis, (i) to investigate Canadian uranium ores for accurate uranium content by X-ray spectroscopy, and (ii) to develop a technique to determine the uranium isotope ratio by γ -ray spectroscopy. The approach adopted in the evolution of the methods reflects, where possible, the suitability of the final techniques for on-stream industrial analysis followed by subsequent computer processing. Chapter 2 presents a description of the interaction mechanism of atoms with photons of electromagnetic radiation. Particular emphasis is placed on the differences between photon encounters with uranium atoms and silicon atoms. The latter was chosen since its attenuation characteristics are similar to those of the host elements found in a uranium bearing granite. Equations are written to show quantitatively how these differences will effect the accuracy of the final X-ray or γ -ray analyses. The distinctions and in some cases similarities are discussed in Chapter 3. Based on these results, several experimental techniques were formulated in order to best accomplish the aims of the thesis.

2 BACKGROUND FUNDAMENTALS

2.1. Attenuation of electromagnetic radiation by matter

As X-rays and γ -rays are passed through matter their initial intensities, I_0 , are decreased according to the Lambert law,

$$I = I_0 e^{-\mu m} \dots \dots \dots 2.1$$

where μ and m are the total absorption coefficient and thickness respectively of the absorber. Four absorption coefficients are derived from equation 2.1 and in general use. (i) the linear absorption coefficient μ_L gives absorption per unit thickness per unit area and has units of cm^{-1} , (ii) the mass absorption coefficient μ_m gives absorption per unit mass per unit area and has units of cm^2/g , (iii) the atomic absorption coefficient σ_{TOT} or cross section gives absorption per atom per unit area and has units of barns ($10^{-24} \text{ cm}^2/\text{atom}$), and (iv) the molar absorption coefficient μ_{mol} gives the absorption per mole per unit area and has units of cm^2/mole .

Of these four coefficients, the mass absorption coefficient is by far the most useful in γ -ray and X-ray analytical work. It is an atomic property of each element - independent of chemical or physical state - and is a function of wavelength and atomic number. Throughout this thesis, the symbol μ will indicate the total mass absorption coefficient and it is related to the linear absorption coefficient by

$$\mu = \mu_L / \rho \dots \dots \dots 2.2$$

The practicability of using the total mass absorption coefficient

becomes immediately obvious when the mass absorption coefficient of a compound, solution or mixture of elements is required. For elements 1, 2, 3, ..., i, ..., m in weight fraction $r_1, r_2, r_3, \dots, r_1, \dots, r_m$ the total mass absorption coefficient is simply given by the sum of the products of the mass absorption coefficient and the weight fraction of each element

$$\mu_{1,2,3,\dots,i,\dots,m} = \sum_{i=1}^m \mu_i r_i \dots \dots \dots 2.3$$

The total mass absorption coefficient is the result of several phenomena each possessing its own mass absorption coefficient

$$\mu = \sigma + \tau + \kappa + \sigma_{ph.n} \dots \dots \dots 2.4$$

in which σ is the total mass scattering coefficient, τ is the photoelectric mass absorption coefficient, κ is the positron-electron pair production mass absorption coefficient, and $\sigma_{ph.n}$ is the photonuclear mass absorption coefficient. Each of these coefficients can be written in the same variety of units as formerly described for μ . For photon energies less than 10 MeV, $\sigma_{ph.n}$ is negligible and the value of κ is zero for energies under 1.022 MeV. Since the energies utilized in this work range from approximately 1 to 200 keV, only the first two terms of μ are of significance and these are discussed individually in the following sections.

2.2. Scattering

The total mass scattering coefficient consists of the sum of several components. Four main types of scattering which can be distinguished are unmodified, modified, coherent and incoherent. The photons

involved in an unmodified scattering process undergo no change in energy while modified scattered photons are observed at an energy lower than the incident radiation. Coherent scattering occurs in such a way that there exists a phase relationship between the incident and scattered X-rays and γ -rays. Incoherent scattering occurs without any such phase relationship. Since modified scattering is necessarily incoherent because of the change in wavelength, it is almost universal practice by γ -ray and X-ray spectroscopists to regard these as synonymous. Also no distinction is generally made between coherent and unmodified scattering. This poses no practical problems although all unmodified scattering is not necessarily coherently scattered. Experimentally, generally two scattered lines are observed, one possessing the energy of the incident radiation and the other shifted to lower energies. Historically these have been named Rayleigh and Compton scattering, respectively.

Rayleigh (coherent) and Compton (incoherent) scattering were formerly regarded as a nuisance as scattered lines complicate the spectrum, increase backgrounds and increase the possibility of spectral line interference. However, scattered X-rays may be beneficial in many ways and require further description.

2.2.1. Rayleigh scattering

In the literature of X-ray and γ -ray analysis Rayleigh scattering is variously referred to as unmodified, elastic or coherent scattering. The Rayleigh scattering cross section is given by:

$$\sigma_R = \frac{2}{3} r_0^2 \int_{-1}^1 (1 + \cos^2 \theta) F(x, Z) 2\pi d(\cos \theta) \dots \dots \dots 2.5$$

in which r_0^2 = the square of the classical electron radius

θ = the angle between the incident and scattered photon directions

$2\pi d(\cos \theta) = d\Omega$ = the solid angle between cones with angles θ and $\theta + d\theta$

Z = atomic number

$F(x,Z)$ = atomic form factor

x = momentum transfer parameter

Many theoretical models and approximations have been used to evaluate the atomic form factor for all elements, but a discussion of their merits is not warranted here, further details can be found in references (1-5). Tables of recently published atomic form factor values are given in reference (1). A simple description of the phenomenon is as follows: In Rayleigh scattering the incident X-rays or γ -rays induce the electrons in the irradiated matter to oscillate at the same frequency as the incident radiation. The oscillating electrons then re-emit photons in all directions, at the same frequency of and maintaining a phase relationship with, the incident radiation.

Equation 2.5 shows that σ_R has an angular, atomic number and energy dependence. The variations of σ_R with energy for a high Z element, uranium, and a low Z element, silicon, can be seen in figure 1. For a fixed atomic number Z , the cross section is largest when the energy of the incident radiation is of the same order as the binding energy of the orbital electrons. Rayleigh scattering cross sections, when correlated with energy, exhibit a maximum at less than 1 keV and decrease very rapidly to low values with larger incident photon energies. The fact

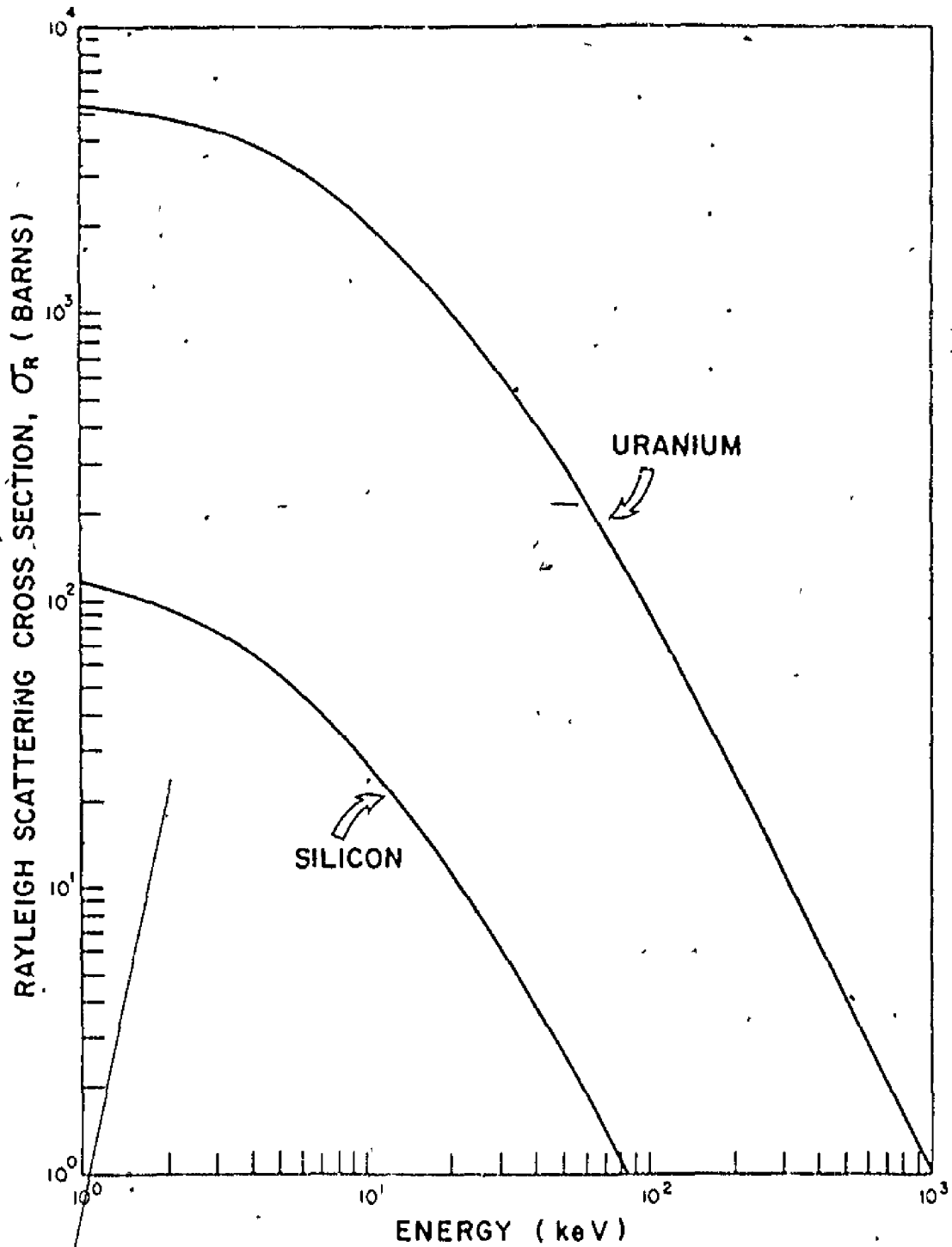


Fig. 1 Rayleigh scattering cross section as a function of incident photon energy for uranium and silicon (taken from reference (6))

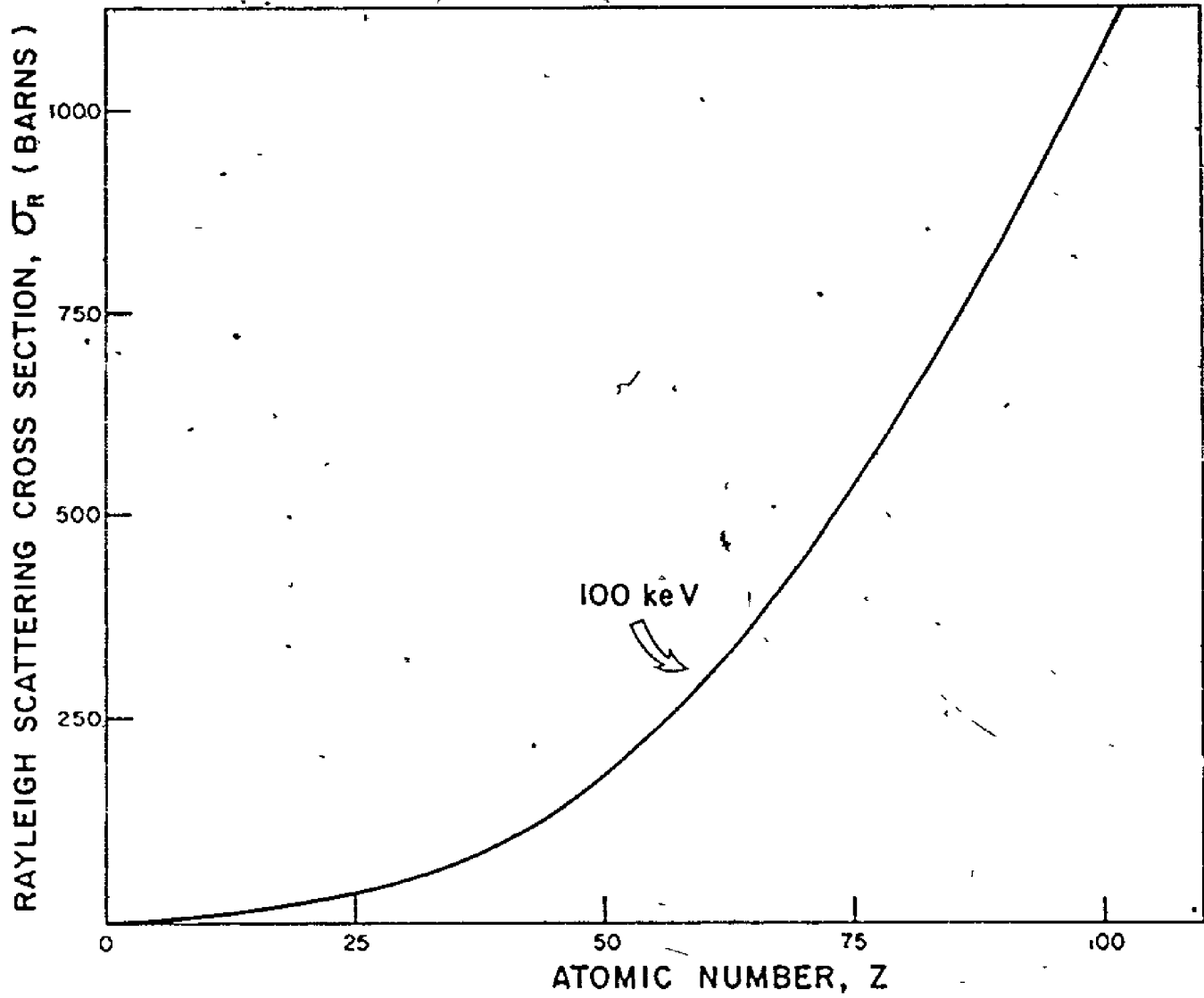


Fig. 2. Rayleigh scattering cross section as a function of atomic number (Z) for 100 keV incident photons (taken from reference (6))

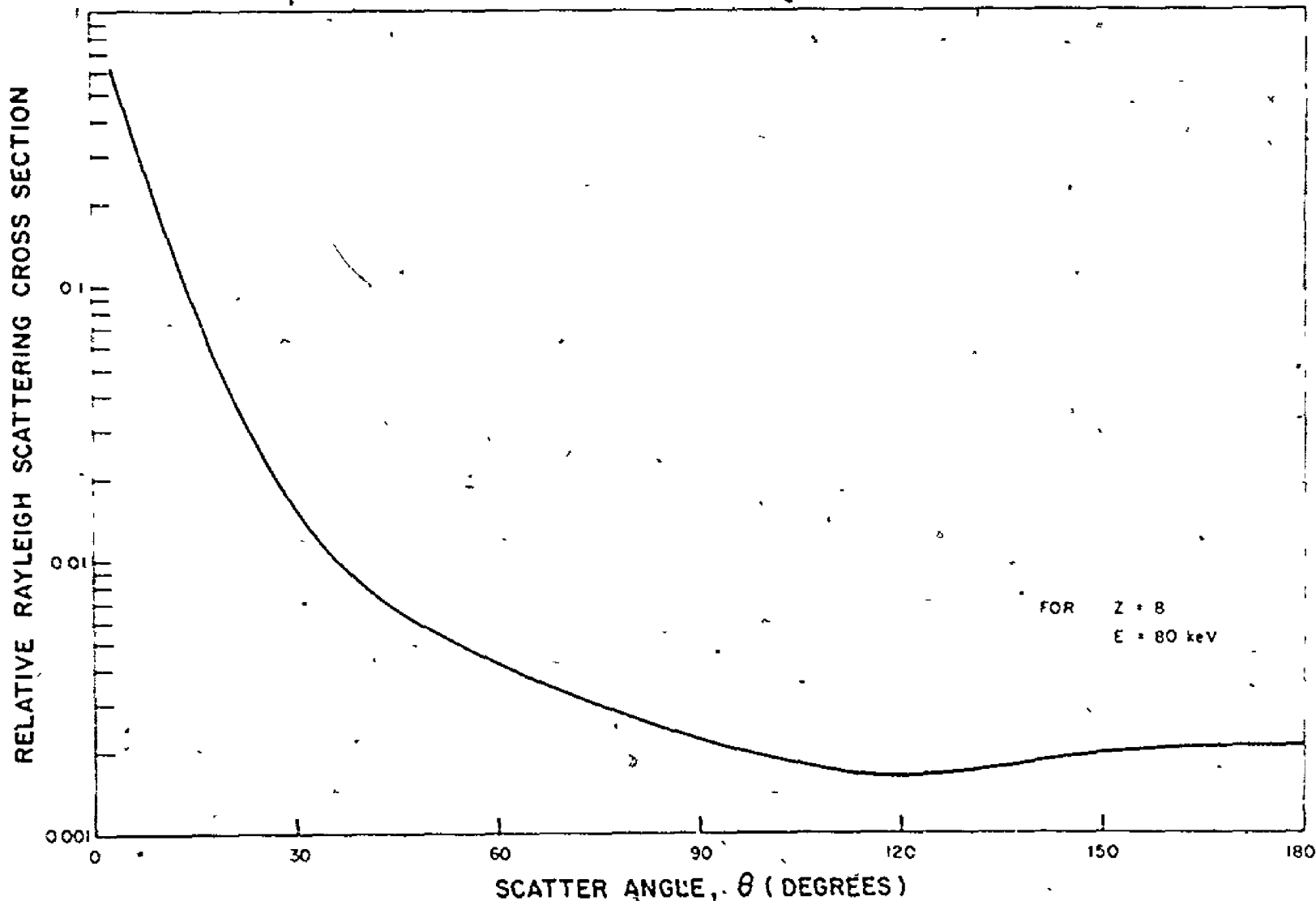


Fig. 3. Variation of Rayleigh scattering cross section with scatter angle for 80 keV photons impinging upon oxygen (taken from reference (7))

that σ_R is very sensitive to atomic number can be seen in figure 2. Typically σ_R is proportional to Z^{2-3} . For a specific example, the probability of Rayleigh scattering for a uranium atom is 130 times that for silicon at 100 keV. The values of σ_R plotted in figures 1-2 are total Rayleigh scattering cross sections, that is, they have been integrated over all solid angles as described in equation 2.5. If this scattering is measured at a particular source, sample and detector geometry, it then typically varies as shown in figure 3. There is a strong dependence of σ_R for the forward ($\theta=0^\circ$) scattering angles with a characteristic minimum for medium angle scattering.

2.2.2. Compton scattering

For practical γ -ray and X-ray analysis, Compton scattering is equivalently referred to as incoherent, modified and inelastic scattering. Both the particle nature and the wave nature of photons and electrons can be used to loosely describe this phenomenon. In the first case, the incident photon collides with a loosely bound electron in an outer orbital of an atom. The electron recoils under the impact, leaving the atom and carrying away some of the energy of the photon, which is deflected with a corresponding loss of energy. Conservation of energy and momentum is observed as the sum of these parameters for the scattered photon and the recoil electron always equals those of the incident photon. In the second case, the initial and final states of the recoil electron mutually interfere to form a space grating of standing matter waves that reflects the incident γ or X-radiation in much the same manner as the space grating of atomic layers in a crystal. The change in energy is attributed to the Doppler shift caused by the

recoil velocity of the reflecting space grating. The Compton scattering cross section is calculable from:

$$\sigma_c = \frac{1}{2} r_0^2 \int_{-1}^1 \frac{[1+k(1-\cos \theta)]^{-2} [1+\cos^2 \theta + \frac{k^2(1-\cos \theta)^2}{1+k(1-\cos \theta)}]}{S(x,Z)} 2\pi d(\cos \theta) \cdot 2.6$$

in which all the symbols used are identical to those defined in the calculation of σ_R , but in addition

k = incident photon energy in units of electron masses

$S(x,Z)$ = incoherent scattering factor

As was the case in describing the atomic form factor, $S(x,Z)$ cannot be analytically calculable for all elements. Various theoretical considerations used in the evaluation of $S(x,Z)$ can be found in references (1-5). Reference (1) also contains tables of $S(x,Z)$.

In general terms, the proportion of Compton scattering increases as the energy of the incident radiation increases to a maximum value, occurring between 30-100 keV as shown in figure 4 for uranium and silicon. The Compton scattering cross section varies more slowly with incident energy than does the Rayleigh scattering cross section. At low energies Rayleigh scattering is the prominent scatter mechanism and at high energies Compton scattering dominates. Compton scattering however is much less sensitive to atomic number. Figure 5 shows a near linear correlation between σ_c and photon energy. The relative probability for Compton scattering as a function of scatter angle shows a minimum for right angle scattering and maxima for forward and backward scattering but in this case the position and magnitude of these features are also a function of energy. Figure 6 shows the relative angular dependence (i.e. normalized to forward scattering cross section) of σ_c at 10 keV

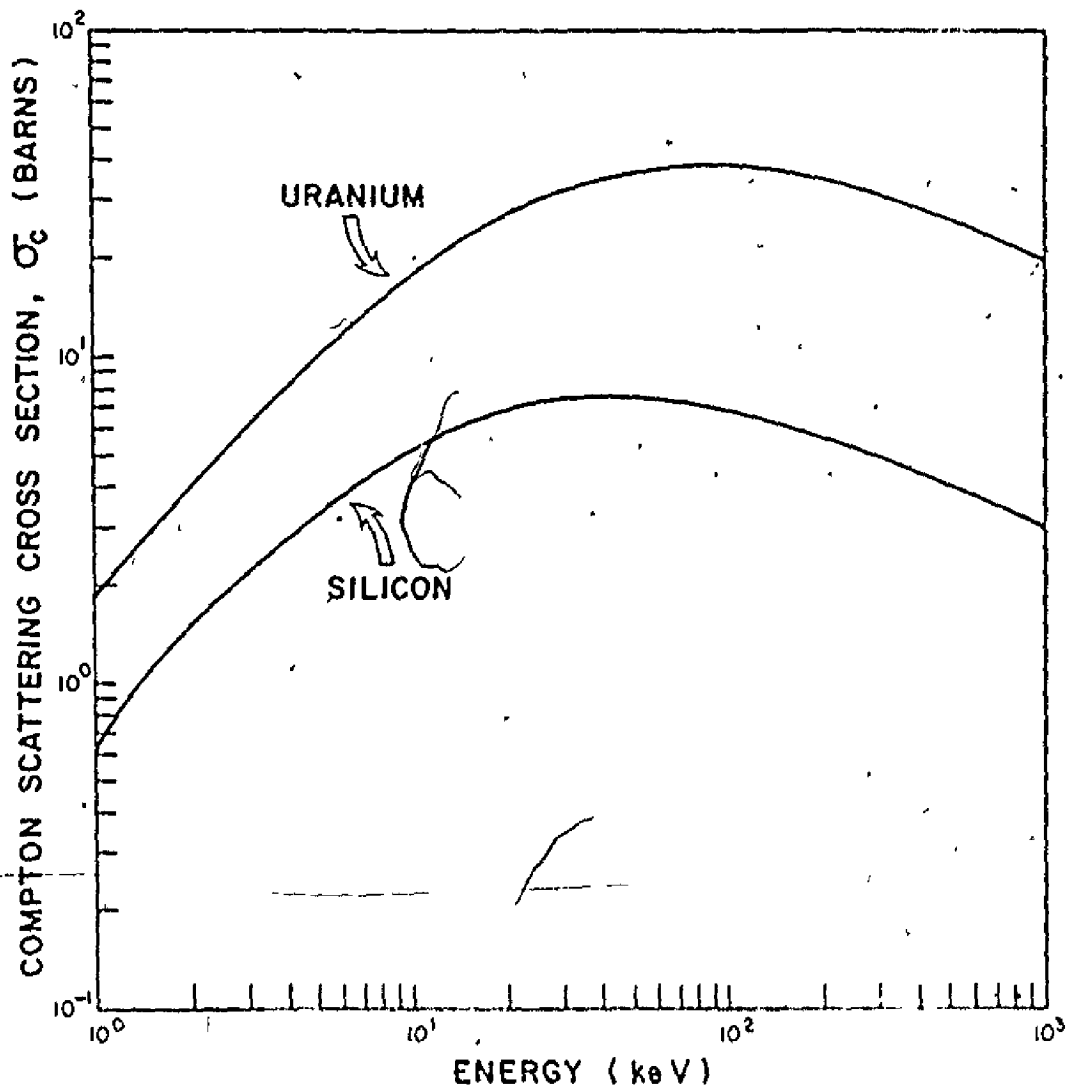


Fig 4. Compton scattering cross section as a function of incident photon energy for uranium and silicon (taken from reference (v))

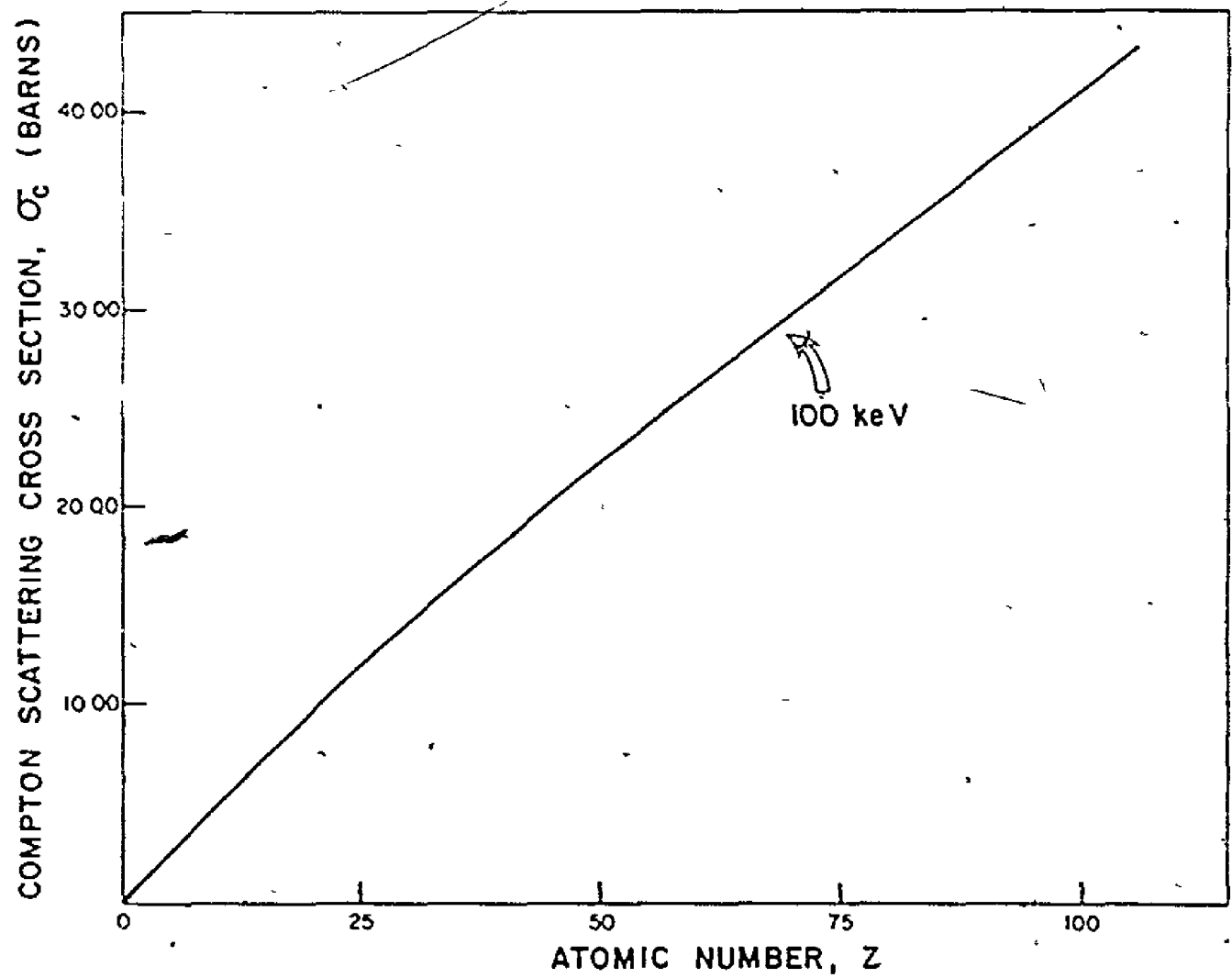


Fig. 5. Nearly linear correlation of Compton scattering cross section with atomic number (Z) for 100 keV incident photons (taken from reference (6)).

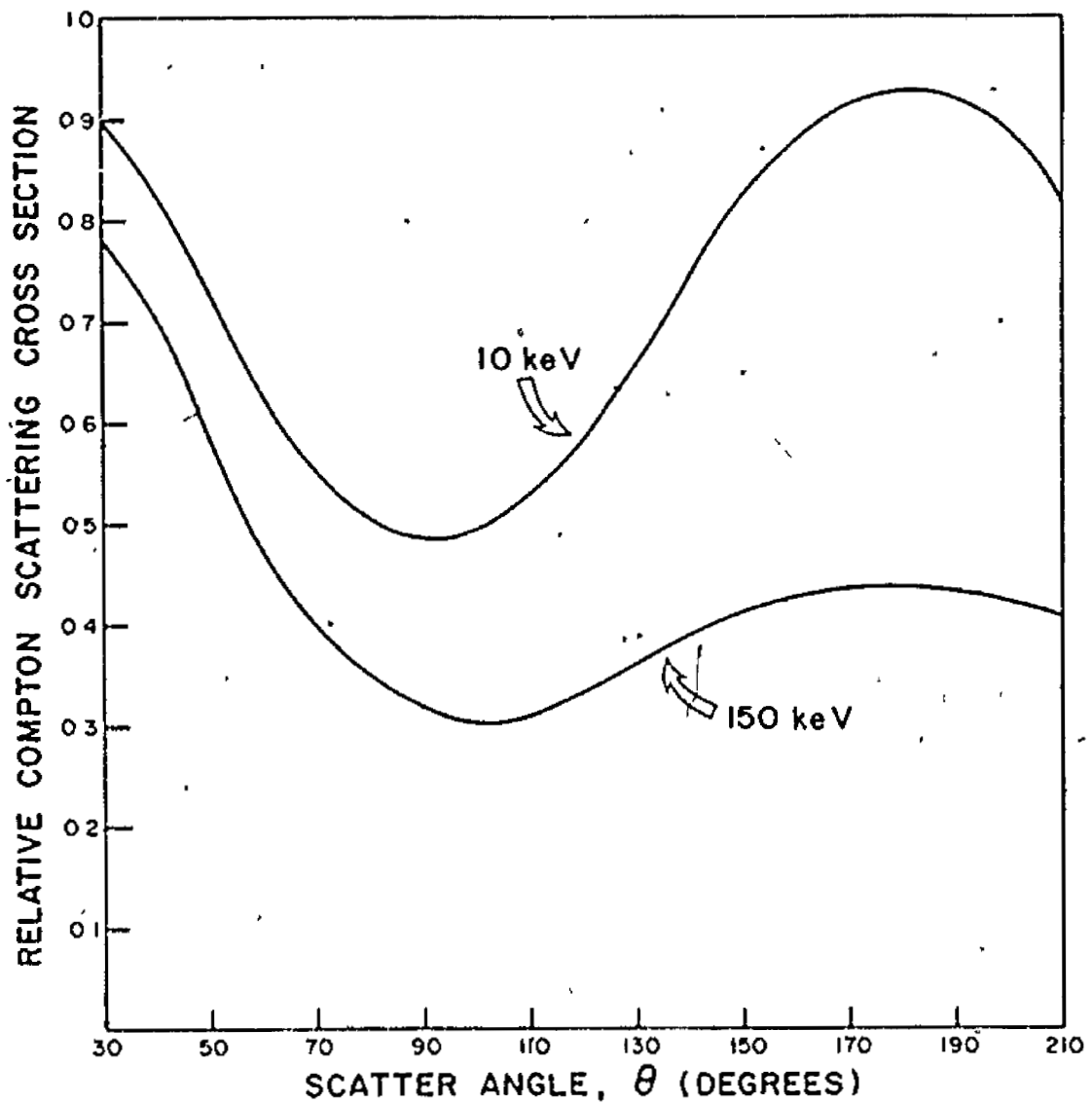


Fig. 6 Typical correlation of relative Compton scattering cross section with scatter angle for 10 and 150 keV photons (taken from reference (8))

and 150 keV.

Because the encounter obeys the laws of conservation of energy and momentum, the energy of the deflected photon is simply related to the incident photon energy through the scatter angle θ . The equation used to compute the energy of the scattered photon is:

$$E' = E / (1 + k(1 - \cos \theta)) \dots \dots \dots 2.7$$

in which all symbols have been previously defined except

E' = energy of the scattered photon

E = energy of the incident photon

The energy difference ($E - E'$) is commonly referred to as the Compton shift. For a fixed energy, the shift is zero for forward Compton scattering ($\theta = 0^\circ$) with a maximum for backward scattering ($\theta = 180^\circ$). The size of the shift is also a function of energy. With the low energies (< 10 keV) commonly encountered in X-ray analysis, the shifts are small, but when the incident photon energy approaches the equivalent mass of an electron (511 keV) the value of k becomes appreciable and the corresponding Compton shifts are relatively large.

2.3. The photoelectric effect

The fundamental basis for production of characteristic atomic X-rays is the photoelectric effect. The photoelectric cross section, τ , is a measure of the probability that this interaction will occur. The process of photon absorption in the visual range is fundamentally different from in the X-ray region. In the first case, a photon is absorbed by an outer orbital and thereby an electron is raised to an unoccupied but bound energy level. In the latter X-ray case, we are dealing with

transitions among inner core electrons whose orbitals are occupied. The most probable electron transition resulting from photon absorption is then to promote an inner core electron to the continuum leaving behind an inner core electron vacancy. In order to create such a vacancy, a 'critical' photon energy equal to a designated electron binding energy is required. As figure 7 illustrates, when τ is plotted against incident photon energy, characteristic discontinuities are exhibited as each 'critical' energy is approached. These are called absorption edges and maximum values of τ occur when the photon energy is just above the absorption edge.

The binding energies of inner core electrons and consequently the energies of their observed absorption edges increase in a regular fashion with atomic number. The corresponding absorption edges for uranium therefore occur at much higher energies than their counterparts for silicon, as is shown in figure 7. τ is a function of incident photon energy and atomic number. In this figure, the slope between absorption edges is approximately -3 indicating the inverse cube dependence of the photoelectric cross section with energy. This relationship remains valid up to 1 MeV where τ changes to a high-energy-limit, E^{-1} , dependence. Below 1 keV, the photoelectric cross section becomes characterized by outer-subshell maxima and minima with little regularity as a function of E and Z . To illustrate the dependence of τ on atomic number, the photoelectric cross section at 100 keV is plotted in figure 8 for most elements. Generally, for a photon incident energy substantially above an absorption edge, τ increases as Z^4 indicating a very strong dependence on atomic number.

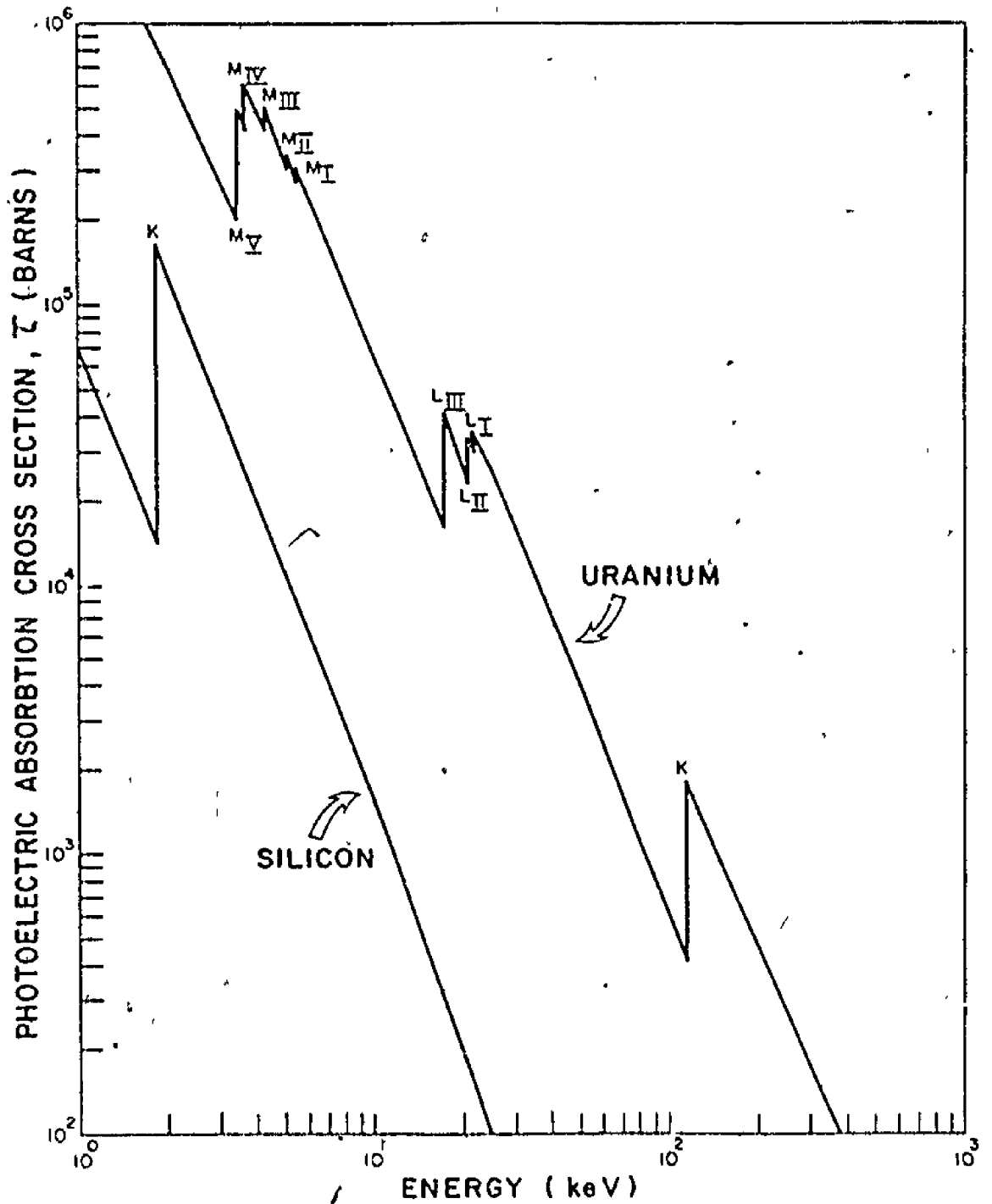


Fig 7 Photoelectric cross section as a function of energy for uranium and silicon (taken from reference (6))

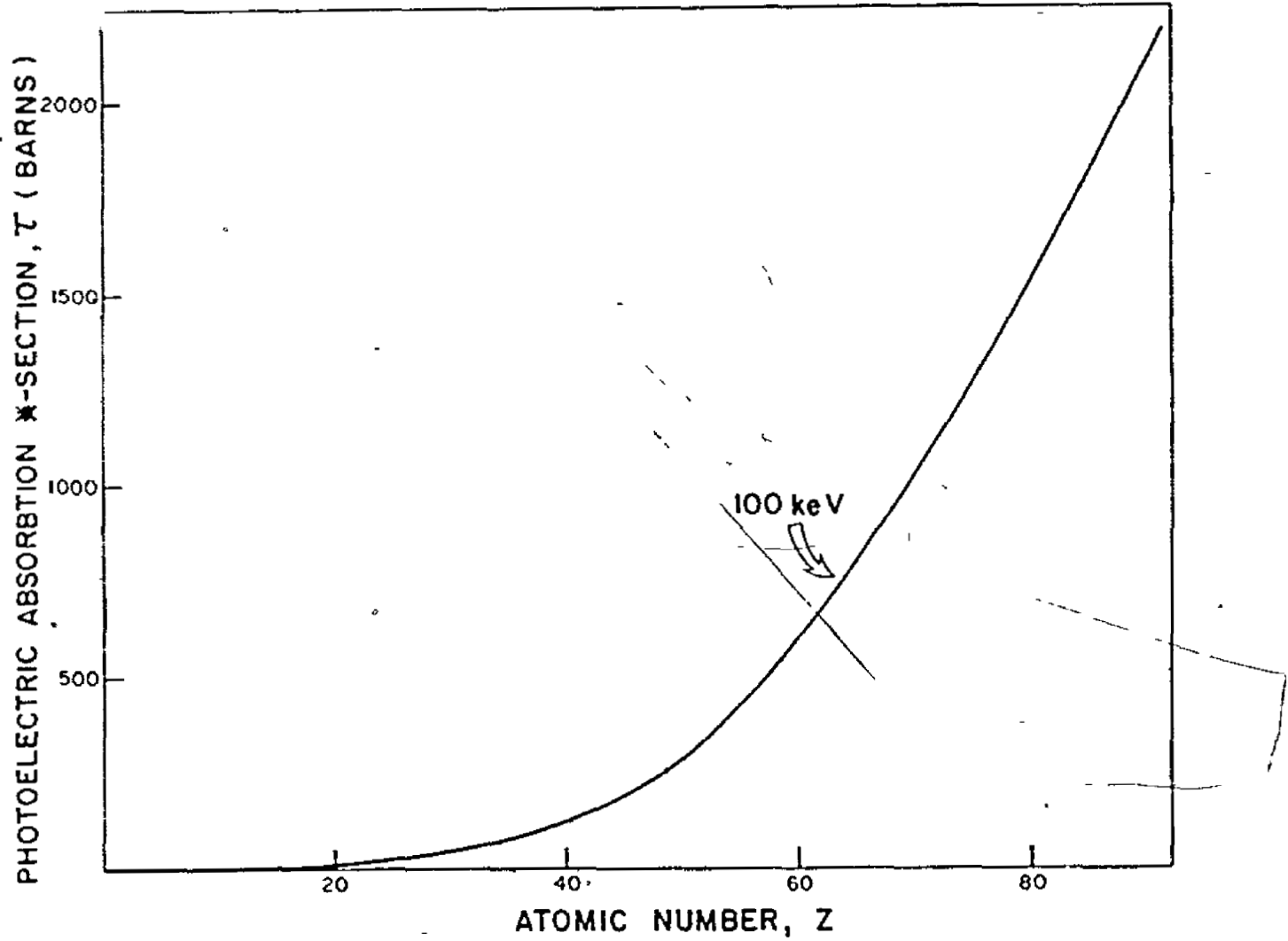


Fig. 8. Photoelectric cross section as a function of atomic number for 100 keV incident photons (taken from reference (6))

2.4. Atomic structure and X-ray spectra

An understanding of the nature and origin of characteristic X-ray line spectra requires some knowledge of atomic structure. For illustrative purposes, a simplified model of the atom such as the Bohr structure is sufficient. As can be seen from figure 9, the atom consists of a dense central nucleus containing all of its Z protons and $A-Z$ neutrons, with its corresponding Z electrons revolving about the nucleus. The electrons are grouped into shells designated K, L, M, N, etc. in order of increasing distance from the nucleus. The electrons in each shell are classified further with respect to angular momentum and direction of spin. Each of these parameters - shell, momentum and spin - is designated by a discrete quantum number. Each individual electron possesses a unique set of quantum numbers. Table 1 lists these quantum numbers and the allowed values each may assume for an electron in an atom. From figure 9 it is evident that on the basis of these quantum numbers, the electrons fall into subgroups - one K, three L, five M and seven N, etc. These are the subgroups of principle significance in X-ray spectroscopy. Table 2 shows how the subshell energy levels can be derived by appropriate assignment of quantum numbers n , l , s and j .⁽¹⁰⁾ Included in table 2 for comparison, are the optical and X-ray notations used to describe the same atomic states.

As discussed in section 2.3., characteristic discontinuities in the photoelectric cross section known as absorption edges occur at discrete energies. These 'critical' energies correspond to the energy levels of the various atomic states. To create a K shell vacancy, for example, the incident photon energy must be equal to or greater than the

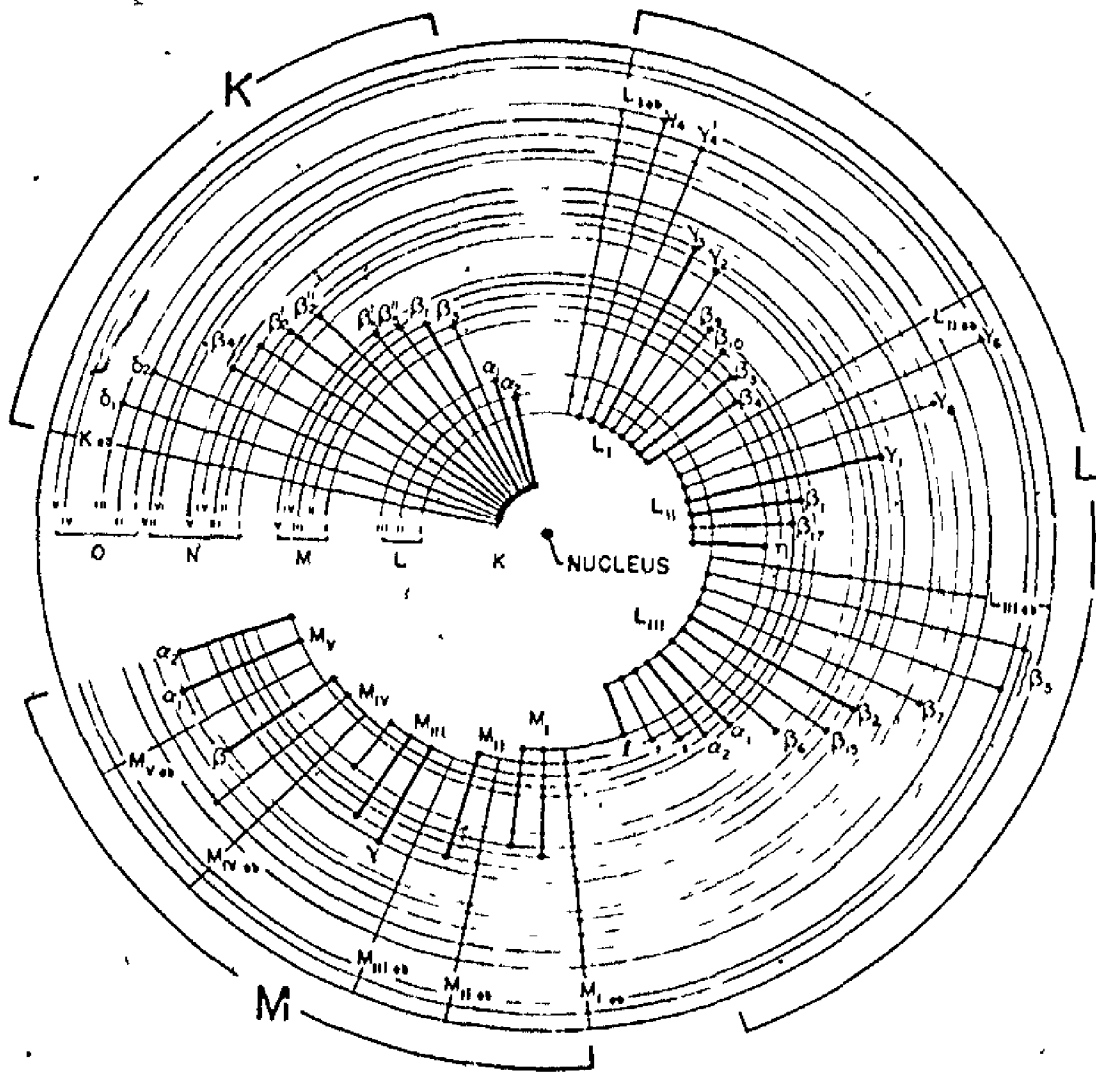


Fig. 9. Simplified model of the atom illustrating the origin of the principle X-ray lines (taken from reference (9))

Table 1
Quantum numbers

Symbol	Name	Allowed Values	Selection Rules
n	principle	$1, 2, 3, \dots, n$ K, L, M, N, \dots	$\Delta n \neq 0$
l	azimuthal	$0, 1, 2, \dots, (n-1)$ s, p, d, f, \dots	$\Delta l = \pm 1$
m	magnetic	$-\ell, \dots, 0, \dots, +\ell$	--
s	spin	$\pm \frac{1}{2}$	--
j	inner precession	$l \pm \frac{1}{2}$, except $j \neq 0 - \frac{1}{2}$	$\Delta j = +1$ or 0

Table 2
Inner core atomic energy levels

Quantum Numbers				Number of Electrons in Filled Subshell (2j + 1)	Atomic State	
n	l	s	j		Optical Notation	X-ray Notation
1	0	$\pm 1/2$	$1/2$	2	$1^2S_{1/2}$	K
2	0	$\pm 1/2$	$1/2$	2	$2^2S_{1/2}$	L _I
2	1	-1/2	$1/2$	2	$2^2P_{1/2}$	L _{II}
2	1	+1/2	$3/2$	4	$2^2P_{3/2}$	L _{III}
3	0	$\pm 1/2$	$1/2$	2	$3^2S_{1/2}$	M _I
3	1	-1/2	$1/2$	2	$3^2P_{1/2}$	M _{II}
3	1	+1/2	$3/2$	4	$3^2P_{3/2}$	M _{III}
3	2	-1/2	$3/2$	4	$3^2D_{3/2}$	M _{IV}
3	2	+1/2	$5/2$	6	$3^2D_{5/2}$	M _V
4	0	$\pm 1/2$	$1/2$	2	$4^2S_{1/2}$	N _I
4	1	-1/2	$1/2$	2	$4^2P_{1/2}$	N _{II}
4	1	+1/2	$3/2$	4	$4^2P_{3/2}$	N _{III}
4	2	-1/2	$3/2$	4	$4^2D_{3/2}$	N _{IV}
4	2	+1/2	$5/2$	6	$4^2D_{5/2}$	N _V
4	3	-1/2	$5/2$	6	$4^2F_{5/2}$	N _{VI}
4	3	+1/2	$7/2$	8	$4^2F_{7/2}$	N _{VII}

energy of the atomic state K in order to promote the electron to the continuum. The energy at which this occurs is referred to as the K shell absorption edge and is generally written as K_{ab} . The removal of an inner core electron from its appropriate shell constitutes an excitation of the atom, raising its energy above the stable configuration. The atom will subsequently seek to regain a stable energy by reverting back to the original electronic configuration. This takes place by an electron transition from some higher atomic energy level to the energy level of the vacant site. The energy difference between these two atomic states, is a unique property of the atomic number of the nucleus. An X-ray photon is then emitted whose energy is characteristic of this difference and thereby of the atom. The X-ray or fluorescent photon must have an energy less than that originally absorbed. Electron transitions cannot occur from any higher level to any lower state. Only certain transitions are 'allowed' according to the selection rules (11) listed in table 1. The resulting atomic emission consists of a series of discrete X-ray spectral lines for each shell characteristic of the emitting element and having various relative intensities. Figure 9 shows the principle lines observed in X-ray analysis and the appropriate absorption edges.

The notation almost universally used to identify X-ray spectral lines is the Siegbahn designation scheme. The line is identified by (i) the symbol of the chemical element, (ii) the symbol of the series (K, L, M, N, etc.) i.e. the subshell the vacancy was created in and (iii) a lower-case Greek letter, usually with a numerical subscript to denote the particular line in a series. Examples of this notation are. Cu $K\alpha_1$, Se $K\beta_1$, W $L\alpha_2$, U $M\alpha_1$, and Au Ly_1 . The $\alpha_{1,2}$ lines are always the strongest

Table 3
Commonly observed X-ray spectral lines

Siegbahn Line Notation	Atomic Level Transition
$K\alpha_1$	KL_{III}
$K\alpha_2$	KL_{II}
$K\beta_1$	KM_{III}
$L\alpha_1$	$L_{III}M_{IV}$
$L\alpha_2$	$L_{III}M_{IV}$
$L\beta_1$	$L_{II}M_{IV}$
$L\beta_2$	$L_{III}N_{V}$
$L\gamma_1$	$L_{II}M_{IV}$
$L\gamma_2$	$L_{I}N_{II}$
$M\alpha_1$	$M_{V}N_{VII}$
$M\alpha_2$	$M_{V}N_{VI}$

in the series and generally originate from $\Delta n = 1$ transitions. The β_1 line is commonly the second strongest line. The β and γ lines arise from $\Delta n = 1, 2$ or 3 transitions. Aside from these conventions, the notation is not systematic. However, the line resulting from a given transition in any element is always given the same symbol, i.e. an $L\beta_2$ line always results from a $L_{III}N_V$ transition. In practice, this poses little problem because only the most intense $\alpha, \beta,$ and γ lines are sufficiently strong to be analytically significant. Some of the frequently observed spectral lines and their respective origins ⁽¹²⁾ are given in table 3.

2.4.1 The Auger effect

The creation of an inner core electron vacancy by the photoelectric effect or some other process does not always result in the emission of characteristic X-ray fluorescence. The energy of the transition may also be released as an emitted electron known as an Auger electron. In both cases, the energy of the X-ray photon or Auger electron is characteristic of the emitted element. This process is competitive with X-ray fluorescence and is known as the Auger effect although occasionally referred to as radiationless transition or internal conversion.

The mechanism of the Auger effect can be described in two ways. In the first case, an initial inner core vacancy is created and then filled by an electron accompanied by the emission of an Auger electron from the appropriate level. In the second case, the initial vacancy and transition results in the production of an X-ray photon in the usual manner. However, in this case, the photon undergoes an internal photoelectric absorption, with the expulsion of an electron, and does not

leave the atom of its origin, hence the name internal conversion.

Because Auger electrons can create further vacancies, additional photons or Auger electrons may be emitted. This leads to multiple vacancy creation and complicates some areas of the X-ray fluorescent spectrum. Electron transitions in such multiply ionized atoms result in emissions of lines having energies slightly different from those emitted by the corresponding electron transition in singly charged atoms. Such lines are known as satellite lines. For elements of high and intermediate atomic number, satellite lines usually have low intensity and are of little significance in X-ray spectroscopy. However, for very light elements, boron to aluminum, they may be relatively intense.

The Auger effect is also more favoured in elements of low atomic number because the characteristic X-ray fluorescence is of lower energy and more readily internally absorbed. For the same reason, the effect is more marked on the L and M series than for the K series of any given element.

2.4.2. Fluorescent yield

The fluorescent yield is the probability that the filling of a vacancy in a specified shell results in an emission of a characteristic X-ray photon. For example, the K shell fluorescent yield is defined by:

$$\begin{aligned}\omega_K &= \frac{\sum (n_k)_i}{N_k} \\ &= \frac{nK\alpha_1 + nK\alpha_2 + nKB_1 + \dots}{N_k}\end{aligned}\quad \dots \dots \dots 2.8$$

where ω_K is the K shell fluorescent yield

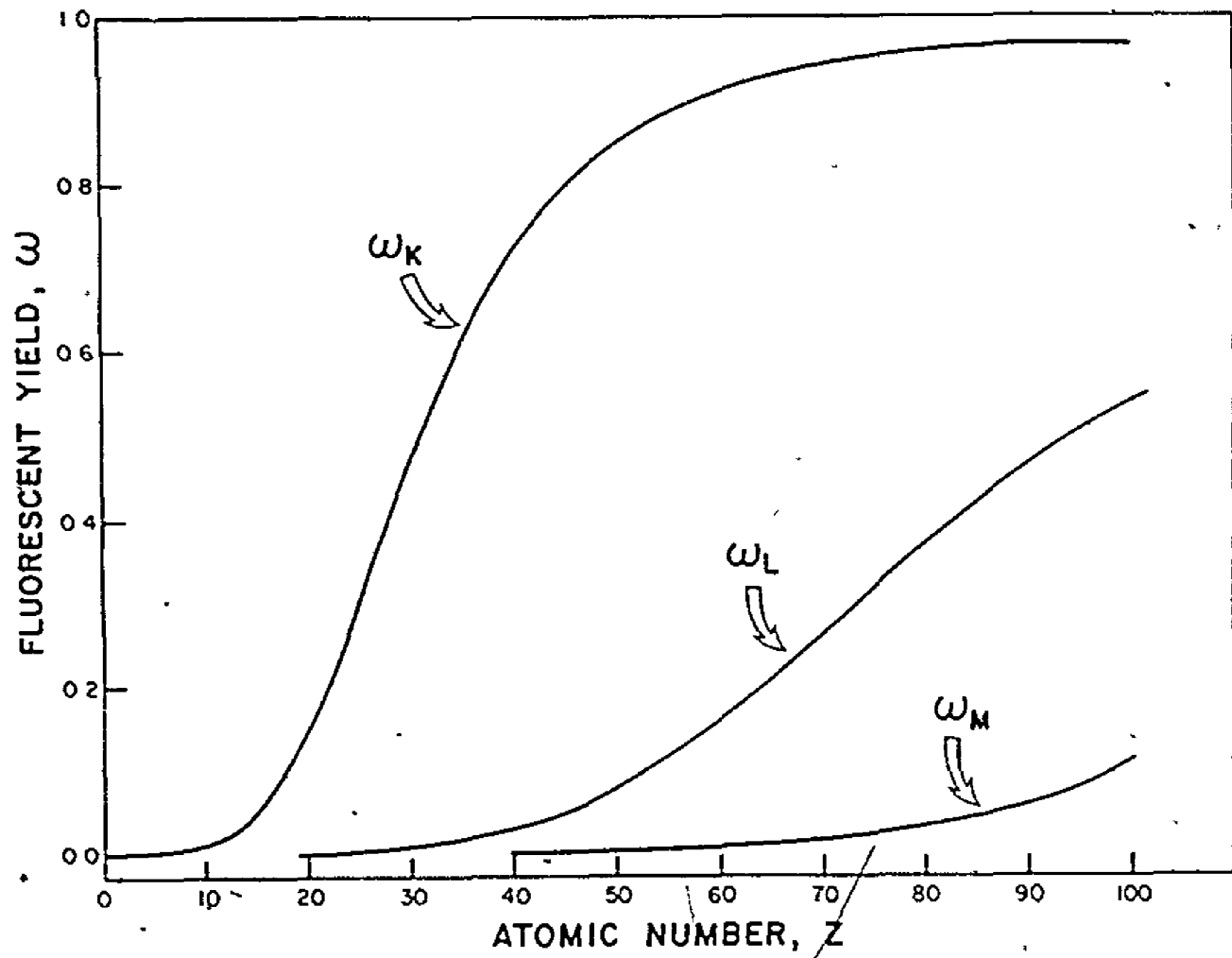


Fig. 10. Illustration of the K, L and M fluorescent yield dependence on atomic number (taken from reference (13))

N_K is the rate at which K shell vacancies are created

$(n_K)_i$ is the rate at which photons of spectral line 'i' are emitted.

The other shell fluorescent yields are derived in a parallel fashion.

The principle consequence of the Auger effect on the fluorescent yield is that w is not unity and that the lines in a given series are not as intense as would be predicted from the number of vacancies originally created in the associated orbital. The fluorescent yield diminishes with decreasing Z and becomes the major limitation to sensitivity for elements of low atomic number with X-ray analysis. Figure 10 depicts the K, L, and M fluorescent yield dependence on atomic number. As can be seen from the figure, elements of atomic number less than 10 (neon) have very low fluorescent yields and the intrinsic sensitivity for detection would be far greater with electron spectroscopy (Auger spectroscopy).

2.5. Quantitative X-ray analysis

X-ray analysis of an element in a specimen principally consists of exciting the element in the sample and recording the observed intensity of the characteristic spectral lines emitted from that element. An analysis constitutes a knowledge of the weight fraction of that element in the sample as obtained from spectral line intensities. In general, this useful emitted intensity is affected by five factors: (i) the spectral energy distribution of the excitation X-ray photons, (ii) absorption of excitation photons by the analyte and matrix elements, (iii) the excitation probability and fluorescent yield of the analyte, (iv) absorption of the analyte line by the analyte and matrix elements and (v) the geometry of the X-ray spectrometer.

A schematic excitation system is shown in figure 11 depicting a

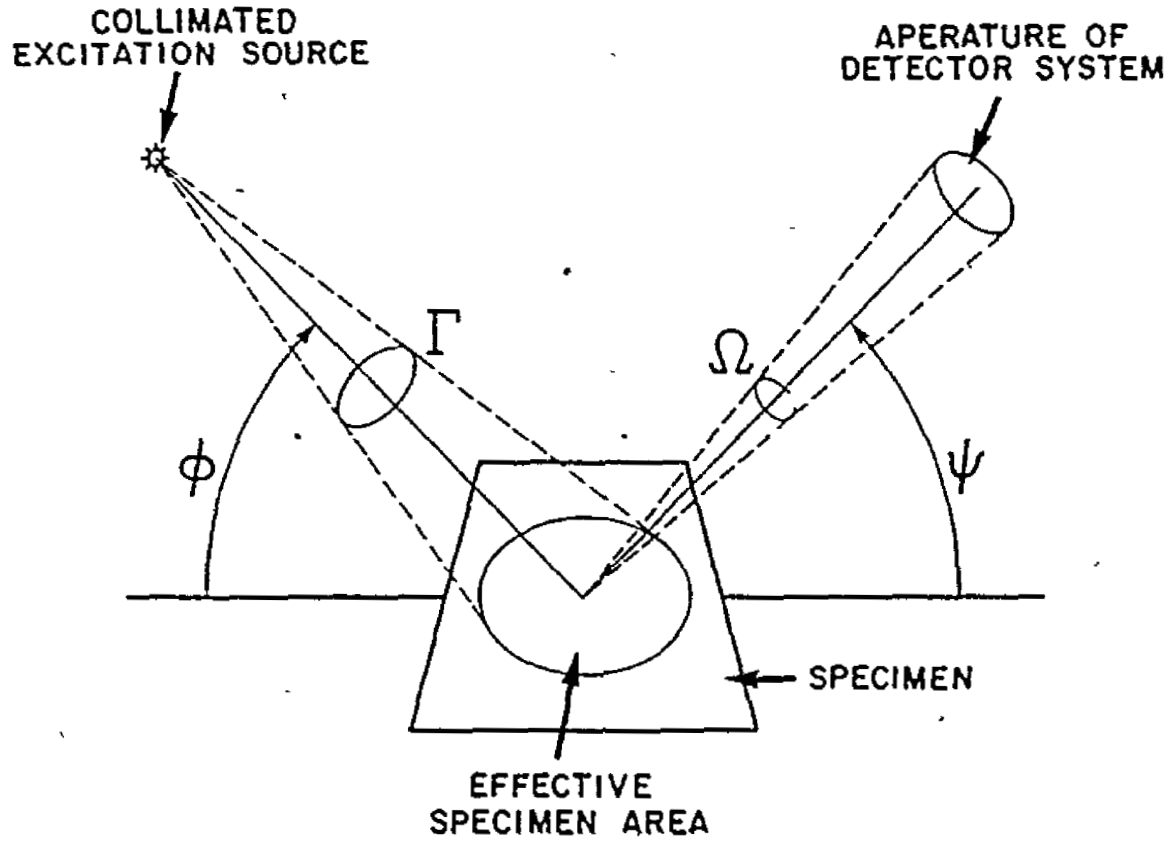


Fig. 11. General source, sample and detector geometry employed for X-ray analysis

general source, sample and detector geometry where

r is the solid angle subtended at the excitation source by the effective specimen area,

Ω is the solid angle subtended at the specimen by the aperture of the detector system,

ϕ is the angle between the excitation radiation and the specimen plane and

ψ is the take-off angle required for characteristic X-ray fluorescent radiation to pass through the centre of the detector aperture.

Using figure 11 and previously defined phenomena, a fundamental excitation equation can easily be derived showing the relationship between characteristic spectral line intensity of an element and the weight fraction of that element in a multi-element sample. By assuming a monochromatic excitation source, of energy ϵ_e and intensity I_e , the fraction of incident photons penetrating to a thickness m (g/cm²) and arriving at a layer dm is

$$I_e e^{-m \sum_i (\mu_e)_i r_i} \csc \phi$$

where $\sum_i (\mu_e)_i r_i$ is the total mass absorption coefficient of the specimen for excitation energy ϵ_e as delineated by equation 2.3.

Of the photons arriving at layer dm , the fraction absorbed in the layer is

$$\sum_i (\mu_e)_i r_i \csc \phi dm$$

Of the photons absorbed in layer dm , the fraction absorbed by an analyte A in a specimen having an analyte weight fraction r_A , which create electron vacancies in an atom shell corresponding to the series of the analyte is

$$\frac{r_A \tau_A \csc \phi \, dm}{\sum_i (\mu_e)_i r_i \csc \phi \, dm}$$

$$= \frac{r_A \tau_A}{\sum_i (\mu_e)_i r_i}$$

where τ_A is the photoelectric mass absorption coefficient of element A for the excitation energy ϵ_e .

Of the photons causing such vacancies, the fraction that leads to actual emission of photons of the spectral lines in that series, is given by the fluorescent yield of the analyte series ω_A . Generally, only the intensity of a specific line in a series is measured. Given a shell vacancy, the probability that a photon corresponding to a specific line in the series observed will be given by

$$g_f = \frac{I_f}{\sum_i (I_f)_i} \dots \dots \dots 2.9$$

in which $\sum_i (I_f)_i$ is the sum of the intensities of all the fluorescent lines in the series.

The total intensity of photons of spectral line f, dI_f , possessing an energy ϵ_f and emitted from a dm in all directions is:

$$dI_f = (I_e e^{-m \sum_i (\mu_e)_i r_i \csc \phi}) (\sum_i (\mu_e)_i r_i \csc \phi \, dm) \left(\frac{r_A \tau_A}{\sum_i (\mu_e)_i r_i} \right) (\omega_A g_f)$$

$$= I_e r_A \tau_A \omega_A g_f \csc \phi e^{-m \sum_i (\mu_e)_i r_i \csc \phi} \, dm \dots \dots \dots 2.10$$

Of the total number of photons emitted, only those that are emitted toward the detector can contribute to the measured line intensity. This fraction is given by $d\Omega/4\pi$. The fraction of photons of energy ϵ_f

that emerge from the overlying layer m and enter the detector is then given by

$$\frac{d\Omega}{4\pi} e^{-m \sum (\mu_f)_1 r_1 \csc \psi}$$

where $\sum (\mu_f)_1 r_1$ is the total mass absorption coefficient of the specimen for the fluorescent line radiation of energy ϵ_f . The analyte line intensity actually entering the detector from the layer dm is given by.

$$dI_f = \frac{I_e r_A \tau_A \omega_A g_f \csc \phi \, d\Omega}{4\pi} e^{-m \{ \sum (\mu_e \csc \phi + \mu_f \csc \psi) \}_1 r_1} dm \quad \dots \quad 2.11$$

Integration of equation 2.11 over all thicknesses up to m will give the total intensity of the spectral line f entering the detector emitted from within thickness m .

$$I_f = \frac{I_e r_A \tau_A \omega_A g_f \csc \phi \, d\Omega}{4\pi} \int_0^m e^{-m \{ \sum (\mu_e \csc \phi + \mu_f \csc \psi) \}_1 r_1} dm$$

$$= \frac{I_e r_A \tau_A \omega_A g_f \csc \phi \, d\Omega}{4\pi \sum (\mu_e \csc \phi + \mu_f \csc \psi)_1 r_1} \{ 1 - e^{-m \sum (\mu_e \csc \phi + \mu_f \csc \psi)_1 r_1} \} \quad \dots \quad 2.12$$

Equation 2.12 is the fundamental excitation equation relating the observed intensity of the analyte spectral line f , I_f , to the analyte weight fraction, r_A , in the specimen. The function is complicated by the fact that the mass absorption coefficients for both excitation and fluorescence radiation as well as the weight fraction of every element in the sample is required to evaluate the equation. The excitation

equation involves these parameters in two factors which affect the observed fluorescent intensity. a matrix element factor, contained in the denominator, which determines absorption effects produced by the presence of the matrix elements, and a sample thickness factor evaluated by the exponential term.

Two assumptions required to maintain the validity of equation 2.12 are (i) the sample is homogeneous, and (ii) the sample presents a smooth surface to both the source and the detector. In most X-ray analytical work, only a thin layer of the specimen surface undergoes excitation and subsequent characteristic fluorescence, therefore it is essential that the composition of the small volume analyzed be identical to that of the bulk specimen. If, for example, the surface of the specimen presents irregular physical features, such as non-uniform packing densities or particle sizes in the case of powdered samples, fluorescent and excitation X-rays will be radically scattered and reliable, consistent intensity measurements cannot be performed. This effect is particularly prominent with low energy investigations where the X-ray wavelength approaches the magnitude of the surface anomalies. A further shortcoming of equation 2.12 concerns the matrix factor. As described in the equation, it can only evaluate absorption effects by the matrix elements. However, enhancement of the analyte line intensity is sometimes observed. This arises because only the initial encounter of the excitation photons with the analyte atoms was considered in the development of equation 2.12. Photoelectric absorption of (i) multiply scattered excitation or (ii) secondary fluorescence radiation from the matrix elements by the analyte element will lead to an increment in the observed spectral line intensity.

Enhancement effects are usually minor when compared with absorption effects but in the second case, when major matrix elements have a higher atomic number than the analyte element the enhancement effects can gain considerable prominence. The matrix factor then is responsible for both absorption and enhancement effects.

Considerable simplification can be achieved in equation 2.12 by adjusting the sample thickness. If the sample thickness is such that a significant amount of excitation radiation is both absorbed by the specimen and also transmitted through it, the sample is described as being 'partially thick' and no simplification can be made. In practice, such samples forms are virtually not used for analytical work since a means must be found to compensate for both matrix and thickness factors.

If the thickness is increased so that a negligible amount of excitation radiation is transmitted through the sample, the specimen is said to be 'thick' and equation 2.12 reduces to

$$I_f = \frac{I_e r_A \tau_A \omega_A g_f \csc \phi \, d\Omega}{4\pi \lambda (\mu_e \csc \phi + \mu_f \csc \psi) \rho_A r_A} \dots \dots \dots 2.13$$

This is the most commonly used sample type in X-ray analysis and only a matrix factor affects the observed line intensity I_f . Were it not for this factor, the analyte line intensity I_f from analyte A in a thick specimen would simply be a function of weight fraction r_A . The strategy of quantitative X-ray analysis of thick samples is to eliminate, circumvent, minimize or correct for absorption and enhancement effects. Two basic approaches have been developed to accomplish this. (i) comparative methods and (ii) absolute methods.

)

In the first case, most of the methods used to reduce absorption and enhancement effects involve the use of calibration standards in which X-ray spectrometric intensity data are converted to analytical concentrations by the use of calibration curves established from measurements initially performed on standards. Many of the techniques to remove matrix effects are employed in all areas of chemical analysis, for example, the method of standard addition, the method of comparison to matrix standards, the method of matrix dilution and the method of internal standardization. Under appropriate excitation and specimen conditions, matrix effects can be minimized by standardizing with scattered X-rays. Included in this group of comparative methods are a host of techniques which transform observed analyte intensities to analyte weight fractions through mathematical relationships originally derived from measurements from standards. For two component samples, where enhancement effects may be absent and matrix effects are due only to absorption processes, matrix effects can be eliminated by a simple absorption correction technique (14-15); for ternary systems, geometrical (graphical) techniques (16-17); a technique using empirical correction factors (18-20) has been used for up to seven components and multielement analysis techniques using 'influence coefficients' (21-25) have evolved to a refined status.

In the latter case of absolute methods, no standards of any kind are required. This approach has gained greater significance in the last decade as sufficient computing capability becomes increasingly available. In these techniques, known as fundamental parameter methods (26-27), X-ray analytical properties, such as mass absorption coefficients, fluorescent yields, energy of characteristic fluorescence etc., are

stored in a computer. The line intensities of all elements in the sample are measured, and the analyte weight fraction is calculated by mathematical iteration procedures.

Equation 2.12 can be further reduced by preparing 'thin' samples. The sample thickness is adjusted to a sufficiently small value so that the exponential thickness term can be replaced by a geometric series of which all but the first two terms can be neglected. The excitation equation for such a sample is then approximated by:

$$I_f = \frac{I_e \mu_e^{\tau} A^{\tau} \omega_A g_f^m \csc \phi \, d\Omega}{4\pi \sum_i (\mu_e \csc \phi + \mu_i \csc \psi)_i r_i} [1 - [1 - m_i^2 (\mu_e \csc \phi + \mu_f \csc \psi)_i r_i]]$$

$$= \frac{I_e r A^{\tau} \omega_A g_f^m \csc \phi \, d\Omega}{4\pi} \dots \dots \dots 2.14$$

Absorption and enhancement effects substantially disappear in thin specimens because neither excitation nor fluorescent X-rays are appreciably absorbed in the short path length of the thin layer. Each atom absorbs and emits essentially independently of the other atoms without significantly altering the incident beam. The advantage of using thin samples is obvious in that no matrix standards are required. Generally, intensities observed from thin samples are much lower than from thick samples and consequently thin samples are applicable principally to major constituents. The main disadvantage of utilizing thin samples is the necessity and in some cases, difficulties encountered in preparing sufficiently thin specimens.

2.6. Quantitative γ -ray analysis

The distinguishing factor between α -rays and γ -rays is their source

of origin. γ -rays are produced from within the atomic nucleus and X-rays from extra-nuclear phenomena. Following the disintegration of an unstable radionuclide, the daughter nucleus may be left in an excited state. Subsequent nuclear transitions to lower energy levels result in photon emissions of energy corresponding to the difference in energy of the initial and final nuclear states. Such gamma emissions are characteristic of the emitting nuclide.

As was the situation with X-rays, the principle objective in quantitative analysis is to derive an accurate value of the quantity of analyte present from the measured intensity of a particular γ -ray photopeak. By initially assuming that the specimen has some degree of gamma activity, either artificially produced or natural radiation, the number of measured characteristic gamma photons is affected by two factors. (i) absorption of the gamma photons by the matrix elements and (ii) the geometry of the γ -ray spectrometer.

Using figure 11, the total number of photons of energy ϵ_γ emitted in all directions from a layer dm situated at a thickness m (g/cm^2) is.

$$\lambda_A r_A(t) \alpha_A dm$$

where, λ_A is the decay constant of radionuclide analyte A (sec^{-1})
 $r_A(t)$ is the weight fraction of radionuclide A present (sec)
 α_A is the abundance of the analyte line expressed as the number of photons of analyte energy ϵ_γ per nuclear disintegration.

In γ -ray spectroscopy, the number of radioactive analyte nuclides present during the period of observation is generally a function of time. For measuring activities of naturally occurring nuclides, the time

dependence can frequently be removed since the nuclide possesses or is in secular equilibrium with a parent possessing a very long half-life.

The fraction of photons of characteristic analyte energy that emerge from the overlying layer m and enter the detector is then given by:

$$\frac{d\Omega}{4\pi} e^{-m\Sigma(\mu_\gamma)_i r_i \csc \psi}$$

in which μ_γ is the total mass absorption coefficient for the measured γ -emission and all other symbols have been previously defined.

The number of photons entering the detector from the layer dm is then

$$dI_\gamma = \frac{\lambda_A r_A(t) \alpha_A d\Omega}{4\pi} e^{-m\Sigma(\mu_\gamma)_i r_i \csc \psi} dm \quad \dots \quad 2.15$$

The total intensity of the characteristic γ -ray observed from a sample of thickness m is then obtained from:

$$I_\gamma = \frac{\lambda_A r_A(t) \alpha_A d\Omega}{4\pi} \int_0^m e^{-m\Sigma(\mu_\gamma)_i r_i \csc \psi} dm$$

$$= \frac{\lambda_A r_A(t) \alpha_A d\Omega}{4\pi \Sigma(\mu_\gamma)_i r_i \csc \psi} (1 - e^{-m\Sigma(\mu_\gamma)_i r_i \csc \psi}) \dots \quad 2.16$$

Just as in the X-ray case, the observed intensity is affected by a matrix and a thickness factor. In gamma spectroscopy only absorption effects are observed in the matrix factor as enhancement of nuclear transitions cannot occur within the specimen. In this sense, equation 2.16 is more rigorous than equation 2.12, however the two assumptions

regarding sample homogeneity and presentation are still required. The photon energies encountered in γ -ray spectroscopy are frequently much higher than those emitted by inner core atomic electron transitions. They are generally substantially above all X-ray absorption edges so that mass absorption coefficients are much smaller than in the X-ray range. The sample volume analyzed is then much greater and specimen homogeneity requirements are not as severe. For the same reason, the importance of sample surface consistency is not a salient point as in X-ray analysis.

Correspondingly the analysis can be performed on thick or thin samples. Due to the high penetrating ability of the emitted gamma photons, thin samples are more conveniently prepared. For example, a thin sample of cobalt metal can be several centimeters thick when measuring the 1.33 MeV ^{60}Co γ -ray intensity but must be less than 15 micrometers when observed by Co $K\alpha$ X-rays (6.9 keV). The total intensity of the characteristic gamma photons entering the detector from a thin sample of thickness m (g/cm^2) is:

$$I_{\gamma} = \frac{\lambda_A r_A(t) \alpha_A m d \Omega}{4\pi} \dots \dots \dots 2.17$$

Thick samples are used for very low energy γ -rays or for specimens containing very little activity so that a large sample volume is required in order to measure the analyte photopeak intensity with sufficient precision. In this case, the matrix factor has to be compensated for by employing standard correction techniques mentioned in section 2.5. Equation 2.18 shows the intensity of a particular spectral line as a function of the analyte weight fraction for thick samples.

$$I_{\gamma} = \frac{\lambda_{\gamma} r_{\gamma} (t) \epsilon_{\gamma} d\Omega}{4\pi \sum_{i} (\mu_{\gamma})_i r_i \csc \psi} \dots \dots \dots 2.18$$

Since no excitation source is required while observing γ -rays, highly efficient 2π or 4π counting geometry techniques are employed. That is, the solid angle subtended at the specimen by the aperture of the detector or detectors, $d\Omega$, is either 2π or 4π steradians respectively.

3. EXPERIMENTAL WORK

3.1. Preliminary considerations

To reiterate the stated objectives in the introduction, application of the research undertaken in this thesis is directed toward use in the primary uranium extraction industry. Two topics of current interest in this industry are. (1) investigation of analytical techniques that would be suitable for computerized on-stream uranium analysis and subsequent processing, and (11) development of a rapid, accurate, non-elaborate procedure to determine uranium isotope ratios suitable for routine use at the mine location. The extraction plant feed material consists of uranium bearing geological material. The ores processed in northern Saskatchewan customarily contain 0.1 to 0.3% U_3O_8 in a silica based host mineral such as granite. Ores in general, are characterized by a very wide range of chemical composition with tenacious absorption and enhancement effects. Severe spectral-line interference often results from the presence of many elements in complex minerals. Standards conventionally required to minimize this matrix factor are often difficult to prepare. A variety of dissimilar sample forms are encountered in extraction plant process streams, i.e. crushed ore, slurries and solutions. Each of these forms continually exhibits diverse physical features. For example, inconsistent particle size for solid specimens and varying solids content for slurry samples. If single photon counting techniques, such as X-ray and γ -ray spectroscopy are applied to analyzing uranium in industrial process streams then the matrix and specimen errors present must be overcome.

Comparative standards approximating the specimen with regard to physical form, analyte concentration, matrix composition and physical features, cannot be used to directly standardize the in situ analysis performed in industrial circuits. Other experimental approaches to circumvent this problem are required. As outlined in chapter 2, all the fundamental X-ray analytical parameters, such as μ , τ , σ , and ω are functions of atomic number, Z . In this regard, uranium possesses the largest atomic number of all the natural occurring nuclides and its analytical properties are not only unique, but substantially different from most of the other elements found in innate geological specimens. The principal constituent of granite is silica and in figures 1, 4, 7 the attenuation coefficients of silicon were plotted in addition to those of uranium as an indication of the expected magnitude of these X-ray parameters for the matrix elements in a uranium bearing granite. It is the intention of this section to contrast the various X-ray analytical properties of uranium and silicon and thereby to deduce experimental approaches to accomplish the above objectives without the need for comparative matrix standards.

Rayleigh scattering cross sections, as shown in figures 1-3 possess a strong Z dependence. For any given incident photon energy, the probability of this type of scattering being produced by an encounter with uranium atoms is far higher than for silicon atoms. For specimens consisting of a heavy element in light element medium, measurement of Rayleigh scattering intensity can have some diagnostic value. For example, in a binary component system, such as uranium and water, changes in uranium concentration will produce quantitative intensity fluctuations

in the observed Rayleigh scattering. In multielement specimens, Rayleigh scattering originating from the analyte is not generally distinguishable from that of the matrix elements; it therefore is normally of little analytical benefit. For uranium, present in a host granite, the atomic numbers of the matrix elements are very much smaller than that of uranium. The weighted mean atomic number of the matrix elements would have to be significantly altered to produce a deviation in the Rayleigh scattering intensity equivalent to that from a much smaller variation in uranium weight fraction. For this situation, uranium analysis performed on certain natural geological specimens by measuring Rayleigh scattering intensity may be useful. However, figure 12 shows cross sections for each of the attenuation mechanisms, (σ_R , σ_C and τ) expressed as a fraction of the total absorption cross section, σ_{TOT} , versus incident photon energy. The relative contribution of σ_R for both uranium and silicon is not a major component of σ_{TOT} . Maximum values of only 13% occur for most elements between 50 and 100 keV indicating poor sensitivities. For comparison, the relative photoelectric effect cross sections are 80 to 95% for most elements in the same energy interval.

From figure 5, the Compton scattering cross section is less sensitive to atomic number and appears to be very nearly a linearly function of Z . Similarly σ_C is roughly proportional to mass number. This fact, under appropriate circumstances can be capitalized upon by measuring sample thicknesses. Consider the case of a high energy incident radiation impinging upon specimens consisting principally of low Z elements. For a thin or partially thick sample, the total Compton scattering observed from the specimen will be proportional to the sample mass. If

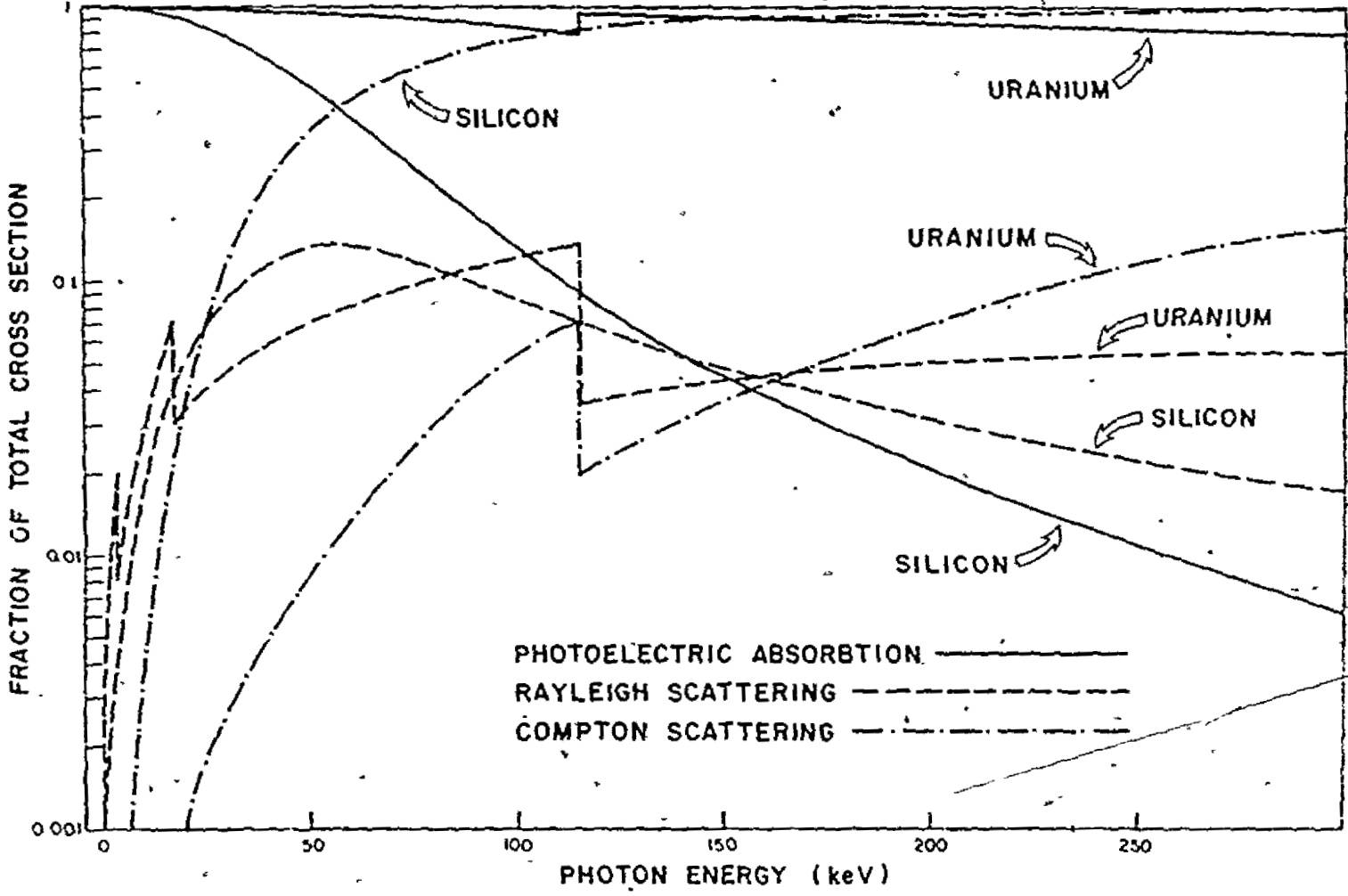


Fig. 12. Relative contribution of each attenuation mechanism to the total absorption cross section versus photon energy for both uranium and silicon atoms

the surface area of the specimen is known and of constant value, Compton scattering intensity then functions as a thickness (g/cm²) gauge. This conclusion can be indirectly utilized to evaluate the magnitude of the matrix and thickness factors. The transmitted radiation through such samples is given by:

$$I_T = I_0 e^{-m \sum (\mu_e)_1 r_1} \dots \dots \dots 3.1$$

where I_T and I_0 are the transmitted and initial intensities respectively, m is the sample thickness (g/cm²) and $\sum (\mu_e)_1 r_1$ is the total mass absorption coefficient of the specimen for photons of the excitation energy.

If the sample thickness, m , is determined from the Compton scattering intensity, and a technique is devised to measure the initial to transmitted intensity ratio, then the total mass absorption coefficient has been indirectly experimentally measured. For a heavy metal analyte in a sufficiently low Z matrix, the total mass absorption coefficient for the fluorescent radiation will be a constant function of that for the excitation radiation, hence all the terms required to evaluate the matrix and thickness factors of equation 2.12 are known.

Compton scattering can also be used to minimize the matrix factor for thick samples. A set of rough approximations can be used to demonstrate qualitatively that for a given minor analyte component normalizing observed analyte peak intensity to Compton scattering intensity can be much less sensitive to varying Z (changing composition) than the observed analyte intensity itself⁽²⁸⁾. The argument is as follows. An emitted analyte line intensity may be represented as

$$I_f = \frac{i}{[\sum (\mu_e)_1 r_1 + \sum (\mu_f)_1 r_1]} \dots \dots \dots 3.2$$

where the denominator is the sum of the total mass absorption coefficients of the specimen for the excitation and fluorescent radiation respectively. If discrete excitation energy is used, then the Compton scattering peak intensity can be written as

$$I_C \propto \frac{\sigma_C}{[\sum_i (\mu_e)_i r_i + \sum_i (\mu_C)_i r_i]} \dots \dots \dots 3.3$$

in which $\sum_i (\mu_C)_i r_i$ is the total mass absorption coefficient of the analyte and matrix elements for the Compton scattered line. The principal component of the total mass absorption coefficient for energies commonly encountered in X-ray analysis is τ , figure 12. From figure 8, τ is proportional to Z^4 and therefore

$$I_f \propto Z^{-4} \dots \dots \dots 3.4$$

however, σ_C exhibits a linear dependence with Z , figure 5, so that

$$I_C \propto Z^{-3} \dots \dots \dots 3.5$$

The intensity ratio of the analyte line to Compton scattered line is then

$$I_f/I_C \propto Z^{-1} \dots \dots \dots 3.6$$

A comparison of equation 3.4 and 3.6 shows that the ratio is much less dependent on atomic number - and therefore on matrix composition - than the analyte fluorescent intensity alone. A more rigorous mathematical treatment is given in reference (29). Equation 3.6 applies when the fluorescent and Compton scattered photon energies are about the same. Actually, scattering and absorption processes are also energy dependent, and it may be possible to optimize an analytical system by selecting a scattered energy for which the ratio I_f/I_C is substantially independent of matrix composition. It should be noted that this technique is only

capable of reducing the absorption errors caused by a varying matrix factor and is ineffective against enhancement effects. An additional benefit of peak ratio techniques is that they can provide an effective means for dealing with non-uniform particle-size, surface texture effects, packing and instrumental errors. As can be seen from figure 7, there are striking differences between the photoelectric cross sections for uranium and silicon over the energy range from 1 to 120 keV. Two main distinguishing features are: (i) for any given energy, τ is much higher for uranium than it is for silicon, and (ii) characteristic lines can be observed from uranium K, L, and M shell excitations but only those of the K shell from silicon. As a consequence of the first item, uranium can be highly selectively excited when present in a silicon matrix. That is, by choosing a photon excitation energy just above a designated uranium absorption edge, uranium fluorescent photons will be created at a preferential rate when related to the fluorescence of the other matrix elements. The second point requires further consideration.

Table 4 summarizes some X-ray excitation parameters for uranium at each of the three major absorption edges. Values of τ_U , the photoelectric attenuation coefficient for uranium, are presented for each absorption edge. For thin samples of equal thickness, the quantity $w\tau_U$ is proportional to the potential intrinsic sensitivity achievable by selectively exciting each of the major subshells. The absorption characteristics of the most intense uranium line in each of the three spectral series by silicon is presented in table 5. Optimum sample and excitation conditions for analyzing uranium in a silicon based matrix by measurement of the major line intensity from each series can be in-

Table 4*

Some X-ray excitation parameters for uranium

Absorption Edge	Energy (keV)	ω	τ_U (cm ² /g)	$\omega\tau_U$ (cm ² g)
U K _{ab}	115.6	0.960	4.55	4.37
U L _{IIIab}	17.17	0.478	102.5	49.0
U M _{Vab}	3.552	0.064	1245.	79.7

* data taken from reference (6).

9

Table 5*

Silicon absorption characteristics of some major uranium lines

X-ray Line	Energy (keV)	μ_{Si} (cm ² /g)	'Infinite' Thickness (cm)
U K α_1	98.44	.183	10
U L α_1	13.61	13.2	0.2
U M α_1	3.17	810.	0.002

* data taken from reference (6).

ferred from the data displayed in these two tables.

The first particular to notice is that the energies of the uranium K X-rays are very high and are better suited for observation with γ -spectroscopy equipment than with the conventional X-ray semiconductor detectors. The U K_{ab} is vastly different from the absorption edges of the expected matrix elements in a uranium bearing granite so that selective excitation of the uranium K shell can be ideally performed. The effect of the very large energy differences in the major uranium lines, listed in table 5, becomes apparent in the sample thickness necessary to produce a thick sample in silicon. For the U $K_{\alpha 1}$ line, thick samples would be inconvenient to prepare as a sample 10 cm in thickness would require approximately 3 kg of material. At these high energies, Compton scattering becomes the major contribution to the total mass absorption coefficient for silicon, figure 12. Since Compton scattering intensities increase with sample mass, very high spectral backgrounds are produced through multiple Compton scattering phenomena, typically characteristic of gamma spectra taken from a low Z matrix. Analyzing by thin samples would improve the background, but sensitivities would be poor because the probability for excitation ($\omega\tau_{ij}$) of the K shell is much lower than for vacancy creation in the other shells. Advantage can be taken of the penetrating power of the high energy K X-rays and a compromise reached by analyzing partially thick samples. By simultaneously measuring the transmitted radiation and the Compton scattering intensities, the matrix and thickness factors may be evaluated as described earlier. Experimental conditions can be arranged so that both these intensities are precisely determined by. (1) adjusting the sample thickness, and

(ii) noting that for this energy range, σ_C is the major component to σ_{TOT} .

From table 5, thick samples are comparatively easy to prepare for analysis with U $L\alpha_1$ fluorescence. Since the energies of the uranium L subshells still lie substantially above the absorption edges of the major elements found in a silica based matrix, the analysis can practically benefit from selective excitation. At this energy level, τ is the major component to the total attenuation cross section. Because the specimens may be infinitely thick, the technique of normalizing analyte line intensity to Compton scattering intensity can be employed to compensate for matrix absorption effects.

Elements such as Si, O, K, Al, Fe, Ca, Na, Mg, Ti, etc. are the principle components of a granite⁽³⁰⁾. Selective excitation of the M states of uranium in a natural occurring ore cannot be accomplished, because the K shell absorption edges of these major matrix elements encompass those of the uranium M shells. Absorption and enhancement effects from these matrix elements very severely affect the U $M\alpha, \beta$ spectral line intensity. If thin samples were prepared to alleviate matrix effects, analysis by M shell fluorescence would offer no advantage over analysis by L shell X-ray emissions i.e. from table 4 the potential sensitivity for uranium with M shell excitation is slightly greater than in the L shell case, but from table 5, thin samples prepared for L X-ray analysis can be much thicker and the greater quantity of uranium present eliminates this advantage. If the uranium were chemically separated from the ore and thin specimens of uranium chemical precipitate analyzed, no comparative matrix standards would be required.

The only beneficial feature of uranium M X-ray analysis is its potential to observe smaller quantities of uranium than by excitation of any of the other principle subshells. In the case of a uranium separation from a low grade ore, where the total amount of chemical precipitate was just sufficiently small to prepare a thin sample for M X-ray analysis, then selective excitation of the γ_{ab} would provide the greatest sensitivity.

There are essentially two possible sample locations for which the isotope ratio analysis might be considered in a uranium extraction plant. That is, the analysis can be performed on the ore entering the plant or on the final product. The ideal procedure would optimize accuracy, precision and counting time. In this regard, analyzing the product, normally called yellow cake or $\text{Na}_2\text{U}_2\text{O}_7$ has an advantage for all three concerns. In a naturally occurring uranium ore, the uranium isotope contents cannot be directly measured with γ -spectroscopy due to spectral interferences from other natural radiation contained in the ore. Consequently, uranium is generally determined indirectly. In processed ores, this can lead to considerable inaccuracies. The nature of these errors are described more fully in section 3.6.1. For the low concentrations (0.1 to 0.3% U_3O_8) commonly experienced in plant feed material, photopeak precisions are poor unless very long counting times are used. On the other hand, the uranium content of the product from an extraction plant is approximately 70% uranium metal resulting in greatly improved counting rates. Figure 12, illustrates a further disadvantage to doing γ -spectroscopy on the ore. At energies greater than approximately 50 keV, Compton scattering becomes the dominant mode of attenuation. As described earlier, this results in the high backgrounds commonly observed in.

γ -spectroscopy due to multiple Compton scattering. In a specimen consisting predominately of uranium however, Compton scattering is still a very minor component of the total cross section and the quality of spectrum observed is strikingly improved. In addition, the normal extraction process removes the spectral interferences observed in the natural ore allowing a more accurate determination. As previously stated, thin samples are generally straightforwardly prepared for the energies involved in normal γ -spectroscopy.

In summary then, by collating the various absorption and fluorescent characteristics of uranium with those of the expected matrix elements, the most beneficial analytical approaches - as correlated with the objectives of the present work - have been formulated. These are: (i) determination of uranium in ores by K shell fluorescence using partially thick specimens. The matrix and thickness factor may be experimentally obtained by measuring both the Compton scattering and transmitted radiation intensities, (ii) determination of uranium in ores by L shell fluorescence employing thick specimens. Matrix compensation may be achieved by normalizing uranium L fluorescent intensities to measured Compton scattering intensities; (iii) determination of small quantities of uranium chemical precipitates by M shell fluorescence using thin specimens, and (iv) determination of the $^{235}\text{U}/^{238}\text{U}$ isotope ratio by γ -spectroscopy using thin specimens of uranium chemical precipitates. All approaches, except (iv), require highly selective excitation techniques. No matrix standards are required for any of the above propositions.

3.2 Experimental facilities

The analytical systems used in this work are shown schematically in figure 13. In essence, they consist of an X-ray and a γ -ray spectrometer linked to a common data storage and output facility. The uranium L and M X-ray experiments were performed with the X-ray spectrometer while the γ -ray spectrometer was employed for the uranium isotope ratio and K X-ray analyses. For a description of the operation of these detectors and associated electronics, see references (31-32).

The X-ray spectrometer consists of the following components: a Kevex-ray model 3000 Si(Li) detector, a Kevex-ray model 2002A preamplifier with pulse optical feedback, a TMC #353 high voltage bias supply, a Kevex-ray model 4510P X-ray amplifier containing pulse pileup rejection circuitry, a Kevex-ray model 4710 energy calibrator and a Didac multi-channel analyzer, model SA44 with a 100 MHz ADC and 4000 channels of analysis. The active area of the detector was 30 mm² with a resolution of about 165 eV (FWHM) at 5.9 keV. The detector was operated with a bias supply of 900 V negative. Maximum detection efficiency occurs at approximately 10 keV and is thus well suited for the observation of U L α (13.6 keV) and U M α (3.2 keV) spectral lines. Energy calibration of the spectrometer for the L and M X-ray projects was conveniently performed using the energy calibrator (pulse generator). This unit was initially graduated against ²⁴¹Am, ⁵⁷Co, ¹⁰⁹Cd and ⁵⁵Fe standard reference sources. The origins and applicable emission energies of these radioactive sources are listed in table 6.

The following integral components comprise the γ -spectrometer: a Nuclear Diodes Ge(Li) detector, model LGCC-13.0-1.80; a model 111A

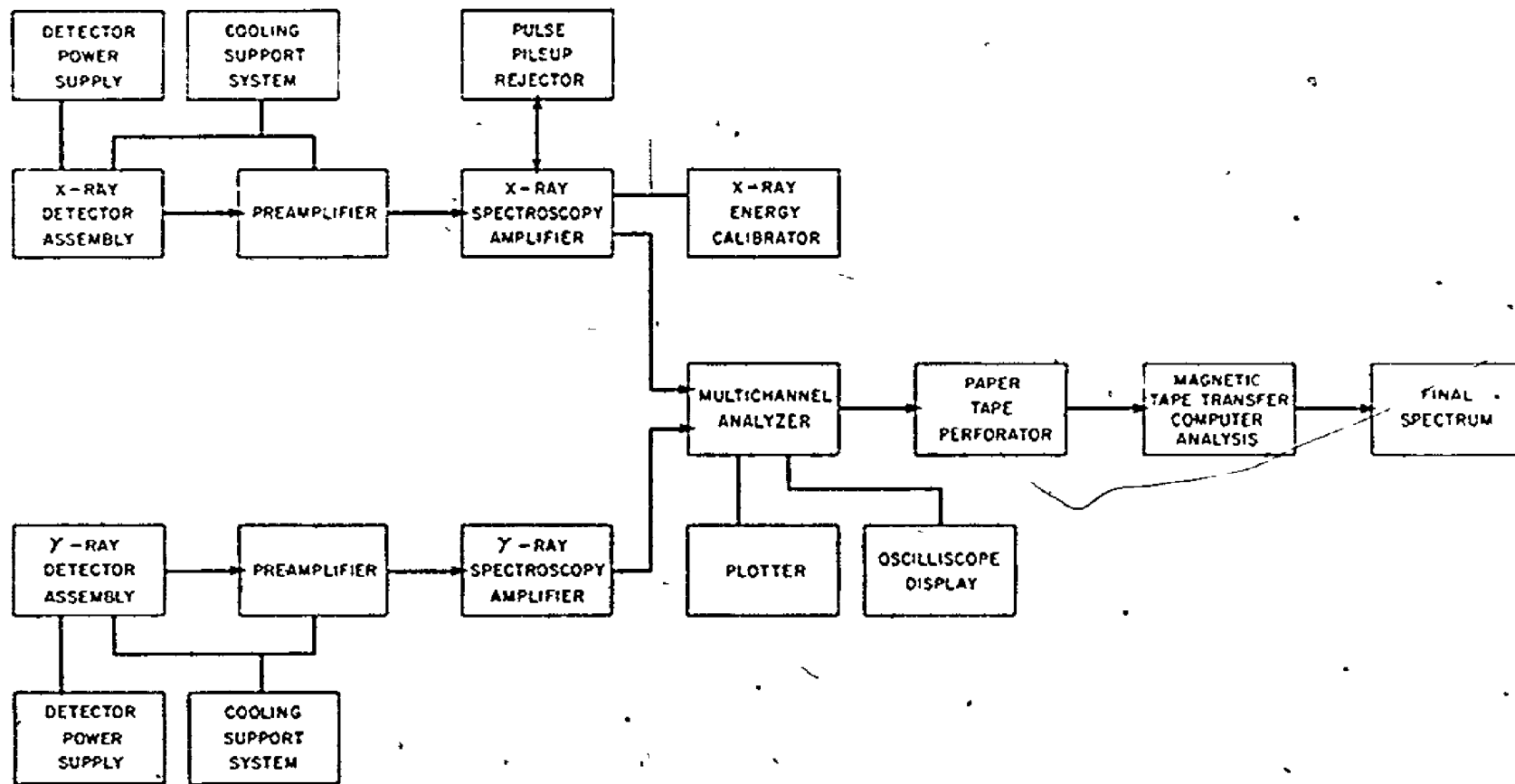


Fig. 13. Block diagram illustrating the major electronic components of the analyzing systems

Table 6
Radionuclides used to standardize the energy calibrator

Nuclide	Emission Energy (keV)	Emission Origin	Absolute Abundance (photons/disintegration)	Reference
^{241}Am	59.54	γ -ray	0.359	(33)
^{57}Co	14.44	γ -ray	0.097	(33)
^{109}Cd	22.1	Ag $K\alpha$ X-rays	unknown	(33)
^{55}Fe	5.9	Mn $K\alpha$ X-rays	unknown	(33)

Nuclear Diodes preamplifier; a Canberra Industries spectroscopy amplifier, model 1417B, and the Didac multichannel analyzer shared with the X-ray spectrometer. The 85 cc detector was operated at 3200 V positive and has a resolution of 854 eV (FWHM) for the ^{57}Co γ -ray at 122 keV. This detector functions with maximum detector efficiency in the vicinity of 100 keV and the U $\text{K}\alpha_1$ X-ray, ^{234}Th and ^{235}U γ -ray lines at 98, 93 and 186 keV respectively can be optimally examined. The spectrometer is energy calibrated directly using reference radioisotopes for each case of interest.

~~Data output facilities from the common multichannel analyzer unit~~ include a visual display, an X-Y recorder and a paper tape perforator (Tally model P-120). For large volumes of data, these paper tapes were serially accumulated and the digital information was transferred to nine track magnetic tape and read into the University of Regina's Xerox Sigma 9 computer. Due to software incapacities between computing systems, this transfer of data from paper to magnetic tape could not be directly accomplished. The assemblage of steps, along with the necessary computer programmes, required to perform this function are fully described in appendix A. The net peak areas or intensities of spectral lines were obtained by the usual procedure of measuring the total peak area and subtracting from it a trapezoidal background. A complete description of the computer subroutines which were developed to accomplish the above calculation and also to evaluate net peak statistical precisions is given in appendix B.

The precision of a measurement in X-ray or γ -ray spectroscopy is a linear combination of the variances for the individual sources of error,

so the total variance may be represented by

$$S_T^2 = S_N^2 + S_I^2 + S_O^2 + S_S^2 \dots \dots \dots 3.7$$

where the subscripts represent, in order, total, counting, instrumental, operational and specimen errors. A similar equation can be written for each of the individual errors, expressing the variance for each as the sum of the variances of several specific sources of error. If the standard deviation of the result of a series of replicate determinations of an analyte intensity does not differ significantly from the standard counting error, the analysis is free of significant error and the precision is limited by the counting statistics. That is, ideally

$$S_T^2 = S_N^2 \dots \dots \dots 3.8$$

A complete precision analysis was performed on both the X-ray and γ -ray spectrometers to determine all of the terms, except S_S^2 , in equation 3.7 as detailed in appendix C. The specimen variance, S_S^2 , is not produced within the spectrometer but is an error related to the presence of the sample; it therefore is evaluated for each individual experiment in the appropriate section.

3.3. The K X-ray experiment

3.3.1. Introduction

In X-ray analysis, as conventionally practised, determination of uranium by the K spectral series is generally not preferred. Several fundamental disadvantages are encountered. (i) excitation of the uranium K shell would require an X-ray tube voltage of 200-300 kilovolts; (ii) the excitation efficiencies of the actinide K shell absorption edges are

lower at high energies than for energies required for L X-ray excitation; (iii) greater resolution of spectral lines is available at lower energy, and (iv) Compton and multiple Compton scattering cause high backgrounds degrading sensitivities with high excitation energies, especially so with a light element matrix. For purposes of on-stream industrial analysis, however, the analytical properties of uranium K shell fluorescence can be very beneficial. The high penetration capability of the excitation and fluorescent radiation lessens the sample homogeneity requirements and makes it possible to achieve direct analysis through the walls of vessels or tubes containing the specimen to be analyzed. For uranium in a low Z medium, matrix effects are greatly reduced due to the low mass absorption coefficient of the matrix elements for the excitation and fluorescent photon energies. The short wavelengths involved in the analysis also minimize specimen surface effects.

In 1959, Ziegler et al. (7), proposed an X-ray Rayleigh scattering method for analysis of heavy atoms in low Z media. Polychromatic, collimated beams of primary energy in the region of 70 to 90 keV were used because in this range, the relative contribution of σ_R to σ_{TOT} is a maximum, see figure 12. The scintillation detectors used in their work typically have a resolution of about 15 - 20% at this energy level. Large scatter angles were employed to allow sufficient resolution of the Rayleigh and Compton scattering peaks. Because Rayleigh scattering is a Z^{2-3} dependent phenomenon, the measured peak intensity exhibits a strong functional dependence on the number of high Z atoms present in the sample. This technique was later applied to analyzing uranium in dilute solutions of nitric acid (34). The influence of appreciable quan-

tities of low Z material, such as iron and aluminum, on the measurement accuracy were shown to be small and easily compensated for.

The weight per cent of uranium in an aluminum-uranium alloy was measured by a modified version of the above technique⁽³⁵⁾. Significant increases in sensitivity were achieved by determining the combined Rayleigh scattered and fluorescent K X-ray flux from uranium. The radioisotope excited X-ray source consisted of ^{85}Kr blended with uranium oxide powder. ^{85}Kr is a strong β^- emitter with some γ -activity. The output of the source then consists of a 514 keV γ -ray⁽³³⁾, bremsstrahlung and strong U K shell X-rays. The primary photons from the source below 115.6 keV cannot excite uranium K shell fluorescence although they can be Rayleigh scattered by uranium, primary photons above 115.6 keV (principally 514 keV) are able to generate uranium fluorescence but, have a low probability of being Rayleigh scattered. By incorporating right angle scattering geometry, the Rayleigh scattering was adequately separated from the Compton scattering over the range from 85 to 116 keV. By using both Rayleigh and K X-ray fluorescent radiation for uranium determination, it was possible to use a large part of the broad primary X-ray spectrum produced resulting in a corresponding increase in sensitivity. These techniques based on Rayleigh scattering measurements are limited for the case of a single heavy element in a light variable matrix; the analytical specificity is lost in a mixture of high Z elements.

Gorski⁽³⁶⁾ determined the concentration of aqueous solutions of uranium in the range from 0.05 to 1.0 M. He mentioned four different sources capable of exciting the K shell spectral lines of uranium, namely ^{75}Se , ^{141}Ce , ^{144}Pr and ^{154}Lu . The characteristic X-rays were detected by

a flat NaI scintillation crystal of optimum thickness. Forberg et al.⁽³⁷⁾ showed that ^{57}Co was superior to all these nuclides in the lack of high energy components and also because its main gamma energy is just above the K shell absorption edge of uranium. They studied partially thick uranium solutions, which had to be previously weighted to correct for the thickness factor, under a variety of geometrical conditions. Best results were obtained for right angle scattering. They also stated that Compton scattering intensity varies, in the first degree, with sample mass and matrix effects were relatively minor. Scintillation detectors were also used and did not have adequate resolution to separate the Compton scattering peak from the U K fluorescence; the same situation applies to elements adjacent to uranium on the periodic table. They subtracted an appropriate blank from the spectrum to reveal the net uranium K shell fluorescence.

The advent of high resolution Ge(Li) detectors permits sufficient resolution for the specific detection of all high Z elements. Baldin and Ioannesyants⁽³⁸⁾, used these detectors to analyze uranium solutions. A ^{57}Co point source was employed along with right angle scattering geometry. Burkhalter⁽³⁹⁾ used twin ^{57}Co point sources for analysis of Au in gold bearing ores as thick specimens. Uranium analysis by K X-rays was also investigated with synthetically prepared samples of uranium in silica. Large scatter angles were utilized. Better sensitivities were reported with this discrete monochromatic source than were achievable by using continuum radiation produced from bremsstrahlung sources or a 200 to 300 keV X-ray generator. Matrix correction was accomplished by normalizing fluorescent peak intensities to the Compton scattering

intensities. Bacharov et al. (40) reported the analysis of thin samples of gaseous UF_6 using a point ^{57}Co source with a 90° scatter angle.

In this work, uranium bearing ores from the major uranium producing areas of Canada were prepared and analyzed as partially thick specimens. A ^{57}Co point source is used, and the matrix and thickness factors are evaluated from a measurement of the Compton scattering and transmitted peak intensities. The scatter angle resulting in the optimum U K shell fluorescence peak to background ratio is determined.

3.3.2. K X-ray experimental

A 10 mCi ^{57}Co point source was designed and manufactured to induce uranium K shell vacancy production. The principle γ -emission from this nuclide, at 122 keV, is favourably positioned above the uranium K_{ab} , at 115.62 keV, to promote the high energy characteristic uranium fluorescence. An outline of the general source, sample and detector geometry is shown in figure 14. 10 mCi of ^{57}Co in 0.1N HNO_3 solution was obtained from New England Nuclear Ltd., Boston, Massachusetts. The point source was prepared at the Radioisotope Laboratory of the Faculty of Science at the University of Regina by evaporating, with an infrared lamp, small aliquots of the radioactive solution into the cavity of the source holder until essentially all the activity had been transferred. The source cavity was 1.5 mm in diameter and depth. Difficulties, due to surface tension are often encountered when depositing aqueous solutions into small apertures. For this purpose, insulin, from a 1% solution of zinc-insulin crystals (available from Connaught Laboratories Ltd., Willowdale, Ontario) in ethanol was initially evaporated onto the cavity surfaces to relieve



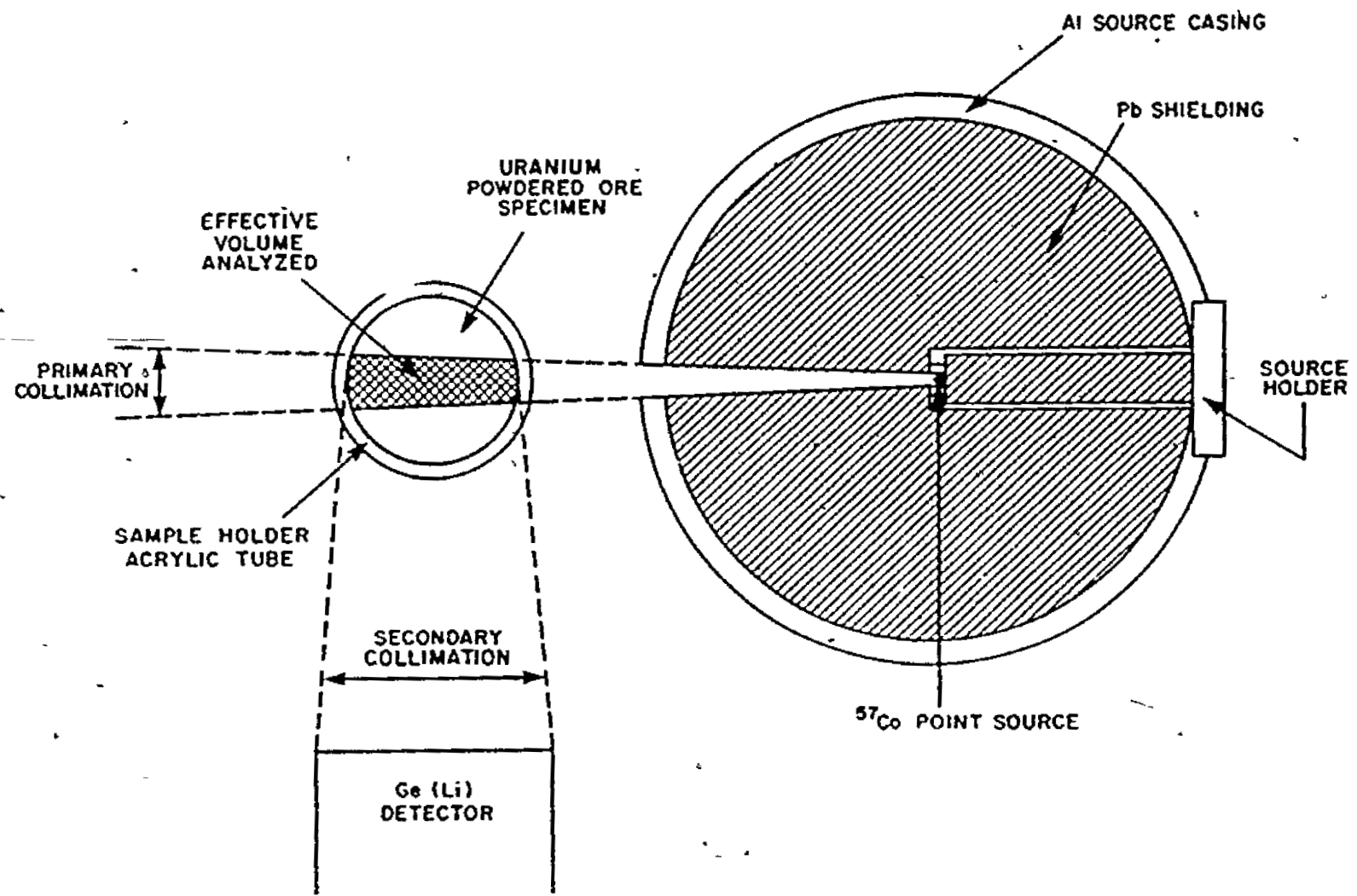


Fig. 14. Schematic diagram of the general source, sample and detector geometry as employed for the K X-ray experiment

these surface tension effects. The source holder was then inserted into the rear of the source housing. The source housing comprises a solid lead cylinder, approximately 9 cm in diameter encased in an aluminum jacket. Excitation radiation from the point source emerges from the front of the housing through a 5° machined collimating slit.

The Compton shifts of the primary excitation radiation (at 122 keV) are large enough to overlap the uranium K spectral lines. The background under these peaks is accordingly a function of scatter angle. To determine the conditions for optimum peak to background ratio, the source assembly was mounted on a one dimensional goniometer as shown in figures 15-17. Scatter angles ranging from 0 to 135 degrees, in 5° divisions can be obtained by rotating the source, along the degree ring, about the stationary specimen. The degree of secondary collimation also affects the peak to background ratio by altering the Compton scattering peak width. The one dimensional goniometer facility effects changes in secondary collimation by varying the height of the source - specimen platform in 2.5 cm increments from 0 to 50 cm. Both these adjustment features can be clearly seen in figure 15. While the degree of primary collimation is fixed, the effective specimen volume analyzed, figure 14, can be regulated by sliding the source assembly along the source support arms. Five settings at 1 cm intervals allows the point source to specimen distance to vary from 5 to 10 cm. Figure 16 illustrates the rear of the source assembly showing the primary collimation adjustment function.

The geometrical settings of the goniometer which gave optimum peak to background values were found by mounting a specimen of powdered waste

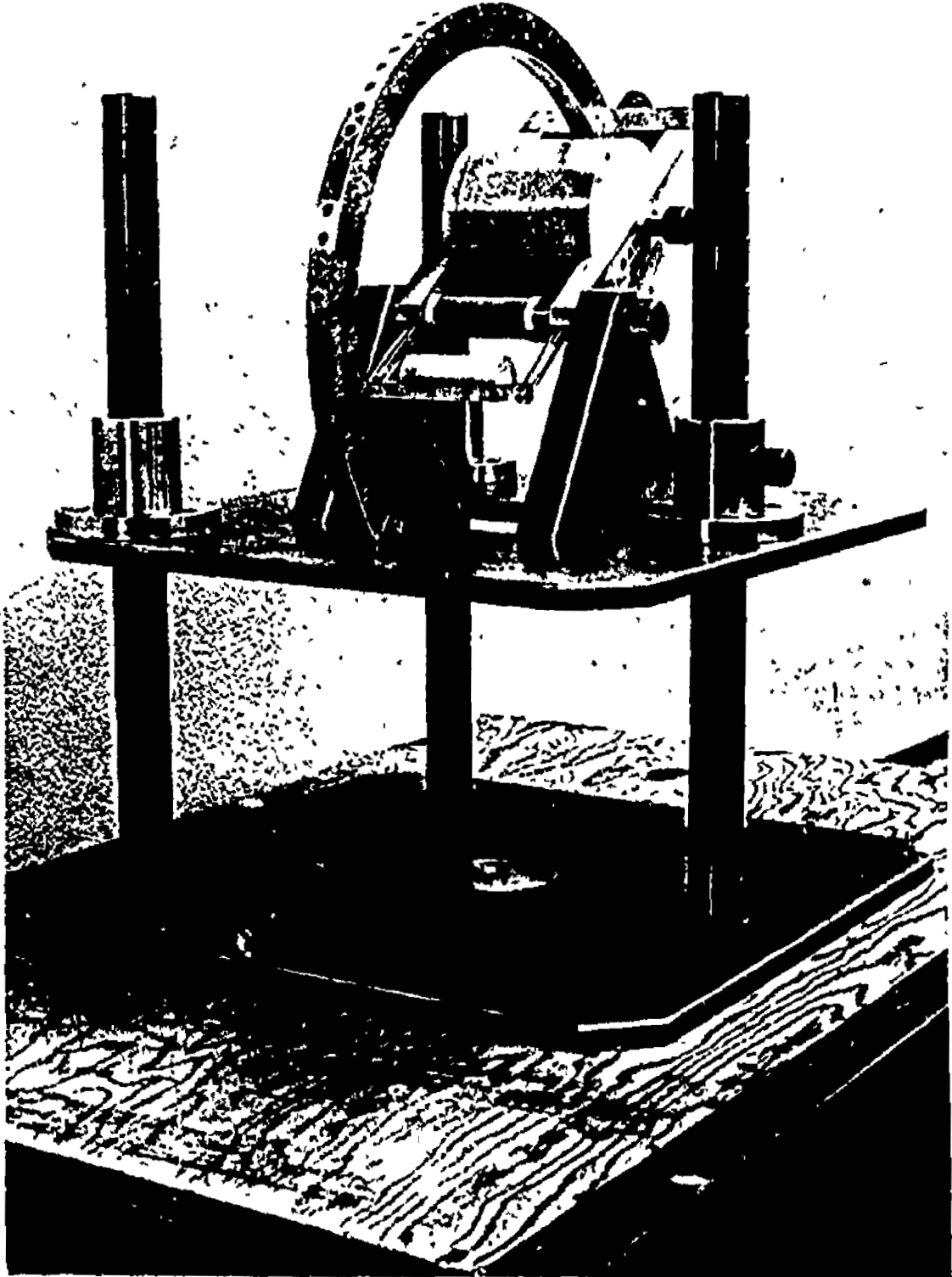


Fig. 15. Overall view of the K X-ray apparatus showing: the source, sample and detector geometry, the secondary collimation and scatter angle adjustment features



Fig. 16. Rear view of the X-ray apparatus illustrating the source insertion location and the primary collimation adjustment feature

rock of uranium content below the limit of detection from the Beaverlodge Mining District of northern Saskatchewan and measuring the background in the location of the major uranium K shell X-ray peaks - U $K\alpha_1$, U $K\alpha_2$, U $K\beta_1\beta_3$, U $K\beta_2\beta_4$. In addition, the net intensity of the Rayleigh scattered peak was evaluated. Secondary collimation settings of 5.0, 12.5, 20.0, 27.5 and 35.0 cm were used. For each of these height selections, spectra were recorded and analyzed for scatter angles of 10°, 40°, 55°, 70°, 85°, 100°, 115° and 135°. The entire series of background measurements were duplicated using primary collimation settings of 7.0 and 10.0 cm, respectively.

For maximum precision in measuring the fraction of incident radiation transmitted through the specimen, it is desirable that the sample linear thickness be such that the attenuation of the excitation beam by the specimen be equivalent to the transmitted flux. For a specimen of powdered granite, a linear thickness of approximately 2.5 cm was found to be suitable. That being the case, all specimens, in the form of homogenized powders of particle size -250 mesh, were placed in thin walled 2.5 cm od acrylic tubes of length 6.4 cm. The sample tubes were completely filled and .020" mylar disks glued to the tube ends to confine the specimen.

The transmitted radiation was detected by measuring the secondary fluorescence emitted from an X-ray target placed behind the specimen directly in line with the excitation beam. The most favourable target material to select is bismuth since the energy of its K X-ray lines are as high as can be practically attained without interfering with the uranium spectral line, or the Compton scattered peak. Normal uranium

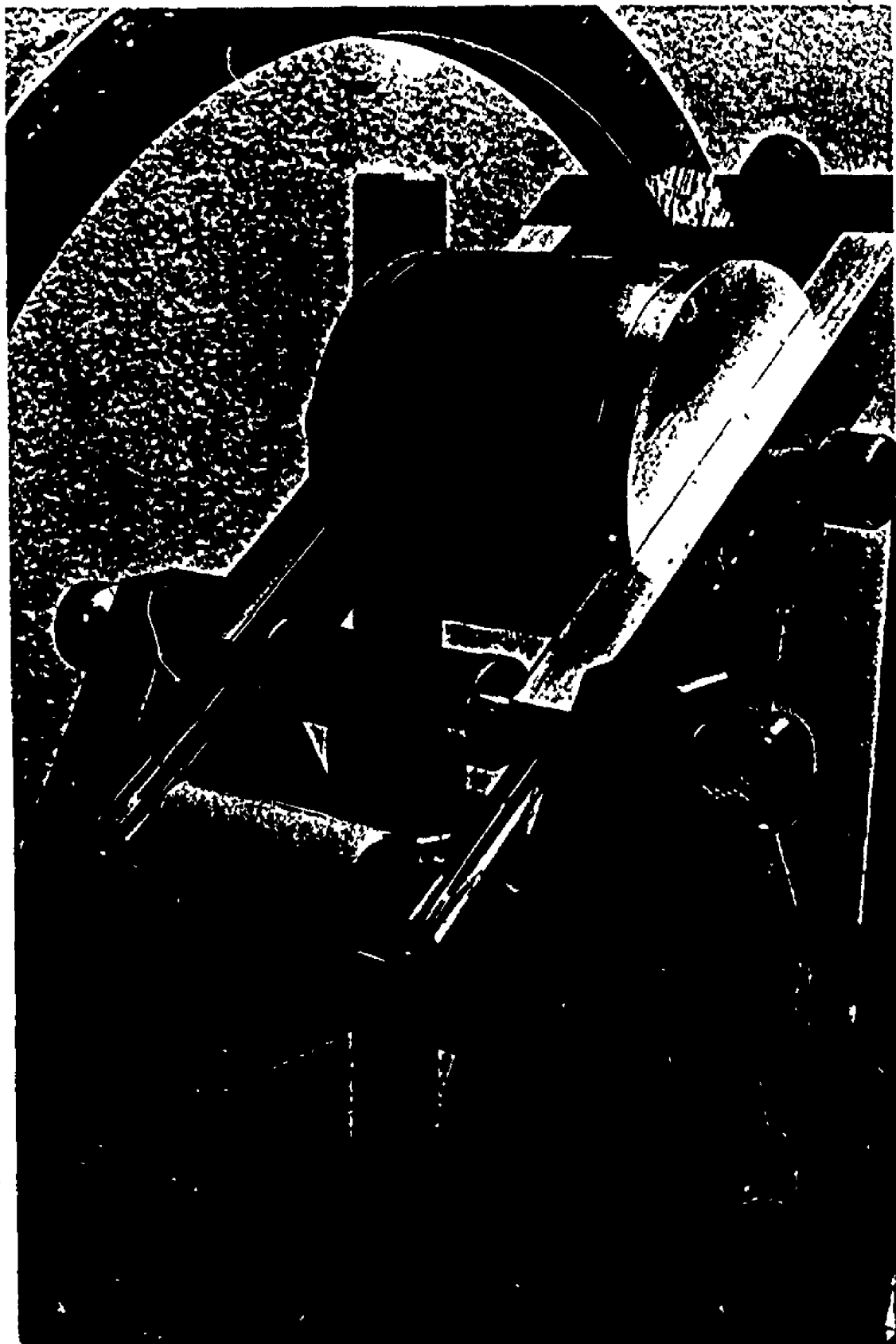


Fig. 17. Front view of the K X-ray apparatus showing the installation of the bismuth target used to measure the transmitted radiation intensity

bearing ores contain a negligible amount of Bi. The Bi target was fabricated by filling a sample tube with a mixture of BiOCl (bismuth oxychloride) and epoxy. After hardening, the Bi target was mounted on the source support arms as shown in figure 17. The incident source strength, I_0 , was determined by measuring the intensity of the observed Bi $K\alpha_1$ X-ray photopeak with only an empty sample container as a specimen. The transmitted intensity, I_T , through a sample is then proportional to the intensity of the Bi $K\alpha_1$ peak at 77.1 keV.

The relationship between sample mass and Compton scattering of 122 keV photons was determined for specimens of naturally occurring uranium bearing geological material. By using dissimilar packing densities, seven samples were prepared by filling specimen tubes with a measured mass of uranium ore. Since the specimens are all at constant volume, the mass of the sample present will then be proportional to the specimen thickness, measured in units of g/cm².

The spectrometer was calibrated so that approximately 1000 channels spanned the energy range from 70 to 125 keV. This conveniently incorporates both the Bi $K\alpha$ X-rays and the ⁵⁷Co Rayleigh scattered excitation γ -ray. Appropriate gamma emissions from ¹³³Ba, ¹⁰⁹Cd and ⁵⁷Co, used for this purpose, are presented in table 7. The instrumental settings, which remained constant for the entire uranium K X-ray analytical work, are listed in table 8.

The optimum geometrical settings as disclosed by the goniometer were used to analyze a total of 46 uranium ore samples originating from the major uranium mineral regions of Canada. These included material from the Rabbit Lake, Key Lake and Beaverlodge Lake deposits of northern

Table 7.

Reference sources used to calibrate the
 γ -spectrometer for the K X-ray experiment

Nuclide	Emission Energy (keV)	Absolute Abundance (photons/disintegration)	Reference
^{133}Ba	81.0	0.36	(33)
^{57}Co	122.06	0.852	(33)
^{109}Cd	88.03	0.039	(33)

Table 8

Instrumental settings used for the K X-ray experimental work

Unit	Function	Position
Ge(Li) detector	bias supply	+3200 Volts
amplifier	coarse gain	64
	fine gain	1.59
	shaping	4 μ seconds
	input impedance	+ 1K
ADC	conversion gain	400
	zero threshold coarse gain	2
	zero threshold fine gain	0
MCA	time	180 seconds
	output	3151-3990

Saskatchewan and from the Elliot Lake region of northern Ontario. The ores, from the Beaverlodge Mining District, were fluorimetrically standardized for uranium by Eldorado Nuclear Ltd., Mining Division, Uranium City, Saskatchewan, and those from Rabbit, Key and Elliot Lakes by Eldorado Nuclear Ltd., Research and Development Division, Ottawa, Ontario. Several samples were commonly standardized by both participating laboratories. The counting duration was fixed at 180 seconds and three spectra were recorded and analyzed from each sample and the average result taken. The net peak intensities of the $\text{Bi } K\alpha_1$, $\text{U } K\alpha_2$, $\text{U } K\alpha_1$, $\text{U } K\beta_1\beta_3$ and $\text{U } K\beta_2\beta_4$ X-rays were evaluated for each sample as well as the ^{57}Co Compton scattered peak. Serious interference occurs between the primary ^{57}Co Compton scattered peak (at 88 keV) and the $\text{Bi } K\beta$ X-rays of the same energy; therefore the Compton peak intensity was not directly measured. The occurrence of multi-Compton scattering phenomena results in a high background under the $\text{Bi } K\alpha_1$ peak. This quantity was taken as being representative of the primary Compton scattering intensity.

The variance due to specimen error, S_S^2 , principally consists of two components in this experiment: (i) errors due to the sample itself, and (ii) errors produced when loading the specimen onto the spectrometer. The first term was evaluated from the data produced from the analysis of 16 consecutive spectra taken from the same sample under precisely identical conditions. For determination of the second term, the specimen was removed, shaken and relocated on the spectrometer before each of 16 spectra were recorded. The total variance, S_T^2 , of an experimental measurement was then determined by adding the specimen variance, S_S^2 , to the instrumental variances itemized in appendix C for the γ -ray

spectrometer.

3.4. The L X-ray experiment

3.4.1. Introduction

The L shell absorption edges of uranium, while much lower than their K shell counterparts, are still substantially above the K_{ab} of the host matrix elements found in a naturally occurring uranium ore. This high Z element in a low Z matrix circumstance has been exploited by many workers to eliminate the necessity for matrix standards.

In determining trace quantities of uranium, in geological samples, analyte self-absorption effects vanish. The principal inaccuracy incurred while analyzing thick samples is then matrix element absorption of the analyte line. In recent years, several techniques have been reported⁽⁴¹⁻⁴³⁾ that analyze thick geological samples of loose powder featuring analyte peak to scattered background intensity ratios for matrix compensation. These methods all employ X-ray tube excitation for greater sensitivity. Analyte calibration curves are generally linear as long as the analyte concentration remains sufficiently small. As the analyte weight fraction in the specimen begins to be a significant amount (approximately 1% by weight), self-absorption effects initiate deviations from linearity. For industrial on-stream analysis, a higher useable concentration range is desirable.

By adopting radioisotope excitation, a higher degree of selectivity is achieved thereby significantly extending the linear portion of the analyte calibration curve. For example, ^{109}Cd (Ag $K\alpha$ X-rays) has been used to determine: Rb and Sr concentrations in rocks by Basco and

Balogh⁽⁴⁴⁾, Zr in zirconium bearing ores by Holynska and Langer⁽⁴⁵⁾, the iron content of kaolins by Bialek⁽⁴⁶⁾, and uranium in solutions by Kierzek and Parus⁽⁴⁷⁾, and Mackay⁽⁴⁸⁾.

In some cases, by selecting the appropriate isotope and geometry the primary excitation energy lies just above the analyte absorption edge but the Compton scattered peak is shifted below the edge. This situation is the essence to potential wide range matrix compensation by utilization of Compton scattering and is similar to the situation described by Burkhalter⁽⁴⁹⁾ for analysis of silver in silver ores. This author was able to take advantage of the fact that Te K α X-rays emitted from ¹²⁵I were able to excite the Ag K shell but that the energy of the Compton scattered Te K α X-ray was below the Ag K_{ab}. Under these conditions, with a light ore matrix, while analyzing for a heavy element, the analyte to Compton scattering intensity ratio tends to be proportional to the heavy element concentration. In most investigations, however, radionuclides suitable for this purpose do not exist and appropriate source target assemblies are required. Shenburg et al.⁽⁵⁰⁾ have reported utilizing a ²⁴¹Am annular source to excite the K X-rays of an As target for accurate determination of Cu in copper ores. The same source combined with a Cs target assembly was employed by Rhodes et al.⁽⁵¹⁾ for the analysis of Sn in tin bearing ores.

Shenburg and Amiel⁽⁵²⁾ have pointed out the analytical significance of the ratios of the major uranium L X-rays - U L α , U L γ , U L β_2 and U L β_1 - to backscattered target X-rays. By investigating uranium in pure solutions with a ²⁴¹Am source and iodine target assembly, similar to the one described by Glauque⁽⁵³⁾, the above authors have quantitatively

demonstrated that only the ratio of U L_{III} radiation to Compton scattering intensity will give a linear relationship over a wide range of uranium concentrations.

In this experiment, these findings were incorporated into the design of a source target assembly which selectively excites only the U L_{III} absorption edge. A scatter angle geometry sufficient to shift the Compton scattered excitation X-rays below the U L_{IIIab} was employed. With such a source, matrix enhancement effects are not possible. Absorption of U L_{III} fluorescence, principally $L_{\alpha_1\alpha_2}$ and L_{β_2} , by the matrix elements and the analyte can be adequately compensated for over a very wide range of uranium concentration by normalizing analyte intensity to the Compton scattering intensity. A technique was developed to analyze uranium bearing ores from northern Saskatchewan.

3.4.2. L X-ray experimental

Approximately 50 mCi of ^{241}Am in 0.1N HNO_3 was purchased from ICN Corp., Irvine, California. An annular shaped source was manufactured in an analogous fashion to that described in the K X-ray experiment. A molybdenum target was chosen to selectively excite only the uranium L_{III} subshell. Both components were incorporated into the housing of the source-target assembly. The assembly features a mean scatter angle of approximately 135° . A schematic representation of the source, target, sample and detector geometry is shown in figure 18.

Samples of uranium bearing ores were supplied in the form of homogenized powders of particle size less than 250 mesh. The powders were placed in acrylic containers, also shown in figure 18, and lightly tapped

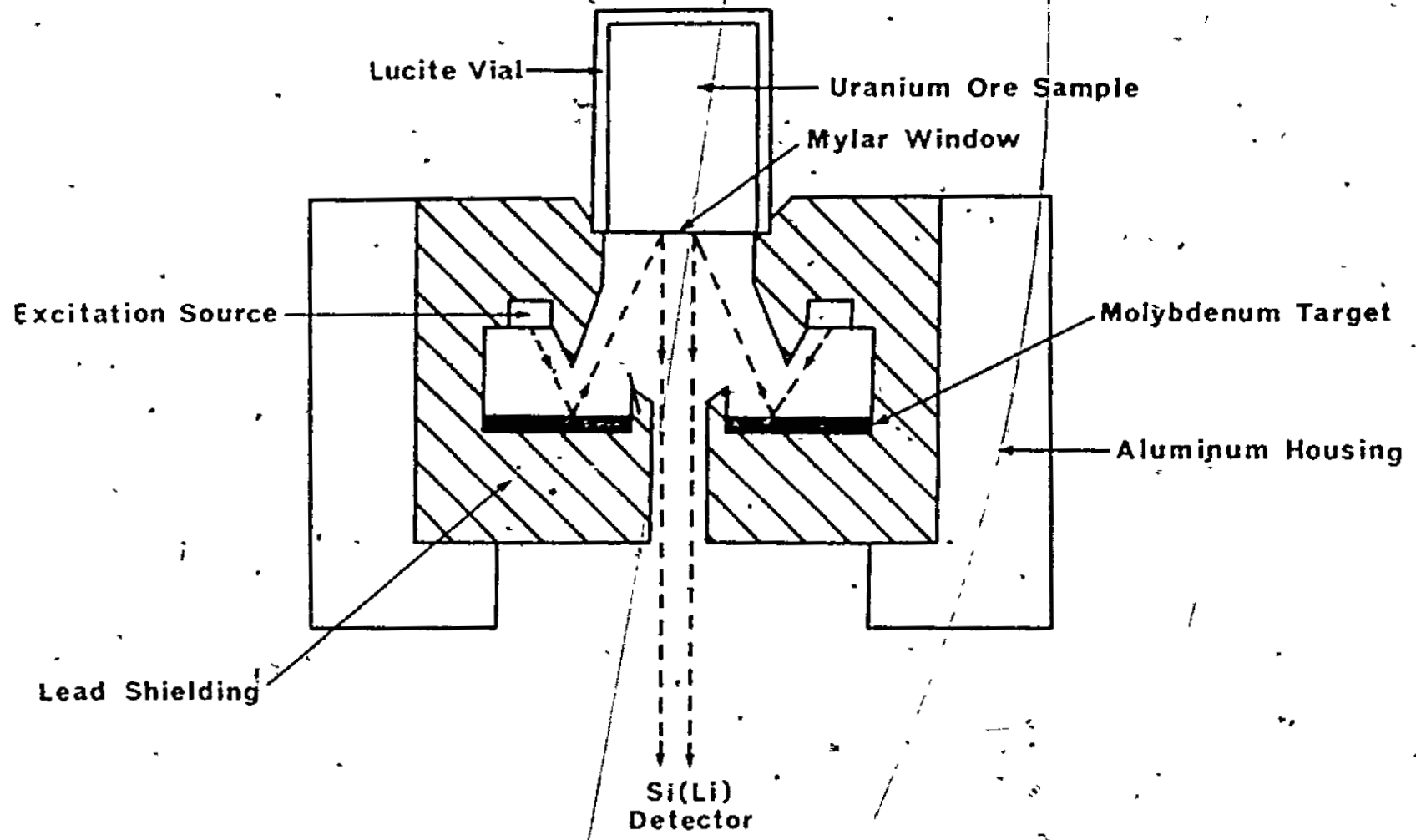


Fig. 18. A schematic representation of the source, target, sample and detector geometry employed for the L X-ray apparatus

to produce close packing. To contain the samples a 0.00025" thickness of mylar film was glued to the open end of the acrylic sample containers. Sample thicknesses were approximately 3 cm and this insured that they were infinitely thick for the X-ray energies involved within this work. Consequently, the sample weight was not required.

The X-ray spectrometer was calibrated with the Kevex-ray energy calibrator so that full scale on the multichannel analyzer spanned the energy range from 10 to 21 keV. The final instrumental settings adopted for all the X-ray work are listed in table 9.

The fluorimetrically standardized uranium ore samples were obtained from Eldorado Nuclear Ltd., Mining Division. In addition, some ore standards were synthetically prepared by adding an appropriate amount of pure U_3O_8 , also obtained from Eldorado Nuclear Ltd., to powdered samples of waste rock from the Beaverlodge Mining District of northern Saskatchewan. A total of fourteen standards were prepared ranging from less than 0.05 to 50% U_3O_8 .

Each standard used for the construction of the calibration curve was counted three times and the average result taken. The counting duration varied depending upon the amount of uranium present in the sample. From each spectrum, the net intensities and statistical precisions of the $La_{1\alpha_2}$ peaks, the $UL\beta_2$ peak and the Mo $K\alpha$ Compton peak were evaluated using a computer as outlined in appendix B. A method was developed to analyze uranium in uranium bearing ores using these peak intensities. To evaluate the performance of this technique, an additional set of fourteen ore samples of unknown concentrations was analyzed. The results were then compared with the fluorimetric analysis.

Table 9

Instrumental settings used for the L,X-ray experimental work

Unit	Function	Position
Si(Li) detector	bias supply	-990 Volts
	coarse gain	8
amplifier	fine gain	458
	conversion gain	200
ADC	zero threshold coarse gain	4
	zero threshold fine gain	227
MCA	output	3201-3880

The total variance introduced by the specimen errors, S_S^2 , was evaluated and added to the instrumental variances. As in the K X-ray case, the specimen error consists principally of two components. The first term sample error, was evaluated by an analysis of the dispersion of the net $U\text{La}_{1,2}$ peak intensities about the mean value of a set of 21 spectra consecutively recorded under the same sample conditions. For the second term, the loading error was also determined from a set of 21 spectra but the specimen was reloaded onto the spectrometer before each measurement.

3.5. The M X-ray experiment

3.5.1. Introduction

X-ray analysis for the actinide elements has usually meant utilizing the L series lines. In contrast, the M series of X-ray spectral lines have received little attention. The practical reasons for this are summarized in section 3.1. Briefly stated, under most analytical situations encountered, determination of actinide concentrations with M X-rays would not offer any advantage over the L X-ray facsimile. An exception was made for the analysis of thin samples of actinide chemical precipitates, it was expected that a significant improvement in sensitivity would be obtained using selective M X-ray rather than L X-ray techniques. These predictions have been verified in the literature. In 1976, Miller⁽⁵⁴⁾ investigated the analytical utility of the M series X-ray emission lines applied to precipitates of uranium, neptunium, plutonium and americium. Thin specimens were prepared by co-precipitating aliquots of actinide and carrier-internal standard with NH_4OH and

filtering onto a membrane filter. The $M\alpha, \beta$ X-rays, under optimum conditions, are several times more sensitive than their L series counterparts and appreciably lower backgrounds are observed for the lower energy lines. With the greater sensitivity, in addition to the lower backgrounds, peak to background ratios for M lines of up to 40 times greater than those for the L lines were reported.

The fabrication of thin samples of actinide chemical precipitate poses a major difficulty when utilizing M X-rays. Uniformly thin samples of approximately $300 \mu\text{g}/\text{cm}^2$ or less are required. The two commonly used techniques for thin sample preparation are: (i) evaporation, and (ii) co-precipitation. The former procedure is not desirable in this application because of the lower analyte content of the sample. The higher the actinide weight fraction in the specimen, the more beneficial the analysis by M X-rays will be. Co-precipitation of the actinides is also unsatisfactory for this purpose due to the fact that infinitely thin character tends to be lost through contracting or piling up while drying, the actinide precipitates. Visible changes such as mottling and reduced precipitate area size also often occur during the drying process. An alternative technique is electrodeposition of the analyte onto an electrode.

This technique is commonly utilized to prepare thin specimens for alpha spectroscopy. Thicknesses of less than $100 \mu\text{g}/\text{cm}^2$ are typically required and can be readily achieved. The principle drawback to the use of this procedure, is that electrodeposition yields are extremely critical where interferences are concerned; hence a high purity uranium electrolyte must be used in the electrodeposition cell. Sill et al. (55-56)

have intensely investigated and developed actinide separation schemes suitable for thin sample preparation by electrodeposition and subsequent analysis by α -spectroscopy. In 1977, this author reported⁽⁵⁷⁾ an isolation procedure for uranium from uranium bearing ores which was compatible with thin sample preparation by electrodeposition. All the long lived actinide radionuclides are α -emitters and accordingly, several electro-deposition techniques for uranium have been published⁽⁵⁸⁻⁶¹⁾. The procedure of Puphal and Olsen⁽⁶²⁾, using a mixed oxalate-chloride electrolyte, was adapted and employed in this work. It was judged superior because. (i) very high reliable yields are obtained, (ii) interference from many anions and cations have been quantitatively investigated, (iii) the electrolyte is only mildly corrosive allowing the use of stainless steel cathodes rather than Pt, (iv) the required deposition time is a minimum, and (v) the electrodeposition is inherently chemically compatible with the uranium separation procedure as described by Sill.

The use of ^{55}Fe , as an excitation source for low Z material, has received some application^(46, 63). This nuclide decays by electron capture and the principal applicable emissions are the Mn K_{α} X-rays at 5.9 keV. The energy of these lines are well suited for excitation of the U M_{Vab} at 3.5 keV.

In this experimental work, the small quantities of uranium found in soils and other geological material are chemically separated from the host medium and prepared as thin specimens of uranium precipitate by electrodeposition. The samples were then analyzed via M X-ray spectral line intensities after selective radioisotopic excitation. In keeping with the other X-ray analytical approaches presented in this thesis,

no matrix standards are required, however, the technique obviously cannot be employed for industrial on-stream analysis. The project was pursued because of its promising potential to analyze uranium at naturally found environmental concentrations.

3.5.2. M X-ray experimental

An electrodeposition apparatus was designed and manufactured to prepare thin samples of uranium chemical precipitate. Figure 19 is an exploded view of the cathode construction. Due to the high current densities used in this work, the cathode base must be water cooled to prevent the electrolyte from overheating. Large temperature variations affect the values of chemical equilibrium constants and thereby electrodeposition yields; hence the necessity to modulate the electrolyte temperature. The deposition cell consists of a 15 mm id glass joint 3.2 cm in height with a rubber "O"-ring seal (Ace Glass Company, Vineland, New Jersey). Stainless steel planchets having a 2.54 cm diameter (Beckman Instruments Ltd., Vancouver, B.C.) serve as the deposition surface. The cell is fastened to the brass cathode base by a threaded lucite collar. The total area of deposition is approximately 200 mm². A rotating platinum anode was fabricated from .020" Pt wire (95% Pt and 5% Rh -- Johnson, Matthey and Mallory, Toronto, Ontario) as shown in figure 20. The electrodeposition power supply unit employed was a Kepco, model KS 120-1, operated in the constant current mode.

To analyze the electrodeposited uranium precipitates, a compact radioisotopic source and sample holder assembly was constructed as shown in figure 21. 10 mCi of ⁵⁵Fe, as ferrous citrate in 1% citric acid was

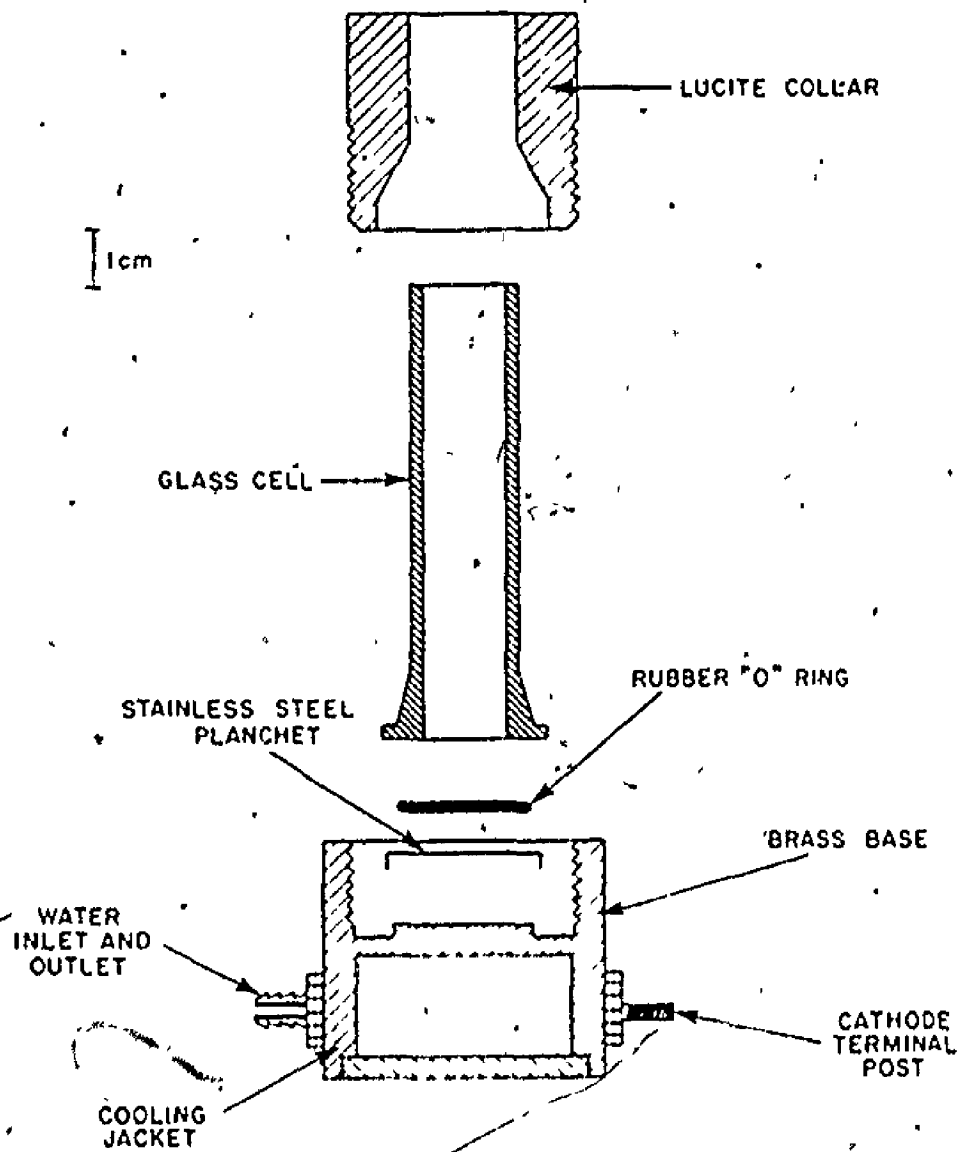


Fig. 19. Exploded view of the combined electrodeposition cell and cathode construction

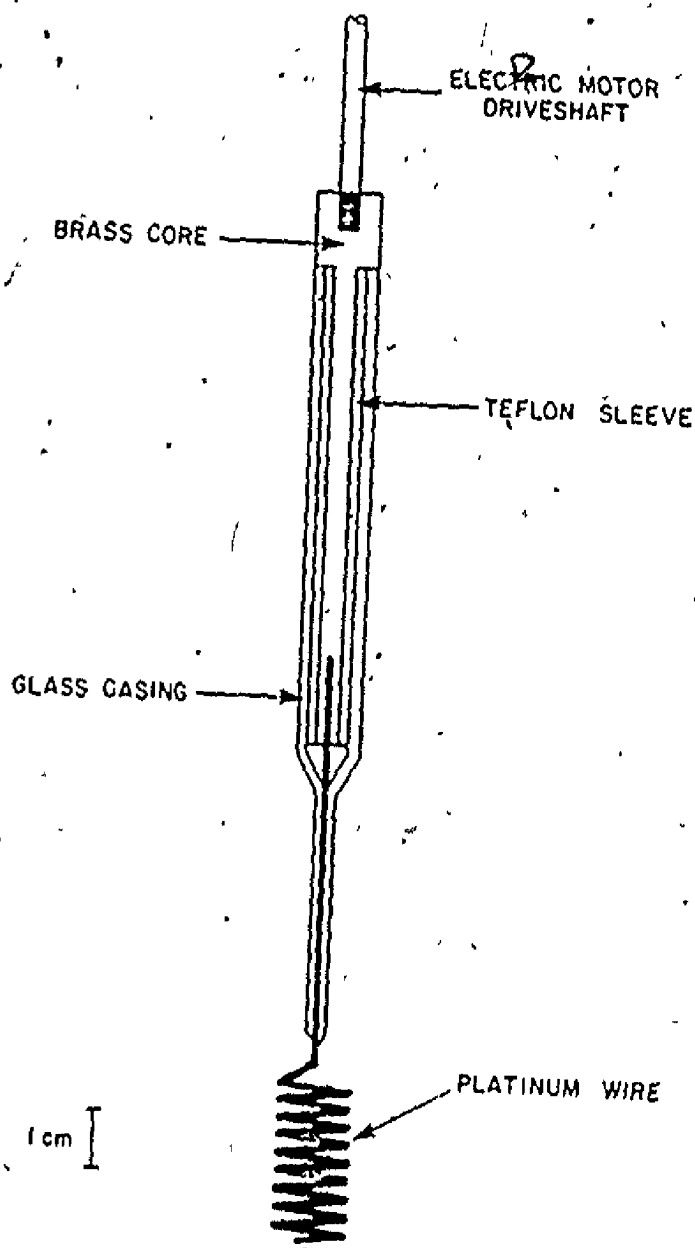


Fig. 20. Drawing illustrating the construction of the rotating platinum anode

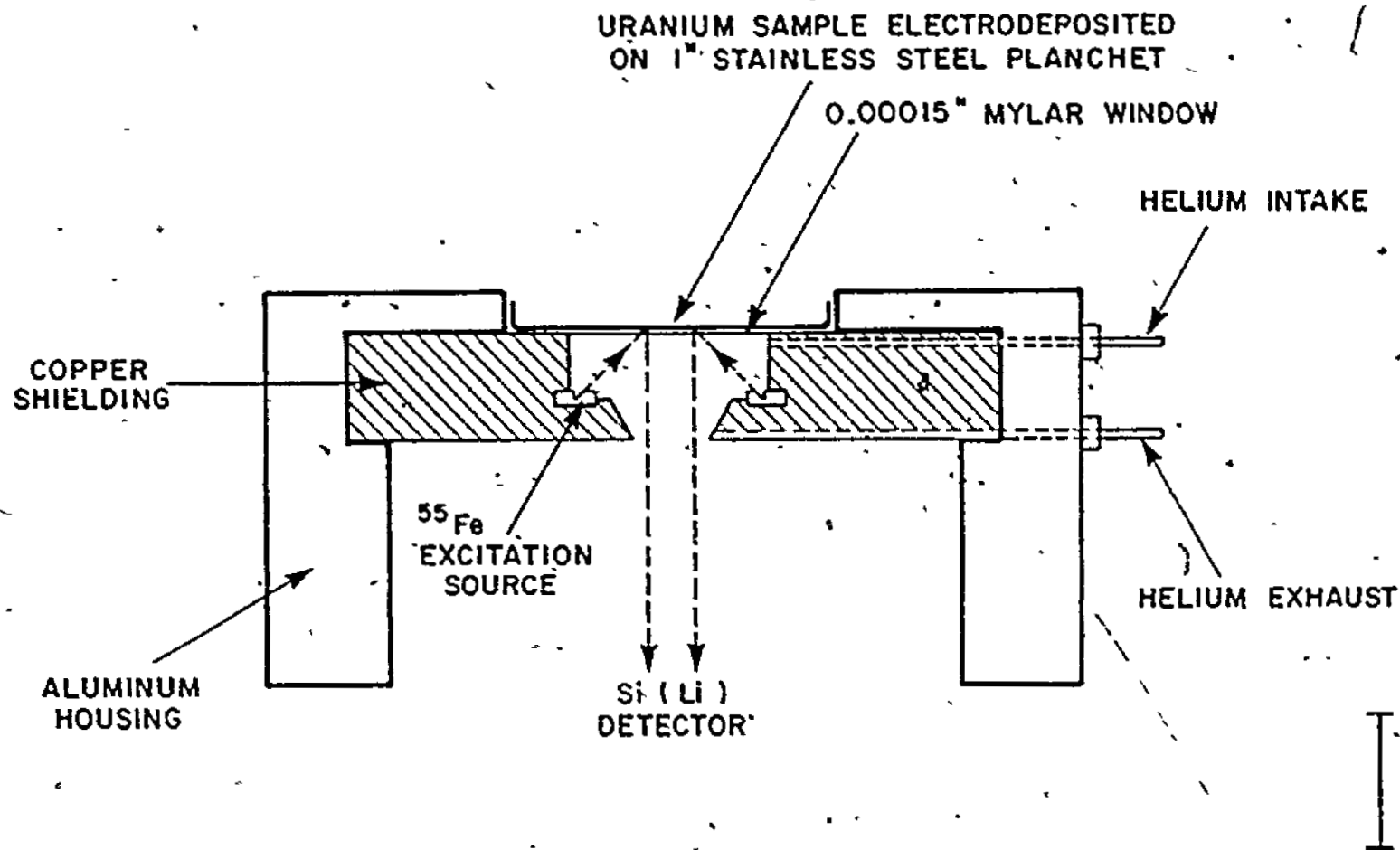


Fig. 21. Radioisotopic source, sample and detector configuration as employed in the M X-ray experiment

obtained from New England Nuclear Ltd., and an annular source prepared as previously described. Copper shielding was employed throughout and the entire assembly was encased in an aluminum housing. A helium flight path is required for two reasons. (i) the excitation energies from the isotope are very low and only a small fraction of the primary and fluorescent radiation would reach the specimen and detector respectively if an air flight path were utilized, and (ii) the atmosphere contains approximately 1% Ar. The Ar K α peaks cannot be resolved from and also dwarf the expected size of the U M α , β lines as observed with the Si(Li) detector. Helium flow rates through the housing were externally adjusted and monitored using a needle valve and flowmeter respectively (Manostat Corporation, New York, New York). The housing is machined to precisely mount the stainless steel planchets immediately adjacent to a .00015" mylar window.

The mixed oxalate-chloride electrolyte employed for all electro-depositions was prepared by adding 9.0 ml of 4% H₂C₂O₄ (oxalic acid), 1 drop of saturated NH₂OH.HCl (hydroxylamine hydrochloride), 1.5 ml of saturated NH₄Cl and approximately 5×10^{-6} moles of La³⁺ to the deposition cell. The latter was obtained by a 1 ml aliquot taken from a 5.0×10^{-3} M LaCl₃·6H₂O bulk solution. A stock standard uranium solution was prepared by dissolving 2.5364 g of 99.99% U₃O₈ (obtained from Eldorado Nuclear Ltd., Mining Division) in 100 ml of dilute HNO₃ to produce a final uranium concentration of 9.036×10^{-2} M UO₂²⁺. Working standard solutions 4.518×10^{-3} , 4.518×10^{-4} and 4.518×10^{-5} M UO₂²⁺ were prepared as required by diluting aliquots taken from the stock solution.

The optimum electrodeposition time was determined by analyzing

the quantity of uranium deposited from an electrolyte containing approximately 1.0×10^{-6} moles of UO_2^{2+} for discrete deposition times ranging from 5 to 110 minutes. The anode was lowered into the cell and positioned about 4 mm above the stainless steel planchet. The power supply unit was set to operate at a constant current of 1 ampere. At the conclusion of each electrodeposition, the temperature, pH at $25^\circ C$ and potential required to pass 1 ampere, were recorded. Using the optimum deposition time found, a calibration curve was prepared from the standard uranium working solutions by electrodepositing several solutions, containing from 10^{-8} to 10^{-6} moles of UO_2^{2+} . Each standard was counted three times and the average result recorded. Both the U $M\alpha_1$, β and La $L\alpha_1\alpha_2$ peak intensities were measured.

The total procedure adopted to analyze uranium in low grade ores or soils consists of four main steps as outlined in figure 22. The four acid dissolution was performed by. (i) weighing the appropriate quantity of sample material and lightly boiling for 10 minutes with 20 ml of a 1:1 mixture of concentrated HCl and HNO_3 , replenishing the HNO_3 as required; (ii) adding 5 ml of 30% HF and 5 ml of 50% H_2SO_4 and heating at high temperature until the absence of SO_3 fumes; (iii) dissolving the residue in 35 ml H_2O and 5 ml of concentrated HNO_3 , boiling lightly for two minutes and filtering through a #1 Whatman paper, and (v) evaporating the filtrate to dryness.

A phase transfer catalyst, Aliquat-336 (available from General Mills Chemicals, Inc., Minneapolis, Minnesota), was utilized to separate uranium from the matrix elements. This was prepared in NO_3^- form by dissolving 300 ml of Aliquat-336 in Cl^- form (as purchased) in 700 ml

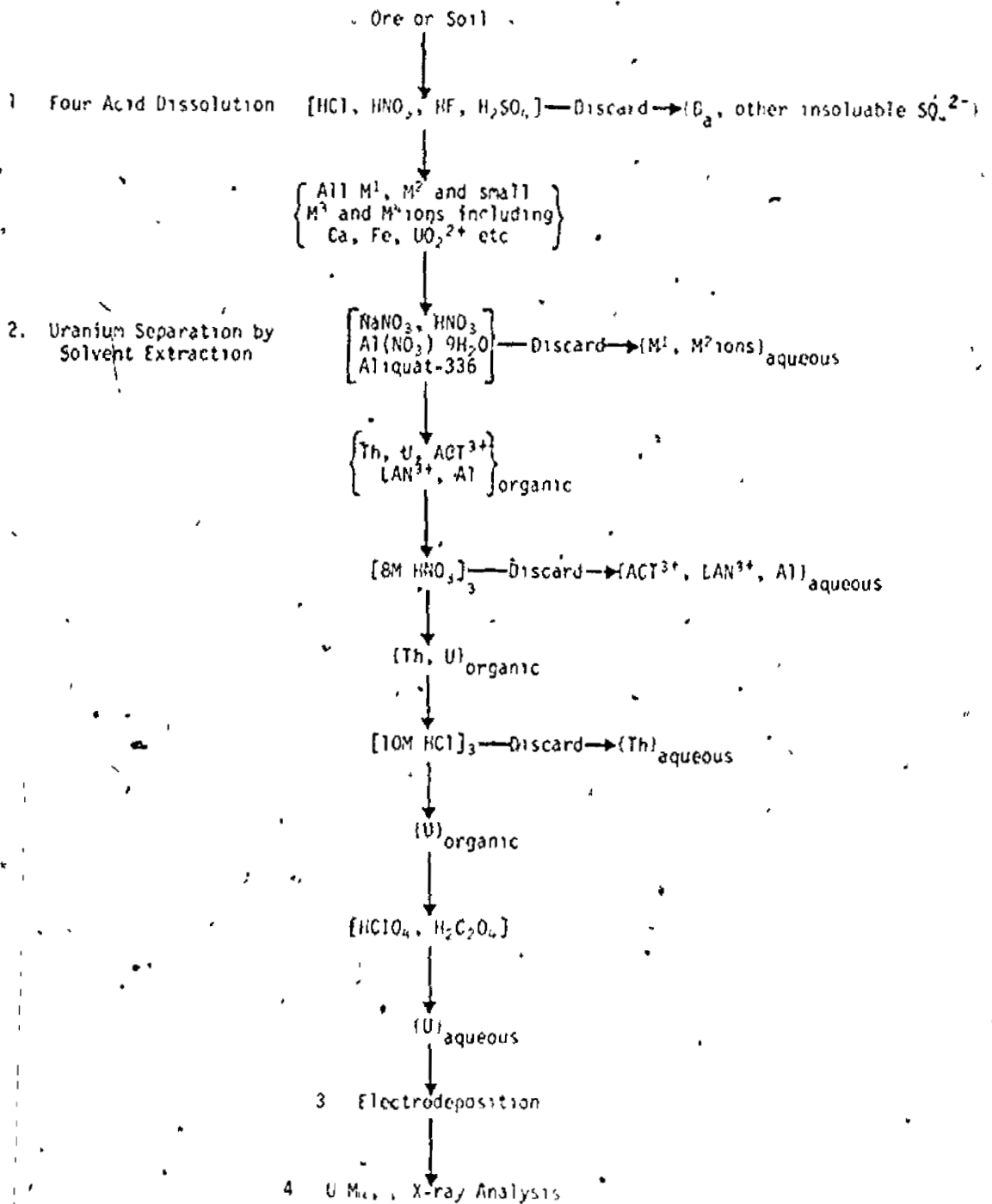


Fig. 22. Outline of total procedure adopted to analyze uranium in low grade ores or soils

of xylene. Using a 2 litre separatory funnel, 2 portions of 175 ml of 4M HNO_3 , were each added and shaken vigorously for 4 minutes. The organic phase was washed 3 times with 300 ml of H_2O , shaken for 4 minutes for each wash. The final reagent was 30% Aliquat-336(NO_3^-) in xylene.

Uranium was separated from the ore or soil by the following procedure: (i) the cake from the dissolution step was dissolved with 10 ml of 2.2 M acidic $\text{Al}(\text{NO}_3)_3$ and transferred to a 60 ml separatory funnel. The solution was washed with 5 ml of the $\text{Al}(\text{NO}_3)_3$ reagent; (ii) 10 ml of 30% Aliquat-336 in xylene and 1 ml of 25% NaNO_3 were added, swirled and the solution allowed to stand for 2 minutes, (iii) it was then shaken vigorously for 3 minutes and allowed to stand for 10 minutes following which the aqueous phase was discarded, (iv) the organic phase was scrubbed 3 times, each with 2 ml portions of 8M HNO_3 allowing 2 minute intervals between scrubs; (v) the organic layer was again scrubbed 3 times with 10 ml of 10M HCl , each followed by a 3 minute standing period, and (vi) the uranium was extracted into the aqueous phase with 10 ml of 10% HClO_4 - 4% $\text{H}_2\text{C}_2\text{O}_4$ solution and washed with 5 ml of H_2O . The final aqueous solution was taken to dryness with 5 ml of 50% H_2SO_4 and heated until the absence of SO_3 fumes and any organic material. The uranium bearing residue was dissolved in approximately 1 ml of hot 4% $\text{H}_2\text{C}_2\text{O}_4$ and transferred to the electrodeposition cell. The addition of the remaining reagents necessary for the electrolyte were added as described earlier. After deposition, the anode was raised out of the cell with the power on. The electrolyte was immediately discarded and the planchet carefully rinsed with 0.1N NH_4OH . The electrodeposition cell was then dismantled and the specimen removed and placed

on a high temperature hot plate for 5 minutes. The specimens were then stored prior to analysis by U M α , β X-rays.

The energy calibrator was employed to suitably calibrate the spectrometer to observe the U M and La L spectral lines. Table 10 lists the instrumental settings required for a full scale energy range from approximately 2 to 7 keV.

This procedure was employed to determine the uranium concentration present in several low grade ores originally from the Elliot Lake, Rabbit Lake and Beaverlodge Lake uranium mining localities. Each planchet was counted three times and the average result recorded. The U M α , β and La L $\alpha_1\alpha_2$ peak intensities were measured as described in appendix B. A method was developed to accurately determine small quantities of uranium using these two peak intensities.

Due to the required chemical separation and electrodeposition steps, the sources of specimen related error are more numerous and of greater magnitude for the M X-ray analysis than for either the K or L X-ray experiments. The total specimen variance, S_S^2 , was measured with and without the presence of La³⁺ in the electrodeposition cell. This was accomplished, for each case, by treating 10 equally weighed samples from the same ore to the entire procedure and then evaluating the dispersion about the mean U M α , β peak intensity. As in the previous experiments, the variance inherent to the specimen itself and the loading variances were both measured, each for 14 consecutive spectra. The total variance for an experimental measurement was then obtained by adding S_S^2 to the instrumental variances found for the X-ray spectrometer.

Table 10

Instrumental settings used for the M_K X-ray experimental work

Unit	Function	Position
Si(Li) detector	bias supply	-990 Volts
amplifier	coarse gain	4
	fine gain	437
ADC	conversion gain	800
	zero threshold coarse gain	0
	zero threshold fine gain	143
MCA	time	180 seconds
	output	3151-3960

3.6. The γ -spectroscopy experiment

3.6.1. Introduction

The $^{235}\text{U}/^{238}\text{U}$ isotopic ratio has been measured by mass spectrometry, α -spectroscopy, neutron activation and γ -spectroscopy. Due to its simplicity, the latter technique is conveniently applicable to industrial routine determination of uranium-isotope ratios. However, the analysis generally relies on daughter activity for measurement of ^{238}U content. Under conditions of secular equilibrium the concentration of the parent nuclide can be determined from a measurement of the concentration of any one of its daughters. In the radium decay series, figure 23, chemical forces causing the separation of uranium from thorium result in the secular equilibrium being broken since it would require approximately 6×10^5 years for the equilibrium to be re-established between ^{234}U and ^{230}Th . For this reason, the radium decay series is conveniently classified into the uranium group, i.e. those daughters disintegrating at the same rate as ^{238}U and the radium group whose members are in equilibrium with ^{226}Ra . By similar arguments, the actinide decay series, figure 24, can be divided into the uranium group and the protactinium group as a result of the long half-life of ^{231}Pa .

The daughters of ^{226}Ra are generally strong γ -ray emitters, most notably ^{214}Pb and ^{214}Bi , and are almost exclusively used for uranium determination with γ -spectroscopy. Although they are short-lived, equilibrium can also readily be disrupted by loss of the gaseous ^{222}Rn . Uranium analysis performed using activity measurements from these nuclides may or may not be satisfactory on natural geological samples, but cannot be accomplished on recently produced uranium chemical precipitates.

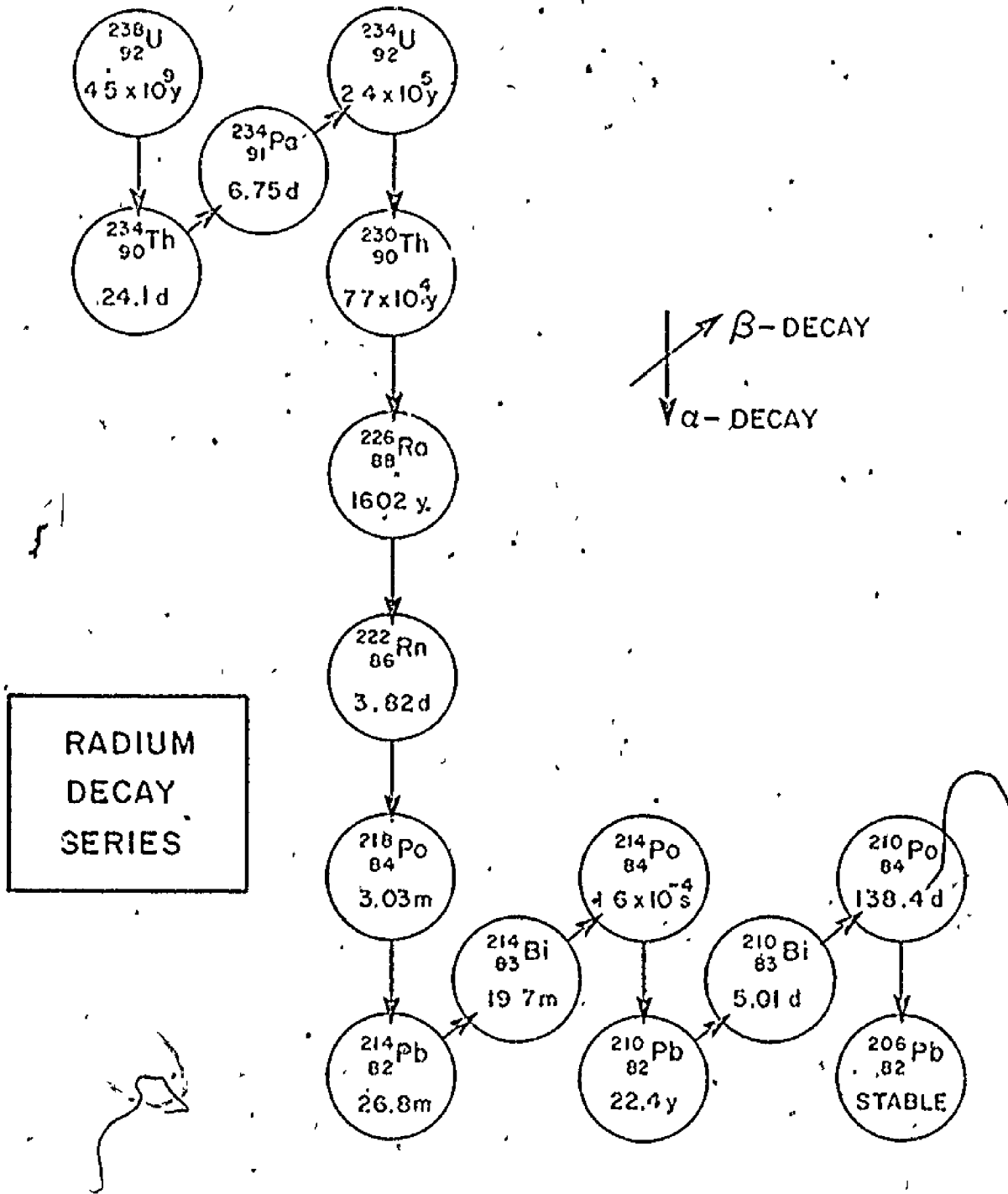


Fig. 23. Radium decay series

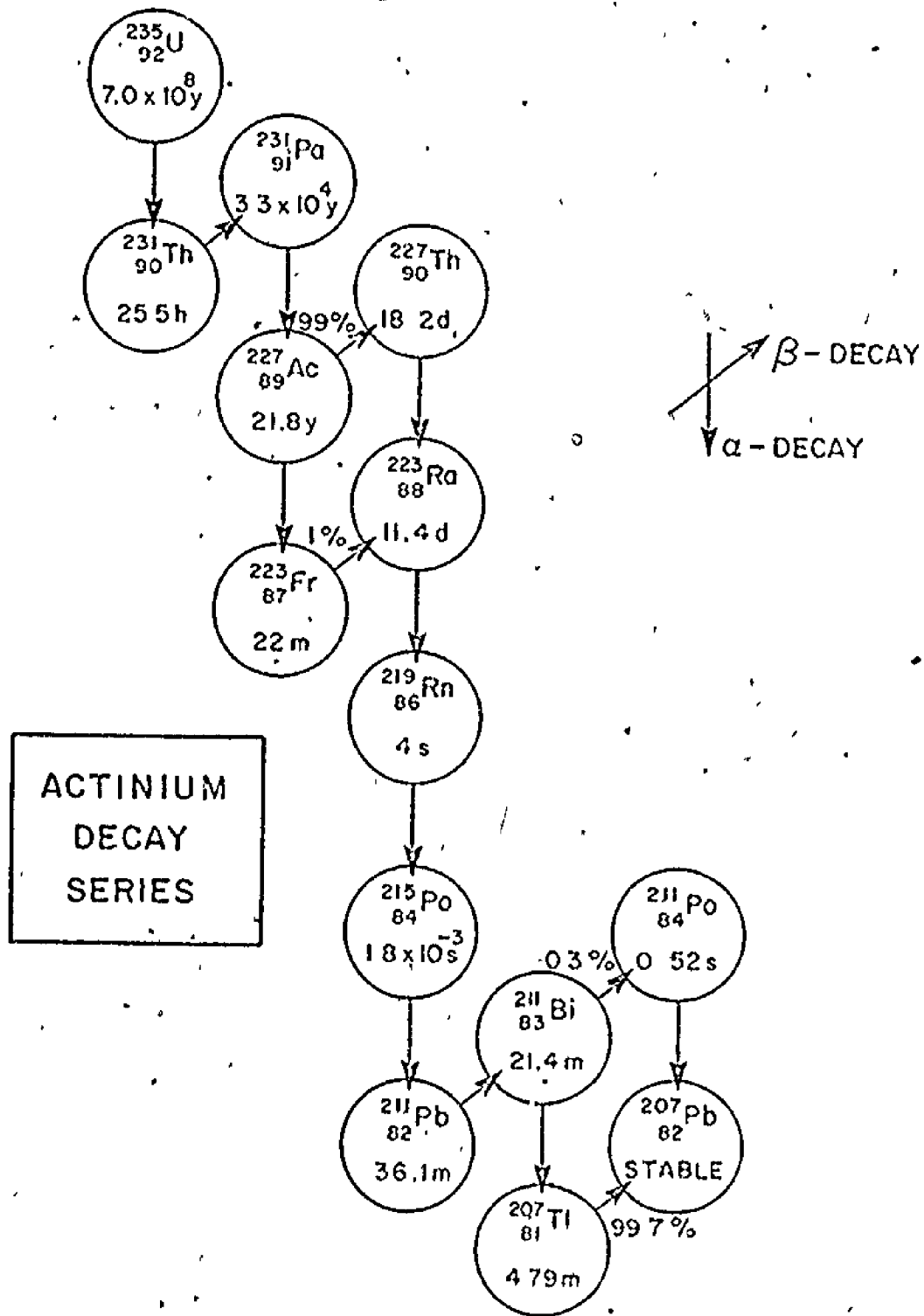


Fig. 24. Actinium decay series

because not enough time has elapsed for sufficient growth of appropriate daughter activity. To obtain accurate determinations of ^{235}U and ^{238}U contents, it is necessary to measure the activities of nuclides in the uranium group of both decay series. Fortunately, a relatively short period of time is required to achieve secular equilibrium between members of the uranium group of ^{235}U and ^{238}U from a recently produced uranium chemical precipitate.

Activity measurements of the ^{235}U group by γ -spectroscopy are readily accomplished. This uranium isotope can be directly determined as several γ -rays are emitted from ^{235}U , the strongest of which occurs at 0.186 MeV^(64 - 67). However, when γ -spectroscopy is applied to photopeak intensity measurements of the ^{238}U group, very few suitable lines are observed. Studies of the γ -spectrum for uranium^(68 - 69) in the range from 0.150 to 2.80 MeV indicated that only two weak lines of $^{234\text{m}}\text{Pa}$ at 0.776 and 1.002 MeV present any possibility for unique quantitative measurements of ^{238}U . The lower energy γ -spectrum of the ^{238}U group has been examined and discussed^(70 - 72) and four prominent lines of ^{234}Th are reported - a gamma doublet centered at 0.0925 MeV and a further small doublet at 0.063 MeV. The origin of these lines is illustrated by the simplified version of the decay schemes⁽⁷³⁾ of ^{238}U , ^{234}Th , $^{234\text{m}}\text{Pa}$ and ^{234}Pa shown in figure 25.

Large volume Ge(Li) detectors are characterized by a fairly broad energy range of high relative detector efficiency. However, at energies immediately below this plateau, detector efficiency decreases very sharply so that the spectrometer is far more sensitive to the 0.0925 MeV γ -emissions than to the 0.0633 MeV photopeaks. In addition, the abundance

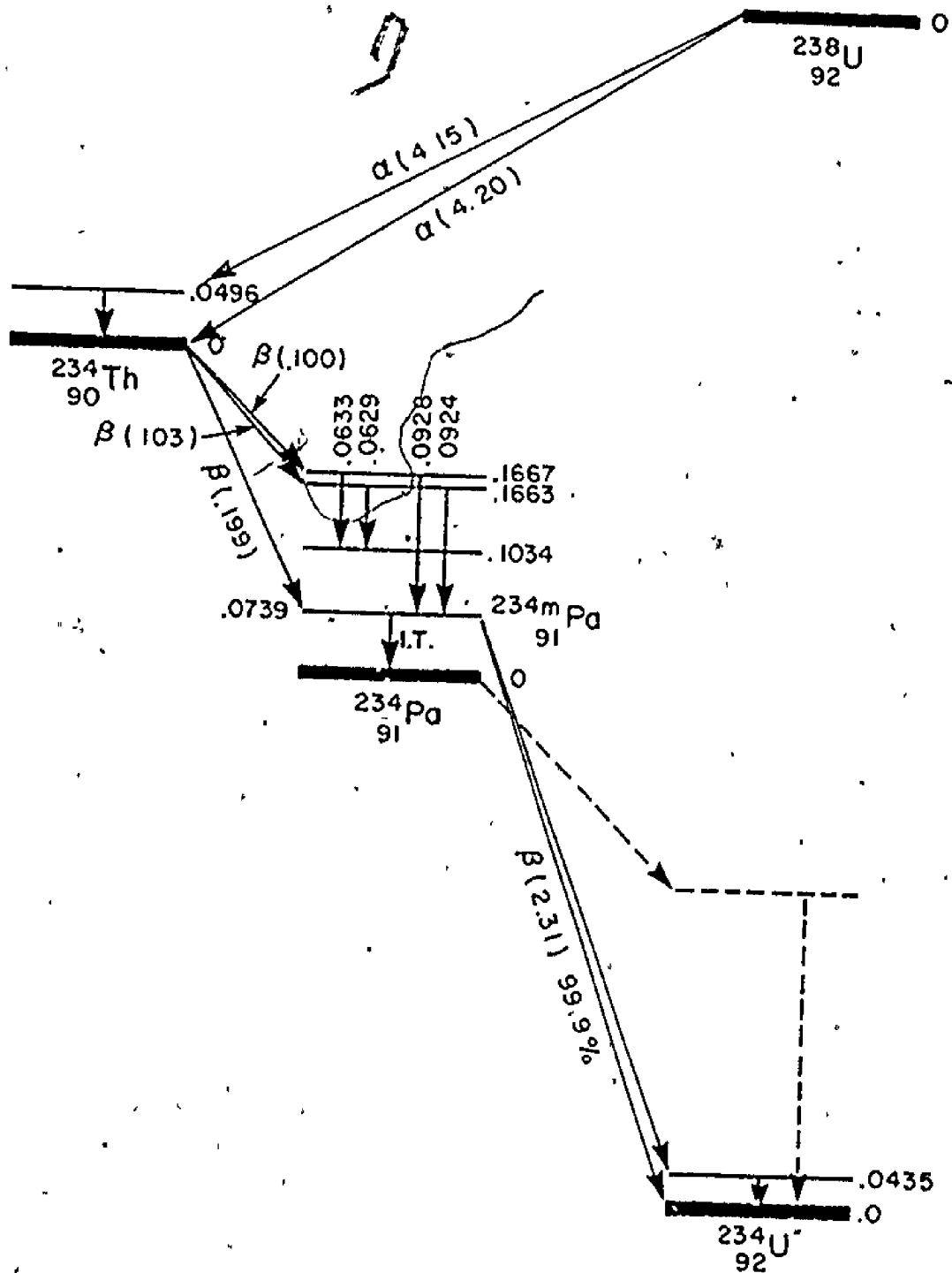


Fig. 25. Simplified version of the decay schemes of ^{238}U , ^{234}Th , $^{234\text{m}}\text{Pa}$ and ^{234}Pa

of this lower energy doublet is approximately a factor of ten less than the 0.0925 MeV doublet⁽³³⁾. These two facts combine to greatly enhance the analytical significance of the higher-energy doublet. Unfortunately the background in the vicinity of this photopeak is complicated by underlying actinide $K\alpha$ X-rays and ^{231}Th γ -rays and for this reason has received little consideration for potential unambiguous ^{238}U analyses. Thorium $K\alpha_1$ and $K\alpha_2$ X-rays may be emitted from several sources but always accompany the decay of ^{235}U . U $K\alpha$ photopeaks can also be produced by self-fluorescence in samples of high uranium concentration, the $K\alpha_2$ peak of which contributes heavily to the intensity of the ^{234}Th doublet.

Matsuda and Abrao⁽⁷⁴⁾ have reported ^{238}U analyses using the 0.0925 MeV ^{234}Th doublet. Adams and Gasparini⁽⁷⁵⁾ have also recognized the need for direct ^{238}U measurements to determine the degree of non-equilibrium in the overall radium decay series. Both workers ignored the inherent Th $K\alpha$ X-ray corrections, and since the specimens to be analyzed consisted of natural soils and rocks, did not require a uranium self-fluorescence subtraction due to low uranium concentration.

In this work, the $^{235}\text{U}/^{238}\text{U}$ ratio has been determined by using the conventional 0.186 MeV photopeak for ^{235}U measurement and the 0.0925 MeV ^{234}Th doublet for ^{238}U measurement in the analysis of uranium chemical precipitates (U_3O_8 , $\text{Na}_2\text{U}_2\text{O}_7$). Both the U $K\alpha$ and the Th $K\alpha$ X-rays are very strong in ^{235}U enriched samples and their interference was removed by approximating the spectrum in this region by a series of Cauchy functions fitted by a best least squares technique. By integrating only the two component ^{234}Th γ -rays an accurate ^{238}U intensity can be obtained even for highly enriched ^{235}U samples.

3.6.2. γ -spectroscopy experimental

The spectrometer was calibrated so that approximately 1000 channels spanned the energy range from 0.070 to 0.200 MeV. A source of uranium oxide, highly enriched in ^{235}U obtained from Union Carbide Corporation, Nuclear Division, Oak Ridge, Tennessee, was used as the standard reference source. Table 11 lists the radionuclides and their useful emissions which conveniently define the above region and were used in the energy calibration. The instrumental settings adopted for the γ -spectroscopy work are shown in table 12.

In order to obtain an accurate determination of ^{230}U , the twin peaks of the ^{234}Th doublet including the background and the surrounding partially resolved peaks were approximated by a series of Cauchy functions fitted by a best least squares technique⁽⁷⁶⁾. The experimental data from the analyzer have the form:

where:

$$y_1, y_2, y_3 \dots y_1 \dots y_n$$

$y_i = y(x_i)$
 x_i is the i^{th} channel number
 y_i is the number of counts recorded in x_i
 n is the number of experimental points in the spectrum

The experimental data were fitted to a function defined by.

$$F = \sum_{j=1}^m (c_j + b) \dots \dots \dots 3.9$$

where:

m is the number of peaks to be fitted
 b is the background under the fitted peaks,
 c_j is the Cauchy function approximation to each peak

Table 11

Emissions from the ^{235}U reference source
used to calibrate the γ -spectrometer

Nuclide	Energy	Emission Origin	Absolute Abundance	Reference
^{235}U	0.186	γ -ray	0.540	(33)
	0.163	γ -ray	0.046	(33)
	0.144	γ -ray	0.097	(33)
	0.0899	Th $\text{K}\alpha_2$ X-ray	unknown	(12)
^{231}Th	0.084	γ -ray	0.079	(33)
--	0.0984	U $\text{K}\alpha_1$ X-ray	--	(12)

Table 12
Instrumental settings used for the γ -spectroscopy work

Unit	Function	Position
Ge (Li) detector	bias supply	+3200 Volts
amplifier	coarse gain	64
	fine gain	1.70
	shaping	4 μ seconds
	input impedance	± 1 K Ω
ADC	conversion gain	200
	zero threshold coarse gain	2
	zero threshold fine gain	0
MCA	time	1200 seconds
	output	3151-3960

i.e.
$$c_j = P_{3j-2} / (1 + [2(x_i - P_{3j-1}) / P_{3j}]^2) \dots \dots \dots 3.10$$

The iteration parameters P for each peak j are defined as follows:

- P_{3j-2} = peak height
- P_{3j-1} = peak location
- P_{3j} = full width half maximum

The best fit is obtained when the parameters are chosen so as to minimize the following function:

$$M(P_1, P_2, P_3, \dots, P_{3m}, b) = \sum_{i=1}^n (F - y_i)^2$$

$$= \sum_{i=1}^n \left\{ \sum_{j=1}^m (c_j + b) - y_i \right\}^2 \dots \dots \dots 3.11$$

A full description of the unfolding procedure and a listing of the required computer programmes is given in appendix H.

Prior to unfolding the spectra, it was necessary to subject the raw data to a nine point best least squares cubic polynomial smoothing subroutine (77 - 78) also detailed in appendix H. The net intensity due to ^{238}U concentration was then calculated by integrating only the two Cauchy functions assigned to the ^{234}Th doublet.

The ^{235}U concentration was determined by direct measurement of the 0.186 MeV ^{235}U γ -ray. For uranium chemical precipitates, this has no interferences and the background was estimated by the conventional technique described in appendix B.

To evaluate the effect of sample thickness on the $^{235}\text{U}/^{234}\text{Th}$ peak intensity ratio, two sets of natural uranium samples of varying thicknesses were prepared from pure black oxide (U_3O_8) and from yellow cake (approximately $\text{Na}_2\text{U}_2\text{O}_7$). Both materials were supplied by Eldorado

Nuclear Ltd., Mining Division. The sample containers were manufactured by glueing a .020" mylar disk to one face of a 3 cm id acrylic ring as shown in figure 26. The uranium was then weighed into the container, evenly distributed and sealed with approximately 20 ml of paraffin wax.

Stock material, in the form of depleted and enriched uranium as U_3O_8 , was obtained from Union Carbide Corporation, Nuclear Division. Standard samples of varying ^{235}U content were prepared as described above and selected so they were suitable for a wide range and a narrow range calibration curve. The former is applicable to samples ranging from 0 to 25% ^{235}U and the latter is designed for samples close to the natural isotopic abundance of uranium.

In addition, the isotope ratio was measured on high grade ores from several uranium mineral zones. Since ^{226}Ra emits a strong γ -ray which cannot be resolved from the 0.186 MeV ^{235}U photopeak, the uranium group must be separated from the radium group in the radium decay series. A four acid dissolution, as described in section 3.5.2., of the ores followed by a double or triple $FeCO_3$ co-precipitation conveniently separates uranium from most elements including radium. The latter was performed by initially neutralizing the acid filtrate from the dissolution step by addition of solid Na_2CO_3 , warming for 10 minutes, then filtering the massive iron precipitate through a Whatman #40 filter paper. This was repeated until all the naturally occurring iron was completely removed, two precipitations were generally sufficient. The final co-precipitation was carried out with the addition of 5 ml of 0.1M $FeCl_3$ and 5 ml of 0.2M Na_2CO_3 solutions. The filtrate was neutralized by concentrated HNO_3 and 5 ml excess added followed by a light boil

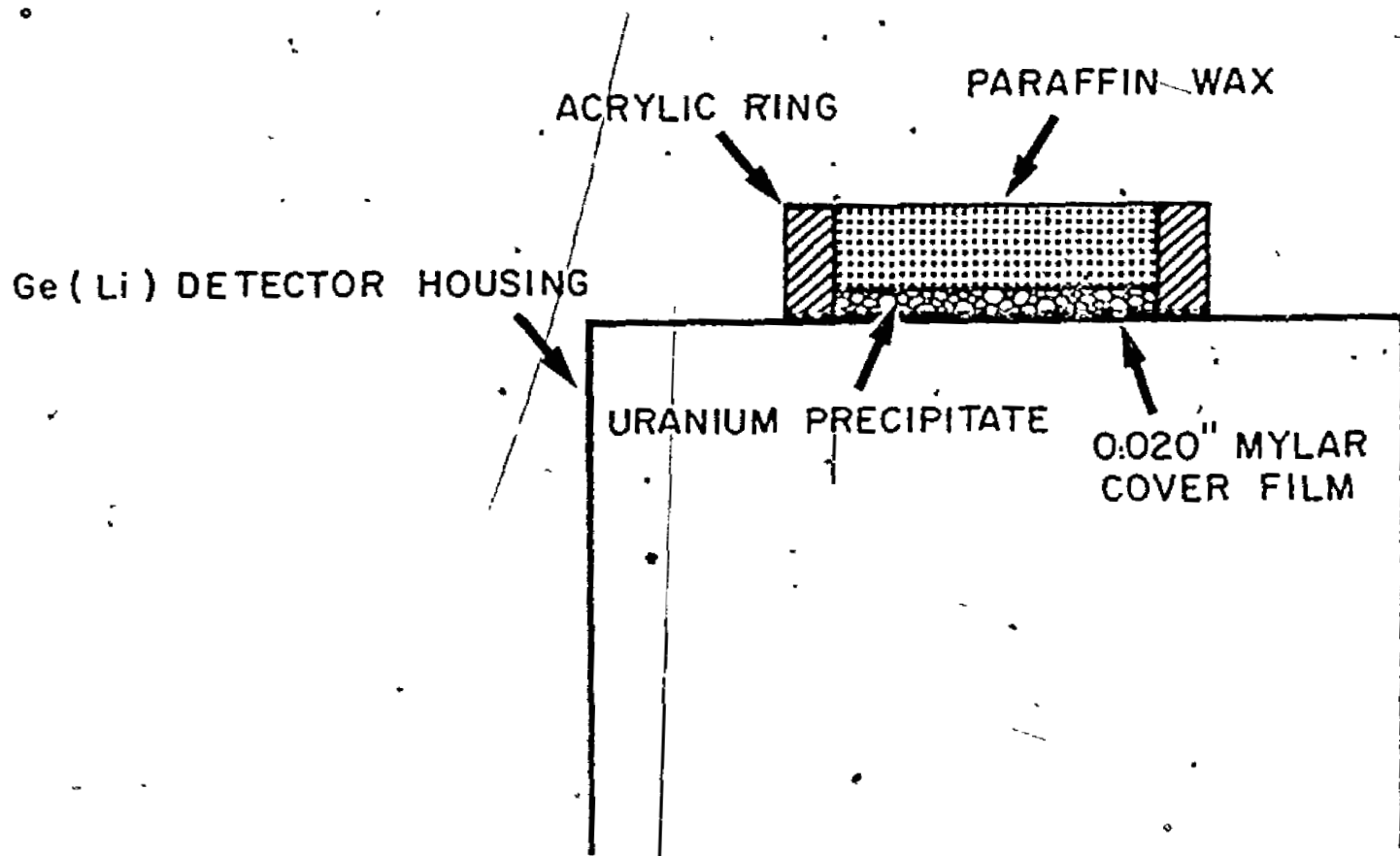


Fig. 26. Sample preparation and placement geometry used in the γ -spectroscopy experiment

required to break up the uranyl carbonate complexes. The uranium was then precipitated as $\text{Na}_2\text{U}_2\text{O}_7$ by addition of excess 1M NaOH. When sufficient material was collected by this procedure, samples were prepared for uranium isotope analysis in the manner described. Counting duration remained fixed at 1200 seconds for all samples. Three spectra were taken from each sample and then averaged.

As before, the total specimen error, S_S^2 , for measuring the ^{235}U peak intensity contains a specimen error and a specimen loading error. Both terms were evaluated using 18 and 17 consecutive spectra respectively for each. The total variance experienced in measuring the ^{234}Th intensity includes a further term, S_U^2 , resulting from errors introduced by the unfolding procedure. This was evaluated by collecting 12 consecutive spectra under identical conditions from the same specimen. The region of each spectrum surrounding the ^{234}Th doublet was subjected to the unfolding programme and the dispersion about a mean value measured. The spectra were then averaged and the unfolding programme allowed to unfold the averaged spectra. The above format was repeated for three concentration ranges, highly depleted, near natural and highly enriched in ^{235}U content. The total variances in an experimental measurement were then determined by adding S_S^2 and S_U^2 to the sum of the instrumental variances.

4. RESULTS AND DISCUSSION

4.1. Precision analysis of experimental facilities

Specimens were purposely selected so that the precision of each spectrometer was appraised under the conditions it was expected to be subjected to. By using the L X-ray source assembly, a pure lead specimen and a preset counting time of 3 minutes, the standard counting error in estimating the Pb $L_{\alpha_1\alpha_2}$ peak intensity as obtained from the X-ray spectrometer amounts to several percent. This error is of the same magnitude as experienced in measuring the uranium spectral line intensities in the K, L and M X-ray experiments. In the γ -ray spectroscopy experiment, much smaller counting errors are encountered when assessing the ^{235}U γ -ray intensity at 0.186 MeV. Accordingly, the highly enriched uranium metal foil was selected to evaluate precisely the γ -ray spectrometer.

From the precision analysis presented in appendix C, it was quantitatively demonstrated that the X-ray spectrometer was free from significant sources of instrumental error. Therefore, the precision of an estimated intensity is limited only by the statistical counting error. It was also shown that a small instrumental operational error exists within the γ -ray spectrometer. The dispersion of a measured intensity about a mean value, on account of this error, has a relative magnitude of $\pm 0.29\%$ (1 σ).

By repeating the entire operational procedure, for each control-setting, the exact location of the control causing the variance could be found. In view of the following argument and because of the small

magnitude of the error, this was not deemed necessary. When determining whether or not two variances are significantly different, it is clear from the data presented in appendix C, that the greater the scatter in the two sets of data the less likely it is that the numerical disagreements between the two variances are real. That is, it is probable that this small operational error exists in both spectrometers. However it becomes insignificant and is not distinguishable when the standard counting error is of the order of several percent. This being the case, the K, L and M X-ray experiments were presumed to be free of any instrumental errors and the precision of intensity measurements limited to statistical counting and specimen errors. The standard counting errors present in the γ -ray spectroscopy experiment are at least an order of magnitude less than for the X-ray work. For this situation, the small operational variance must be considered as it may appreciably alter the total precision of a measured peak intensity.

And finally, it should be pointed out, that all the data output from the multichannel analyzer used in the precision testing, was subjected to the data transfer, conversion, decoding and rearranging computer subroutines as detailed in appendix A. The net intensities and statistical precisions of the Pb L α X-ray and ^{235}U γ -ray were calculated using the subroutines described in appendix B. The results of the precision evaluation procedure concretely validate that the above computer programmes do not contribute any significant variance to the precision of a final analytical determination.

The specimen errors are determined individually for each experiment. The total specimen error, S_S , consists of several components, i.e.

$$S_S^2 = S_{SS}^2 + S_{SL}^2 + S_{SP}^2 \dots \dots \dots 4.1$$

where S_{SS}^2 is the variance resulting from the presence of the specimen itself, S_{SL}^2 is the variance produced by loading the specimen onto the spectrometer and S_{SP}^2 is the variance in sample preparation.

As described in the appropriate experimental sections, S_{SS} can be evaluated by taking many consecutive spectra, under identical conditions and measuring the dispersion, S_4 , about a mean value. Any variance originating from the specimen is then calculated by:

$$S_{SS}^2 = |S_4^2 - S_3^2| \dots \dots \dots 4.2$$

Analogously, the variance introduced in loading the sample onto the spectrometer can be measured by:

$$S_{SL}^2 = |S_5^2 - S_4^2| \dots \dots \dots 4.3$$

where S_5 is the estimated standard deviation about the mean value of many consecutive spectra, each taken after the same specimen was mounted onto the spectrometer.

Both the K and L X-ray procedures analyze bulk quantities of loose powder. Prior to loading, each specimen was shaken and lightly tapped to distribute the material throughout the specimen tube. For these cases, the specimen preparation error is incorporated into the specimen loading error. Also, S_{SP} was not evaluated for the γ -ray spectroscopy experiment because the $^{235}\text{U}/^{238}\text{U}$ isotope ratio was not expected to alter during the procedure. A quantitative separation and electrodeposition of uranium is required for the thin specimens employed in the M X-ray experiment. For this situation, S_{SP} was determined by:

Reproduced with permission of the copyright owner. Further reproduction prohibited without permission.

$$S_{SP}^2 = \left| S_6^2 - S_5^2 \right| \dots \dots \dots 4.4$$

where S_6 is the measured dispersion of the data set collected for this purpose as described in the M X-ray experimental section.

4.2 K X-ray results and discussion .

4.2.1. Determination of optimum goniometer settings

The sample of waste rock, from the Beaverlodge mining district, selected for this purpose contained 0.0014% U_3O_8 . As will be seen in section 4.2.6. this quantity of uranium is many times less than the minimum determinable limit attainable by using the K X-ray analytical procedure. Therefore, through measuring the Compton scattering intensity distribution from such a specimen, at various scatter angles and collimations, a reliable estimate of the expected backgrounds under the uranium peaks in a sample of much higher uranium concentration is obtained. The goniometer settings producing the lowest background intensities at the uranium peak locations will result in optimum peak to background ratios for a specimen of uranium bearing ore.

Due to geometrical design considerations, the largest scatter angle obtainable with the goniometer is 135° . For most cases, the attempt to record spectra at a 10° scatter angle was unsuccessful because of the very large Rayleigh scattering cross section at small scatter angles, figure 25; except for the higher secondary collimation settings, scattering intensities were in excess of the detector counting capability. Figures 27, 28, 29 show typical background spectra for scatter angles of 25° , 70° and 130° , respectively, with the primary collimation set at 10.0 cm and the secondary collimation adjusted to 12.5 cm. By employing

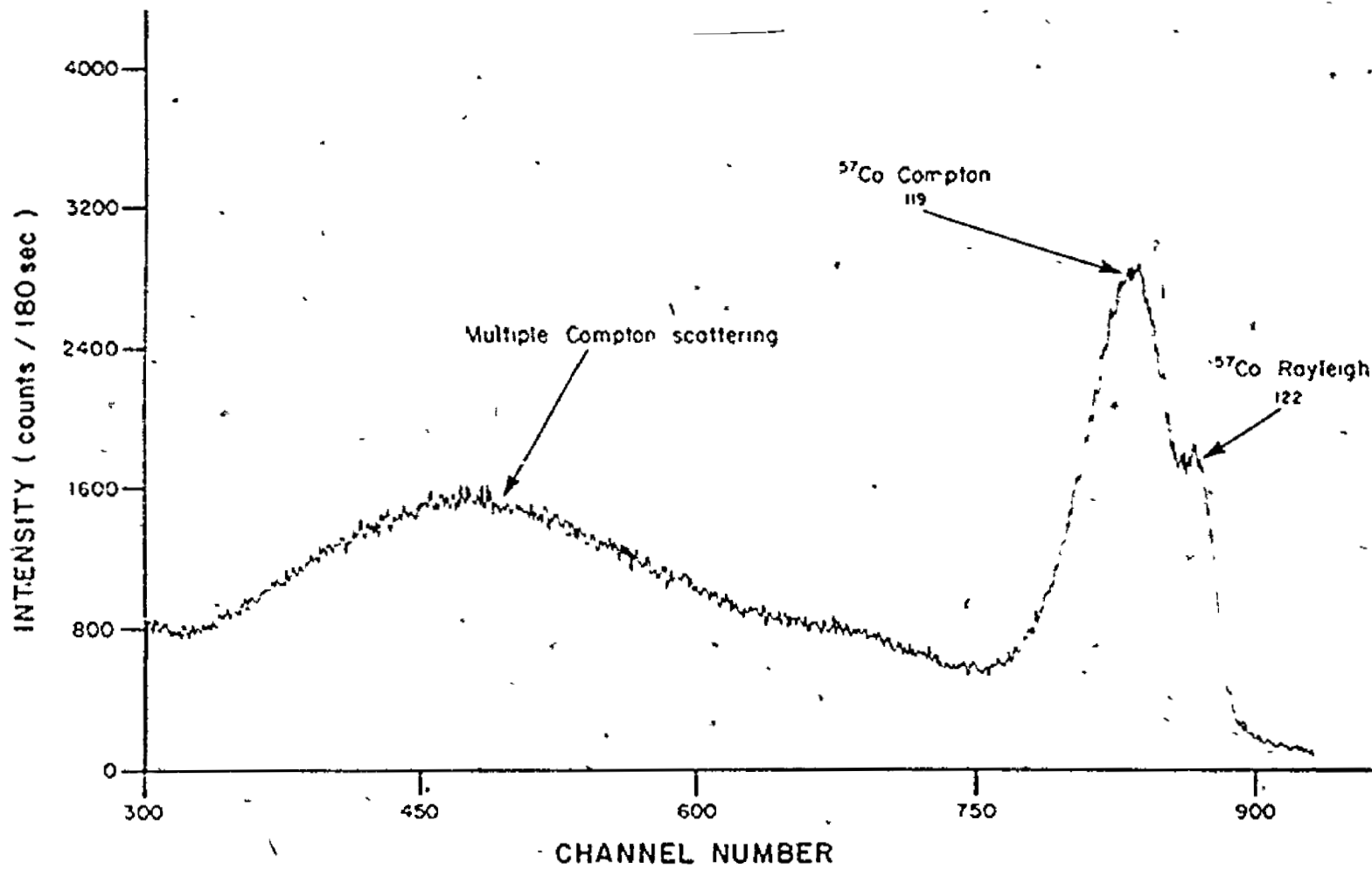


Fig. 27. Background spectrum recorded with scatter angle set at 25°

- 111 -

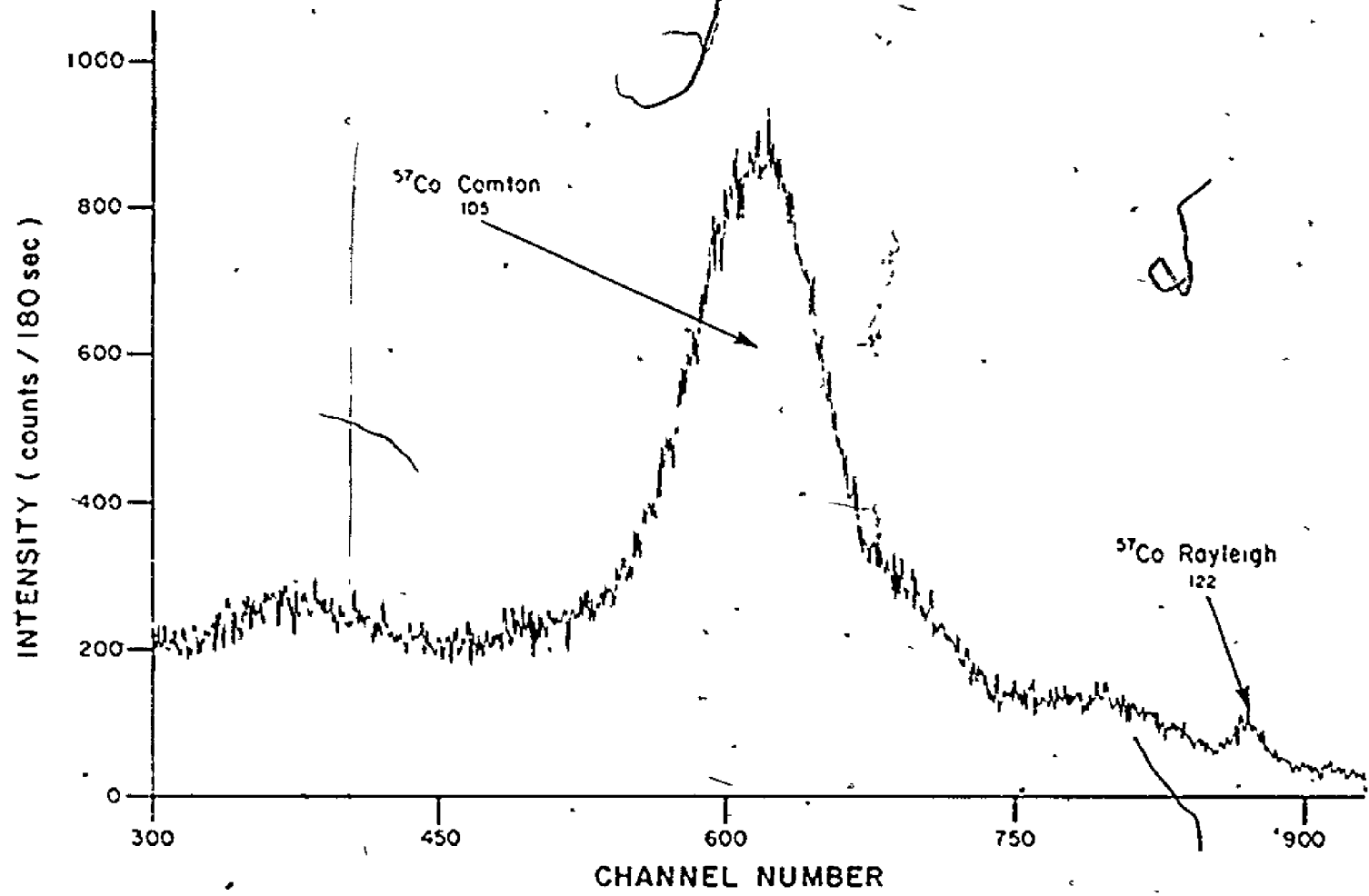


Fig. 28. Background spectrum recorded with scatter angle set at 70°

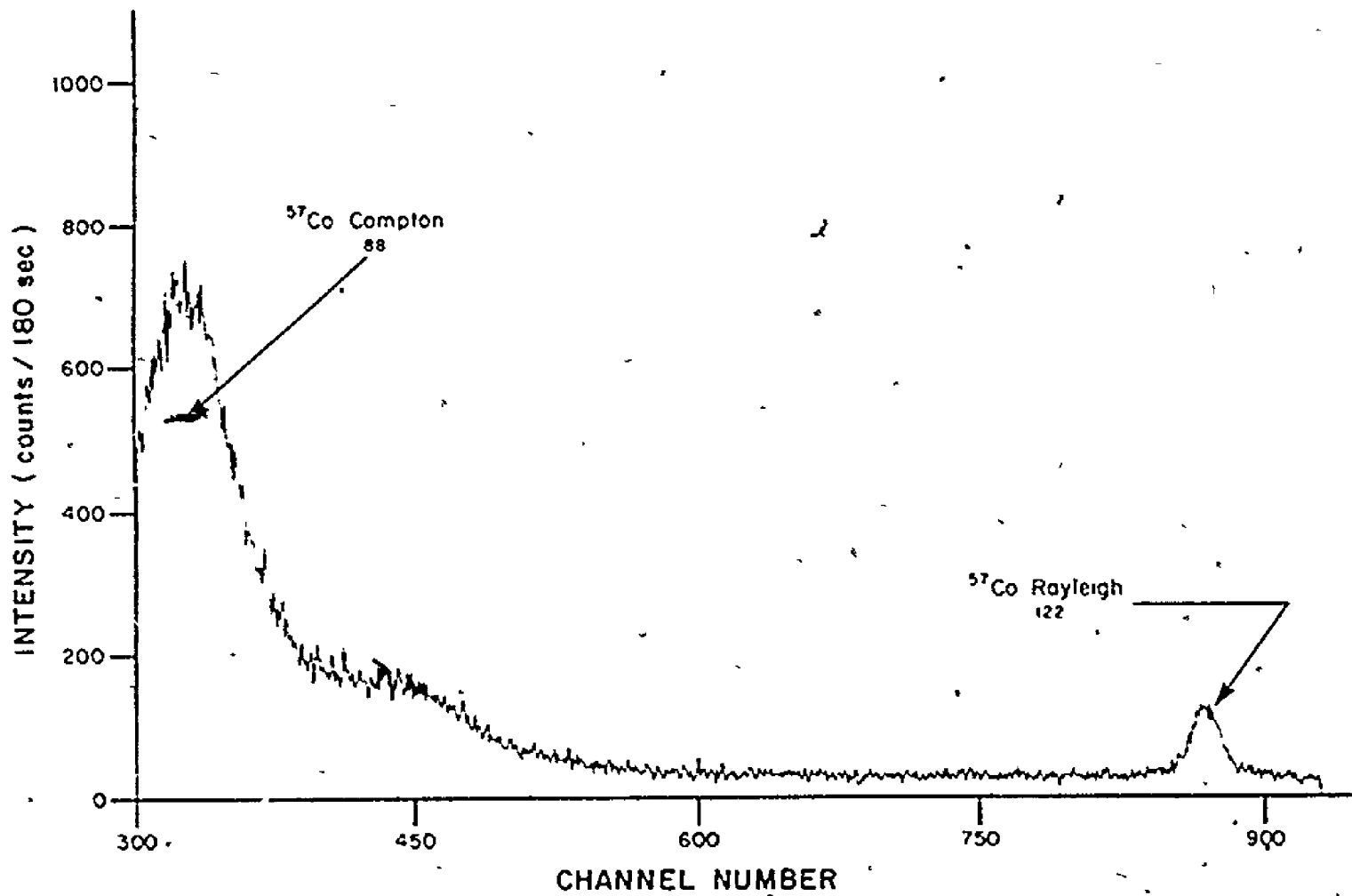


Fig. 29. Background spectrum recorded with scatter angle set at 130°

equation 2.7, the primary Compton scattered peak is then expected to occur at approximately 119, 105 and 88 keV respectively and this is confirmed by these three figures.

Tables 13-17 contain the background data under the four major uranium K-shell fluorescent peaks -- $U K\alpha_2$, $U K\alpha_1$, $U K\beta_1\beta_3$ and $U K\beta_2\beta_4$, -- for all scatter angles, primary and secondary collimation settings. Appendix D contains a full description of the computer programme written to analyze the uranium K shell peak intensities from the spectrum. In this application of the programme, the net peak intensities are always zero, but the background levels normally subtracted from the total peaks areas are recorded in the tables. These values are in units of counts per channel averaged over the full width of each expected uranium peak. As can be seen from the data, the lowest backgrounds under each peak, for all scatter angles, primary and secondary collimation settings, occur at scatter angles in excess of 130° . Figure 30, illustrates the relationship between average background intensity for each K shell spectral line observed and scatter angle with primary and secondary collimations set at 10.0 and 20.0 cm respectively.

To disclose the optimum secondary collimation settings, the goniometer platform must be raised and lowered. This alters the sample to detector distance and the background levels for each setting cannot be directly compared. To determine if any net gain in the background was obtained at each appropriate setting, the Rayleigh scattered peak was normalized by the background under each uranium peak for every secondary collimation setting. These Rayleigh scattering peak to background ratios directly reflect the net effect of varying the secondary collimation

Table 13

Background intensities with secondary collimation set at 5 cm.

Scatter Angle (degrees)	⁵⁷ Co Rayleigh Scattering Intensity (counts/180 sec)		Background Intensity (counts/180 sec)							
			U.Kα ₂		U Kα ₁		U Kβ ₁ β ₃		U Kβ ₂ β ₄	
	7 cm*	10 cm*	7 cm*	10 cm*	7 cm*	10 cm*	7 cm*	10 cm*	7 cm*	10 cm*
25	26215	17908	2433	2531	2834	2939	1444	1520	1300	1371
40	8073	6482	1154	1186	1359	1365	1006	989	2464	2430
55	2648	2677	766	779	612	623	2051	1879	1530	1069
70	1382	920	323	306	359	339	703	539	275	307
85	889	541	328	310	769	752	229	236	131	107
100	1122	636	948	906	868	682	76	72	471	50
115	1854	1090	660	521 ²	300	304 ⁰	47	46	43	41
130	----	1484	----	313	----	179	----	49	----	47

* Primary collimation setting

Table 14*

Background intensities with secondary collimation set at 12.5 cm.

Scatter Angle (degrees)	⁵⁷ Co Rayleigh Scattering Intensity (counts/180 sec)		Background Intensity. (counts/180 sec)							
			U K α_2		U K α_1		U K $\beta_1\beta_3$		U K $\beta_2\beta_4$	
			7 cm*	10 cm*	7 cm*	10 cm*	7 cm*	10 cm*	7 cm*	10 cm*
25	3954	6560	1308	1401	1356	1502	637	728	598	616
40	3299	3806	480	478	519	501	863	809	1641	1505
55	1149	1326	511	509	605	633	1244	1127	676	555
70	537	686	214	220	231	224	286	267	134	137
85	472	468	196	182	471	437	121	115	65	54
100	683	743	573	537	417	337	40	40	28	27
115	939	937	291	247	157	154	29	27	27	25
130	----	1149	----	164	----	89	----	28	----	30

* Primary collimation setting

Table 15

Background intensities with secondary collimation set at 20 cm.

Scatter Angle (degrees)	⁵⁷ Co Rayleigh Scattering Intensity (counts/180 sec)		Background Intensity (counts/180 sec)							
			U Kα ₂		U Kα ₁		U Kβ ₁ β ₃		U Kβ ₂ β ₄	
	7 cm*	10 cm*	7 cm*	10 cm*	7 cm*	10 cm*	7 cm*	10 cm*	7 cm*	10 cm*
25	2432	3461	755	809	708	761	314	344	367	404
40	2745	2678	267	265	273	262	766	742	1105	1027
55	1051	836	281	274	382	381	833	755	425	359
70	420	426	181	200	158	157	166	161	87	83
85	464	428	123	113	293	274	77	72	41	36
100	608	556	365	347	253	207	25	26	20	18
115	603	571	168	150	99	95	19	19	19	18
130	----	892	----	102	----	54	----	21	----	19

* Primary collimation setting

Table 16

Background intensities with secondary collimation set at 27.5 cm.

Scatter Angle (degrees)	⁵⁷ Co Rayleigh Scattering Intensity (counts/180 sec)		Background Intensity (counts/180 sec)							
			U K α_2		U K α_1		U K $\beta_1\beta_3$		U K $\beta_2\beta_4$	
	7 cm*	10 cm*	7 cm*	10 cm*	7 cm*	10 cm*	7 cm*	10 cm*	7 cm*	10 cm*
25	1848	2436	465	493	395	424	179	186	260	282
40	1749	1727	175	171	182	172	573	555	846	790
55	683	812	170	163	231	225	591	543	285	252
70	343	328	120	129	133	143	111	105	60	58
85	386	429	81	78	208	192	55	50	30	26
100	410	293	247	239	172	142	19	19	15	13
115	567	397	115	101	68	68	16	15	14	13
130	----	588	---	71	---	38	---	15	---	15

* Primary collimation setting

Table 17

Background intensities with secondary collimation set at 35 cm.

Scatter Angle (degrees)	⁵⁷ Co Rayleigh Scattering Intensity (counts/180 sec)		Background Intensity (counts/180 sec)							
			U K α_2		U K α_1		U K $\beta_1\beta_3$		U K $\beta_2\beta_4$	
	7 cm*	10 cm*	7 cm*	10 cm*	7 cm*	10 cm*	7 cm*	10 cm*	7 cm*	10 cm*
25	1298	1704	301	317	242	256	121	119	185	196
40	1356	1323	132	120	129	123	400	390	681	635
55	500	632	118	119	146	146	448	414	209	182
70	288	276	78	78	110	123	81	77	45	43
85	339	309	60	58	150	140	43	38	23	20
100	372	286	181	171	124	102	14	15	12	11
115	502	248	83	72	52	48	12	12	11	12
130	----	401	---	51	---	27	---	12	---	12

* Primary collimation setting

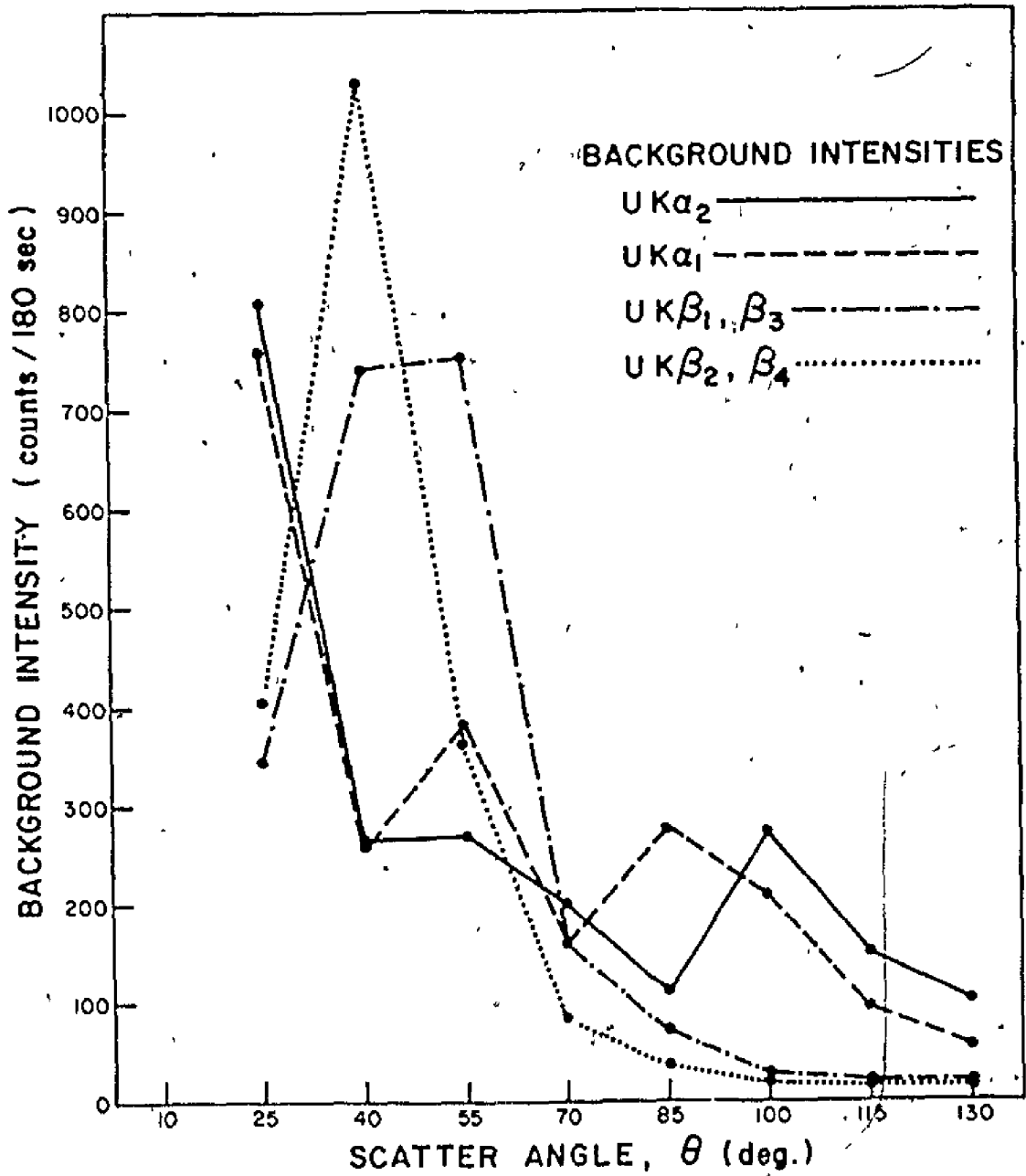


Fig 30 Relationship between average background intensity under each K shell spectral line observed and scatter angle

adjustment for any fixed scatter angle. In this case, Rayleigh scattering has been used as an internal standard; the larger the peak to background ratio, the greater the relative improvement in analytical conditions. To visualize why a net improvement is realized, consider the three principle contributions to the background spectrum: (i) the Rayleigh and Compton scattering processes, (ii) electronic noise in the detection components, and (iii) cosmic radiation. The latter two remain constant while the goniometer platform is raised, but the recorded intensity of the scattering phenomena decreases. This is compensated for by the above peak to background ratio procedure. However, relative improvements in this ratio occur with increasing secondary collimation due to the fact that the observed primary Compton scattering intensity becomes increasingly less dispersed. Neighbouring uranium peaks then have a lower relative background. It is expected that at some height above the detector this ratio will become a maximum. At this point, the improvements gained by greater collimation are being offset by the increasing constant background contribution to the total background spectrum. This has been experimentally corroborated. Table 18 presents data of the ratio comparison for all the secondary collimation settings. The primary collimation and scatter angle adjustments were constant at 10.0 cm and 130° respectively. It is also shown graphically for each uranium peak in figure 31. The maximum peak to background ratio is observed at a secondary collimation setting of 20 cm for all peaks.

The primary collimation setting had little effect on the maximum value of the Rayleigh scattering peak to background ratio. However, as a general trend, changes in the ratio between different secondary

Table 18

Variation of ^{57}Co Rayleigh scattering peak to uranium peak
background intensity ratio with secondary collimation.

The scatter angle is fixed at 130° .

Secondary Collimation (cm)	Peak to background ratio			
	U $K\alpha_2$	U $K\alpha_1$	U $K\beta_1\beta_3$	U $K\beta_2\beta_4$
5.0	4.74	8.29	30.3	31.6
12.5	7.01	12.9	41.0	38.3
20.0	8.75	16.5	42.5	46.9
27.5	8.28	15.5	39.2	39.2
35.0	7.86	14.9	33.4	33.4

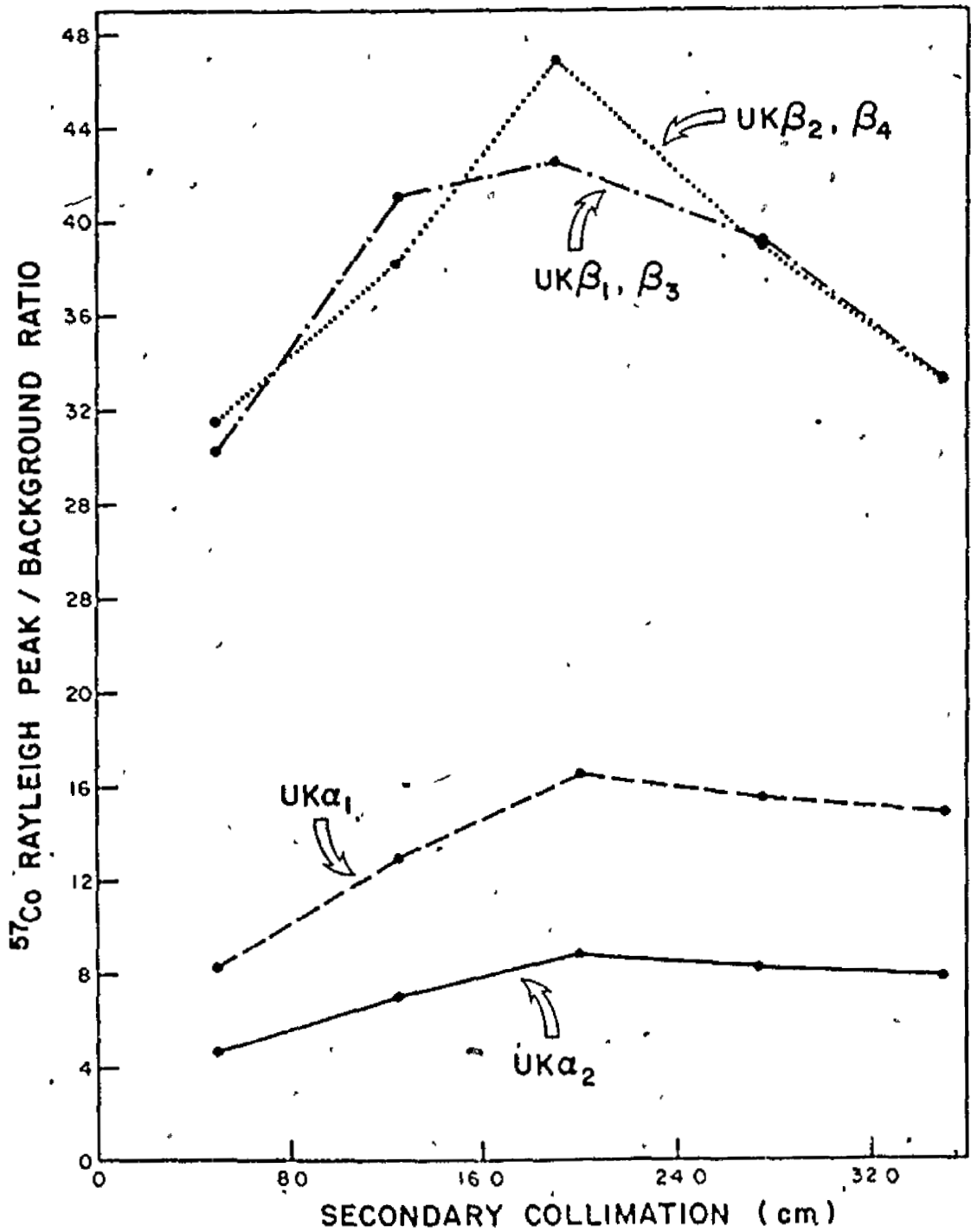


Fig. 31. Variation of ^{57}Co Rayleigh scattering peak to uranium peak background intensity ratio with secondary collimation. The scatter angle is fixed at 130°

collimation settings were more pronounced with the primary collimation set at 10.0 cm than at 7.0 cm. Unfortunately, for scatter angle adjustments in excess of approximately 120° it is not possible to obtain spectra using the 7.0 cm setting. The source housing, at this setting, is very close to the specimen and at large scatter angles blocks the detector's view of the specimen. Therefore only the 10.0 cm primary collimation setting was used with the 130° scatter angle measurements.

From the data presented in this section, it is evident that the largest possible scatter angle of 135° , along with primary and secondary collimation settings of 10.0 and 20.0 cm respectively will result in the optimum geometrical conditions for measuring the intensities for each of the U K shell fluorescent peaks. These values were then adopted for all of the K X-ray experimental work.

4.2.2. Scattering intensity measurements

There are three principal sources contributing to the measured Rayleigh and Compton scattering peak intensities: (i) the specimen, (ii) the specimen tube, and (iii) the Bi target. From the spectrum alone, each component is not distinguishable. However, only the scattering intensities from the specimen are of analytical significance. These were determined by observing the spectra from a series of blanks taken at regular intervals throughout the experimental work. The blank measurement, as described earlier, consists of recording the spectrum with only an empty sample container as a specimen. The total scattering intensities from the sample tube and the Bi target can then be expressed as fraction of the transmitted radiation as measured by the intensity

Table 19

Background data and calculations required for determining the net specimen scattering intensity from the observed scattering intensity.

Observed Rayleigh Scattering Intensity (counts/180 sec)	Observed Compton Scattering Intensity (counts/180 sec)	Bi K α_1 Intensity (counts/180 sec)	$\frac{I(\text{observed Rayleigh})}{I \text{ Bi } K\alpha_1}$	$\frac{I(\text{observed Compton})}{I \text{ Bi } K\alpha_1}$
1725	3734	8755	.1970	.4265
1728	3564	9178	.1883	.3883
1652	3716	9161	.1803	.4056
1683	3649	9254	.1819	.3943
1613	3579	9112	.1770	.3928
1646	3685	9222	.1785	.3996
1797	3722	8857	.1927	.4202
1633	3657	8900	.1835	.4109
1608	3494	9161	.1755	.3814
1740	3627	8981	.1937	.4039
1661	3623	8976	.1850	.4036
1715	3657	9108	.1883	.4015
1424	3589	8903	.1599	.4031

Table 19 continued

Observed Rayleigh Scattering Intensity (counts/180 sec)	Observed Compton Scattering Intensity (counts/180 sec)	Bi $K\alpha_1$ Intensity (counts/180 sec)	$\frac{I(\text{observed Rayleigh})}{I \text{ Bi } K\alpha_1}$	$\frac{I(\text{observed Compton})}{I \text{ Bi } K\alpha_1}$
1706	3602	8796	.1940	.4095
1714	3643	8835	.1940	.4123
1582	3731	8568	.1846	.4354
1668	3624	9335	.1787	.3882
1787	3585	9333	.1915	.3841
1750	3714	9088	.1926	.4087
1686	3650	9137	.1845	.3995

average = 0.1851

1S = $\pm 4.75\%$

average = 0.4035

1S = $\pm 3.40\%$

of the Bi $K\alpha_1$ peak. These fractions are calculated for both Rayleigh and Compton scattering in table 19. The mean values for Rayleigh and Compton scattering are $0.185 \pm 4.75\%$ (1S) and $0.404 \pm 3.40\%$ (1S) respectively. The net Rayleigh scattering intensity due to the specimen, I_{Rayleigh} , can then be calculated by:

$$\begin{aligned} I_{\text{Rayleigh}} &= I(\text{observed Rayleigh}) - I(\text{blank Rayleigh}) \\ &= I(\text{observed Rayleigh}) - 0.185(I_{\text{Bi } K\alpha_1}) \quad \dots \quad 4.5 \end{aligned}$$

and the net specimen Compton scattering intensity, I_{Compton} , expressed as:

$$\begin{aligned} I_{\text{Compton}} &= I(\text{observed Compton}) - I(\text{blank Compton}) \\ &= I(\text{observed Compton}) - 0.404(I_{\text{Bi } K\alpha_1}) \quad \dots \quad 4.6 \end{aligned}$$

4.2.3. Sample thickness measurement.

As mentioned in section 3.1., the Compton scattering intensity observed from a specimen is expected to be a linear function of sample mass for thin or partially thick samples. Data from the seven weighed samples are presented in table 20 showing both the specimen mass and the sample Compton scattering intensity. The linear trend of the data is obvious. However, specimens of known mass could not be satisfactorily prepared. The samples of varying mass, but constant volume, were prepared by using dissimilar packing densities. It is difficult to insure that the packing density of the 'effective volume analyzed' is the same as the average value for the entire sample. The ore in the lighter samples also tended to settle down after they were manipulated so that the volume decreased accompanied by a larger packing density. It was

Table 20

Data illustrating the linear relationship between actual sample mass (g) and the net Compton scattering intensity.

Specimen %U ₃ O ₈	Mass (g)	I Compton (counts/180 sec)	$\frac{\text{Mass}}{\text{I Compton}} \times 10^3$
.204% Beaverlodge Lake	19.82	2598	7.629
.248% Beaverlodge Lake	27.47	3589	7.654
.302% Beaverlodge Lake	30.35	3985	7.616
.352% Beaverlodge Lake	26.55	3570	7.437
.490% Beaverlodge Lake	25.16	3450	7.293
.580% Rabbit Lake	24.10	3166	7.612
.963% Rabbit Lake	33.66	4459	7.549

found more convenient to assume a constant value for the total absorption coefficient, $\sum_i (\mu_e)_i r_i$, measure the initial to transmitted intensity ratio and then calculate the sample thickness, m , from equation 3.1., i.e.

$$m \text{ (g/cm}^2\text{)} = \frac{\ln(I_0/I_T)}{\sum_i (\mu_e)_i r_i}$$

The quantity assumed for $\sum_i (\mu_e)_i r_i$ was a calculated value of 0.162 cm²/g taken from table 22, section 4.2.4. In this application, the presence of significant amounts of uranium will result in lower values of I_T . If an estimate of the uranium weight fraction could be determined, then the uranium contribution to $\sum_i (\mu_e)_i r_i$ can be evaluated. From table 22, the absorption due to uranium in a 1% uranium ore will be 0.041 cm²/g for the 122 keV excitation photons. Sample thicknesses are then calculated by:

$$m \text{ (g/cm}^2\text{)} = \frac{\ln(I_0/I_T)}{\{0.162 + 0.041(\%U_3O_8)\}} \dots \dots \dots 4.7$$

Table 21 contains the specimen data and evaluations of equation 4.7 for each sample listed. Figure 32 illustrates the best least squares straight line through the data giving the required proportionality constant between sample Compton intensity and specimen thickness. All thicknesses in the K X-ray experimental work were calculated from the following equation:

$$m \text{ (g/cm}^2\text{)} = 7.60 \times 10^{-4} I \text{ Compton} \dots \dots \dots 4.8$$

4.2.4. Matrix compensation

With the K X-ray goniometer, as previously described, the excitation radiation strikes the specimen normally to its surface and the fluorescent radiation falls nearly perpendicularly upon the plane of the

Table 21

Data showing the correlation between net Compton scattering intensity and specimen thickness, m (g/cm²).

Specimen	I_{Compton} (counts/180 sec)	I_0 (counts/180 sec)	I_T (counts/180 sec)	m (g/cm ²)
1.19% Key Lake	1781	9223	6998	1.31
.512% Key Lake	2519	9223	6374	2.00
.482% Elliot Lake	3912	8776	4873	2.95
.963% Rabbit Lake	4459	9057	4512	3.44
.580% Rabbit Lake	3166	9057	5796	2.39
.460% Rabbit Lake	3626	9057	5416	2.82
.0215% Rabbit Lake	2984	9057	6197	2.32
1.21% Beaverlodge Lake	4315	9057	4619	3.19
.463% Beaverlodge Lake	3426	9057	5714	2.53
.226% Beaverlodge Lake	2871	9023	6211	2.16

- 130 -

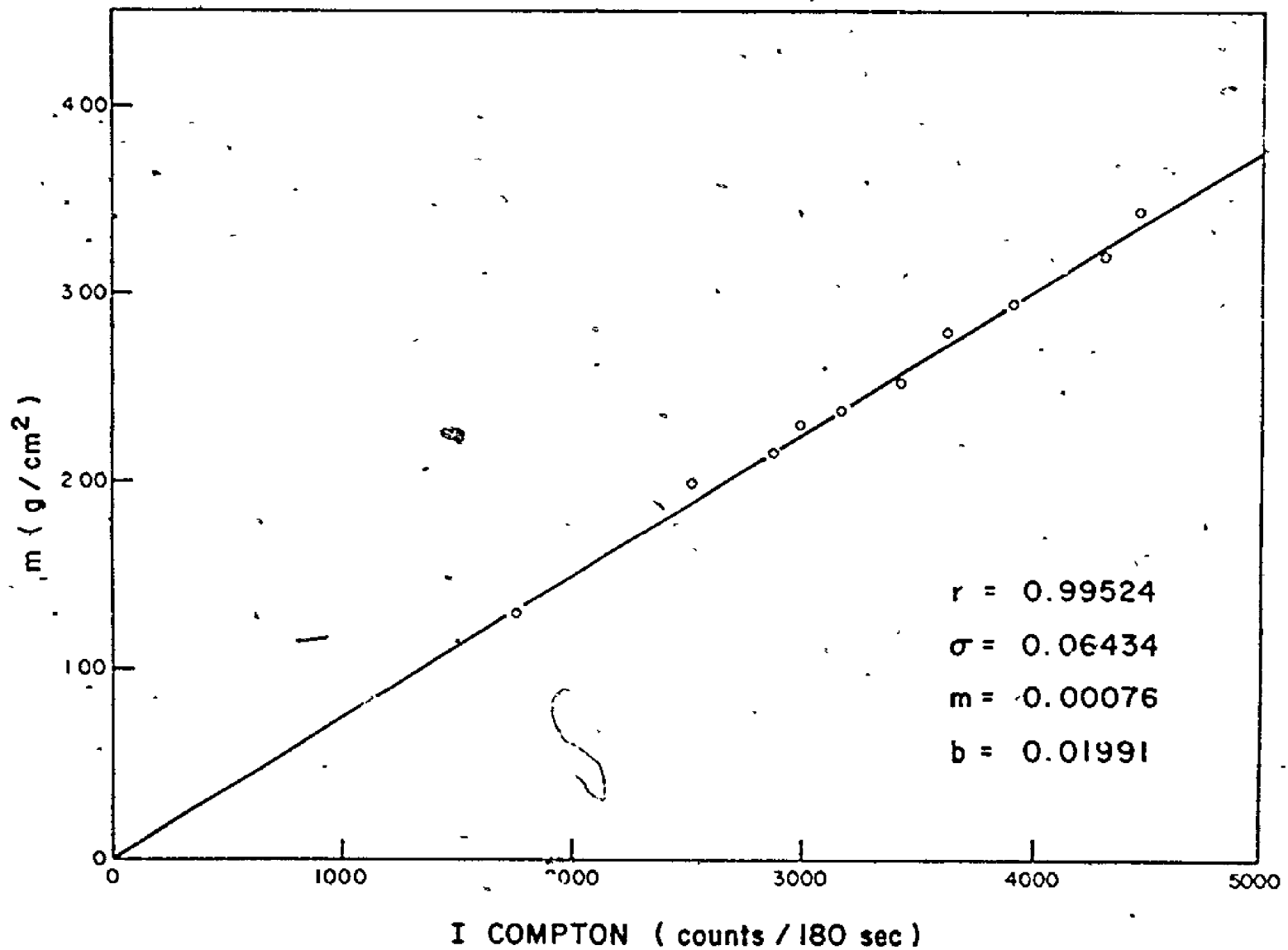


Fig. 32. Correlation between specimen thickness and the net specimen Compton scattering, intensity

detector. The angular dependencies of the fundamental excitation equation, equation 2.12, for partially thick samples can then be neglected. By reducing and rearranging this equation, the weight fraction in a specimen can be expressed as:

$$r_U = \frac{I_U \sum_i (\mu_e + \mu_f)_i r_i}{(1 - \exp[-m \sum_i (\mu_e + \mu_f)_i r_i])} \dots \dots \dots 4.9$$

As discussed earlier, by measuring the transmitted radiation and the sample thickness, all the terms of equation 4.9 may be determined. From the transmitted radiation, the total mass absorption coefficient of the sample for the incident radiation can be obtained from.

$$\sum_i (\mu_e)_{i \text{ total}} r_i = \frac{\ln(I_0/I_T)}{m}$$

Table 22 presents the details of mass absorption coefficient calculation for elemental absorption by an average uranium bearing granite. The absorption coefficients are evaluated for the energies of the U $K\alpha_1$ peak, ϵ_f , and the excitation radiation, ϵ_e , at 98 and 122 keV respectively. Pertinent data used for the construction of table 22 on the average composition of granite were taken from reference (30) and on mass absorption coefficients from reference (6). From the table, it is clear that the value of the mass absorption coefficient for each matrix element is much smaller than it is for uranium. So that the total mass absorption coefficient as evaluated from the transmitted radiation, can be broken into two components: (i) absorption due to matrix elements, and (ii) absorption

Table 22

Calculation of mass absorption coefficients for
an average uranium bearing granite

Element	Weight Fraction r_i	σ_{TOT} (barns)		Mass Absorption Coefficients (cm^2/g)		Elemental Absorption (cm^2/g)	
		$\epsilon_f = 98 \text{ keV}$	$\epsilon_e = 122 \text{ keV}$	μ_f	μ_e	$\mu_f r_i$	$\mu_e r_i$
O	47.7 %	4.12	3.92	.155	.148	.0739	.0706
Si	33.2 %	8.53	7.81	.193	.167	.0607	.0554
Al	7.9 %	7.62	7.04	.170	.157	.0134	.0124
Fe	2.8 %	34.1	27.7	.368	.298	.0103	.0083
Ca	1.6 %	16.9	14.6	.254	.219	.0041	.0035
Na	2.9 %	6.03	5.66	.158	.148	.0046	.0043
Mg	0.16%	6.77	6.31	.168	.156	.0003	.0002
K	3.4 %	15.1	13.1	.233	.202	.0079	.0069
Ti	0.24%	21.5	18.1	.270	.228	.0006	.0005
U	1.00%	748.	1910.	1.89	4.83	.0189	.0483

$$\sum_i (\mu_e + \mu_f) r_i = 2.08 \sum_i (\mu_e) r_i$$

matrix matrix

$$\sum_i (\mu_f) r_i = .1758$$

$$\sum_i (\mu_e) r_i = .1621$$

matrix matrix

by uranium atoms alone, i.e.

$$\sum_i (\mu_e)_i r_i = \sum_i (\mu_e)_i r_i + (\mu_e)_U r_U \dots \dots \dots 4.10$$

total matrix

Since the thickness factor is more important than the matrix factor at this excitation energy, a reliable estimate of the uranium weight fraction can be obtained from normalizing the uranium spectral intensities to their measured thicknesses, i.e.

$$\sum_i (\mu_e)_i r_i = \sum_i (\mu_e)_i r_i + \chi (\mu_e)_U \left(\frac{I_U}{m}\right) \dots \dots \dots 4.11$$

total matrix

where χ is the appropriate proportionality constant.

From table 22, it is readily seen that, for the matrix elements, the mass absorption coefficient for ϵ_f is a constant function of that for ϵ_e , i.e.

$$\sum_i (\mu_e + \mu_f)_i r_i = 2.08 \sum_i (\mu_e)_i r_i \dots \dots \dots 4.12$$

matrix matrix

Therefore, the total mass absorption coefficient of the specimen for photons of energy ϵ_e and ϵ_f can be written as:

$$\begin{aligned} \sum_i (\mu_e + \mu_f)_i r_i &= \sum_i (\mu_e + \mu_f)_i r_i + (\mu_e + \mu_f)_U r_U \\ \text{total} & \qquad \qquad \qquad \text{matrix} \\ &= 2.08 \sum_i (\mu_e)_i r_i + \chi (\mu_e + \mu_f)_U \left(\frac{I_U}{m}\right) \dots \dots \dots 4.13 \\ & \qquad \qquad \qquad \text{matrix} \end{aligned}$$

hence, all the required terms in equation 4.9 can be estimated.

4.2.5. γ -ray spectrometer energy calibration

The storage location within the γ -ray spectrometer for energies of the principle γ -ray emissions of the three reference sources is shown in figure 33. Using the settings listed in table 7, the relationship between photon energy and channel number can be expressed as:

$$\text{Energy (keV)} = \frac{(\text{Channel Number} + 878.273)}{14.345} \dots \dots \dots 4.14$$

All conversions from channel number to energy were performed using equation 4.14 throughout the K X-ray experimental work.

4.2.6. Data and data analysis

The K X-ray spectrum from a uranium ore containing 1.21% U_3O_8 is shown in figure 34. The spectrum was recorded under the optimum geometrical settings as found in section 4.2.1. The Bi $K\alpha_2$ and $K\alpha_1$ X-rays at 74.8 and 77.1 keV; the U $K\alpha_2$, $K\alpha_1$, $K\beta_1\beta_3$ and $K\beta_2\beta_4$ at 94.7, 98.4, 111.3 and 114.5 keV; the primary Compton and Rayleigh scattered peaks at 88.0 and 122.0 keV respectively are plainly discerned. The U $K\beta$ intensities are appreciably weaker than the $K\alpha$ intensities and in most of the ore samples analyzed could not be discriminated from the scattered background intensity. In addition, the high energy shoulder of the primary Compton scattered peak, figures 28-29, underlies the U $K\alpha_2$ peak and also results in excessive and difficult to determine background levels. For these reasons, the U $K\alpha_1$ peak at 98.4 keV was considered to give the most accurate and precise intensity measurement. This quantity was therefore adopted as being representative of the observed uranium K shell fluore-

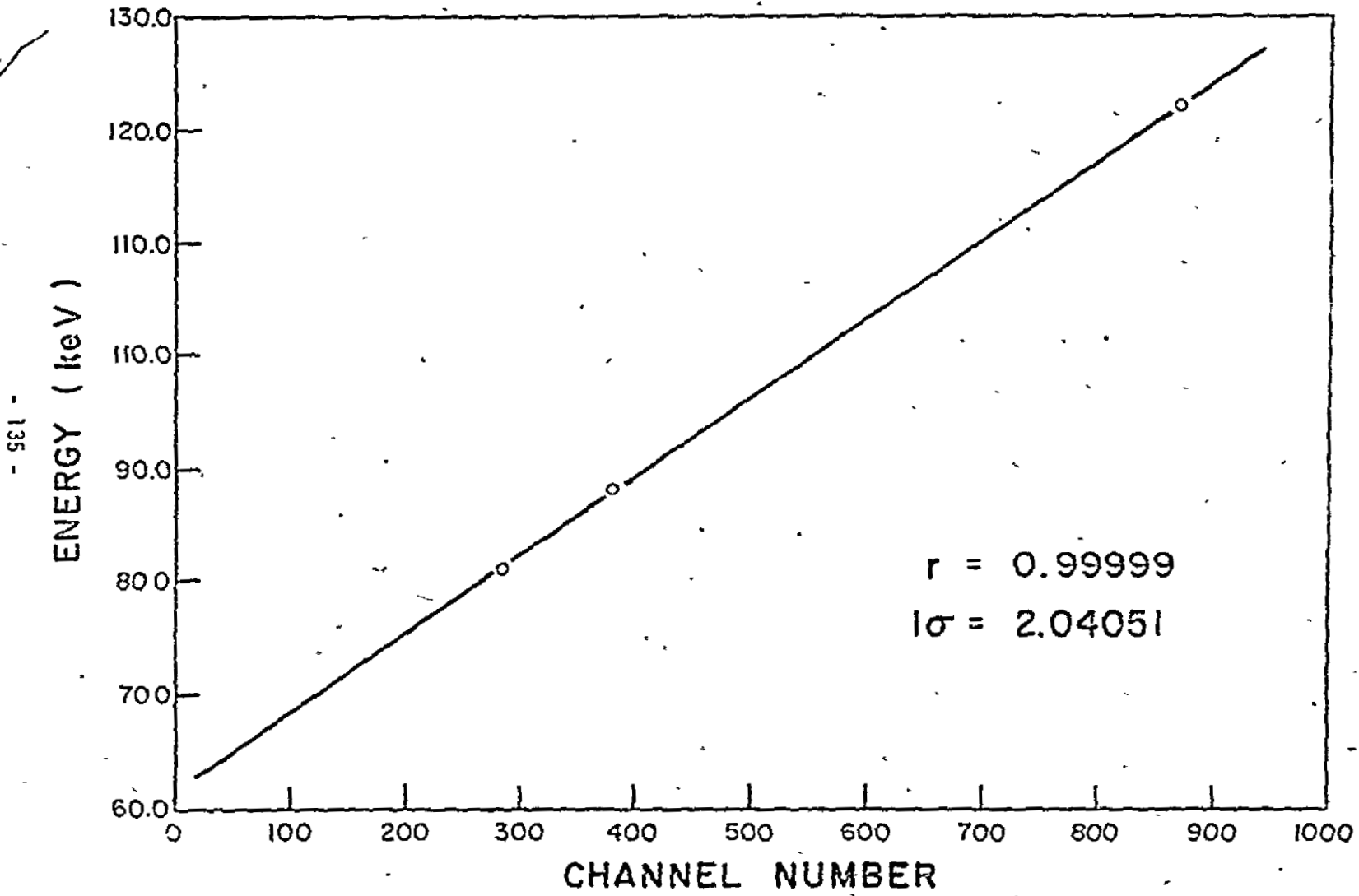


Fig. 33. Photon energy calibration curve for the K X-ray experiment

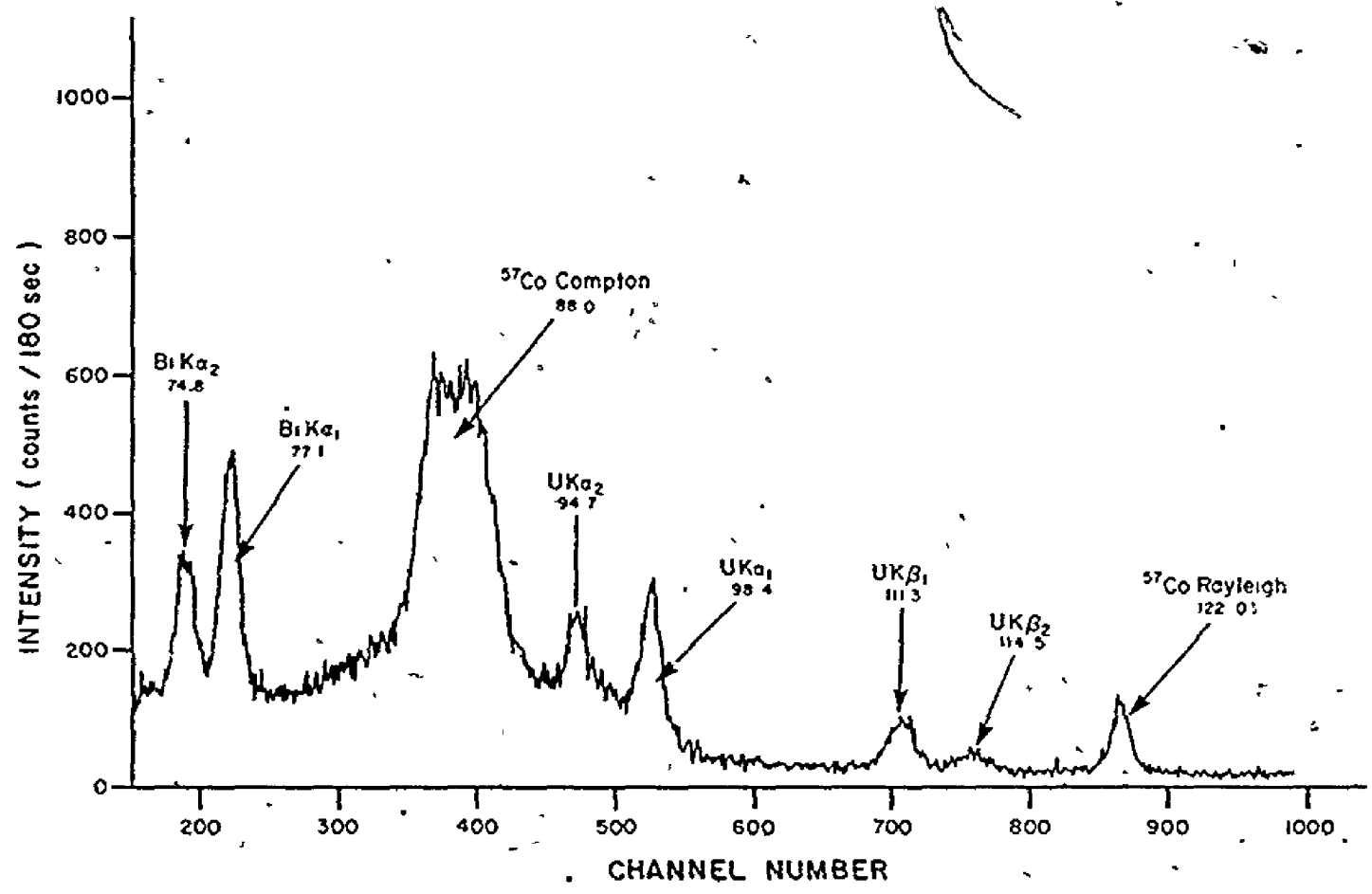


Fig. 34. The K X-ray spectrum from a uranium bearing ore containing 1.21% U_3O_8

science intensity.

Tables 23-26 present the observed Rayleigh and Compton scattering intensity data for the 46 ore sample analyzed for each of the four uranium mining locations. The net specimen Rayleigh scattering intensity, I_{Rayleigh} , and the net specimen Compton scattering intensity, I_{Compton} , are calculated from their observed values from equations 4.5 and 4.6 respectively. Compton scattering cross sections are greater than Rayleigh scattering cross sections at 122 keV, particularly so with large scatter angles. As expected though, the fraction of the total observed Rayleigh scattering intensity that originates from the bismuth target (high Z material) is substantially larger than for the Compton scattering case. For most of the ore samples, about one third of the observed Rayleigh scattering arose from the presence of the specimen, while for the Compton scattering situation this ratio is generally greater than two thirds.

Tables 27-30 contain the $U \text{ K}\alpha_1$, I_0 and I_T net peak intensity data, for the ore samples investigated, from each of the four uranium mineral zones. The sample thickness, m (g/cm^2), listed in these tables was calculated from I_{Compton} using equation 4.8. Thickness precisions are of the order of $\pm 1.5\%$ ($1S_N$). Both I_{Rayleigh} and $I_{U \text{ K}\alpha_1}$ values were normalized to specimen thickness as shown in the tables. For the Rayleigh scattering case, the quantity $(I_{\text{Rayleigh}})/m$ shows a marginal increase in magnitude with increasing uranium concentration. Unfortunately, the scattering intensities are not sufficiently sensitive enough to detect with adequate precision the small amounts of uranium present in these specimens to be of any analytical benefit. The normalized $U \text{ K}\alpha_1$ peak intensity data were plotted against actual concentration for all of the

Table 23

Calculation of net specimen scattering intensities from observed scattering intensities for Beaverlodge Lake ores.

Specimen (%U ₃ O ₈)	I (observed Rayleigh) (counts/180 sec) ±S _N (%)	I Rayleigh (counts/180 sec) ±S _N (%)	I (observed Compton) (counts/180 sec) ±S _N (%)	I Compton (counts/180 sec) ±S _N (%)
0.102	1639 ±2.15	756 ±5.03	6574 ±0.71	4646 ±1.21
0.108	1542 ±1.94	480 ±6.73	5774 ±0.66	3455 ±1.35
0.118	1606 ±1.85	439 ±7.49	5523 ±0.78	2975 ±1.78
0.116	1627 ±1.84	467 ±6.92	5533 ±0.67	2999 ±1.52
0.175	1662 ±1.80	517 ±6.24	5520 ±0.67	3020 ±1.51
0.194	1596 ±2.17	494 ±7.53	5739 ±0.76	3355 ±1.59
0.198	1631 ±1.84	493 ±6.57	5544 ±0.67	3059 ±1.49
0.199	1568 ±1.92	447 ±7.27	5581 ±0.67	3134 ±1.47
0.211	1631 ±1.85	494 ±6.59	5596 ±0.67	3113 ±1.48
0.226	1670 ±1.78	520 ±6.17	5391 ±0.68	2881 ±1.57
0.248	1675 ±1.80	645 ±5.04	5847 ±0.65	3598 ±1.29
0.261	1659 ±1.81	594 ±5.45	5722 ±0.66	3396 ±1.36
0.302	1625 ±2.11	667 ±5.56	6084 ±0.74	3993 ±1.37

Table 23 (continued)

Specimen (%U ₃ O ₈)	I (observed Rayleigh) (counts/180 sec) ±S _N (%)	I _r Rayleigh (counts/180 sec) ±S _N (%)	I (observed Compton) (counts/180 sec) ±S _N (%)	I Compton (counts/180 sec) ±S _N (%)
0.339	1648 ±2.09	573 ±6.49	5752 ±0.76	3404 ±1.57
0.341	1651 ±2.11	540 ±6.95	5519 ±0.78	3094 ±1.71
0.352	1673 ±2.08	638 ±5.88	5838 ±0.76	3579 ±1.51
0.392	1674 ±2.06	616 ±6.04	5687 ±0.77	3377 ±1.58
0.425	1646 ±1.82	603 ±5.33	5637 ±0.67	3360 ±1.35
0.463	1606 ±2.15	548 ±6.80	5697 ±0.76	3380 ±1.56
0.490	1716 ±2.48	674 ±6.76	5683 ±0.94	3408 ±1.88
1.210	1590 ±2.20	735 ±5.12	6151 ±0.74	4284 ±1.28

Table 24

Calculation of net specimen scattering intensities from observed scattering intensities for Rabbit Lake ores.

Specimen (%U ₃ O ₈)	I (observed Rayleigh) (counts/180 sec) ±S _N (%)	I Rayleigh (counts/180 sec) ±S _N (%)	I (observed Compton) (counts/180 sec) ±S _N (%)	I Compton (counts/180 sec) ±S _N (%)
0.0215	1579 ±1.87	432 ±7.39	5447 ±0.68	2943 ±1.55
0.0317	1672 ±1.78	570 ±5.64	5954 ±0.69	3548 ±1.38
0.0680	1578 ±1.86	492 ±6.46	5623 ±0.67	3252 ±1.42
0.0720	1562 ±1.88	484 ±6.58	5727 ±0.66	3373 ±1.37
0.207	1503 ±2.24	547 ±6.67	6086 ±0.74	3999 ±1.36
0.286	1629 ±1.80	677 ±4.68	6016 ±0.64	3938 ±1.19
0.460	1548 ±2.18	546 ±6.69	5873 ±0.75	3684 ±1.46
0.580	1566 ±2.18	493 ±7.48	5571 ±0.77	3229 ±1.63
0.963	1622 ±2.11	787 ±4.70	6331 ±0.73	4508 ±1.23

Table 25

Calculation of net specimen scattering intensities from observed scattering intensities for Key Lake ores.

Specimen (%U ₃ O ₈)	I (observed Rayleigh) (counts/180 sec) ±S _N (%)	I Rayleigh (counts/180 sec) ±S _N (%)	I (observed Compton) (counts/180 sec) ±S _N (%)	I Compton (counts/180 sec) ±S _N (%)
0.0146	1597 ±1.83	511 ± 6.19	5558 ±0.67	3187 ±1.43
0.0505	1583 ±1.86	268 ±11.84	4538 ±0.74	1666 ±2.54
0.0841	1612 ±1.82	240 ±13.18	4408 ±0.75	1411 ±2.97
0.176	1616 ±1.81	557 ± 5.68	5639 ±0.67	3328 ±1.38
0.181	1608 ±2.15	310 ±11.83	4737 ±0.84	1902 ±2.52
0.193	1594 ±1.84	354 ± 8.94	4820 ±0.72	2113 ±2.05
0.230	1623 ±1.82	341 ± 9.33	4683 ±0.73	1883 ±2.27
0.245	1651 ±1.79	449 ± 7.08	4798 ±0.72	2175 ±1.98
0.512	1618 ±1.83	438 ± 7.29	5037 ±0.70	2461 ±1.78
1.19	1552 ±1.98	257 ±13.07	4545 ±0.86	1717 ±2.86

Table 26

Calculation of net specimen scattering intensities from observed scattering intensities for Elliot Lake ores.

Specimen (%U ₃ O ₈)	I (observed Rayleigh) (counts/180 sec) ±S _N (%)	I Rayleigh (counts/180 sec) ±S _N (%)	I (observed Compton) (counts/180 sec) ±S _N (%)	I Compton (counts/180 sec) ±S _N (%)
0.095	1601 ±1.85	595 ±5.38	5765 ±0.66	3568 ±1.30
0.102	1664 ±1.78	615 ±5.20	5720 ±0.66	3430 ±1.34
0.272	1585 ±1.89	607 ±5.32	5797 ±0.66	3662 ±1.27
0.356	1598 ±2.11	677 ±5.39	5948 ±0.75	3936 ±1.37
0.482	1686 ±2.06	784 ±4.77	5934 ±0.75	3965 ±1.36
0.773	1687 ±2.05	820 ±4.54	5856 ±0.75	3963 ±1.34

Table 27

Initial data observed from Beaverlodge Lake ores required to evaluate the matrix and thickness factors

Specimen (% U_3O_8)	$I_{U\ K\alpha_1}$ (cts/180 sec) $\pm S_N(\%)$	I_0 (cts/180 sec) $\pm S_N(\%)$	I_T (cts/180 sec) $\pm S_N(\%)$	m (g/cm) ² $\pm S_N(\%)$	$I_{Rayleigh}$ m cts.cm ² 180 sec.g $\pm S_N(\%)$	$I_{U\ K\alpha_1}$ m cts.cm ² 180 sec.g $\pm S_N(\%)$
0.102	374 ± 10.8	9087 ± 0.71	4772 ± 1.62	3.53 ± 1.21	217 ± 5.17	105 ± 10.9
0.108	401 ± 9.22	9087 ± 0.71	5739 ± 1.15	2.63 ± 1.35	182 ± 6.86	152 ± 9.23
0.118	258 ± 12.7	9087 ± 0.71	6306 ± 1.21	2.26 ± 1.78	194 ± 7.70	114 ± 12.8
0.116	325 ± 11.2	9087 ± 0.71	6270 ± 1.05	2.28 ± 1.52	204 ± 7.09	142 ± 11.3
0.175	504 ± 7.08	9087 ± 0.71	6186 ± 1.06	2.30 ± 1.51	225 ± 6.42	219 ± 7.24
0.194	582 ± 7.37	9087 ± 0.71	5900 ± 1.29	2.55 ± 1.59	193 ± 7.69	228 ± 7.54
0.198	510 ± 7.15	9087 ± 0.71	6150 ± 1.07	2.33 ± 1.49	212 ± 6.74	219 ± 7.30
0.199	507 ± 7.11	9087 ± 0.71	6056 ± 1.09	2.38 ± 1.47	187 ± 7.41	212 ± 7.26
0.211	599 ± 6.18	9087 ± 0.71	6144 ± 1.07	2.37 ± 1.48	208 ± 6.75	253 ± 6.35
0.226	550 ± 6.59	9023 ± 0.71	6211 ± 1.05	2.19 ± 1.57	237 ± 6.37	251 ± 6.77
0.248	728 ± 5.29	9023 ± 0.71	5565 ± 1.18	2.73 ± 1.29	235 ± 5.20	266 ± 5.44
0.261	689 ± 5.47	9023 ± 0.71	5755 ± 1.14	2.58 ± 1.36	230 ± 5.62	266 ± 5.64
0.302	910 ± 5.18	9023 ± 0.71	5175 ± 1.47	3.04 ± 1.37	219 ± 5.72	299 ± 5.36

Table 27 continued

Specimen (% U_3O_8)	I U $K\alpha_1$ (cts/180 sec) $\pm S_N(\%)$	I_0 (cts/180 sec) $\pm S_N(\%)$	I_T (cts/180 sec) $\pm S_N(\%)$	m (g/cm) ² $\pm S_N(\%)$	I Rayleigh m	$\frac{cts.cm^2}{180 sec.g}$ $\pm S_N(\%)$	I U $K\alpha_1$ m	$\frac{cts.cm^2}{180 sec.g}$ $\pm S_N(\%)$
0.339	972 ± 4.68	9023 ± 0.71	5810 ± 1.30	2.59 ± 1.57	221	± 6.67	375	± 4.94
0.341	816 ± 5.39	9023 ± 0.71	6002 ± 1.26	2.35 ± 1.71	229	± 7.16	347	± 5.65
0.352	934 ± 6.55	9023 ± 0.71	5591 ± 1.36	2.72 ± 1.51	234	± 6.07	343	± 6.72
0.392	1057 ± 4.34	9023 ± 0.71	5716 ± 1.32	2.57 ± 1.58	240	± 6.24	411	± 4.62
0.425	1189 ± 3.39	9057 ± 0.71	5634 ± 1.11	2.55 ± 1.35	236	± 5.49	465	± 3.65
0.463	1177 ± 4.00	9057 ± 0.71	5714 ± 1.32	2.58 ± 1.56	212	± 6.97	457	± 4.29
0.490	1412 ± 4.20	9023 ± 0.71	5630 ± 1.56	2.59 ± 1.88	260	± 7.02	545	± 4.60
1.210	3517 ± 1.64	9057 ± 0.71	4619 ± 1.63	3.26 ± 1.28	225	± 5.28	1080	± 2.80

Table 28

Initial data observed from Rabbit Lake ores required to evaluate the matrix and thickness factors.

Specimen (% U_3O_8)	$I_{U K\alpha_1}$ (cts/180 sec) $\pm S_N(\%)$	I_o (cts/180 sec) $\pm S_N(\%)$	I_T (cts/180 sec) $\pm S_N(\%)$	m (g/cm) ² $\pm S_N(\%)$	$\frac{I_{Rayleigh}}{m}$ cts.cm ² 180 sec.g $\pm S_N(\%)$	$\frac{I_{U K\alpha_1}}{m}$ cts.cm ² 180 sec.g $\pm S_N(\%)$
0.0215	34 ± 422	9057 ± 0.71	6197 ± 1.06	2.24 ± 1.55	193 ± 7.55	15 ± 422
0.0317	31 ± 165	9057 ± 0.71	5954 ± 1.10	2.70 ± 1.38	211 ± 5.80	11 ± 165
0.0680	163 ± 28.7	9057 ± 0.71	5867 ± 1.42	2.47 ± 1.42	199 ± 6.61	65 ± 28.7
0.0720	127 ± 68.4	9057 ± 0.71	5826 ± 1.37	2.56 ± 1.37	188 ± 6.72	49 ± 68.4
0.207	582 ± 8.28	8776 ± 0.72	5164 ± 1.36	3.04 ± 1.36	179 ± 6.81	191 ± 8.39
0.286	718 ± 5.99	8776 ± 0.72	5143 ± 1.19	2.99 ± 1.19	226 ± 4.83	239 ± 6.11
0.460	1231 ± 4.09	8776 ± 0.72	5416 ± 1.46	2.80 ± 1.46	195 ± 6.85	439 ± 4.34
0.580	1493 ± 3.31	8776 ± 0.72	5796 ± 1.63	2.45 ± 1.63	200 ± 7.66	608 ± 3.69
0.963	2698 ± 1.90	8776 ± 0.72	4512 ± 1.23	2.43 ± 1.23	229 ± 4.86	845 ± 2.26

Table 29

Initial data observed from Key Lake ores required to evaluate the matrix and thickness factors.

Specimen (% U_3O_8)	$I_{U\ K\alpha_1}$ (cts/180 sec) $\pm S_N(\%)$	I_0 (cts/180 sec) $\pm S_N(\%)$	I_T (cts/180 sec) $\pm S_N(\%)$	m (g/cm) ² $\pm S_N(\%)$	I_{Rayleigh} m $\frac{\text{cts.cm}^2}{180 \text{ sec.g}}$ $\pm S_N(\%)$	$I_{U\ K\alpha_1}$ m $\frac{\text{cts.cm}^2}{180 \text{ sec.g}}$ $\pm S_N(\%)$
0.0146	50 \pm 125	9223 \pm 0.70	5868 \pm 1.11	2.42 \pm 1.43	210 \pm 6.35	20 \pm 125
0.0505	116 \pm 42.3	9223 \pm 0.70	7107 \pm 0.90	1.27 \pm 2.54	211 \pm 12.1	91 \pm 42.4
0.0841	121 \pm 48.4	9223 \pm 0.70	7416 \pm 0.86	1.07 \pm 2.97	223 \pm 13.5	112 \pm 48.5
0.176	474 \pm 6.33	9223 \pm 0.70	5720 \pm 1.14	2.53 \pm 1.38	220 \pm 5.85	187 \pm 6.48
0.181	358 \pm 9.47	9223 \pm 0.70	7016 \pm 0.94	1.45 \pm 2.52	214 \pm 12.1	247 \pm 9.80
0.193	419 \pm 8.74	9223 \pm 0.70	6699 \pm 0.96	1.61 \pm 2.05	220 \pm 9.17	260 \pm 8.98
0.230	343 \pm 10.7	9223 \pm 0.70	6929 \pm 0.92	1.43 \pm 2.27	238 \pm 9.60	239 \pm 10.9
0.245	447 \pm 8.44	9223 \pm 0.70	6492 \pm 0.98	1.65 \pm 1.98	271 \pm 7.36	270 \pm 8.67
0.512	1159 \pm 3.42	9223 \pm 0.70	6374 \pm 1.01	1.87 \pm 1.78	234 \pm 7.50	619 \pm 3.86
1.19	1987 \pm 2.87	9223 \pm 0.70	6998 \pm 1.05	1.31 \pm 2.86	196 \pm 13.4	1522 \pm 4.05

Table 30

Initial data observed from Elliot Lake ores required to evaluate the matrix and thickness factors.

Specimen (% U_3O_8)	$I_U K\alpha_1$ (cts/180 sec)		I_O (cts/180 sec)		I_T (cts/180 sec)		m (g/cm) ²		I_{Rayleigh} m		$I_U K\alpha_1$ m	
		$\pm S_N(\%)$		$\pm S_N(\%)$		$\pm S_N(\%)$		$\pm S_N(\%)$		cts.cm ² 180 sec.g		cts.cm ² 180 sec.g
0.095	217	± 21.9	8776	± 0.72	5436	± 1.20	2.71	± 1.30	219	± 5.53	80	± 21.9
0.102	200	± 20.5	8776	± 0.72	5666	± 1.15	2.61	± 1.34	235	± 5.37	76	± 20.5
0.272	642	± 6.66	8776	± 0.72	5284	± 1.23	2.78	± 1.27	218	± 5.47	230	± 6.78
0.356	786	± 6.37	8776	± 0.72	4978	± 1.51	2.99	± 1.37	226	± 5.56	262	± 6.52
0.482	1188	± 5.45	8776	± 0.72	4873	± 1.53	3.01	± 1.36	260	± 4.96	394	± 5.62
0.773	1848	± 2.94	8776	± 0.72	4685	± 1.58	3.01	± 1.34	272	± 4.73	613	± 3.23

46 uranium ore samples. The slope of this line was used to evaluate the proportionality constant χ . From table 35, the value of this slope is 988 (counts.cm²)/(180 sec.g.%U₃O₈). Following unit conversion from %U₃O₈ to uranium weight fraction, r_U , as required by equations 4.11 and 4.13, the reciprocal was taken. The adopted magnitude of χ was then 8.58×10^{-6} (180 sec.g)/(counts.cm²).

This value of χ was employed to estimate the absorption due to uranium atoms for each of the ore specimens as shown in tables 31-34. The first column of the table lists the total mass absorption coefficient of the matrix elements for the excitation radiation, $\sum_i (\mu_{ei})_i r_i$, as determined from equation 4.11. These values remained reasonably constant for the ores from each location. The average matrix element mass absorption coefficient for both Beaverlodge (0.162 cm²/g) and Rabbit Lakes (0.162 cm²/g) were identical and equivalent to that from an average uranium bearing granite 0.162 cm²/g as detailed in table 22. The coefficients for Elliot and Key Lake ores tended to be notably higher at 0.175 and 0.185 cm²/g respectively. These values were employed to determine the matrix and thickness factors for each ore specimen by using equations 4.12 and 4.13. These data are presented in the second and third columns respectively. The fourth column contains the net U K α_1 peak intensity as corrected by the matrix and thickness factors according to the right hand side of equation 4.9. As such, the data listed in this column are expected to be proportional to the actual uranium weight fraction in each of the specimens analyzed.

The correlation between the initial U K α_1 intensity data and uranium concentration can be seen in figure 35. The identical data as corrected

Table 31

Determination of the matrix and thickness factors for Beaverlodge Lake ores.

Specimen	$\sum_i (\nu_e)_i r_i$ matrix		$\sum_i (\nu_e + \nu_f)_i r_i$ total		$1 - e^{-m \sum_i (\nu_e + \nu_f)_i r_i}$	$\frac{(1 - U \cdot K \alpha_1) \sum_i (\nu_e + \nu_f)_i r_i}{1 - e^{-m \sum_i (\nu_e + \nu_f)_i r_i}}$	
	(cm ² /g)	±S _N (%)	(cm ² /g)	±S _N (%)	±S _N (%)	±S _N (%)	
0.102	0.178	±0.55	0.376	±0.21	0.735	±0.58	191 ±10.8
0.108	0.169	±0.57	0.360	±0.22	0.611	±0.81	236 ± 9.26
0.118	0.157	±0.68	0.333	±0.24	0.529	±1.20	162 ±12.8
0.116	0.157	±0.61	0.335	±0.22	0.534	±1.02	203 ±11.3
0.175	0.158	±0.61	0.342	±0.22	0.544	±1.00	317 ± 7.15
0.194	0.160	±0.64	0.346	±0.23	0.586	±1.00	343 ± 7.44
0.198	0.159	±0.61	0.343	±0.22	0.550	±0.98	318 ± 7.22
0.199	0.162	±0.60	0.348	±0.22	0.564	±0.95	313 ± 7.18
0.211	0.155	±0.60	0.337	±0.21	0.549	±0.97	367 ± 6.26
0.226	0.160	±0.64	0.348	±0.23	0.533	±1.05	358 ± 6.68
0.248	0.166	±0.55	0.360	±0.21	0.626	±0.76	418 ± 5.35
0.261	0.163	±0.57	0.355	±0.21	0.600	±0.84	407 ± 5.54

Table 31 continued

Specimen	$\sum_i (\nu_e)_i r_i$ matrix		$\sum_i (\nu_e + \nu_f)_i r_i$ total		$1 - e^{-m \sum_i (\nu_e + \nu_f)_i r_i}$		$\frac{(I U K \alpha_1) \sum_i (\nu_e + \nu_f)_i r_i}{1 - e^{-m \sum_i (\nu_e + \nu_f)_i r_i}}$	
	(cm ² /g)	±S _N (%)	(cm ² /g)	±S _N (%)		±S _N (%)		±S _N (%)
0.302	0.171	±0.59	0.373	±0.23	0.677	±0.74	500	±5.24
0.339	0.155	±0.63	0.343	±0.23	0.589	±0.98	566	±4.79
0.341	0.159	±0.68	0.351	±0.25	0.562	±1.10	509	±5.51
0.352	0.162	±0.63	0.356	±0.25	0.621	±0.90	536	±6.62
0.392	0.161	±0.65	0.358	±0.24	0.601	±0.97	629	±4.45
0.425	0.167	±0.58	0.373	±0.22	0.615	±0.81	722	±3.49
0.463	0.160	±0.65	0.359	±0.24	0.603	±0.95	700	±4.12
0.490	0.160	±0.75	0.363	±0.29	0.610	±1.14	711	±4.36
1.21	0.162	±0.61	0.399	±0.24	0.728	±0.63	1930	±1.77

Table 32

Determination of the matrix and thickness factors for Rabbit Lake ores.

Specimen	$\sum_i (\nu_e)_i r_i$ matrix		$\sum_i (\nu_e + \nu_f)_i r_i$ total		$1 - e^{-m \sum_i (\nu_e + \nu_f)_i r_i}$	$\frac{(I U K \alpha_1) \sum_i (\nu_e + \nu_f)_i r_i}{1 - e^{-m \sum_i (\nu_e + \nu_f)_i r_i}}$	
	(cm ² /g)	±S _N (%)	(cm ² /g)	±S _N (%)			±S _N (%)
0.021	0.169	±0.68	0.352	±0.44	0.545	±1.05	21 ±422
0.032	0.155	±0.53	0.323	±0.20	0.582	±0.87	17 ±165
0.068	0.173	±0.59	0.364	±0.24	0.593	±0.88	99 ±28.7
0.072	0.170	±0.59	0.357	±0.28	0.599	±0.85	75 ±68.4
0.207	0.167	±0.59	0.358	±0.22	0.663	±0.79	314 ± 8.32
0.286	0.169	±0.53	0.365	±0.21	0.664	±0.66	394 ± 6.03
0.460	0.154	±0.62	0.346	±0.23	0.621	±0.87	686 ± 4.19
0.580	0.144	±0.67	0.334	±0.24	0.560	±1.06	891 ± 3.48
0.963	0.159	±0.59	0.380	±0.22	0.728	±0.60	1512 ± 2.01

Table 33

Determination of the matrix and thickness factors for Key Lake ores.

Specimen	$\sum_i (\mu_e)_i r_i$ matrix		$\sum_i (\mu_e + \mu_f)_i r_i$ total		$1 - e^{-m \sum_i (\mu_e + \mu_f)_i r_i}$	$\frac{(I U K \alpha_1) \sum_i (\mu_e + \mu_f)_i r_i}{1 - e^{-m \sum_i (\mu_e + \mu_f)_i r_i}}$
	(cm ² /g)	±S _N (%)	(cm ² /g)	±S _N (%)	±S _N (%)	±S _N (%)
0.015	0.186	±0.61	0.388	±0.28	0.609 ±0.87	31 ±125
0.051	0.202	±1.05	0.426	±0.49	0.417 ±1.94	118 ±42.4
0.084	0.199	±1.21	0.420	±0.59	0.362 ±2.38	140 ±48.5
0.176	0.282	±0.59	0.388	±0.23	0.625 ±0.82	294 ± 6.39
0.181	0.179	±0.94	0.387	±0.38	0.428 ±1.89	323 ± 9.66
0.193	0.188	±0.85	0.407	±0.36	0.480 ±1.47	355 ± 8.87
0.230	0.190	±0.93	0.409	±0.40	0.443 ±1.69	316 ±10.8
0.245	0.201	±0.84	0.434	±0.38	0.512 ±1.37	378 ± 8.56
0.512	0.172	±0.75	0.393	±0.30	0.521 ±1.21	875 ± 3.64
1.19	0.149	±1.16	0.397	±0.51	0.404 ±2.20	1950 ± 3.65

Table 34

Determination of the matrix and thickness factors for Elliot Lake ores.

Specimen	$\sum_i (\nu_e)_i r_i$ matrix		$\sum_i (\nu_e + \nu_f)_i r_i$ total		$1 - e^{-m \sum_i (\nu_e + \nu_f)_i r_i}$	$\frac{(I U K \alpha_i) \sum_i (\nu_e + \nu_f)_i r_i}{1 - e^{-m \sum_i (\nu_e + \nu_f)_i r_i}}$
	(cm ² /g)	±S _N (%)	(cm ² /g)	±S _N (%)	±S _N (%)	±S _N (%)
0.095	0.173	±0.57	0.365	±0.23	0.628 ±0.77	126 ±21.9
0.102	0.165	±0.57	0.347	±0.21	0.595 ±0.83	116 ±20.5
0.272	0.173	±0.56	0.373	±0.22	0.646 ±0.73	370 ± 6.70
0.356	0.179	±0.62	0.387	±0.25	0.686 ±0.73	443 ± 6.42
0.482	0.179	±0.62	0.395	±0.27	0.696 ±0.71	674 ± 5.50
0.773	0.183	±0.64	0.416	±0.27	0.714 ±0.68	1076 ± 3.03

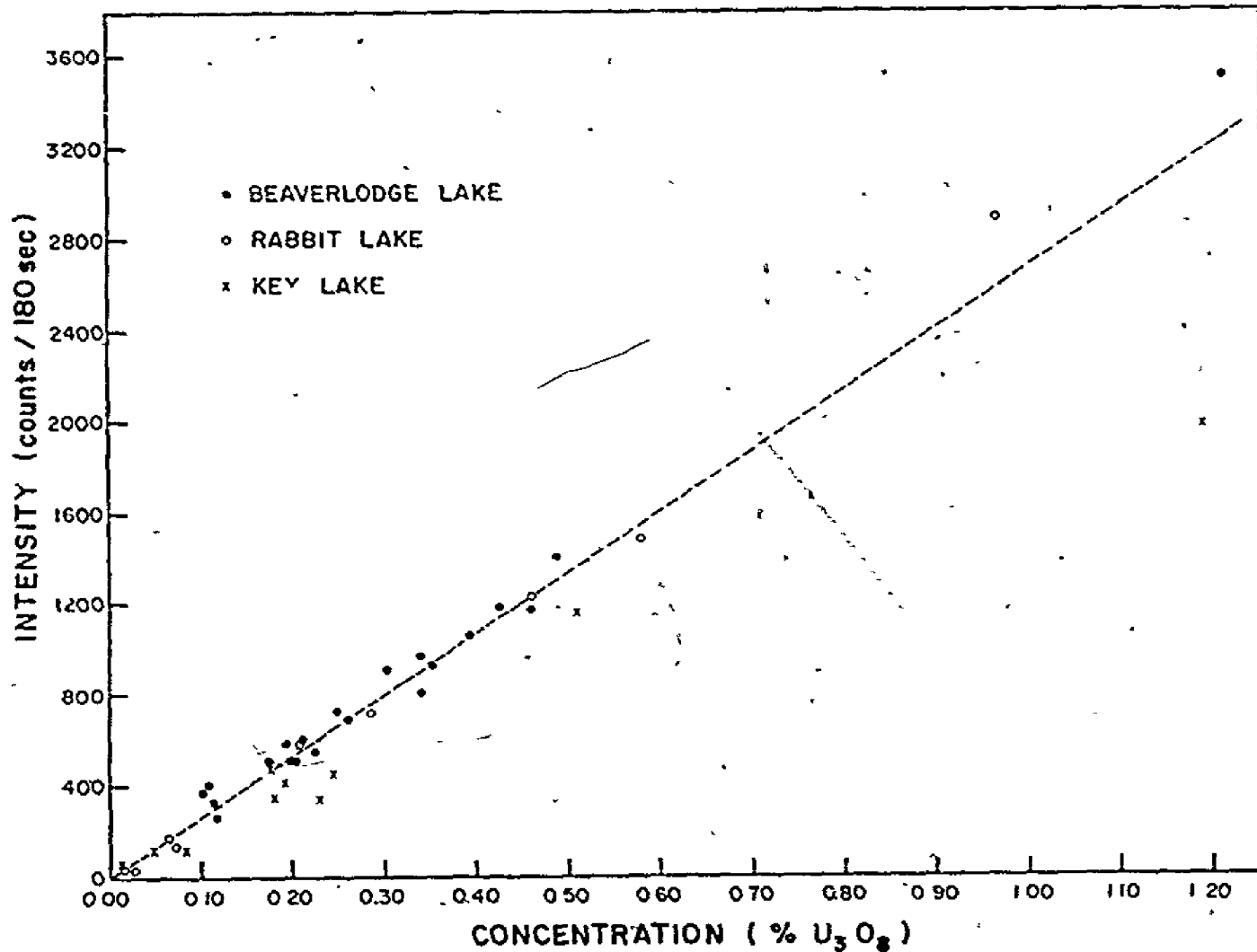


Fig. 35. Correlation between initial U K α_1 intensity data and uranium concentration

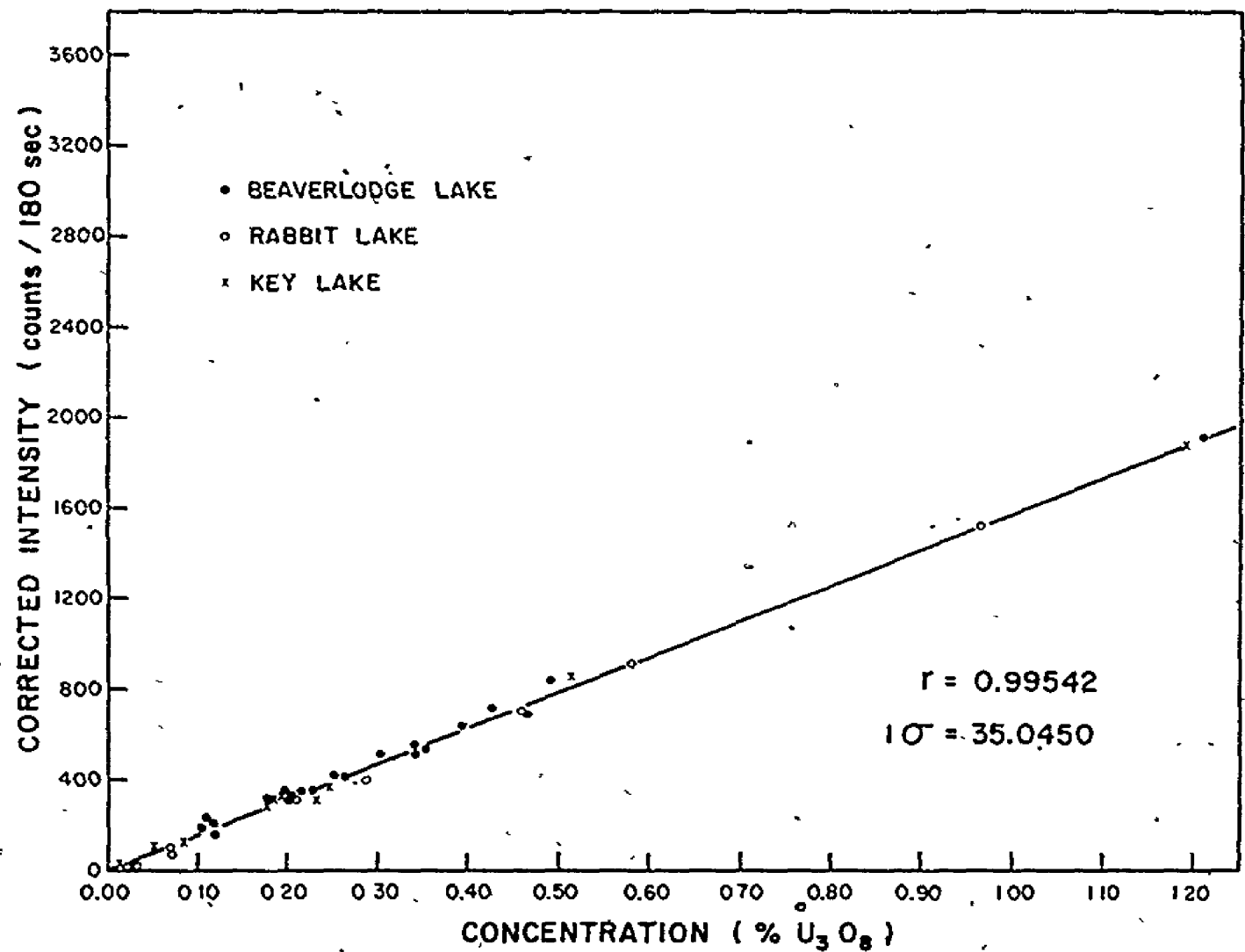


Fig. 36. Correlation of U K α_1 intensity data as corrected by the matrix and thickness factors with uranium concentration

by the matrix and thickness factors is illustrated in figure 36. The best least squares straight lines are constructed through both sets of data. By visual comparison, there is considerably more scatter about the line with the unmodified data in the lower concentration range. Very considerable deviation occurs at higher uranium weight fractions. These appear to be adequately compensated for in the corrected data set. A more comprehensive description of this betterment is given, for all of the data, in table 35. The slope and intercept values were determined by linear best least squares procedures for the original $U K\alpha_1$ intensity data, the $(I U K\alpha_1)/m$ data and the final corrected $I U K\alpha_1$ data. Substantial quantitative improvements in the intercept values, the correlation coefficient r , and the standard error of estimation of the curve, $\pm\sigma$ ($\%U_3O_8$), are realized as a result of the data treatment.

The final corrected $I U K\alpha_1$ data from specimens originating from each of the ore locations were also analyzed separately. Paralleling the total data, an emended best least squares straight line can be constructed through the $U K\alpha_1$ intensity data after modification by the matrix and thickness factors than for the initially observed data. It is of interest to note, table 36, that the calibration slopes of the initial data are radically different for each ore type. This is due principally to dissimilar ore densities from each location. The slopes of the corrected data from Beaverlodge, Key and Rabbit Lakes, however, are essentially identical at 1550, 1566 and 1596 respectively. The corresponding slope for Elliot Lake ores appears to be slightly less at 1424. Earlier it was remarked that the absorption due to matrix elements was significantly higher for Key Lake and Elliot Lake ores than it was

Table 35

Quantitative improvements in the linear curve
fit for all of the ore types analyzed:

parameter	I U Ka ₁	$\frac{I U Ka_1}{m}$	$\frac{(I U Ka_1) \sum_i (\mu_e + \mu_f)_i r_i}{I - e^{-m \sum_i (\mu_e + \mu_f)_i r_i}}$
slope	2478	988	1549
intercept	14.3 *	8.5	2.1
Pearson r	0.959	0.973	0.995
Pearson (r) ²	0.920	0.947	0.991
standard error of estimation $\pm 1\sigma(\%U_3O_8)$	0.087	0.065	0.026

Table 36

Quantitative improvements in the linear curve fit for each of the ore types analyzed.

Ore Location	Intercept		Slope		Pearson r		Pearson (r) ²		1σ(%U ₃ O ₈)*	
	I UKα ₁	Corrected I UKα ₁	I UKα ₁	Corrected I UKα ₁	I UKα ₁	Corrected I UKα ₁	I UKα ₁	Corrected I UKα ₁	I UKα ₁	Corrected I UKα ₁
Beaverlodge Lake	-27.1	21.1	2872	1550	0.995	0.997	0.990	0.994	70.0	28.3
Elliot Lake	-34.4	-21.8	2446	1424	0.999	0.999	0.997	0.997	36.1	22.3
Key Lake	60.7	11.1	1692	1566	0.985	0.998	0.969	0.997	110	32.5
Rabbit Lake	-77.8	-28.0	2966	1596	0.997	0.999	0.993	0.999	83.5	17.6

* 1 standard error of estimation.

'for the others'. In the Elliot Lake case, it is well known that these ores commonly contain as much thorium as they do uranium⁽⁷⁹⁾, whereas the Saskatchewan ores do not. The initial assumption that the total mass absorption coefficient can be broken into a matrix element and a uranium component is therefore violated. Being an actinide, the Th K_{ab} absorbs the ^{57}Co excitation radiation nearly as efficiently as does uranium. To correct for this fact, the total mass absorption coefficient as determined from the transmitted radiation, equation 4.10, should contain three terms. (i) absorption due to matrix elements, (ii) absorption due to uranium atoms, and (iii) absorption resulting from the thorium content. The presence of Th in the Elliot Lake ores is an explanation for higher matrix element absorption as observed in table 34 and because this element is an actinide accounts for the slight decrease in slope of the final uranium concentration calibration curve, table 36. The increase in matrix element absorption of the Key Lake ores does not affect the final calibration curve slope. It is therefore probable that this ore, similar to Cluff Lake ores, may be co-mineralized with a heavier element such as iron or nickel⁽⁸⁰⁾. Increased absorption by elements of this atomic number will not invalidate the assumptions inherent in equation 4.10.

By using the final slope and intercept given in table 35 for all the ore data, the uranium concentration, C, can be calculated from the corrected U K_{α_1} peak intensity by the following equation:

$$C (\%U_3O_8) = (\text{Corrected } I_{U \text{ } K_{\alpha_1}}) / 1549 \dots \dots \dots 4.15$$

The total measured background under the U K_{α_1} peak remained reasonably constant for all the ores analyzed at approximately 2900 counts/180

sec. Using the two sigma rule and taking into account that each specimen was counted three times and then averaged, the smallest significant measured $U\ K\alpha_1$ intensity is 63 counts/180 sec. From equation 4.15, the minimum detectable limit is then approximately 0.04% U_3O_8 with the procedure as described. This is in accordance with the results obtained. From the slope of the calibration curve, the sensitivity is 0.86 counts/sec/% U_3O_8 /mCi. A complete description and listing of the computer programme written to analyze the K X-ray spectra is given in appendix D.

4.2.7. Specimen precision evaluation

The data accumulated to determine the error due to the specimen itself are presented in table 37. The dispersion, S_4 , about the mean for the 16 replicate measurements is $\pm 3.98\%$ (1S). The average standard counting error for the $U\ K\alpha_1$ intensity measurement is $\pm 5.00\%$. The F ratio test was applied to determine if these values are significantly different. The calculated ratio of 1.57 is less than the tabulated values of 2.07 and 2.87 at the 95% and 99% confidence levels respectively; hence no error can be attributed to the presence of the specimen.

Table 38 contains the data used to evaluate the specimen loading error. The dispersion of this data set, S_5 , was $\pm 6.23\%$ (1S) with an average standard counting error of $\pm 5.16\%$. At the 95% and 99% confidence intervals, the F_{tab} values are 1.64 and 1.87. F_{cal} for this set is 1.46. Therefore, no significant error is associated with the loading operation as performed.

In appendix C, the instrumental errors for the γ -ray spectrometer were evaluated. As previously stated, these were shown to be negligible

Table 37
Precision data used to determine the specimen
error for the K X-ray experiment

Corrected I U $K\alpha_1$ (counts/180 sec)	S_N $\pm(\%)$	$(\bar{x} - x_i)$	$(\bar{x} - x_i)^2 \times 10^{-2}$
802	5.24	-26	6.96
802	5.24	-26	6.96
739	5.34	+36	13.41
830	5.07	-54	29.57
795	5.15	-19	3.75
781	4.82	- 5	0.29
767	4.95	+ 8	0.74
740	5.36	+35	12.69
717	5.21	+58	34.37
808	4.94	-32	10.48
775	4.97	+ 0	0.00
779	4.68	- 3	0.11
777	4.98	- 1	0.02
731	4.16	+44	19.91
794	5.01	-18	3.38
773	4.69	+ 2	0.07

$\bar{x} = 775$

$S_N = \pm 3.98\%$

$\Sigma = 142.72$

$S_N = \pm 5.00\%$

Table 38

Precision data used to determine the specimen
loading error for the K X-ray experiment.

Corrected I UK α_1 (counts/180 sec)	S_N $\pm(\%)$	$(\bar{x} - x_i)$	$(\bar{x} - x_i)^2 \times 10^{-2}$
800	5.12	-38	15.11
753	5.27	+8	0.66
758	5.42	+3	0.10
734	5.02	+27	7.36
715	5.08	+46	21.28
886	5.31	-124	155.94
800	5.08	-38	15.11
739	5.17	+22	4.90
783	5.22	-21	4.79
674	5.43	+87	75.91
809	4.95	-47	22.92
742	5.26	+19	3.66
740	5.06	+21	4.46
749	5.37	+12	1.47
748	4.97	+13	1.72
748	4.75	+13	1.72

$$\bar{x} = 761$$

$$S_S = \pm 6.23\%$$

$$\bar{S}_N = \pm 5.16\%$$

$$\Sigma = 337.10$$

for the K X-ray experiment. The only appreciable error in measuring peak intensities with this apparatus is the statistical counting error. In this section, it is demonstrated that no significant specimen error exists. The total precision obtained by an experimental measurement is therefore limited only by the statistical counting error. Accordingly, the precision limits, as written in tables 23-34 are $\pm 1S_N(\%)$, and their magnitudes equal to the original standard counting errors as manifested by the appropriate numerical calculations.

4.3. L X-ray results and discussion.

4.3.1. X-ray spectrometer energy calibration

Figure 37 illustrates the relationship between photon energy and channel number for the instrumental settings as listed in table 9. Linear best least squares analysis of the data gives the following equation:

$$\text{Energy (keV)} = \frac{(\text{Channel Number} + 877.448)}{88.257} \dots \dots \dots 4.16$$

Equation 4.16 was employed to determine all photon energies measured by the X-ray spectrometer for the L X-ray experiment.

4.3.2. Matrix compensation

Under fixed excitation conditions, the fundamental excitation equation for thick specimens, equation 2.13, can be simplified and expressed as:

$$I_f \propto \frac{r_A \text{ csc } \phi}{\sum (\mu_e \text{ csc } \phi + \mu_f \text{ csc } \psi)_i r_i} \dots \dots \dots 4.17$$

- 164 -

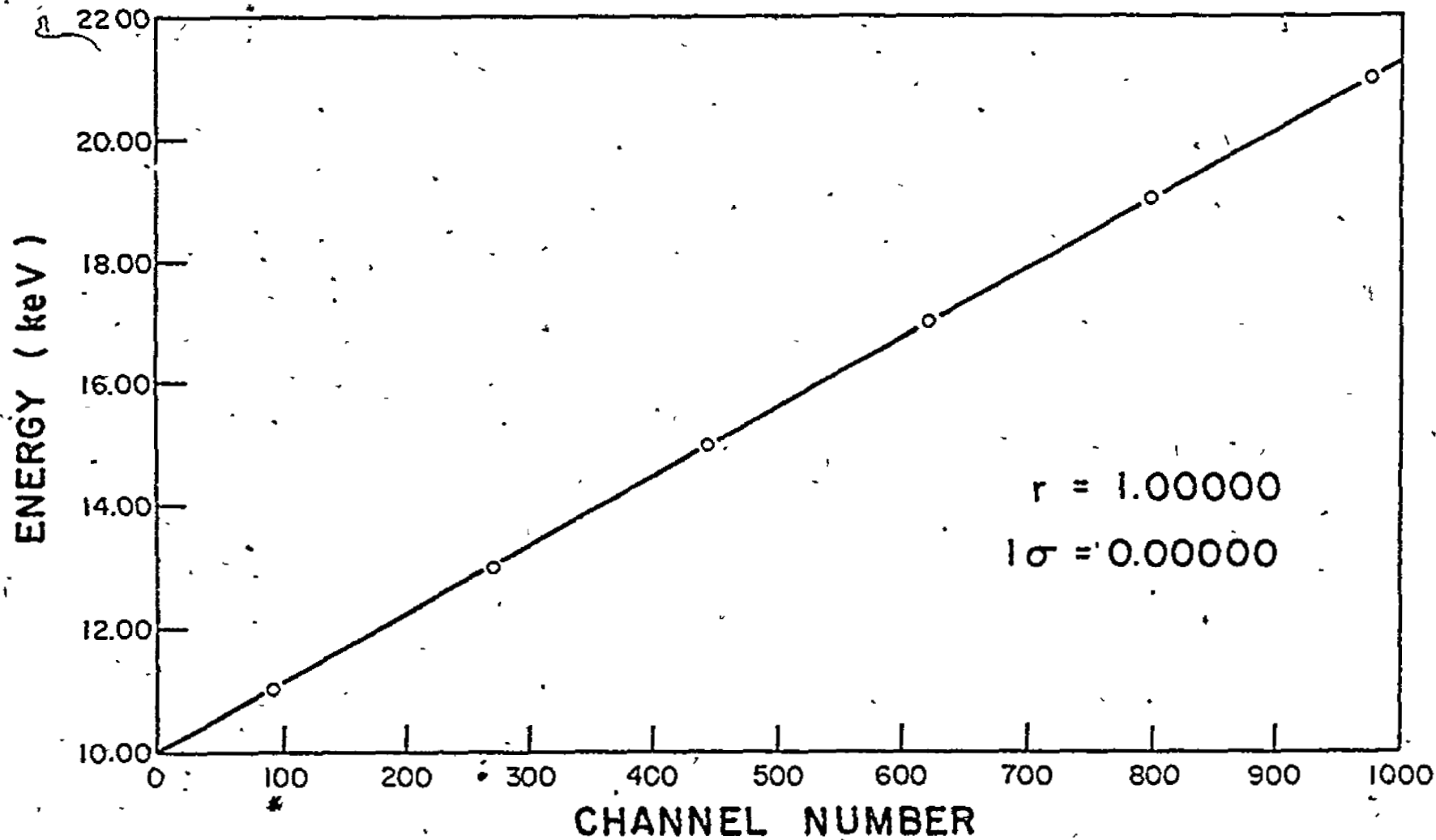


Fig. 37. Photon energy calibration for the L X-ray experiment

Similarly, the intensity of the Compton scattered peak under identical excitation conditions can be written as:

$$I_C \propto \frac{\sigma_C \text{ CSC } \phi}{\sum_i (\mu_e \text{ CSC } \phi + \mu_C \text{ CSC } \psi)_i r_i} \dots \dots \dots 4.18$$

If the specimens to be analyzed are of comparative composition, and the geometrical conditions remain fixed, then the Compton scattering cross section, σ_C , can be regarded as a constant since it possesses a relatively small Z dependence. The characteristic fluorescence to Compton scattering intensity ratio is then given by:

$$\frac{I_f}{I_C} \propto r_A \frac{\sum_i (\mu_e \text{ CSC } \phi + \mu_C \text{ CSC } \psi)_i r_i}{\sum_i (\mu_e \text{ CSC } \phi + \mu_f \text{ CSC } \psi)_i r_i} \dots \dots \dots 4.19$$

As noted from this equation, I_f/I_C is proportional to the analyte weight fraction multiplied by the ratio of two total mass absorption coefficients.

For the specific case of analyzing for uranium in an uranium bearing ore,

$$r_U \propto \eta \frac{(I_f)}{(I_C)} \dots \dots \dots 4.20$$

where η is a coefficient compensating for the preferential absorption of the U L α peak intensity over the higher energy Compton scattered line by the matrix elements. It is defined by:

$$\eta = \frac{\sum_i (\mu_e \text{ CSC } \phi + \mu_C \text{ CSC } \psi)_i r_i}{\sum_i (\mu_e \text{ CSC } \phi + \mu_f \text{ CSC } \psi)_i r_i} \dots \dots \dots 4.21$$

The success of the L X-ray experiment is therefore dependent upon η being

of constant value. By exploiting the fact that the energies of U L_{III} characteristic fluorescence are substantially above the absorption edges of the major matrix elements and by using highly selective techniques, this requirement is practically obtained.

A molybdenum target was chosen to selectively excite only the U L_{III} subshell at 17.17 keV. The Mo K_{α1,α2} secondary radiation at 17.48 and 17.37 keV is ideally positioned for this purpose. The principal γ -ray emitted from ²⁴¹Am occurs at 59.57 keV⁽⁸¹⁾. The total scattering cross section, i.e. $\sigma_R + \sigma_C$, of the Mo target for this energy is approximately 55 barns/atom while τ for the Mo K shell is 625 barns/atom⁽⁶⁾. Thus, the strength of the Mo K shell X-ray fluorescence is more than a factor of ten greater than the intensity of the primary scattered ²⁴¹Am γ -ray radiation. Furthermore, the uranium L shell photoelectric cross section for the Mo K α radiation is 40,500 barns/atom, but is only 2500 barns/atom for energies of the scattered radiation⁽⁶⁾. Thus, the fraction of the L shell vacancies created by Mo fluorescence compared to those induced by ²⁴¹Am scattered radiation is nearly 200:1. In addition, only a small percentage of the vacancies created by this scattered radiation will be in the L_I or L_{II} subshells. In practice, therefore, this radioisotope system specifically excites only the U L_{III} subshell. In none of the ore spectra taken was there any evidence of higher energy subshell excitation, i.e., no U L_{Y1} peak at 20.17 keV. Since no element has a principal absorption edge between the Mo K α excitation and the U L_{IIIab} energies, enhancement effects are not possible. Only absorption phenomena will affect the magnitude of τ .

Table 39 presents the details of mass absorption coefficient calcu-

Table 39

Calculation of mass absorption coefficients for an average uranium bearing granite.

Element	Weight fraction r_i	σ_{TOT} (barns/atom)			Mass absorption coefficient (cm ² /g)			Elemental absorption (cm ² /g)			
		$\epsilon_f = 13.6$ keV	$\epsilon_C = 16.4$ keV	$\epsilon_e = 17.5$ keV	μ_f	μ_C	μ_e	$\mu_f r_i$	$\mu_C r_i$	$\mu_e r_i$	
O	47.7%	60.1	34.4	28.3	2.26	1.29	1.07	1.08	0.62	0.51	
Si	33.2%	614.	351.	289.	13.2	7.53	6.20	4.38	2.50	2.06	
Al	7.9%	468.	267.	220.	10.4	5.96	4.91	0.82	0.47	0.39	
Fe	2.8%	6270.	3580.	2950.	67.6	38.6	31.8	1.89	1.08	0.89	
Ca	1.6%	2440.	1400.	1150.	36.7	21.0	17.3	0.59	0.34	0.28	
Na	2.9%	230.	131.	108	6.03	3.43	2.83	0.17	0.10	0.08	
g	0.16%	328	187	155	8.12	4.63	3.84	0.01	0.01	0.01	
K	3.4%	2020	1150	951	31.1	17.7	14.6	1.06	0.60	0.50	
Ti	0.24%	3470	1980	1630	43.6	24.9	20.5	0.10	0.06	0.15	
U	1.0%	27500	15700	39400	69.9	39.7	99.7	0.70	0.40	1.00	
Sr	0.029%	3550	15500	12800	24.4	107.	88.0	0.01	0.03	0.03	
Pb	0.03%	48800	51600	39600	142.	150.	15.	0.43	0.45	0.35	
					$\sum_i (\mu_f)_i r_i$	$\sum_i (\mu_C)_i r_i$	$\sum_i (\mu_e)_i r_i$				
					= 11.24	= 6.66	= 6.15				

lation for elemental absorption at energies of the U L α peak, ϵ_f , at 13.6 keV, the Mo K α Compton scattered peak, ϵ_c , at 16.4 keV and the excitation radiation, ϵ_e , at 17.5 keV. This table is employed to calculate an approximate value for η and to demonstrate that η will remain reasonably constant over a wide range of possible matrix compositions as expected from geological specimens. Pertinent data used for the construction of table 39 on the average composition of granites were taken from reference (30) and on mass absorption coefficients from reference (6). From the data presented, the total mass absorption coefficient for an average granite at energies of 13.6, 16.4 and 17.5 keV is 11.24, 6.66 and 6.15 cm²/g respectively. For a mean scatter angle, θ , of 135° the values of ϕ and ψ can be determined from figure 18. to be 45° and 90° respectively. The calculated value for η from equation 4.21 is then 1.30.

From the data presented in table 39 it can readily be seen that large variations in the concentration of the major matrix components will produce substantially different total mass absorption coefficients for each of the energies. However, the ratio of these coefficients as determined by η , will not be significantly altered. Included in this table are data for two potential interferences, Sr and Pb. Although large quantities of strontium could drastically affect the value of η , concentrations of several times the amount found in the average granite would be required to produce an observable effect. Uranium bearing ores are generally associated with a much greater lead content (of radiogenic origin) than the average granite. The amount of lead shown in table 39 is the expected quantity of radiogenic lead in a 1% uranium bearing ore.

It has been observed that both the analyte and the Compton scattered

peaks would be approximately equally attenuated in the presence of lead. This is due to the analyte peak energy being slightly above the Pb L_{IIIab} and the Compton peak energy marginally above the Pb L_{IIab} . The value of η will then be affected by large variations in lead content but the magnitude would not change as severely as the individual peak attenuation.

In addition, the absorption of other elements having K or L absorption edges slightly below the energy of the analyte and or Compton scattered peak must be considered. Elements bearing a-K shell absorption edge in such a position are: Sr, Y, Rb, Kr, Br, Se and As. The Sr concentration is by far the largest, but none of these potential interferences are major constituents of the average granite. Similarly, elements with L shell absorption edges in this position are: Th, Ac, Ra, Fr, Rn, At, Po, Bi, Pb, Hg, Au and Pt. The ores of interest contain very low quantities of Th (except for Elliot Lake specimens) and of the remaining elements, only Pb exists in any appreciable amount. It is therefore expected that for naturally occurring silica based geological specimens, such as uranium bearing granites, the value of η will not vary significantly. The ratio, I_f/I_C , will then be proportional to the uranium weight fraction in the specimen.

4.3.3. Compton scattering intensity measurements

Due to a mean scatter angle of about 135° , the Compton shift of the Mo K_α scattered radiation is approximately 1 keV, thus the Mo K_α Compton peak superimposes itself on the U L_{β_2} line at 16.43 keV. As a result of the monoenergetic excitation used, the peaks due to scattered radiation are quite distinct. The Mo K_α Compton peak has a FWHM about 60% broader.

than the corresponding Rayleigh peak and lies below the uranium L_{IIIab} energy. The net Compton scattering intensity is obtained by measuring the total peak intensity at 16.4 keV and subtracting from it the $U L\beta_2$ contribution. Since both the $U L\alpha$ and $U L\beta_2$ lines result from L_{III} transitions, the ratio, R , of fluorescence to Compton scattering, may be given by:

$$\begin{aligned}
 R &= \frac{\eta I(U L\alpha)}{I(Mo K\alpha \text{ Compton})} \\
 &= \frac{\eta I(U L\alpha)}{I(Mo K\alpha \text{ Compton} + U L\beta_2) - \eta I(U L\beta_2)} \\
 &= \frac{\eta I(U L\alpha)}{I(Mo K\alpha \text{ Compton} + U L\beta_2) - \xi \eta^2 I(U L\beta_2)} \dots \dots \dots 4.22
 \end{aligned}$$

where $I(Mo K\alpha \text{ Compton} + U L\beta_2)$ is the total intensity observed at 16.4 keV, and ξ is a coefficient expressing the relative intensity of the $U L\beta_2$ peak with respect to the $U L\alpha$ line in the hypothetical case of no matrix absorption.

4.3.4. Data and data analysis

Typical ore spectra showing the uranium L_{III} lines and molybdenum scattered lines are shown in figures 38-40 for 0.038%, 1.21% and 9.95% U_3O_8 specimens respectively. The reciprocal nature of Mo $K\alpha$ Compton intensity to uranium concentration is clearly evident.

The initial data measured from the spectra of the fourteen ore standards are presented in table 40. The $U L\alpha$ peak intensity and the combined ($U L\beta_2 + Mo K\alpha \text{ Compton}$) peak intensity are listed with their statistical counting errors. The values of η and ξ which give the best linear

Reproduced with permission of the copyright owner. Further reproduction prohibited without permission.

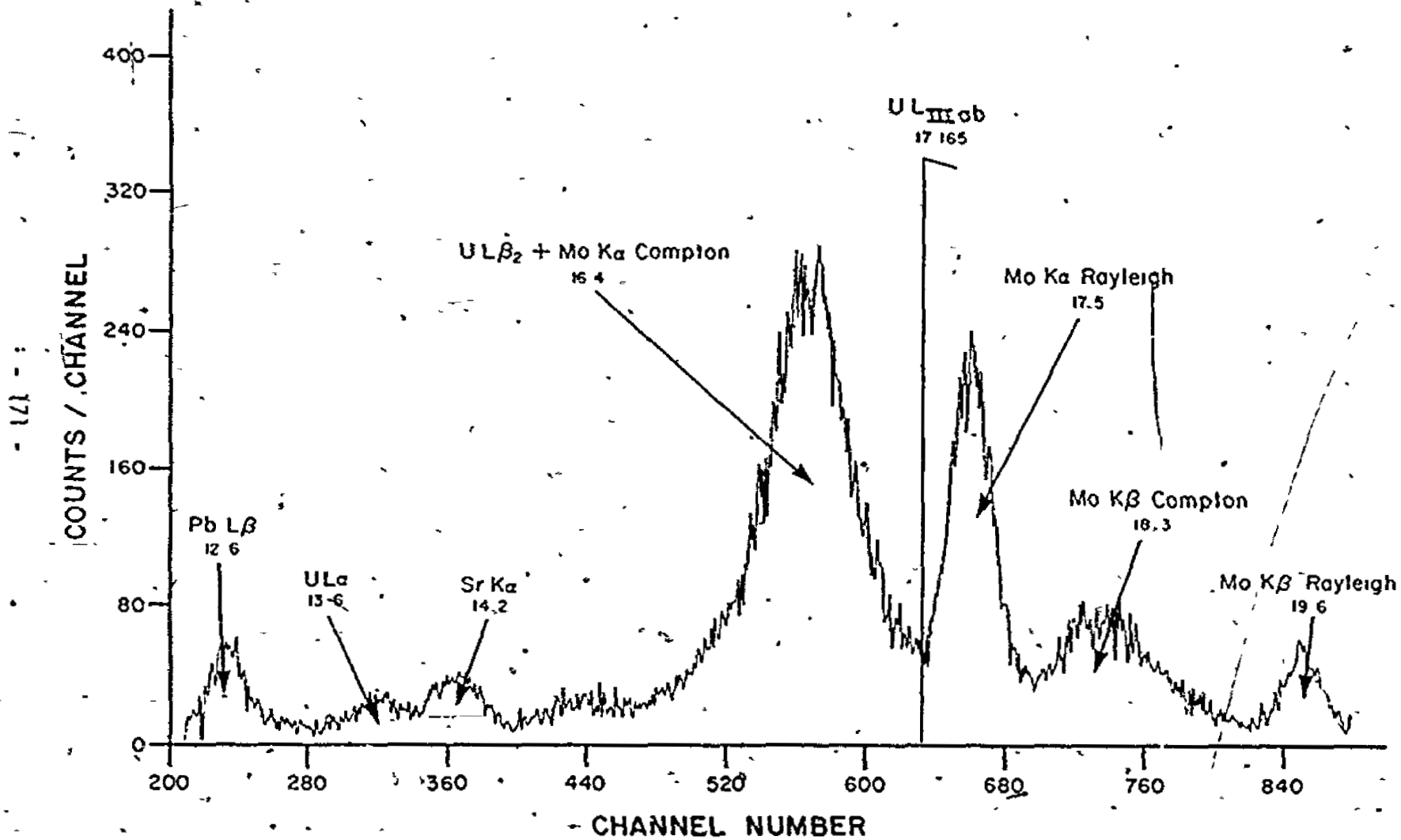


Fig. 38. Spectrum as observed with the L.X-ray apparatus from a uranium bearing ore containing 0.038 %U₃O₈

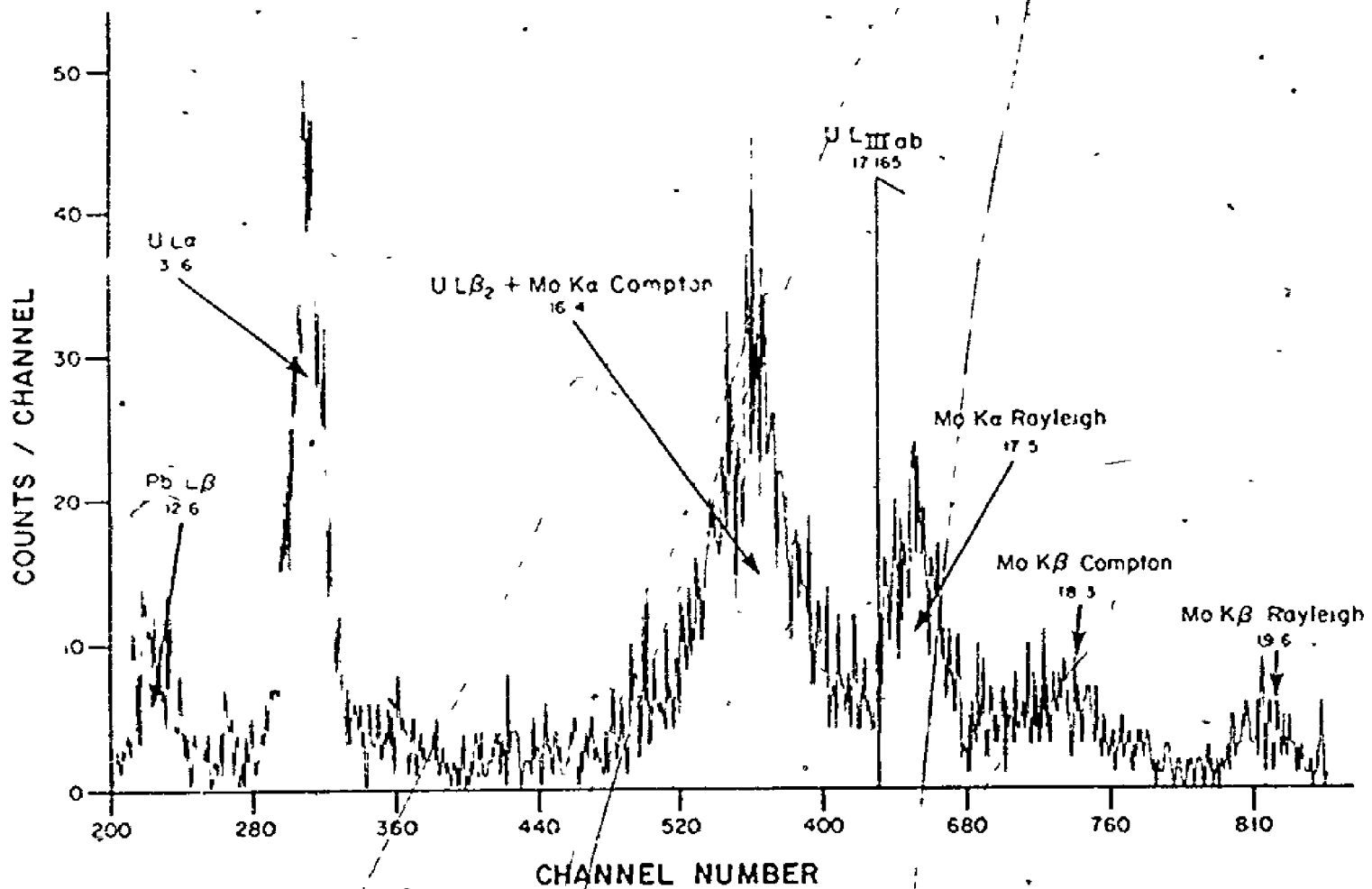


Fig. 39. Spectrum as observed with the L X-ray apparatus from a uranium bearing ore containing 1.21 %U₃O₈

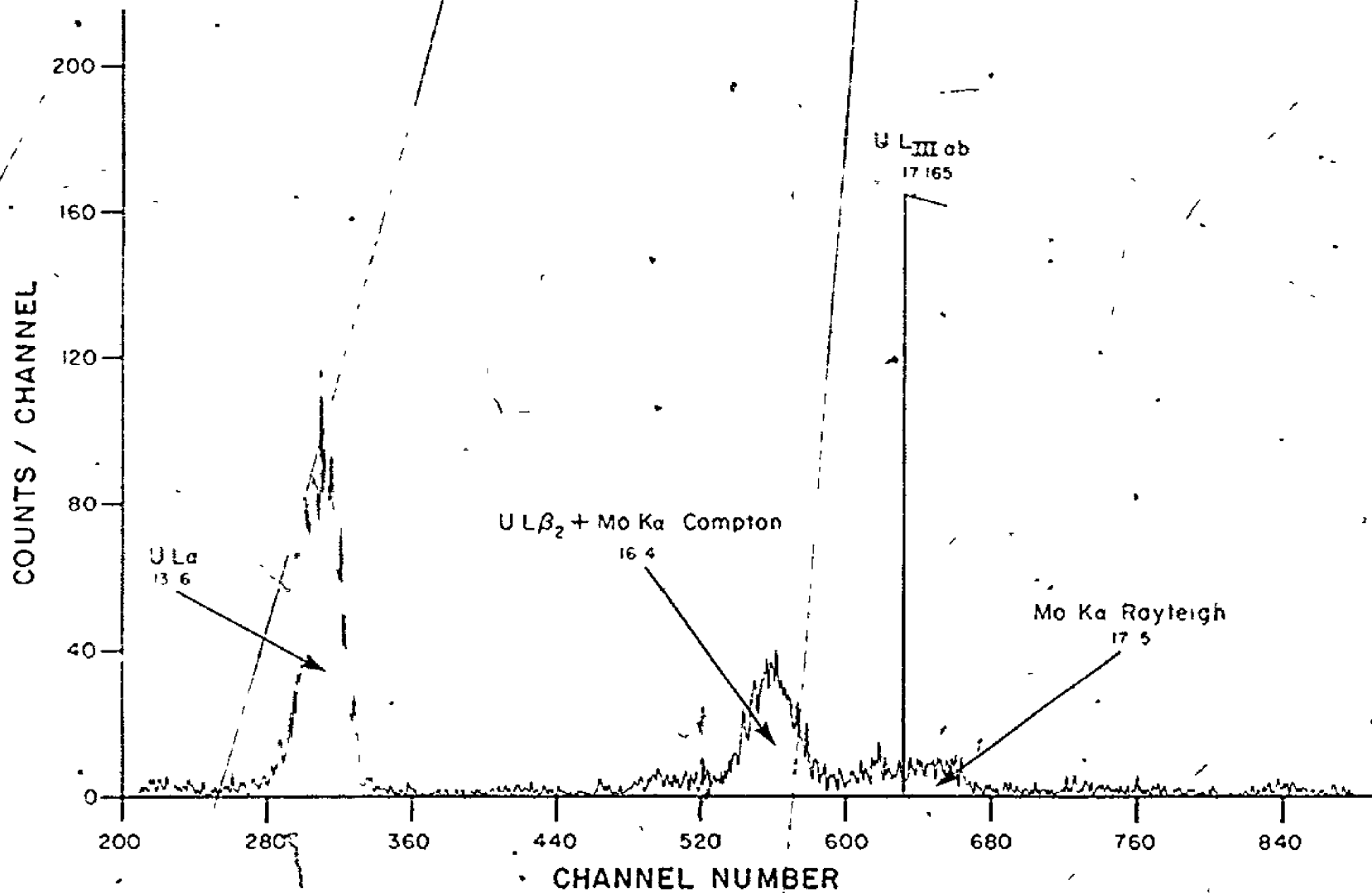


Fig. 40. Spectrum as observed with the L X-ray apparatus from a uranium bearing ore containing 9.95 U_3O_8

Table 40

Initial data measured from the L X-ray
spectra of several uranium ores.

Concentration (% U_3O_8)	I U L α		I (U L β_2 + Mo K α Compton)	
	(counts/hour)	$\pm S_N$ (%)	(counts/hour)	$\pm S_N$ (%)
0.038	35	± 5.95	1439	± 0.55
0.102	66	± 7.68	1513	± 1.19
0.108	70	± 10.3	1438	± 1.74
0.194	161	± 4.10	1497	± 1.18
0.204	184	± 5.29	1467	± 1.70
0.211	186	± 5.27	1441	± 1.74
0.248	195	± 5.09	1422	± 1.73
0.302	237	± 4.47	1481	± 1.70
0.352	270	± 4.15	1359	± 1.81
0.490	339	± 3.60	1280	± 1.85
0.531	407	± 3.23	1333	± 1.82
1.21	852	± 2.14	1427	± 1.74
9.95	4417	± 1.26	2148	± 1.85
50.1	10195	± 0.97	3586	± 1.77

calibration curve according to a linear least squares criterion, were calculated by a computer using the function minimization subroutine utilized in the γ -ray spectroscopy experiment and listed in appendix H. The function to be minimized was defined by:

$$M(\eta, \xi, m', b) = \sum_1^n [R_i(\eta, \xi) - m'C_i - b]^2 \dots \dots \dots 4.23$$

where $R_i(\eta, \xi)$ is the ratio of the i^{th} sample, calculated according to equation 4.22, n is the number of experimental points, C_i is the concentration of uranium ($\%U_3O_8$) in the i^{th} sample, m' and b are the slope and intercept respectively of the resulting calibration curve. The programs iterated on the four arguments η , ξ , m' and b to minimize M .

The ratio R as calculated from equation 4.22 is shown in figure 41. For nearly four orders of magnitude this ratio varies linearly with concentration indicating the range of applicability of the technique. Outside the range shown in figure 41 either the intensity of the $U \text{ L}\alpha$ peak or that of the Compton scattered peak is very weak, and the statistical precision of the calculated ratio, R , is poor unless unacceptably long counting times are used. In figure 42 the net intensities of $U \text{ L}\alpha$ and $Mo \text{ K}\alpha$ Compton peaks are shown versus concentration. The non-linear reciprocal characteristics of both these curves is clearly apparent.

The values of the coefficients η and ξ , obtained from the iteration procedure are 1.32 and 0.183 respectively. The value of 1.32 determined for the preferential absorption compensation factor η is in very good agreement with the estimated value of 1.30 derived from mass coefficients for an average uranium bearing granite, table 39, and calculated by equa-

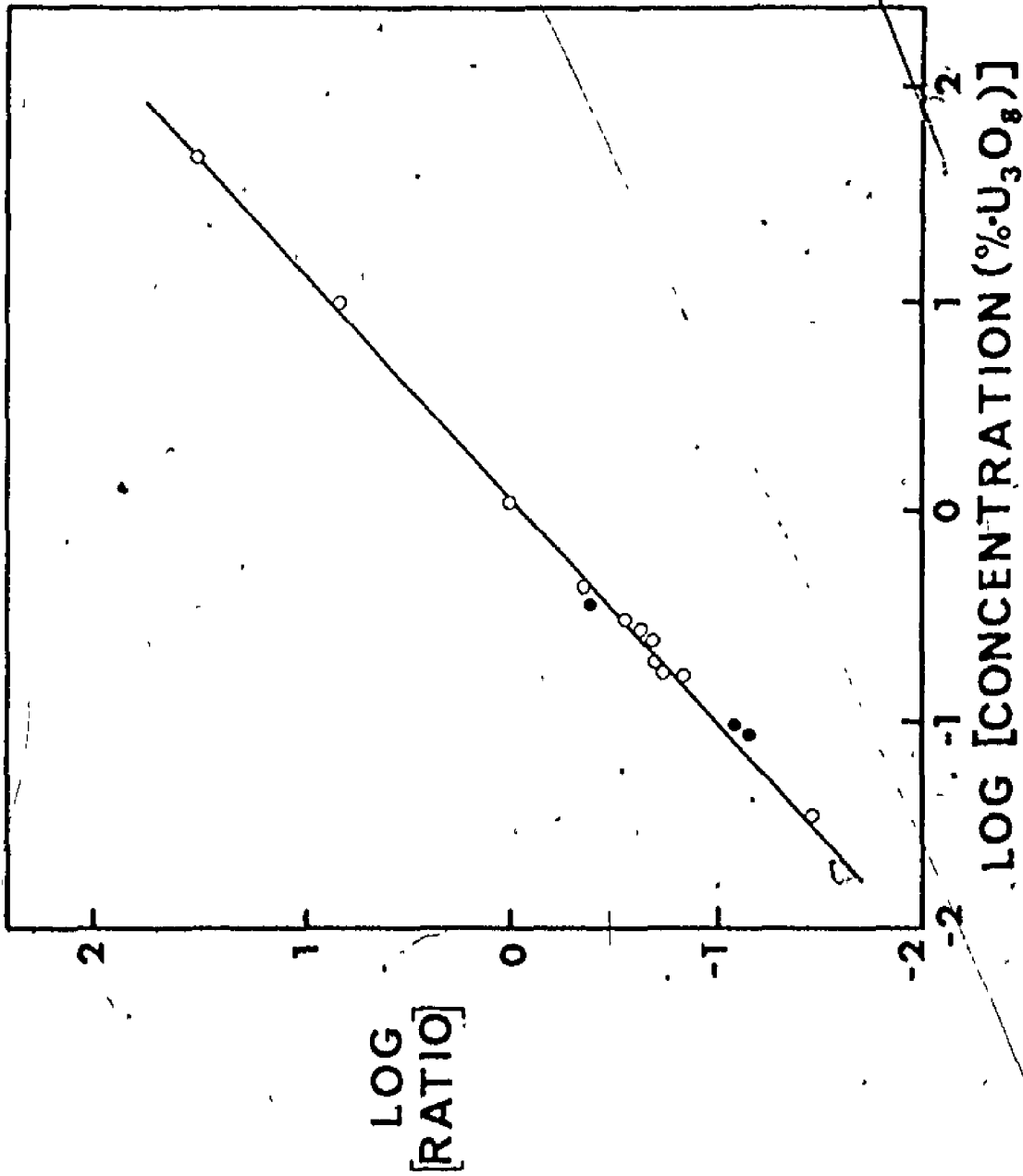


Fig. 41. Variation of U L α to Mo K α Compton intensity ratio with uranium concentration

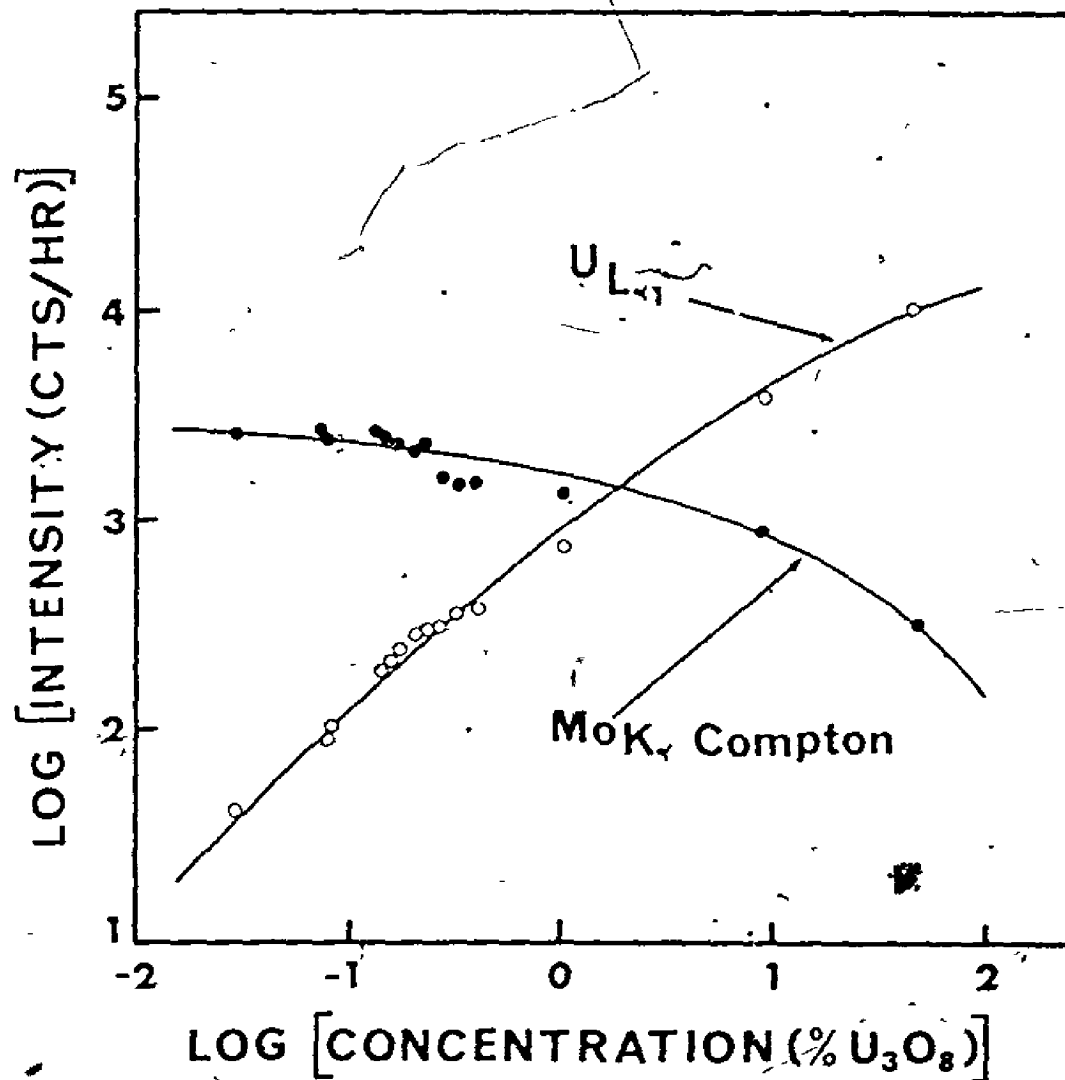


Fig. 42. Variation of U L_α and Mo K_α Compton peak intensities with uranium concentration

Table 41

Net peak intensities evaluated from
experimentally measured intensities.

Concentration (%U ₃ O ₈)	I U Lβ ₂ ±S _N (%)	I MoKα Compton ±S _N (%)	R ±S _N (%)
0.036	11 ± 5.95	1428 ± 2.67	0.032 ± 6.52
0.102	21 ± 7.68	1493 ± 2.62	0.058 ± 8.11
0.108	22 ± 10.3	1416 ± 2.70	0.066 ± 10.6
0.194	51 ± 4.10	1447 ± 2.72	0.147 ± 4.92
0.204	59 ± 5.29	1410 ± 2.77	0.173 ± 5.97
0.211	59 ± 5.27	1383 ± 2.80	0.178 ± 5.97
0.248	62 ± 5.09	1362 ± 2.83	0.189 ± 5.82
0.302	76 ± 4.47	1408 ± 2.80	0.223 ± 5.27
0.352	86 ± 4.15	1275 ± 2.98	0.280 ± 5.11
0.490	108 ± 3.60	1175 ± 3.17	0.381 ± 4.80
0.531	130 ± 3.23	1207 ± 3.16	0.446 ± 4.52
1.21	272 ± 2.14	1163 ± 3.54	0.974 ± 4.14
9.95	1411 ± 1.26	778 ± 6.27	7.96 ± 6.40
50.1	3257 ± 0.97	424 ± 15.8	40.6 ± 15.8

tion 4.21. The relative intensities of the U L α and U L β_2 peaks can be found in tables of relative X-ray emission intensities. The value of ξ reported⁽⁶⁾, is 0.190 and is in close agreement with the value of 0.183 produced by the iteration procedure. Table 41 presents the calculated data shown in figures 41-42. The I U L β_2 and the net I Mo K α Compton are evaluated using these experimentally determined values of η and ξ . The magnitude of R is derived from equation 4.22.

The precision to which the U L α peak intensity can be determined is the limiting factor in establishing the minimum detectable limit. For all ores analyzed, the background under this peak was approximately 50 counts/hour. By applying the two sigma rule, the minimum detectable peak intensity is then 8 counts/hour giving a value of 0.006 for R. Substitution into equation 4.24 results in a minimum detectable limit of approximately 0.02% U₃O₈. The sensitivity of the apparatus as measured from the U L α fluorescent intensity is of the order of 0.004 counts/sec/%U₃O₈/mCi. Appendix E contains a detailed description of the computer programmes developed to analyze the L X-ray spectrum.

4.3.5. Comparison of fluorimetric and X-ray analyses

To evaluate the performance of this technique, an additional set of fourteen uranium ore samples of unknown concentration were analyzed both fluorimetrically and by using this procedure. The uranium concentrations varied over the narrow range of 0.1% to 0.4% U₃O₈. Accordingly, a close range calibration curve was prepared using only the nine lowermost points shown in figure 41. The linear best least squares slope and intercept were 0.816 and -0.010 respectively. The uranium concentration C was

Table 42

Comparison of X-ray and fluorimetric analyses data.

*

% U ₃ O ₈ (fluorimetric)	Ratio	% U ₃ O ₈ (X-ray)	Coefficient of Variation (X-ray)
0.118	0.089	0.121	±9.84
0.166	0.122	0.162	±8.14
0.199	0.159	0.207	±7.04
0.226	0.183	0.236	±6.59
0.261	0.188	0.243	±6.18
0.276	0.197	0.254	±6.32
0.290	0.227	0.290	±5.65
0.339	0.260	0.331	±5.41
0.341	0.268	0.341	±5.52
0.358	0.288	0.365	±5.23
0.392	0.314	0.397	±5.37
0.415	0.320	0.404	±5.12
0.425	0.320	0.404	±6.18*
0.463	0.347	0.438	±4.83

* Statistical error for duplicate determination only.

calculated from the X-ray spectra using the equation given by.

$$C (\%U_3O_8) = \frac{R + 0.010}{0.816} \dots \dots \dots 4.24$$

where R is the ratio evaluated by equation 4.22. The values of η and ξ used to determine R were calculated from all the data shown in table 40. Table 42 presents a comparison between the results obtained by X-ray spectrometric determination and the results as obtained by Eldorado Nuclear Ltd., Mining Division using a fluorimetric determination. For each of the fourteen samples analyzed, the difference between the fluorimetric and X-ray assays is less than $\pm 2S_N$ and 79% of the results are within $\pm 1S_N$.

4.3.6. Specimen precision analysis

Table 43 contains the data used to evaluate the specimen error for the L X-ray experiment. The average counting error for the set of 21 measurements was +4.44% while the standard dispersion about the mean, S_N , was $\pm 4.38\%$. As with the K X-ray experiment, the F ratio test was applied to determine if these dispersions were significantly different. The values of F_{tab} at the 95% and 99% confidence limit are 1.85 and 2.51 respectively. The magnitude of F_{cal} is less than these values at 1.03 and no source of error can be attributed to the presence of the specimen.

Similarly the data used to determine the error in loading the specimen onto the spectrometer is presented in table 44. $\overline{S_N}$ for the set of 21 measurements was +4.44% while the standard deviation of the measurements about a mean, S_N , was $\pm 5.01\%$. The value of F_{cal} at 1.27 is less than the tabulated values of 1.60 and 1.92 at confidence intervals of 95% and 99% respectively; hence no appreciable error is incurred by

Table 43

Precision data used to evaluate the L X-ray
experiment specimen error.

I U La (counts/hour)	S_N ±(%)	$(x_1 - \bar{x})$	$(x_1 - \bar{x})^2 \times 10^{-4}$
10480	4.44	-179	3.21
10540	4.44	-119	1.42
10320	4.54	-339	11.50
10600	4.45	-59	0.35
9980	4.57	-679	46.11
10340	4.50	-319	10.18
9880	4.62	-779	60.69
11340	4.26	+681	46.37
10920	4.36	+261	6.81
10340	4.39	+181	3.27
10840	4.40	+181	3.27
10860	4.36	+201	4.04
11200	4.36	+541	29.26
10820	4.40	+161	2.59
11580	4.25	+921	84.82
11200	4.31	+541	29.26
10100	4.66	-559	31.25
10560	4.42	-99	0.98
10900	4.41	+241	5.81
10520	4.44	-39	0.15
9920	4.66	-739	54.62
$\bar{x} = 10659$	$S_N = +4.38\%$	$S_N = +4.44$	$\Sigma = 435.96$

Table 44

Precision data used to evaluate the L X-ray
experiment specimen loading error.

I U L α (counts/hour)	S_N $\pm(\%)$	$(x_i - \bar{x})$	$(x_i - \bar{x})^2 \times 10^{-4}$
11000	4.33	+269	7.26
11880	4.19	+1150	132.14
11200	4.28	+470	22.05
11180	4.32	+450	20.21
10140	4.54	-590	34.87
10220	4.55	-510	26.06
10740	4.43	+10	0.00
9920	4.83	-810	65.69
11000	4.38	+270	7.26
10160	4.57	-570	32.54
10480	4.46	-250	6.27
11020	4.37	+290	8.38
10480	4.48	-250	6.27
10940	4.44	+210	4.39
10180	4.56	-550	30.30
10500	4.48	-230	5.31
11000	4.32	+270	7.26
9920	4.60	-810	65.69
10680	4.44	-50	0.25
11040	4.39	+310	9.58
11660	4.21	+930	86.40
$\bar{x} = 10730$	$S_0 = +5.01\%$	$S_N = +4.44\%$	$\Sigma = 578.21$

the specimen loading operation.

Since no errors are introduced by the specimen, and from appendix C, no errors originate within the X-ray spectrometer, the only significant error present in the L X-ray experiment is the statistical counting error. The error limits in the tables are defined as one standard deviation, $\pm 1 S_N(\%)$. The statistical counting error for R can conveniently be calculated by the following equation:

$$1 S_N(\%) = \frac{100\%}{n^{\frac{1}{2}}} \left\{ \left[\frac{\sqrt{(N_p + N_b) U L_{\alpha}}}{(N_p - N_b) U L_{\alpha}} \right]^2 + \left[\frac{\sqrt{(N_p + N_b) (Mo K_{\alpha} \text{ Compton} + U L_{\beta_2}) + \epsilon_n^2 (N_p - N_b) U L_{\alpha}}}{(N_p - N_b) (Mo K_{\alpha} \text{ Compton} - U L_{\beta_2}) - \epsilon_n^2 (N_p - N_b) U L_{\alpha}} \right]^2 \right\}^{\frac{1}{2}} \quad \dots \dots 4.25$$

where N_p and N_b are the total counts under a peak and the background counts under a peak respectively, and n is the number of observations.

4.4 M X-ray results and discussion

4.4.1. Energy calibration of the X-ray spectrometer

With the settings listed in table 10 the X-ray spectrometer was calibrated with the energy calibrator (pulse generator) from 2 to 7 keV. The linear correlation between energy and channel number can be seen in figure 43. Best least squares analysis gives

$$\text{Energy (keV)} = \frac{(\text{Channel Number} + 226.619)}{174.286} \quad \dots \dots 4.26$$

All conversions from channel number to photon energy were performed using this equation for the M X-ray experimental work.

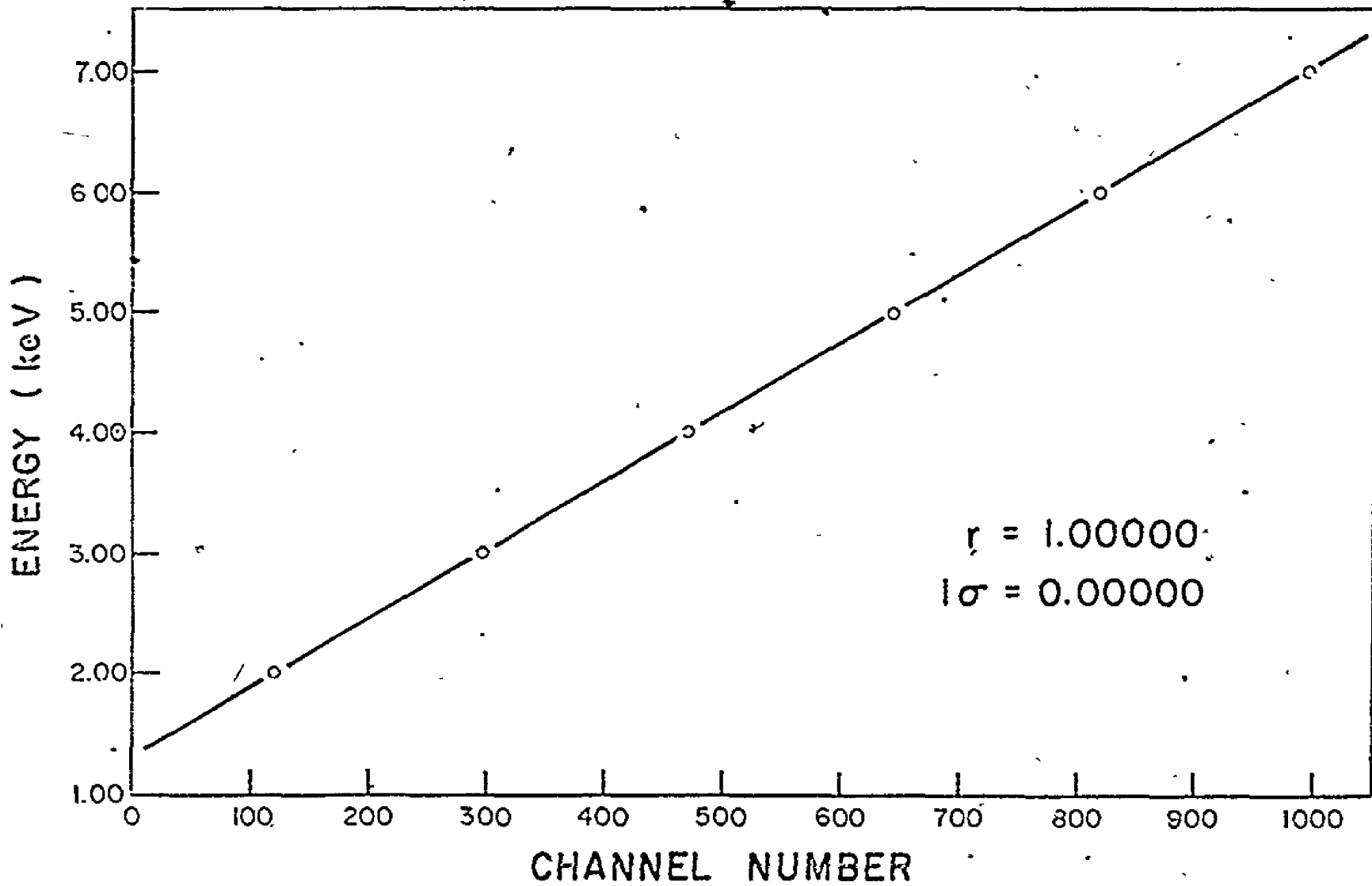


Fig. 43. Photon energy calibration curve for the M X-ray experiment

4.4 2 Matrix element effects

The K shell absorption edge energies of the principal matrix elements present in most geological specimens encompass the $U M_{\alpha, \beta}$ energy. In table 45 the total mass absorption coefficient, for each of the expected matrix elements, is calculated for energies of the $U M_{\alpha, \beta}$ fluorescent, ϵ_f , and $Mn K\alpha$ excitation, ϵ_e , radiations. The composition of the specimen is identical to the average uranium bearing granite used as an example in the K and L X-ray experiments. By comparison to tables 22 and 39 it is readily seen that minor changes in matrix composition will affect the observed intensity of the uranium M lines to a much greater extent than for the K and L lines. On account of this, uranium cannot be analyzed by M X-rays using thick specimens unless a reliable set of matrix element standards can be prepared. For thin specimens, these matrix standards are not required. Equation 2.14, the fundamental excitation equation for thin specimens can be simplified under fixed excitation conditions to give:

$$I_f \propto r_U m \dots \dots \dots 4.27$$

As noted previously, only analysis of thin samples of actinide chemical precipitate by M X-ray fluorescence is expected to offer a sensitivity advantage over analysis using L X-ray fluorescence. For this case, the uranium weight fraction in the precipitate remains a constant and the observed $U M_{\alpha, \beta}$ fluorescent intensity can be expressed simply as:

$$I_f \propto m \dots \dots \dots 4.28$$

Table 45

Calculation of mass absorption coefficients for an average uranium bearing granite.

Element	Weight fraction r_i	σ_{TOT} (barns/atoms)		Mass absorption coefficient (cm^2/g)		Elemental absorption (cm^2/g)	
		$\epsilon_f=3.2$ keV	$\epsilon_e=5.9$ keV	μ_f	μ_e	$\mu_f r_i$	$\mu_e r_i$
O	47.7%	4740	773	178	29.1	84.9	13.9
Si	33.2%	37800	6870	810	147	268.9	48.8
Al	7.9%	29200	5180	652	116	51.5	9.2
Fe	2.8%	42400	7730	457	83.3	12.8	2.3
Ca	1.6%	14400	42800	216	643	3.5	10.3
Na	2.9%	16000	2740	419	71.8	12.2	2.1
Mg	0.16%	21800	3800	540	94.1	0.9	0.2
K	3.4%	34800	20500	536	316	18.2	10.7
Ti	0.24%	21300	33800	268	425	0.6	1.0
U	1.0%	244000	248000	617	627	6.2	6.3

$$\begin{aligned} & \Sigma(\mu_f)_i r_i & \Sigma(\mu_e)_i r_i \\ & \text{matrix} & \text{matrix} \\ & = 453.5 & = 98.5 \end{aligned}$$

4.4.3. Optimum electrodeposition time determination

The data recorded to determine the optimum electrodeposition time are presented in table 46. The uranium $M_{\alpha, \beta}$ peak intensity, the potential required to pass 1 ampere and the electrolyte temperature and pH are listed for electrodeposition times ranging from 5 to 110 minutes.

Figure 44 shows the measured $I_{U M_{\alpha, \beta}}$ for each electrodeposition time. As can be seen in the figure, the shape of the curve is similar to that of a polarographic wave indicating that the electrodeposition is rate determined by a diffusion process or processes. Essentially no uranium is deposited until the electrolysis has been carried out for approximately 60 minutes. Most of the uranium is then rapidly deposited in the following short time interval of 10 minutes. The highest yield obtainable occurred for an electrolysis period of 100 minutes. All specimens were therefore prepared for the M X-ray experiment using this electrodeposition time.

As the electrodeposition progressed, the potential required to pass one ampere increased in a stepwise fashion with seemingly no relation to the rate at which uranium was deposited. As expected, the electrolyte temperature rose in accordance with the potential. With electrodeposition durations of more than 110 minutes, the electrolyte temperature could no longer be adequately controlled by adjusting the flow rate of cooling water around the cathode. The surface of the stainless steel planchet would begin to show evidence of corrosion after a 120 minute electrodeposition. This was enhanced by excessive temperatures and the ammonium chloride concentration.

A qualitative explanation for the electrodeposition of uranium

Table 46

Data recorded for optimum electrodeposition time determination.

Time (min.)	I U M _{α,β} (cts/180 sec)	Electrolyte Temperature (°C)	Potential (Volts)	Electrolyte pH @ 25°C
0.00	43	--	---	----
5.00	75	24	4.2	0.60
10.00	14	34	4.2	0.60
15.00	65	38	4.2	0.60
20.00	69	41	4.8	1.08
25.00	80	42	5.6	1.51
30.00	74	42	5.8	1.80
35.00	138	42	6.3	2.29
40.00	257	43	6.3	2.67
45.00	375	46	7.0	1.88
50.00	928	46	7.0	1.86
55.00	2249	46	7.4	1.64
60.00	5671	45	8.0	1.60
65.00	16869	46	8.6	1.60
70.00	17823	48	9.2	1.58
80.00	19220	50	10.5	1.60
90.00	20311	54	13.0	1.60
100.00	21422	60	13.2	1.59
110.00	21064	62	13.2	1.61

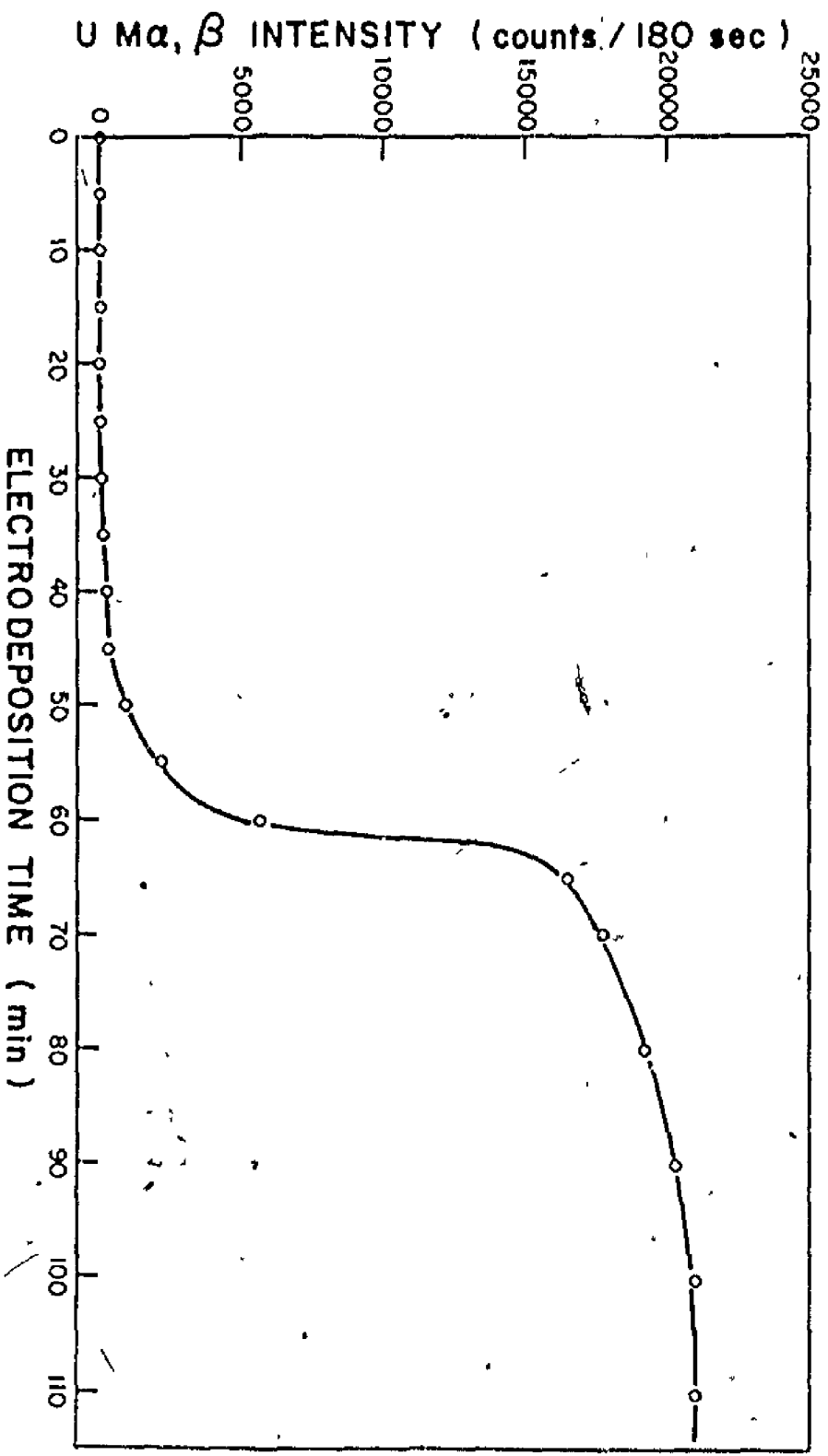


Fig. 64. Effect of electrodeposition time on the quantity of uranium deposited

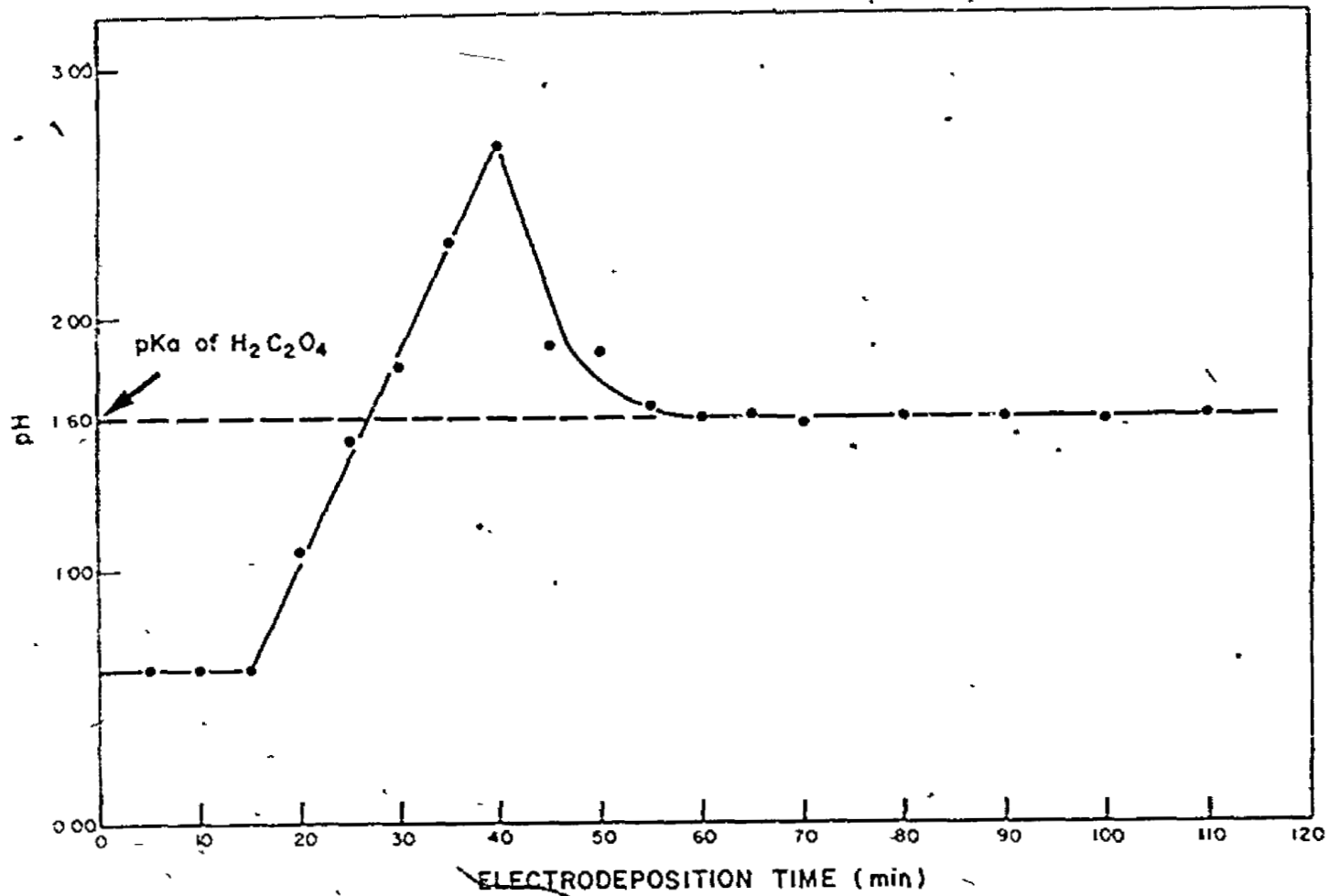


Fig. 45. Variation of electrolyte pH at 25° C with electrodeposition time

process can be deduced from figure 45. In this figure, the electrolyte pH as function of electrolysis time is shown. The pH initially remains constant at 0.60 for the first 15 minutes. During this period, very heavy frothing occurs. From 15 - 40 minutes, the pH climbs steadily to a maximum of 2.7. No electrodeposition of uranium occurs until roughly 60 minutes has elapsed and the pH has fallen to 1.60. This pH is maintained for the remainder of the electrodeposition.

The passage of an electric current across an electrolyte-electrode interface sets up a gradient between the electrode surface and the electrode, with diffusion of ions to and from the surface occurring within this gradient⁽⁶²⁾. If the electrolysis is performed using a strongly acidic electrolyte, the pH at the cathode surface must increase through the discharge of H^+ . Hydrogen ion must then be supplied by diffusion and eventually by the oxidation of water. If a weak acid is added to the electrolyte, H^+ can also be supplied by dissociation of this acid once the pH at the cathode approaches the pKa of the weak acid, in this case oxalic acid. At high current densities, such as employed in this procedure, most of the hydrogen ions from the strong acid are initially discharged at a rate faster than they can be replenished by oxidation of water or dissociation of oxalic acid. Hence the rapid initial rise in the electrolyte pH between 15 and 40 minutes of electrodeposition. As the deposition progresses, the $H_2C_2O_4$ begins to contribute H^+ by dissociation causing the bulk pH to fall. With H^+ supplied principally from the weak acid, the OH^- layer on the cathode becomes thick enough to hydrolyze and deposit any hydrolytic ions entering this layer. The best depositing rate then takes place at a pH corresponding to the

pKa value of the weak acid as is observed in figure 45.

4.4.4. Data and data analysis

By adding appropriate aliquots of the standard uranium working solutions to the electrolyte as outlined in section 3.5.2, a series of specimens were prepared over a range of thicknesses. Figure 46 shows the M X-ray spectrum obtained from electrodepositing 1.81×10^{-7} moles of UO_2^{2+} . The Mn $K\alpha$ and $K\beta$ peaks result from Rayleigh scattering of excitation radiation from the ^{55}Fe source. The chromium, present in the stainless steel planchets, produces the Cr $K\alpha$ and $K\beta$ fluorescence. The occurrence and position of the La $L\alpha$ and $L\beta$ and the U $M\alpha, \beta$ peaks are clearly evident. The data observed from the series of specimens are presented in table 47. Since the specimen areas are all identical, the sample thickness, m , is proportional to the moles of UO_2^{2+} deposited. The intensities of the uranium $M\alpha, \beta$ and lanthanum $L\alpha$ peaks versus moles of UO_2^{2+} are shown in figure 47. The U $M\alpha, \beta$ curve is linear up to approximately 5×10^{-7} moles of UO_2^{2+} . At this point, the infinitely thin character of the specimen begins to be lost and the slope tends toward zero as infinite thickness approaches. It was found that if La^{3+} was added to the electrolyte before electrodeposition, the intensity of the La $L\alpha$ peak could be employed as an internal standard to correct for the increasing thickness effects.

The material deposited onto the planchet primarily consists of uranium and lanthanum. The quantity of lanthanum remains constant at approximately 5×10^{-6} moles. However, the uranium M shells are in a position to strongly absorb the La $L\alpha$ radiation. Therefore, as the

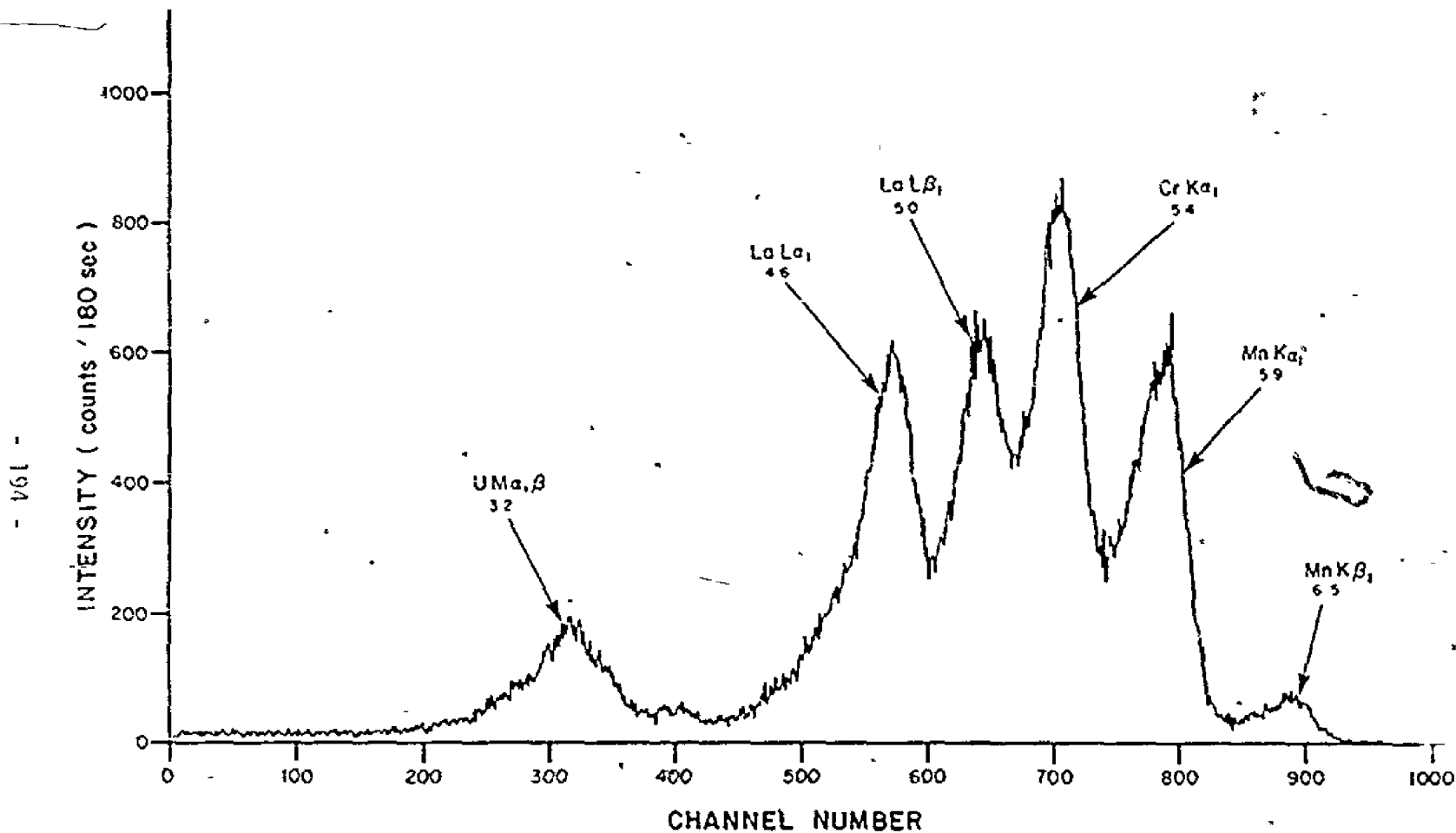


Fig. 46. Spectrum as obtained with the N X-ray apparatus from 1.81×10^{-7} moles UO_2^{2+} electrodeposited on a stainless steel planchet

Table 47

Intensity data measured from M X-ray spectra taken of thin electrodeposited uranium specimens.

Thickness, m (moles UO_2^{2+})	I U $M_{\alpha,\beta}$ (cts/180 sec) $\pm S_N(\%)$	I La L_{α} (cts/180 sec) $\pm S_N(\%)$	ζ I U $M_{\alpha,\beta}$ (cts/180 sec) $\pm S_N(\%)$	I (La L_{α} + ζ U $M_{\alpha,\beta}$) (cts/180 sec) $\pm S_N(\%)$	R_M $\pm S_T(\%)$
9.04×10^{-8}	1744 ± 3.15	50692 ± 0.26	153 ± 3.15	50845 ± 0.26	0.034 ± 3.75
1.81×10^{-7}	4610 ± 1.43	56265 ± 0.25	403 ± 1.43	56668 ± 0.25	0.081 ± 2.03
2.71×10^{-7}	6870 ± 1.04	51414 ± 0.26	601 ± 1.04	52015 ± 0.26	0.132 ± 2.28
3.62×10^{-7}	9275 ± 0.84	51226 ± 0.26	812 ± 0.84	52038 ± 0.26	0.178 ± 2.19
4.52×10^{-7}	11341 ± 0.72	49091 ± 0.26	992 ± 0.72	50083 ± 0.26	0.226 ± 2.15
9.04×10^{-7}	20748 ± 0.48	38850 ± 0.30	1815 ± 0.48	40665 ± 0.30	0.510 ± 2.09
1.81×10^{-6}	32244 ± 0.32	29005 ± 0.30	2821 ± 0.32	31826 ± 0.27	1.013 ± 2.05
2.71×10^{-6}	36938 ± 0.33	22121 ± 0.31	3232 ± 0.33	25353 ± 0.36	1.457 ± 2.07
3.62×10^{-6}	36520 ± 0.33	15336 ± 0.50	3196 ± 0.33	18532 ± 0.42	1.971 ± 2.08

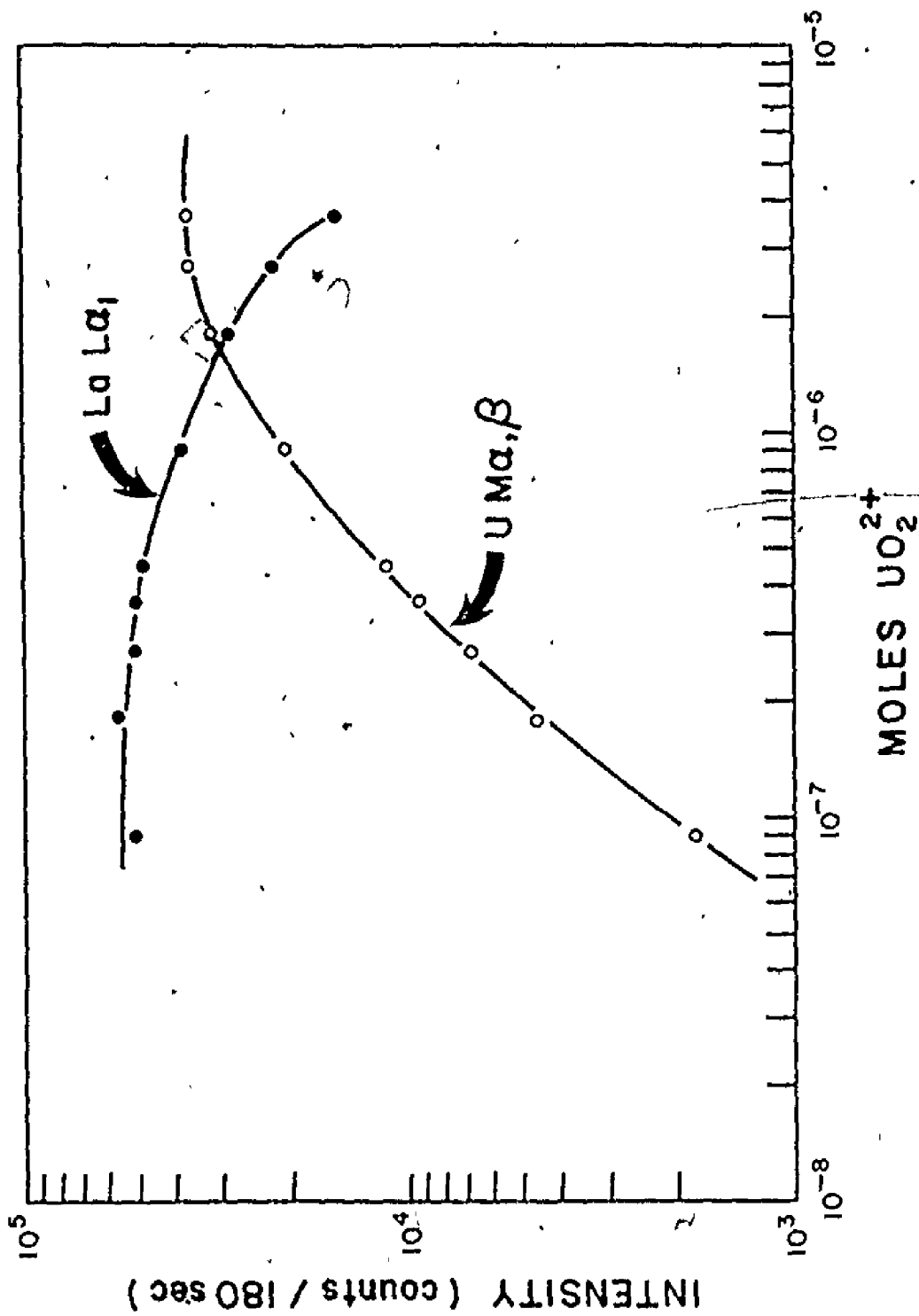


Fig. 47. The observed intensities of the uranium α, β and the lanthanum α_1 peaks versus moles of UO_2^{2+} electrodeposit

amount of uranium present increases, the observed lanthanum intensity decreases as is clearly seen in figure 47. Unfortunately, the effect does not quantitatively compensate for increases in uranium thickness. This is due to the fact that uranium absorbs the characteristic La L α fluorescence more readily than it self-absorbs its own M α , β fluorescence. The U M α , β at 3.5 keV is at an ideal energy to absorb the La L α radiation at 4.6 keV. The principal mechanism for attenuation of U M α , β intensity is via self-absorption with the U N α , β at 0.38 keV. Because the La L α fluorescence is more sensitive to thickness effects than U M α , β fluorescence, the net result of using lanthanum as an internal standard is that it tends to slightly over compensate. This can be overcome, at least on a limited scale, by introducing a correction coefficient, ζ , to increase the observed La L α intensity such that the increment is proportional to the observed U M α , β intensity, i.e.

$$R_M = \frac{I_{U M_{\alpha,\beta}}}{(I_{La L_{\alpha}} + \zeta I_{U M_{\alpha,\beta}})} \dots \dots \dots 4.29$$

The value of ζ giving the best linear calibration curve according to a linear least squares criterion was found by minimizing the following function:

$$M(\zeta, m', b) = \sum_1^n [R_{M_i}(\zeta) - m' m_i - b]^2 \dots \dots \dots 4.30$$

where R_{M_i} is the ratio of the i^{th} sample calculated according to equation 4.29, n is the number of experimental points, m_i is the thickness of the i^{th} sample as expressed in moles of UO_2^{2+} , m' and b are the slope and

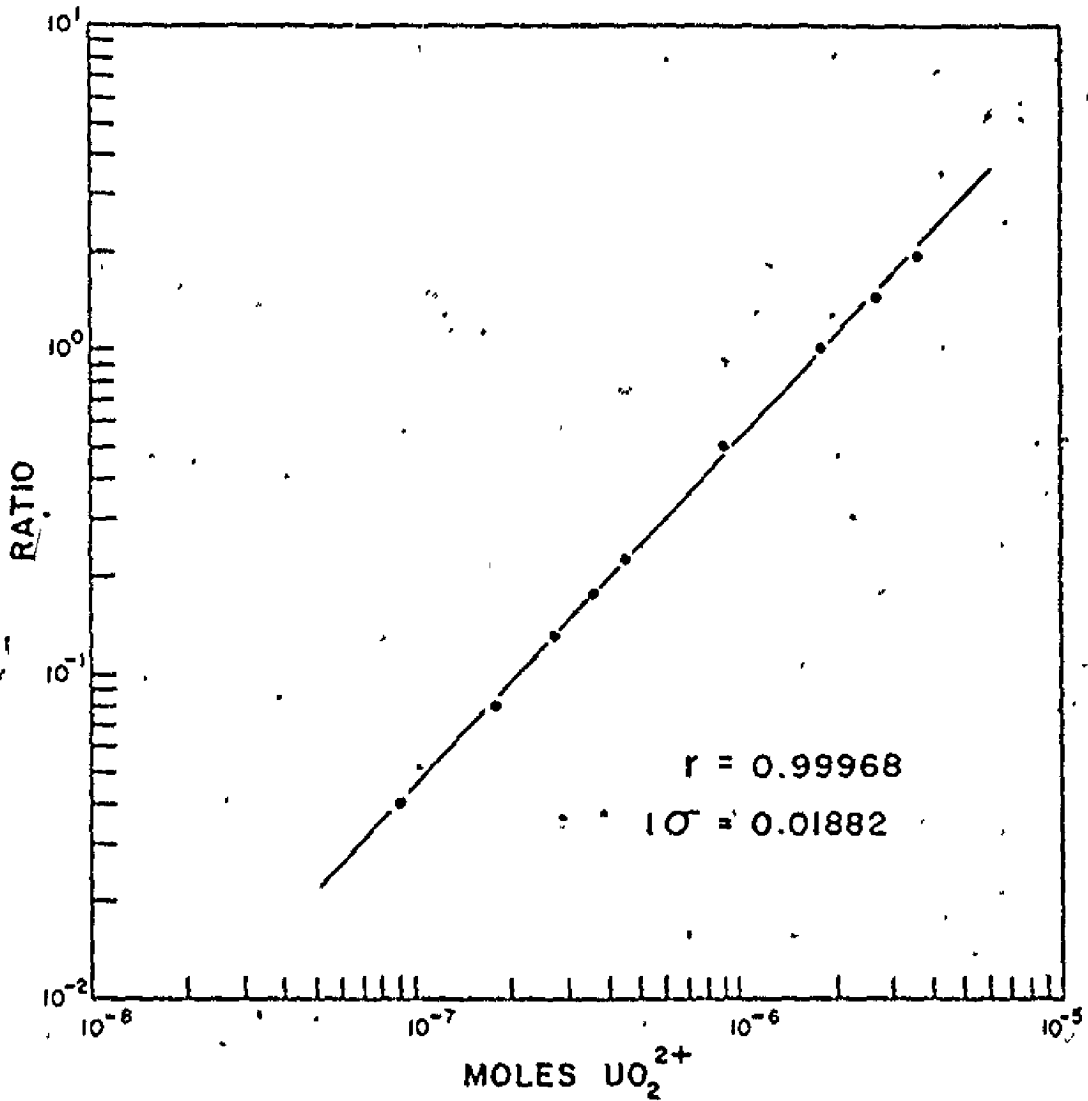


Fig. 46. Variation of uranium $L_{\alpha,\beta}$ to lanthanum L_{α} corrected intensity ratio with moles of UO_2^{2+} electrodeposited

intercept, respectively of the resulting calibration curve. The function was minimized with the same subroutine as employed in the L X-ray experiment and listed in appendix H. The value generated for z was 0.0875. Table 47 also details the calculation for this correction of I La $L\alpha$. The linear correlation between R_M and specimen thickness (moles UO_2^{2+}) is shown in figure 48. The slope and intercept are 5.48×10^5 and -0.012 respectively. Suitably thin specimens can therefore be quantitatively prepared using the electrodeposition technique.

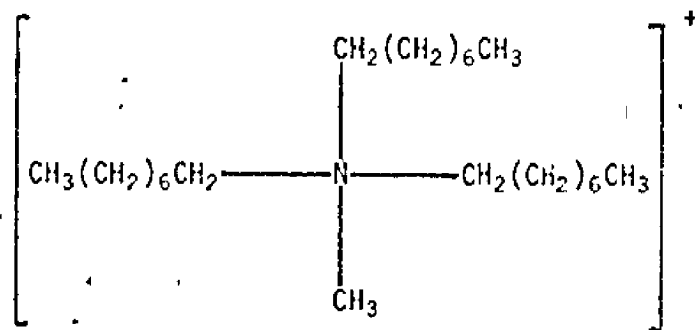
4.4.5 Uranium separation procedure

To analyze the uranium content of low grade ores or soils requires a uranium separation. Electrodeposition procedures are generally very sensitive to interfering elements present in the electrolyte. As such, the separation technique used was adapted from Sill⁽⁵⁷⁾. This author has developed several techniques for separating actinide elements from low grade ores, mill wastes and soils. Sufficient purity is achieved to allow quantitative preparation of thin specimens by electrodeposition techniques followed by isotope analysis using α -spectroscopy. In a natural uranium ore there are a large number of possible interfering radionuclides which must be removed prior to alpha counting of uranium isotope activity. However, if the specimen is analyzed by X-rays and only the uranium content desired, the separation scheme can be considerably simplified since prolific α -emitting daughters, such as ^{210}Po , do not have to be removed.

The first step in the uranium separation procedure is the four acid dissolution of the ore. The primary function of this step is to

insure that all of the uranium originally in the solid sample is brought into solution. The procedure as written is satisfactory for the purpose as long as the sample size remains reasonably small, approximately 1 g or less. For greater sample masses, up to 10 g, a KF fusion would be preferred.

A phase transfer catalyst, known commercially as Aliquat-336 (methyl tricaprylyl ammonium chloride) was used to separate uranium after the dissolution step. The quaternary ammonium cation has the following structure:



In order for uranium to be associated with this cation in the organic phase, the UO_2^{2+} must be present as a complex with a negative charge. The uranyl ion in aqueous solution forms simple complexes of the type $[\text{UO}_2^{2+}\text{X}^n]^{(2-n)+}$ where X is an anion present in solution. In strong nitric or hydrochloric acid solutions, the uranyl ion is complexed⁽³²⁾ as $[\text{UO}_2(\text{NO}_3)_3]^-$ or $[\text{UO}_2\text{Cl}_3]^-$ and tends to remain strongly associated with the phase transfer catalyst in the organic phase. The other elements are not and remain in the discarded aqueous layer. In the final step, uranium is transferred back to the aqueous phase by the addition of ClO_4^- which immediately releases free UO_2^{2+} containing no complexes with the anions present⁽⁸²⁾. In this procedure, the UO_2^{2+} solution is then taken

to dryness and ashed to remove any organic material prior to the electro-deposition step as previously described.

4.4.6. Uranium analysis of low grade ores

Table 48 contains the initial data from specimens prepared from several low grade ores originally from Elliot Lake, Rabbit Lake and Beaverlodge Lake ore bodies. The quantities of material weighed for analysis were selected so that the expected uranium thickness after electrodeposition would fall within the range of the calibration curve as shown in figure 47.

The results of applying the entire analytical procedure are also presented in table 48. No difference could be discerned during the electrolysis or in the appearance of the final electrodeposited specimen between samples prepared from uranium after chemical separation from the ores and those prepared from aliquots taken from the pure uranium working solutions. The ratio, R_M , is calculated according to equation 4.29 and is shown as a function of thickness in figure 49. Best least squares analysis of the plotted data gives the following expression relating specimen thickness to observed peak intensities:

$$m \text{ (moles } \text{UO}_2^{2+}) = \frac{R_M + 0.0043}{3.69 \times 10^5} \dots\dots\dots 4.31$$

The difference in slope between this calibration curve and the one prepared from pure uranium solutions indicates that approximately 30% of the uranium originally present in the ore was lost during the separation procedure. In this step, the aqueous phase is equilibrated with the

Table 48

Data from U M X-ray analysis of several low grade ores.

U_3O_8 (%)	Location	Weight (g)	m (moles UO_2^{2+})	I U $M_{\alpha,\beta}$ (cts/180 sec) $\pm S_N$ (%)	I La L_{α} (cts/180 sec) $\pm S_N$ (%)	R_M $\pm S_T$ (%)
0.0153	Elliot Lake	0.3175	1.80×10^{-7}	3358 ± 1.08	53457 ± 0.25	0.0625 ± 2.30
0.0375	Elliot Lake	0.3278	4.55×10^{-7}	8336 ± 0.69	48463 ± 0.27	0.169 ± 2.14
0.0665	Elliot Lake	0.3173	7.81×10^{-7}	13160 ± 0.55	45208 ± 0.28	0.284 ± 2.10
0.0496	Rabbit Lake	0.2712	4.98×10^{-7}	8670 ± 0.69	48625 ± 0.27	0.176 ± 2.03
0.0200	Rabbit Lake	0.3238	2.40×10^{-7}	3878 ± 1.00	51294 ± 0.26	0.0751 ± 2.26
0.0730	Rabbit Lake	0.3308	8.94×10^{-7}	14783 ± 0.53	43987 ± 0.28	0.326 ± 2.10
0.108	Beaverlodge Lake	0.3826	1.53×10^{-6}	22716 ± 0.42	38672 ± 0.30	0.559 ± 2.08
0.017	Beaverlodge Lake	0.3187	2.01×10^{-7}	3793 ± 1.03	49788 ± 0.26	0.0757 ± 2.27

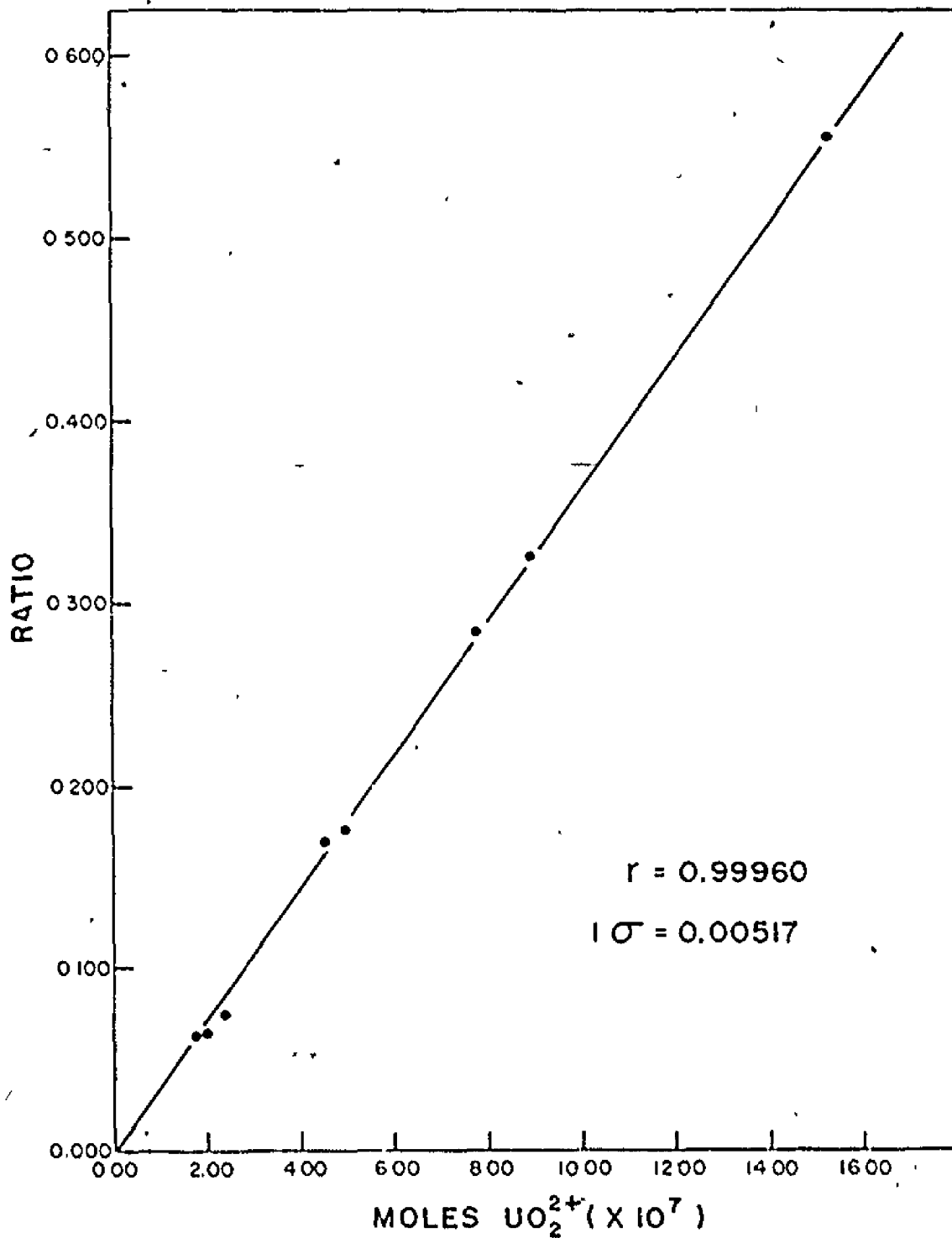


Fig. 49. Calibration curve prepared for analyzing low grade uranium ores or soils with the M X-ray apparatus

organic layer for a total of 11 times. A mean extraction efficiency of slightly more than 97% for each equilibration would be sufficient to account for this loss. As in the L X-ray case, the limiting factor in determining the minimum detectable quantity is the precision to which the U $M_{\alpha,\beta}$ peak can be measured. The background measured under the U $M_{\alpha,\beta}$ peak averaged around 1800 counts/180 sec. The smallest significant value of R_M detectable using the two sigma rule is then 0.001. Substitution into equation 4.31 gives a minimum detectable limit of 1×10^{-8} moles of UO_2^{2+} or 0.0001% U_3O_8 for a 1 g ore sample. The sensitivity as measured from the U $M_{\alpha,\beta}$ intensity is 300 counts/sec/% U_3O_8 /mCi again assuming 1 g samples. The computer programmes written to analyze the M X-ray spectra are listed in appendix F.

4.4.7. Specimen precision determination

The data accumulated to measure the specimen error is shown in table 49. As in the previous sections, the instrumental errors for the M X-ray experiment were shown to be insignificant in appendix C. The only source of error within the X-ray spectrometer is the statistical counting error. The dispersion, S_4 , for the data in this table is compared to the average counting error, \overline{S}_N , in table 53. From the F ratio test, no significant difference exists between these two distributions and the error attributed to the specimen itself is negligible.

Table 50 contains the intensity data recorded to evaluate the specimen loading error. This error is determined by taking the difference in variance between this dispersion, S_4 , and the previous dispersion, S_4 . From table 53, these two distributions are significantly different

Table 49

Precision data used to determine the specimen error for the M X-ray experiment.

I U $M\alpha, \beta$ (counts/180 sec)	S_N $\pm(\%)$	$(x_i - \bar{x})$	$(x_i - \bar{x})^2 \times 10^{-4}$
11764	1.07	+120	1.21
11747	1.08	+ 93	0.87
11512	1.09	-142	2.01
11788	1.08	+134	1.80
11504	1.09	-150	2.25
11791	1.07	+137	1.87
11440	1.10	-214	4.62
11573	1.09	- 81	0.66
11549	1.09	-105	1.11
11680	1.08	+ 26	0.07
11458	1.10	-196	3.86
11791	1.07	+137	1.87
11749	1.08	+ 95	0.90
11810	1.07	+156	2.44

$$\bar{x} = 11651$$

$$\lambda = 25.54$$

$$\bar{S}_N = \pm 1.08\%$$

$$S_{\lambda} = \pm 1.20\%$$

Table 50

Data accumulated to evaluate the specimen loading error for the M X-ray experiment.

I U M α , β (counts/180 sec)	$\frac{S}{N}$ +(%)	$-(\bar{x} - x_1)$	$-(\bar{x} - x_1)^2 \times 10^{-14}$
12138	1.05	+501	25.10
11827	1.07	+190	3.61
12027	1.05	+390	15.20
11544	1.09	- 93	0.86
11603	1.09	- 34	0.12
11682	1.08	+ 45	0.20
11692	1.08	+ 55	0.30
11664	1.08	+ 27	0.07
11456	1.10	-181	3.28
11822	1.07	+185	3.42
11370	1.10	-267	7.13
11118	1.11	-519	26.94
11430	1.09	-207	4.28
11538	1.10	- 99	0.98

$$\bar{x} = 11637$$

$$\bar{S}_N = +1.08\%$$

$$\Sigma = 91.49$$

$$S_5 = +2.28\%$$

and hence a real source of error can be attributed to the loading operation. The variance is evaluated by equation 4.3 to be

$$\begin{aligned} S_{SL}^2 &= |S_5^2 - S_{11}^2| \\ &= (2.28)^2 - (1.08)^2 \\ &= 4.03 \end{aligned}$$

or $S_{SL} = \pm 2.01\%$. Since the M X-ray source holder was precisely machined to accommodate the stainless steel planchets, it is unlikely that the loading variance is caused by inconsistent positioning of the specimen. The most probable cause is that the uranium is not uniformly electro-deposited over the entire area of the planchet and also the ^{59}Fe activity is not evenly distributed around the annular source ring so that re-loading the specimen at different orientations results in a change of geometrical conditions producing the observed variance.

In addition to providing a means to compensate for thickness effects in the electrodeposited specimens, the use of lanthanum in the electrolyte also markedly improved the precision of specimen preparation. As stated in the M X-ray experimental section, the specimen preparation variance for the entire procedure was measured with and without the presence of the La^{3+} in the electrodeposition cell. Data used to evaluate S_{Sp} with La^{3+} are presented in table 51 and without La^{3+} in table 52. Their dispersions, S_6 and S_7 , were compared to S_5 using the F ratio test at 9 and 13 degrees of freedom respectively.

From table 53, the variances, S_5^2 and S_6^2 , are not significantly different and no appreciable error can be calculated for specimen prepara-

Table 51

Data recorded to determine the specimen preparation error using La^{3+} for the M X-ray experiment

I U $\text{M}\alpha, \beta$ (counts/180 sec)	S_N $\pm(\%)$	$(\bar{x} - x_j)$	$(\bar{x} - x_j)^2 \times 10^{-4}$
11883	1.09	+ 37	0.14
12452	1.09	-531	28.23
11404	1.10	+516	26.70
11994	1.08	- 73	0.54
11992	1.09	- 71	0.51
11442	1.10	+478	22.23
12541	1.04	-620	38.48
11826	1.06	+ 94	0.90
12114	1.07	-193	3.74
11559	1.10	+361	13.08

$$\bar{x} = 11920$$

$$\bar{S}_N = \pm 1.08\%$$

$$\Sigma = 135.22$$

$$S_6 = \pm 3.25\%$$

Table 52

Data recorded to determine the specimen preparation error without La^{3+} for the M X-ray experiment.

I U $\text{M}\alpha, \beta$ (counts/180 sec)	S_N ±(%)	$(\bar{x} - x_1)$	$(\bar{x} - x_1)^2 \times 10^{-4}$
8887	1.27	+3156	996.00
11505	1.09	+ 538	28.96
11461	1.10	+ 582	33.88
11725	1.09	+ 318	10.12
12586	1.03	- 542	29.47
15507	0.92	-3463	1199.90
10919	1.13	+1124	126.36
14202	0.97	-2158	466.61
12053	1.06	- 9	0.00
11586	1.09	+ 457	20.89

$$\bar{x} = 12043$$

$$S_N = \pm 1.08\%$$

$$\Sigma = 2911.7$$

$$S_7 = +14.94\%$$

Table 53

Application of the F ratio test for equality of variance resulting
 from specimen errors within the M X-ray experiment.

Dispersion Measured	Number of Determinations	Coefficient of Variation (%)	Average Relative Counting Error (%)	Dispersion Compared	F _{cal}	F _{tab @95%}	F _{tab @99%}
S ₄	14	± 1.20	±1.08	S _N	1.23	2.21	3.16
S ₅	14	± 2.28	±1.08	S ₄	4.46	2.69	4.16
S ₆	10	± 3.25	±1.08	S ₅	2.03	2.72	4.19
S ₇	10	±14.94	±1.08	S ₅	42.9	2.72	4.19

tion with La^{3+} . In contrast, the magnitude of the specimen preparation error without La^{3+} is:

$$S_{SP}^2 = |S_7^2 - S_5^2|$$

$$= 218.0$$

or S_{SP} (without La^{3+}) = 14.8%

The total specimen error is then found by summing all of the specimen error variances, i.e.

$$S_S^2 = S_{SS}^2 + S_{SL}^2 + S_{SP}^2$$

$$= (0.00)^2 + (2.01)^2 + (0.00)^2$$

or $S_S = \pm 2.01\%$

For the data from the M X-ray experiment, as presented in tables 47 and 48, two precision limits are indicated. (i) for the measured or calculated peak intensities, only the statistical counting error experienced with the measurements is listed, and (ii) the precision limits for R_M are the total precisions. The statistical counting error for R_M can be evaluated from:

$$S_N(\%) = \pm \frac{100\%}{n^2} \left\{ \left[\frac{\sqrt{(N_p + N_b) U M_{\alpha, \beta}}}{(N_p - N_b) U M_{\alpha, \beta}} \right]^2 + \left[\frac{\sqrt{(N_p + N_b) \text{La } L_{\alpha} + (N_p + N_b) U M_{\alpha, \beta}}}{(N_p - N_b) \text{La } L_{\alpha} + (N_p - N_b) U M_{\alpha, \beta}} \right]^2 \right\}^{1/2} \quad 4.32$$

and the total precisions given by:

$$S_T(\%) = \pm [S_S^2 + S_N^2]^{1/2}$$

4.5 γ -spectroscopy results and discussion

4.5.1 Energy calibration of the γ -ray spectrometer

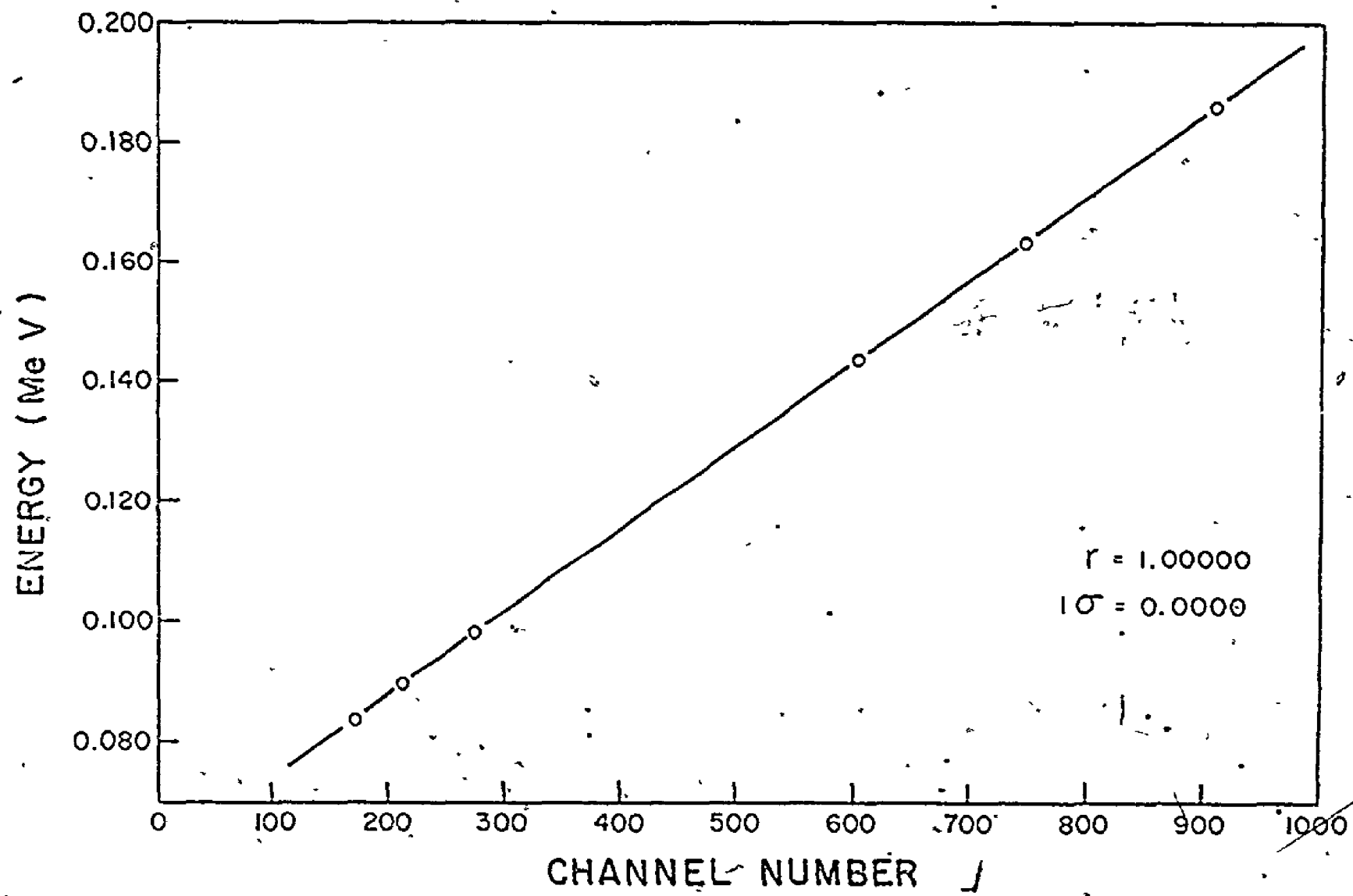


Fig. 50. Photon energy calibration curve for the γ -spectroscopy experiment

Using the reference radioisotope sources, table 11, and the instrumental settings listed in table 12, the operating energy range of the spectrometer conveniently observes the major gamma activities resulting from both ^{235}U and ^{238}U . The linear correlation between channel number and energy is shown in figure 50. Linear best least squares analysis gives the following relation:

$$\text{Energy (MeV)} = \frac{(\text{Channel Number} + 596.670)}{7283.30} \quad \dots \quad 4.33$$

All conversions from channel number to energy (MeV) in this section were performed using equation 4.33.

4.5.2. Spectral unfolding using Cauchy functions

An examination of the spectral region neighbouring the ^{231}Th doublet indicated that there were a possible eight photopeaks that required unfolding. The sources of these interferences are itemized in table 54.

(Literature values for energies and abundances were taken from references (33) and (12) for γ -ray and X-ray photopeaks, respectively.) Of these, the ^{231}Th γ -ray at 0.0899 MeV superimposes itself on the Th $K_{\alpha 2}$ X-ray of nearly the same energy so that their sum was treated as a single peak. Another ^{231}Th photopeak at 0.0955 MeV is listed but was judged to be too weak and too distant from the ^{231}Th doublet to contribute significantly. The minimization function was therefore set to fit a total of six Cauchy functions to the observed spectrum. The background plus the function parameters required nineteen iteration arguments. Standards ranging from 0.027% to 24.29% ^{235}U were unfolded by this technique. Generally, conver-

Table 54

Spectral interference encountered in
measuring the ^{234}Th doublet intensity.

Photopeak	Energy (MeV)	Abundance	Half-Life	Decay Mode
^{231}Th	0.0899	1.1×10^{-2}	25.52 hours	β^-
Th $K\alpha_2$	0.089953	0.60 [†]	-	-
^{234}Th	0.0923	$4.7 \times 10^{-1*}$	24.10 days	β^-
^{234}Th	0.0928	$5.3 \times 10^{-1*}$	24.10 days	β^-
Th $K\alpha_1$	0.093350	1.00 [†]	-	-
U $K\alpha_2$	0.094665	0.61 [†]	-	-
^{231}Th	0.0955	4.9×10^{-3}	25.52 hours	β^-
U $K\alpha_1$	0.098439	1.00 [†]	-	-

[†] Relative to $K\alpha_1$ peak intensity.

* Relative to total 0.0925 MeV ^{234}Th doublet intensity.

gence was difficult, time consuming and expensive. It was found that initially the function had to be constrained to fit only the larger peaks first. With this completed, the parameters of the smaller peaks were allowed to be iterated upon. Table 55 details the convergent values for peak energy, parameter P_{3j-1} from equation 3.10, and it is evident that the programme has correctly located all the constituent peaks for the set of standards with excellent accuracy. Also listed are several references reporting the energies of the ^{234}Th doublet. There is appreciable disagreement among the earlier results but it is seen that these results agree closely with the most recent work of Sampson⁽⁷¹⁾. Peak height ratios, parameter P_{3j-2} from equation 3.10, were reasonably stable in view of the fact that the interfering peaks' intensities vary by a factor greater than 1000 relative to the ^{234}Th doublet intensity. Sampson⁽⁷¹⁾ and Coles, Meadows and Lindeken⁽⁶⁴⁾ both have suggested that the $\text{Th } K\alpha_1$ intensity can be estimated by measuring the $\text{Th } K\alpha_2$ intensity since the $\text{Th } K\alpha_2/\text{Th } K\alpha_1$ intensity ratio is normally 0.60⁽¹²⁾. This work indicates that this would lead to negative errors in the ^{234}Th peak intensity because the contribution of the $^{231}\text{Th } \gamma$ -ray to the $\text{Th } K\alpha_2$ X-ray is significant. The $(^{231}\text{Th} + \text{Th } K\alpha_2)/\text{Th } K\alpha_1$ peak intensity ratios remained constant at 0.96. A literature value of this ratio cannot be calculated because the abundance of $K\alpha$ Th X-rays emitted from ^{235}U decay remains unknown. Table 56 lists the relative peak heights of the two component $^{234}\text{Th } \gamma$ -rays from the same set of standards and their values are in satisfactory accord with those found in the literature.

In order to save computer time and expense, the number of iteration parameters was reduced from nineteen to ten by fixing the peak locations

Table 55
Unfolded Peak Energies

Photopeak	- Peak Energy (Parameter P_{3j-1}) For Various Enriched U Standards (MeV)						Average Energy (MeV)	Literature Energy (MeV)	
	0.027%	5.59%	10.25%	15.39%	20.17%	24.29%			
$^{231}\text{Th} + \text{Th } K\alpha_2$	-	0.089912	0.089906	0.089920	0.089942	0.089930	0.089922	0.0899(33)	± 0.00005
$^{234}\text{Th} (0.0923)$	0.092447	0.092311	0.092317	0.092343	0.092384	0.092410	0.092369	0.09308(84)	
								0.09226(85)	
								0.0923(33)	± 0.0006
								0.092367(71)	± 0.000005
								0.09247(70)	± 0.00008
$^{234}\text{Th} (0.0928)$	0.092944	0.092783	0.092791	0.092800	0.092833	0.092853	0.092834	0.09352(84)	
								0.09269(85)	
								0.0928(33)	± 0.0006
								0.092792(71)	± 0.000005
								0.09282(70)	± 0.00008
$\text{Th } K\alpha_1$	-	0.093272	0.093313	0.093319	0.093343	0.093353	0.093320	0.093350(12)	± 0.000003
$\text{U } K\alpha_2$	0.094388	0.094639	0.094614	0.094614	0.094636	0.094644	0.094673	0.094665(12)	± 0.000004
$\text{U } K\alpha_1$	0.093570	0.098424	0.098393	0.098403	0.098414	0.098408	0.098435	0.098439(12)	± 0.000003

Table 56
Unfolded Relative Peak Heights

Photopeak	Relative Intensities (Calculated From Parameter P_{3j-2})						Average Relative Intensity ¹	Literature Intensity
	For Various Enriched ^{235}U Standards							
	0.027%	5.59%	10.25%	5.39%	20.17%	24.29%		
^{234}Th (0.0923)	46.2%	49.7%	48.5%	47.6%	48.5%	48.5%	48.2%	47% ⁽³³⁾ 50.3% ⁽⁷¹⁾ ± 0.7%
^{232}Th (0.0928)	53.7%	50.3%	51.5%	52.4%	51.5%	51.5%	51.8%	53% ⁽³³⁾ 49.7% ⁽⁷¹⁾ ± 0.7%

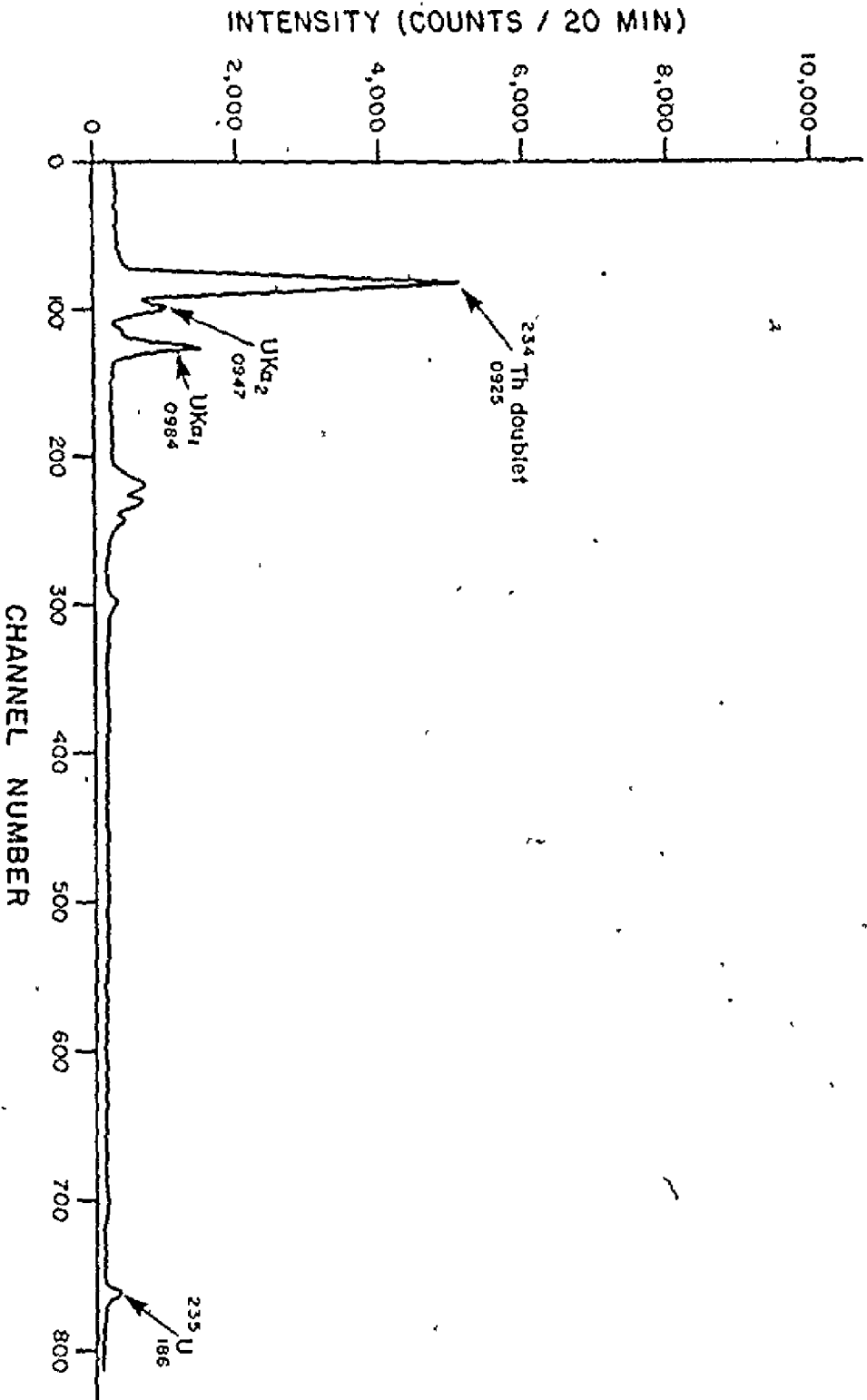


Fig. 51a. Gamma spectrum of a 0.027 ^{235}U standard

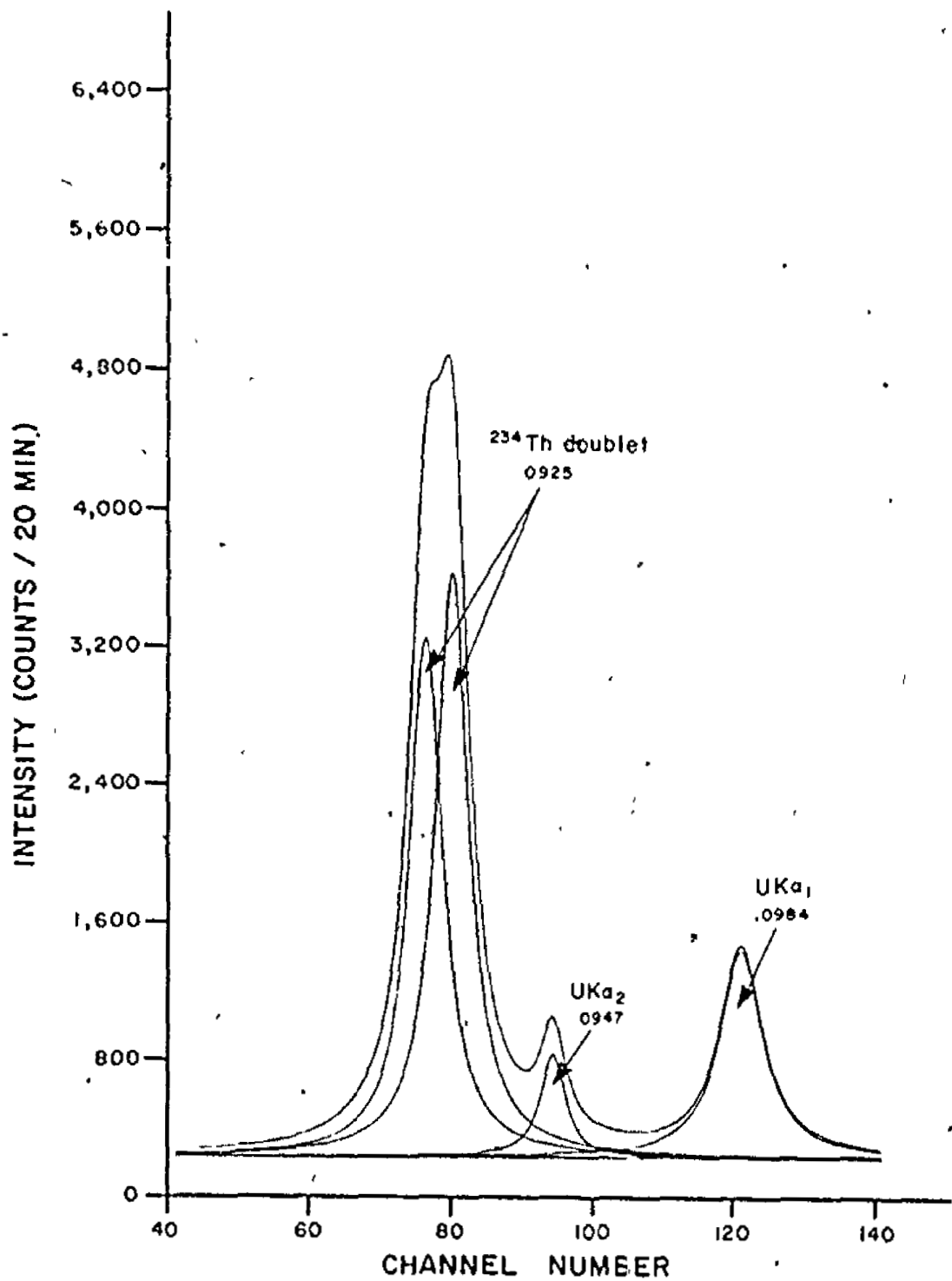


Fig. 51b. Unfolding detail of figure 51a near 0.0925 MeV showing the ^{234}Th doublet

- 220 -

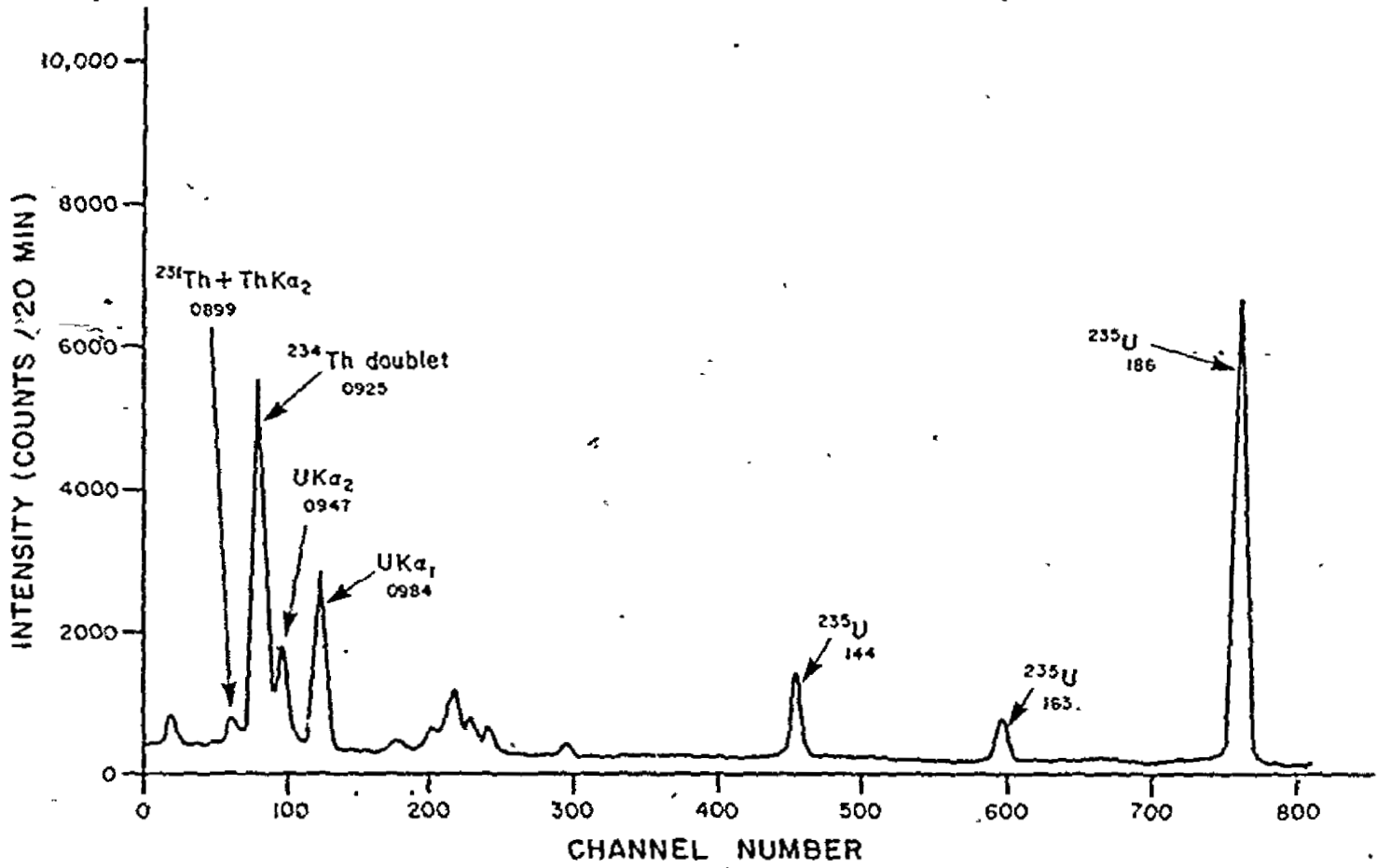


Fig. 52a. Gamma spectrum of a 1.44% ^{235}U standard

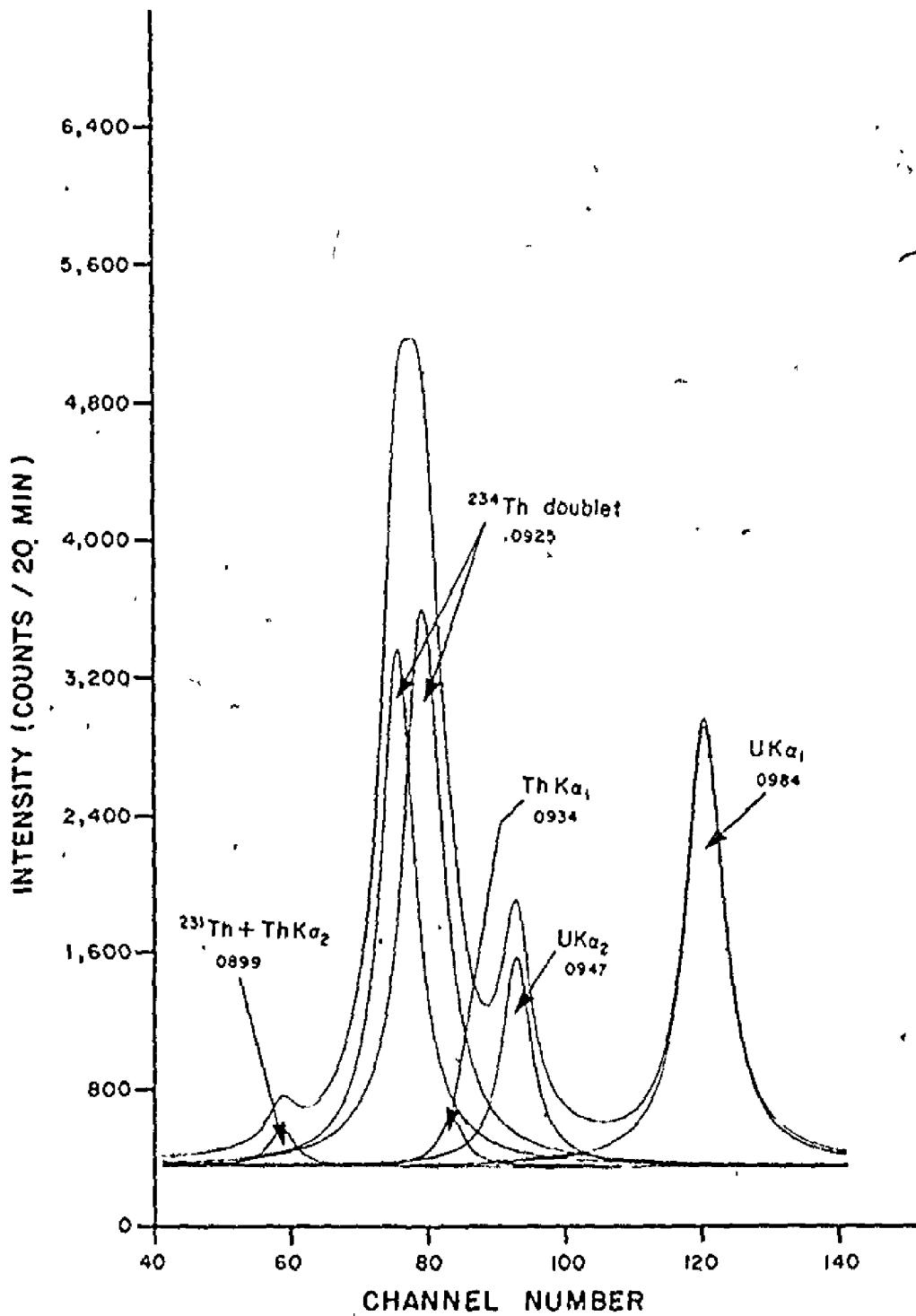


Fig. 52b. Unfolding detail of figure 52a

- 222 -

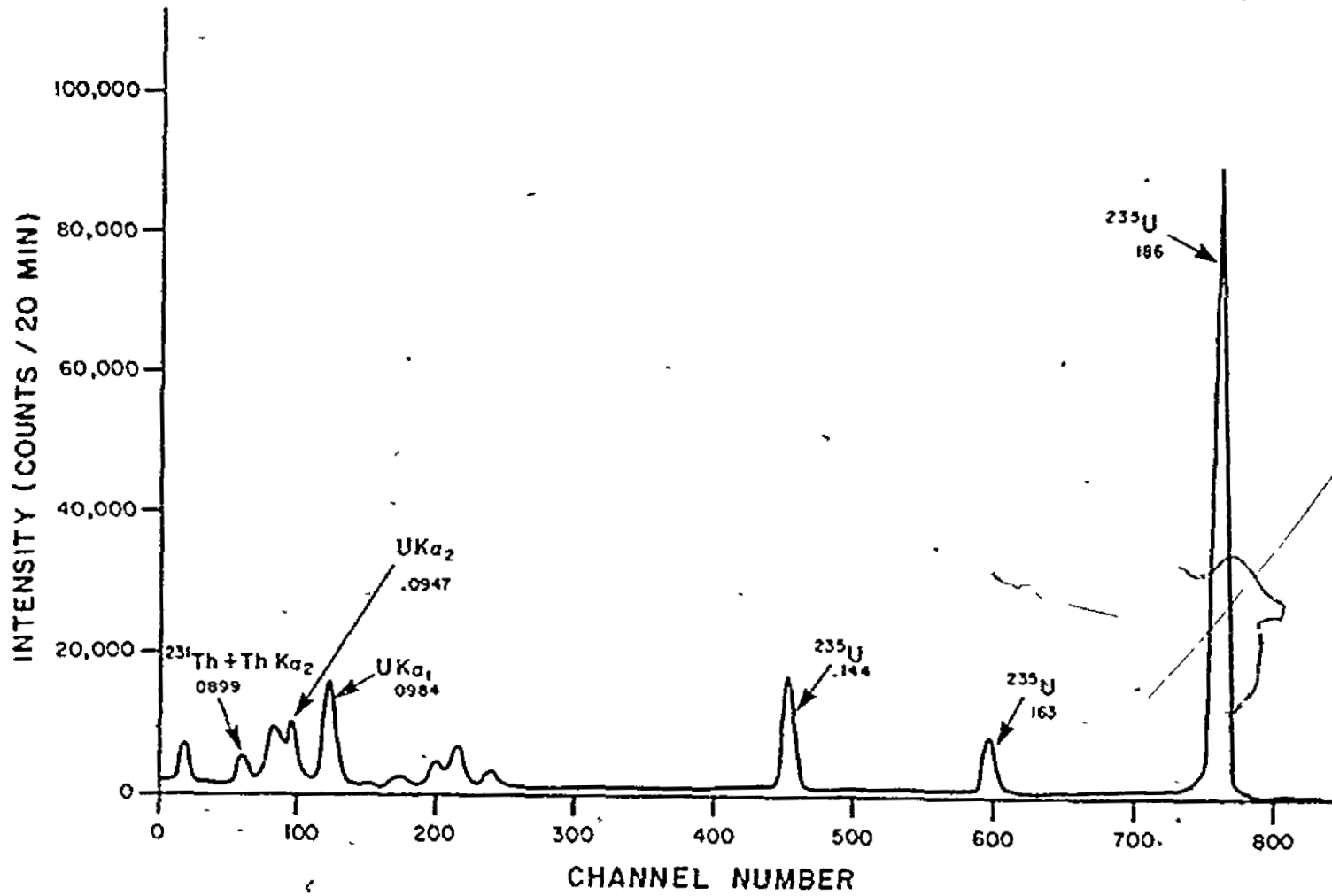


Fig. 53a. Gamma spectrum observed from a 15.39% ^{235}U standard

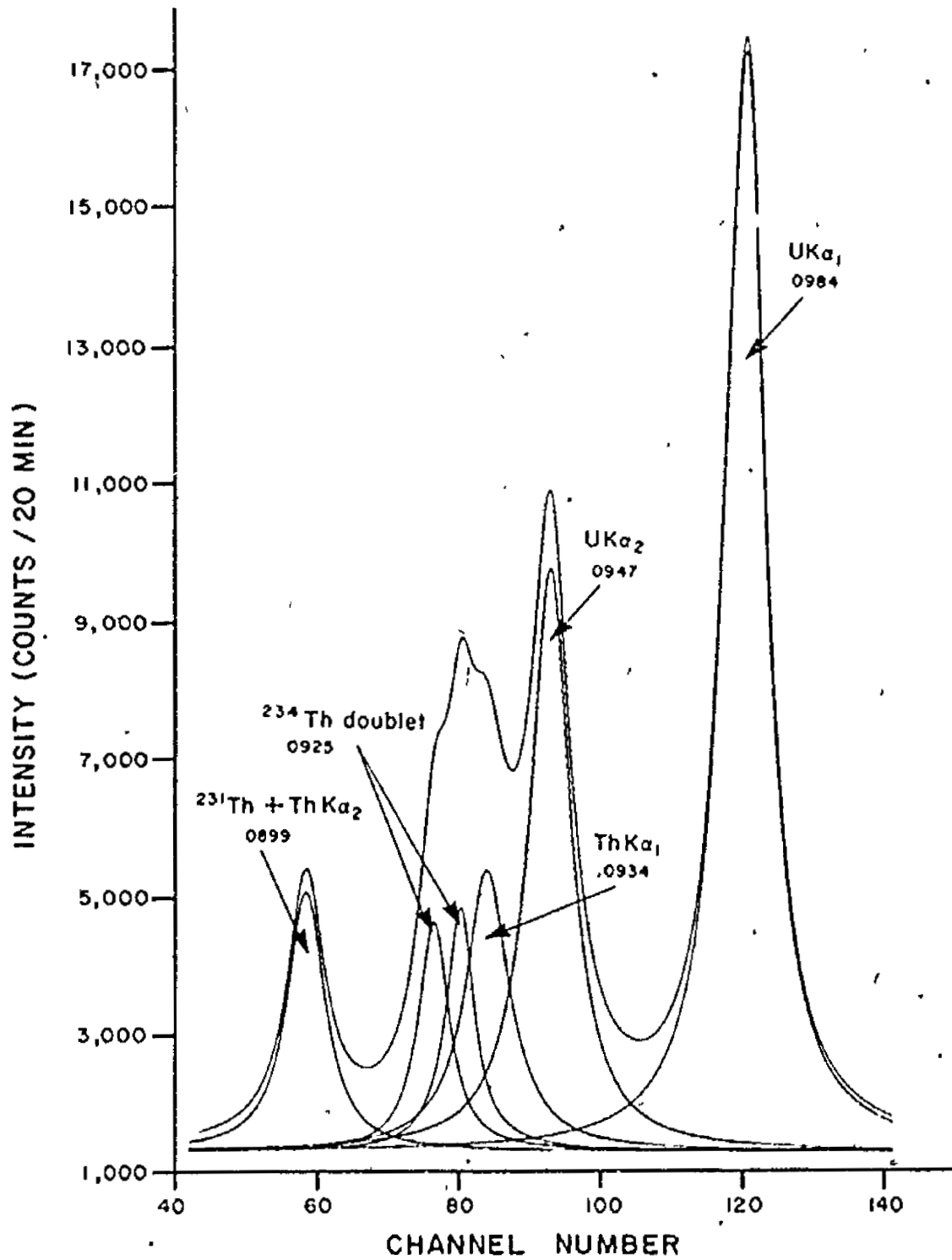


Fig. 53b. Unfolding detail of figure 53a

to the energies shown in table 5b and some relative intensities to their average experimental values. The background was also found to be horizontal and its iteration parameter could be replaced by a constant value measured at a convenient location. The minimization subroutine⁽⁸³⁾ now would converge rapidly, unattended without any constraints for virtually any reasonable input parameter set, accompanied by only a slight increase in function value. This modified minimization function was then used to produce the analytical data reported in this experiment. Figures 51a, 51a and 52a are spectra taken of 0.027%, 1.44% and 15.39% ^{235}U standards showing the relative heights of the ^{235}U γ -ray at 0.186 MeV and the 0.0925 MeV ^{234}Th doublet. Figures 51b, 52b and 53b illustrate the unfolding detail of the same spectra in the vicinity of 0.0925 MeV. A full description of the unfolding procedure and a listing of the required computer programmes is given in appendix H.

4.5.3 Evaluation of specimen thickness effects

Low energy γ -rays, such as experienced in this work, are strongly attenuated by matter, especially high Z material. Peak intensity ratios are expected to be a function of sample thickness as well as nuclide concentration. Tables 57 and 58 contain the data recorded to evaluate the effect of sample thickness on the $^{235}\text{U}/^{234}\text{Th}$ peak intensity ratio for industrial quality yellow cake and pure black oxide respectively. Figure 54 depicts a plot of intensity versus thickness (g/cm^2) of yellow cake for the ^{235}U and ^{234}Th peaks and indicates strong absorption of both γ -rays with thicknesses greater than $0.3 \text{ g}/\text{cm}^2$. This figure is also representative of the behavior of the data accumulated from various

Table 57

Data used to evaluate the effect of specimen thickness on the $^{235}\text{U}/^{234}\text{Th}$ peak intensity ratio for yellow cake (approximately $\text{Na}_2\text{U}_2\text{O}_7$).

Thickness (g/cm ²)	I ^{235}U (cts/20 min) $\pm S_T$ (%)	I ^{234}Th (cts/20 min) $\pm S_T$ (%)	I $^{235}\text{U}/\text{I }^{234}\text{Th}$ $\pm S_T$ (%)
0.045	5404 ± 1.58	7759 ± 2.65	0.697 ± 3.03
0.139	15624 ± 0.91	21715 ± 1.49	0.720 ± 1.75
0.268	27303 ± 0.70	39391 ± 1.09	0.693 ± 1.30
0.346	32793 ± 0.66	45236 ± 1.03	0.725 ± 1.21
0.494	42583 ± 0.60	60735 ± 0.89	0.701 ± 1.07
0.779	54639 ± 0.54	75757 ± 0.82	0.721 ± 0.98

Table 58

Data used to evaluate the effect of specimen thickness on the $^{235}\text{U}/^{234}\text{Th}$ peak intensity ratio for pure black oxide (U_3O_8).

Thickness (g/cm ²)	I ^{235}U (cts/20 min) $\pm S_T$ (%)	I ^{234}Th (cts/20 min) $\pm S_T$ (%)	I $^{235}\text{U}/\text{I }^{234}\text{Th}$ $\pm S_T$ (%)
0.058	10654 ± 0.92	14614 ± 1.80	0.729 ± 2.02
0.138	24157 ± 0.66	31970 ± 1.23	0.756 ± 1.39
0.250	43093 ± 0.54	59609 ± 0.93	0.723 ± 1.07
0.331	54186 ± 0.49	77459 ± 0.84	0.700 ± 0.97
0.497	71598 ± 0.45	99956 ± 0.75	0.716 ± 0.87
0.781	87522 ± 0.43	108009 ± 0.75	0.810 ± 0.86
0.997	97186 ± 0.42	116529 ± 0.75	0.834 ± 0.86

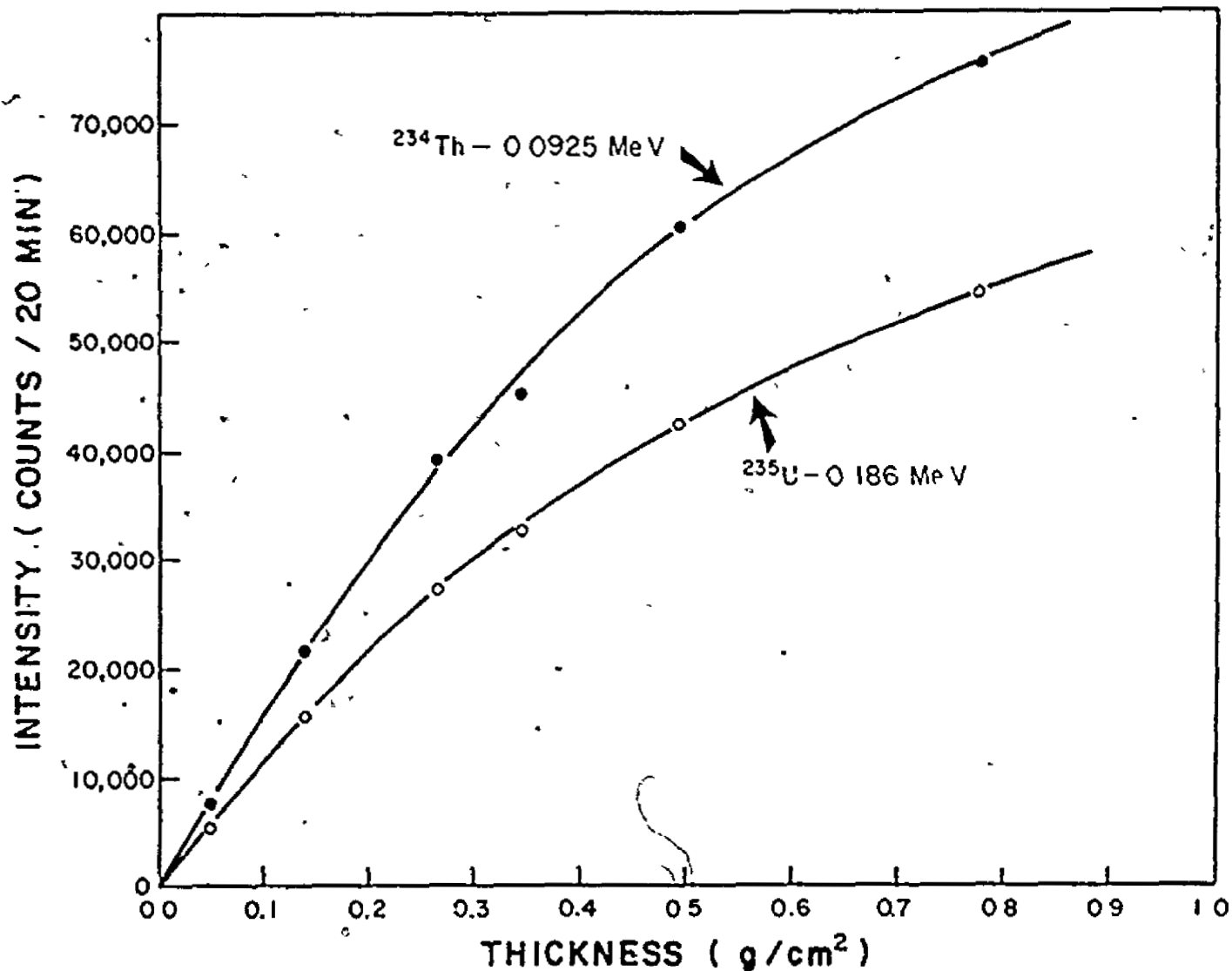


Fig. 54. Attenuation of the ²³⁴Th and ²³⁵U γ -rays at various thicknesses of yellow cake

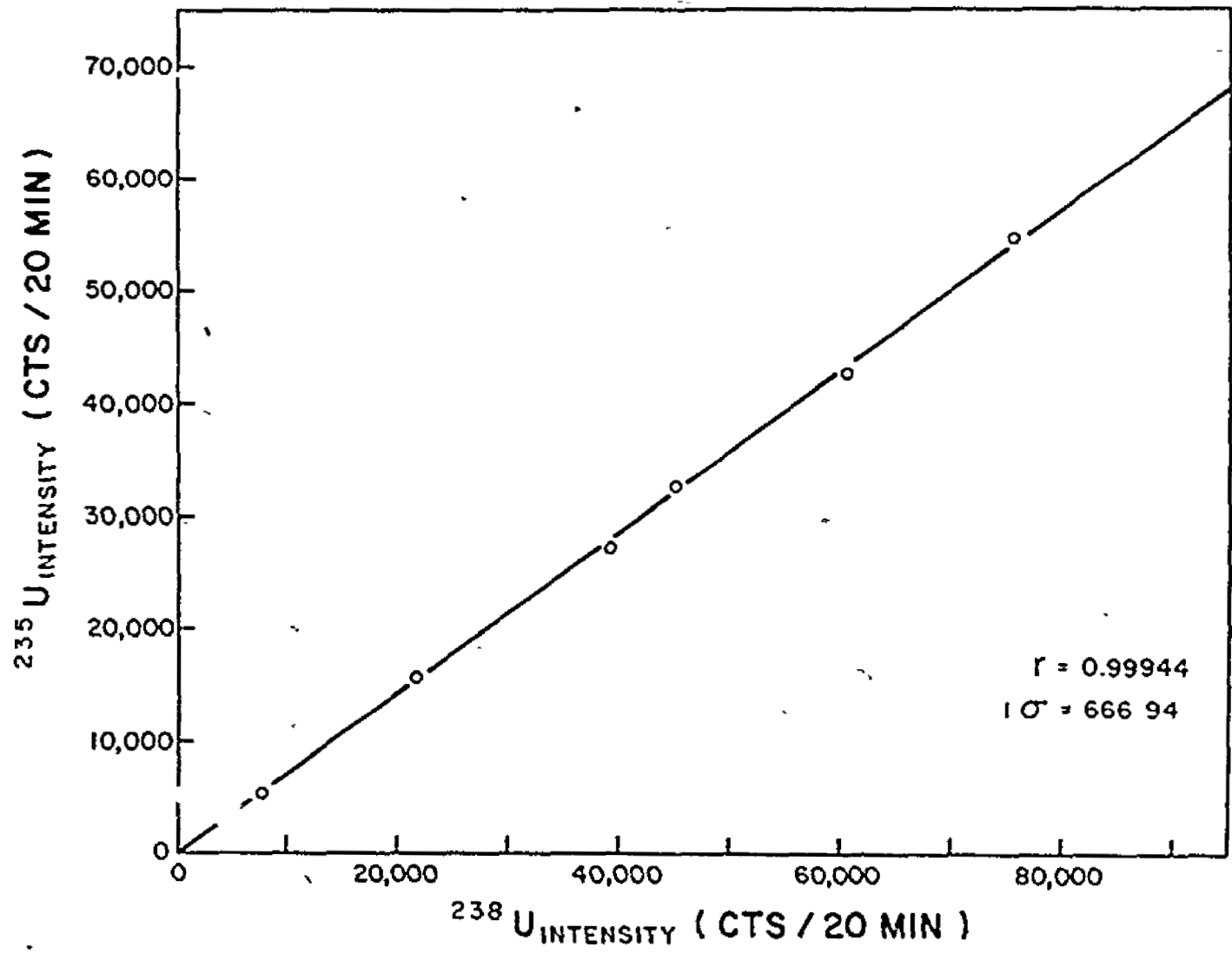


Fig. 55. Linear correlation between the 0.0925 MeV ^{234}Th and the ^{235}U γ -ray intensities over a wide range of sample thicknesses

thicknesses of black oxide as presented in table 58. However, for yellow cake, both peaks appear to be equally attenuated and the ratio is not a sensitive function of sample thickness. For the black oxide, slight preferential absorption of the lower energy peak does occur, but the peak ratio remains constant up to a thickness of 0.5 g/cm². All samples and standards in this experiment were therefore prepared approximately 0.3 g/cm² in thickness. Figure 55 is a plot of ²³⁴Th intensity versus ²³⁵U intensity which illustrates the above thickness effects for both Na₂U₂O₇ and U₃O₈.

The explanation for the unusual occurrence of non-preferential absorption of a lower energy γ -ray with increasing specimen thickness is contained in the following argument. In these uranium compounds, the principal mechanism for attenuation of the two γ -rays is through photoelectric absorption by the appropriate X-ray absorption edge. All actinides possess a very high K_{ab} energy. In the case of uranium, the K_{ab} energy lies between the 0.186 MeV ²³⁵U and the 0.0925 MeV ²³⁴Th γ -rays and tends to compensate for the thickness effects. These ²³⁵U and ²³⁴Th γ -rays are essentially equidistant in energy above the uranium K_{ab} and L_{IIIab} respectively. As can be seen from figure 7, τ for pure uranium is approximately 850 barns for both energies. For specimens consisting of yellow cake, this results in the intensity ratio being independent of sample thickness.

4.5.4. Data and data analysis

The two principle isotopes of uranium have very long half-lives. Accordingly, the uranium isotope weight fraction does not change over a

Table 59

Data observed from wide range uranium isotope standards.

$^{235}\text{U}/^{238}\text{U}$ (atom ratio)	Thickness (g/cm ²)	I ^{235}U (cts/20 min) $\pm S_T$ (%)	I ^{234}Th (cts/20 min) $\pm S_T$ (%)	I $^{235}\text{U}/\text{I }^{234}\text{Th}$ $\pm S_T$ (%)
0.000266	0.311	1340 ± 5.76	55399 ± 0.93	0.0242 ± 5.83
0.00725	0.333	40648 ± 0.60	58741 ± 0.93	0.692 ± 1.10
0.0593	0.312	304390 ± 0.34	54226 ± 1.07	5.61 ± 1.12
0.114	0.317	548613 ± 0.32	49040 ± 1.23	11.2 ± 1.27
0.182	0.321	826681 ± 0.31	47369 ± 1.38	17.5 ± 1.41
0.253	0.312	1064950 ± 0.31	42877 ± 1.63	24.8 ± 1.66
0.322	0.324	1313542 ± 0.30	41452 ± 1.78	31.7 ± 1.81

Table 60

Data observed from narrow range uranium isotope standards.

$^{235}\text{U}/^{238}\text{U}$ (atom. ratio)	Thickness (g/cm ²)	I ^{235}U (cts/20 min) $\pm S_T$ (%)	I ^{234}Th (cts/20 min) $\pm S_T$ (%)	I $^{235}\text{U}/\text{I }^{234}\text{Th}$ $\pm S_T$ (%)
0.00228	0.310	12587 ± 1.09	54594 ± 0.94	0.231 ± 1.44
0.00378	0.295	19002 ± 0.86	52627 ± 0.96	0.361 ± 1.29
0.00503	0.310	25816 ± 0.74	54207 ± 0.94	0.476 ± 1.19
0.00612	0.318	30743 ± 0.68	55623 ± 0.93	0.553 ± 1.15
0.00751	0.290	36716 ± 0.62	52729 ± 0.96	0.696 ± 1.14
0.00902	0.319	48542 ± 0.55	57919 ± 0.94	0.838 ± 1.09
0.0110	0.299	56775 ± 0.53	55601 ± 0.96	1.021 ± 1.10
0.0134	0.315	70562 ± 0.49	57344 ± 0.94	0.231 ± 1.06
0.0147	0.318	79432 ± 0.47	57864 ± 0.94	0.373 ± 1.05
0.0165	0.322	90269 ± 0.45	57721 ± 0.94	0.564 ± 1.04
0.0175	0.309	89539 ± 0.45	55533 ± 0.96	0.612 ± 1.06

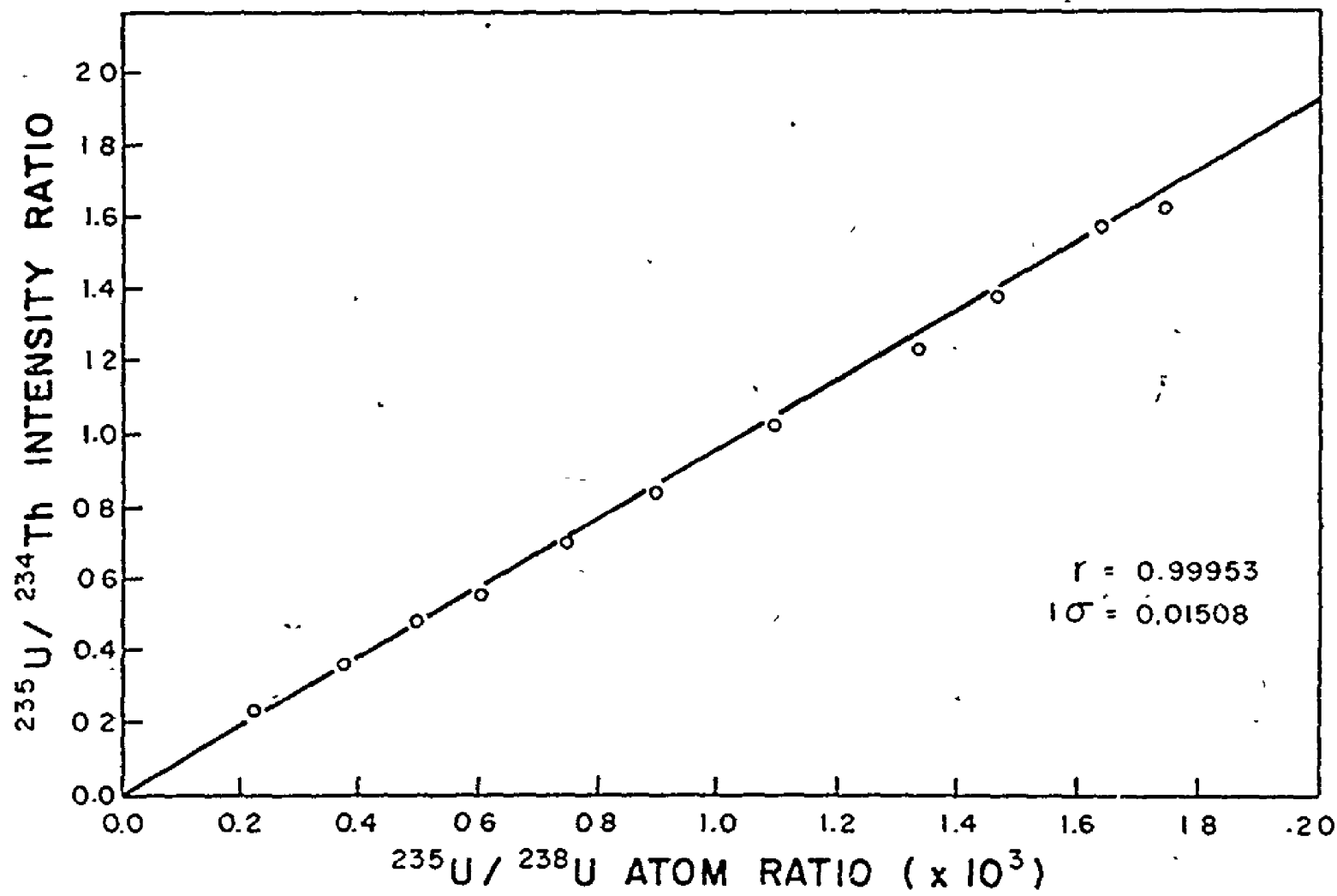


Fig. 56. Narrow range calibration curve encompassing the natural uranium abundance

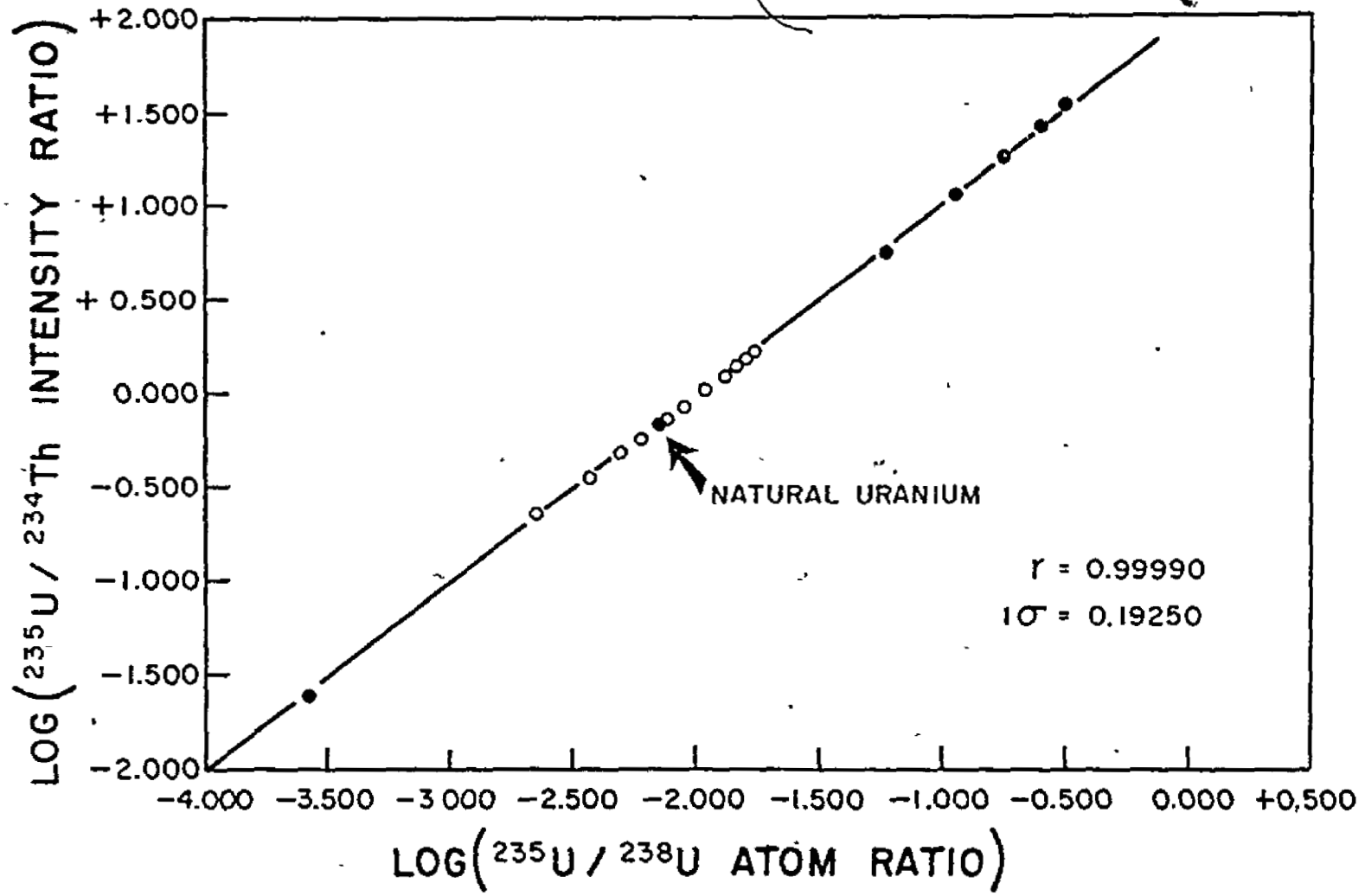


Fig. 57. Log plot containing all the standards from 0.027% to 24.29% ^{235}U

reasonable time period of observation. By employing equation 2.17 for thin samples, the peak intensity ratio is then simply proportional to the ratio of the weight fraction of the uranium isotopes present, i.e.

$$\frac{I_{^{235}\text{U}}}{I_{^{234}\text{Th}}} \propto \frac{r_{^{235}\text{U}}}{r_{^{234}\text{Th}}} \dots \dots \dots 4.34$$

Correspondingly, the atom ratio of the two uranium isotopes will be proportional to the observed intensity ratio

Data collected and computed from the wide and narrow range standards are presented in tables 59 and 60 respectively. Figure 56 shows the calibration curve produced by the narrow range standards which encompass the natural ^{235}U abundance. In this range, the net ^{234}Th and ^{235}U photo-peak intensities are nearly equivalent in magnitude. Linear best least squares gives.

$$^{235}\text{U}/^{238}\text{U} \text{ (atom ratio)} = (R_{\infty} - 0.00842)/92.447 \dots \dots \dots 4.35$$

where R_{∞} is the measured $^{235}\text{U}/^{234}\text{Th}$ peak intensity ratio under conditions of secular equilibrium between ^{238}U and ^{234}Th . Analysis of the data obtained from the wide range standards produced similar values of 98.202 and -0.105 for the slope and intercept respectively. All of the standards are shown on a log-log plot, figure 57, and R_{∞} varies linearly for at least three orders of magnitude. A complete listing of the computer programmes used to analyze the γ -ray spectrum is provided in appendix G.

4.5.5. Isotope ratio analysis of high grade uranium ores

Equation 4.35 was used to determine the isotope ratio on several

Table 6I

 $^{235}\text{U}/^{238}\text{U}$ ratios from some Canadian ores

Sample Location	$^{235}\text{U}/^{234}\text{Th}$ Intensity Ratio	$^{235}\text{U}/^{238}\text{U}$ Atom Ratio
Rabbit Lake	0.688	0.00735
Rabbit Lake	0.679	0.00726
Rabbit Lake	0.678	0.00725
Cluff Lake	0.669	0.00715
Cluff Lake	0.674	0.00720
Cluff Lake	0.684	0.00731
Cluff Lake	0.687	0.00734
Cluff Lake	0.676	0.00722
Beaverlodge Lake	0.679	0.00726
Beaverlodge Lake	0.697	0.00745
Beaverlodge Lake	0.678	0.00725
Beaverlodge Lake	0.683	0.00730
Beaverlodge Lake	0.678	0.00724
Beaverlodge Lake	0.700	0.00748

high grade uranium ores and the results are presented in table 61. The average analysis is 0.00729 with a dispersion of 0.4% (+1S). This dispersion is equivalent to the experimental precision of the technique indicating that no significant differences exist between the individual results.

Secular equilibrium between ^{235}U and ^{234}Th requires several months to re-establish after a chemical separation of uranium and thorium. In this case, it was convenient to wait the necessary ingrowth period and as such, the chemical separation of the radium group from uranium was sufficient. By modifying the extraction procedure so that thorium is also completely separated from uranium, the complete analysis can be performed within a few days. A barium sulphate co-precipitation such as described by Sill et al. (55-57) quantitatively separates radium and thorium from uranium in the same step. This would insure that ^{238}U would be free of ^{234}Th at the time of separation ($t = 0$). The following relationship could then be used:

$$R_{\infty} = R_1(1 - e^{-\lambda t_1}) \dots \dots \dots 4.36$$

where R_1 is the measured $^{235}\text{U}/^{234}\text{Th}$ peak intensity ratio at time t_1 (10 to 20 days would be suitable) and λ is the decay constant for ^{234}Th . Substitution of equation 4.36 into equation 4.35 would then yield the appropriate $^{235}\text{U}/^{238}\text{U}$ isotope ratio.

4.5.6. Determination of specimen errors for the γ -ray experiment

As in the previous experiments, the specimen and specimen loading errors were evaluated for the thin specimens used in the γ -spectroscopy

Table 62

Data used to determine the specimen error in
the γ -ray spectroscopy experiment.

$I^{235}\text{U}$ (cts/20 min)	S_N + (%)	$-(\bar{x} - x_i)$	$-(\bar{x} - x_i)^2 \times 10^{-4}$
31395	0.60	-312	9.72
31619	0.59	- 88	0.77
31605	0.59	-102	1.04
31550	0.60	-157	2.46
31777	0.59	+ 70	0.49
31770	0.59	+ 63	0.40
31626	0.59	- 81	0.65
31628	0.59	- 79	0.62
31577	0.60	-130	1.68
31972	0.59	+265	7.03
31671	0.59	- 36	0.13
31884	0.59	+177	3.14
31983	0.59	+276	7.63
32139	0.59	+432	18.68
31782	0.59	+ 75	0.57
31544	0.60	-163	2.65
31576	0.60	-131	1.71
31624	0.59	- 83	0.69

$$\bar{x} = 31707$$

$$\lambda = 60.06$$

$$\bar{S}_N = +0.59\%$$

$$S_i = \pm 0.59\%$$

Table 63

Data used to determine the specimen loading error in
the γ -ray spectroscopy experiment.

I^{235U} (cts/20 min)	S_N $\pm(\%)$	$-(\bar{x} - x_1)$	$-(\bar{x} - x_1)^2 \times 10^{-4}$
31770	0.59	+ 60	0.36
31626	0.59	- 84	0.70
31628	0.59	- 82	0.67
31577	0.60	-133	1.76
31972	0.59	+262	6.88
31671	0.59	- 39	0.15
31884	0.59	+174	3.04
31983	0.59	+273	7.47
32139	0.59	+429	18.43
31782	0.59	+ 72	0.52
31395	0.60	-315	9.91
31619	0.59	- 91	0.82
31550	0.60	-160	2.55
31777	0.50	+ 67	0.45
31544	0.60	-166	2.75
31544	0.60	-166	2.75
31605	0.59	-105	1.10

$$\bar{x} = 31710$$

$$\Sigma = 60.30$$

$$\bar{S}_N = 0.59\%$$

$$S_5 = \pm 0.61\%$$

work. The data collected to measure the specimen error are presented in table 62. Both \overline{S}_N and S_n were numerically equivalent at $\pm 0.59\%$. Thus the thin specimens of uranium chemical precipitate present no source of error. Table 63 presents the data accumulated to calculate the specimen loading error. The data dispersion, S_5 , was $\pm 0.61\%$ compared to the average counting error, \overline{S}_N , of $\pm 0.59\%$. Hence no significant source of error is incurred in loading the specimen onto the γ -ray spectrometer.

4.5.7. Determination of the spectral unfolding error

The evaluation of the standard counting error for a peak intensity measurement by the procedure described in appendix B is invalid for the ^{234}Th γ -ray doublet precision determination. Firstly, the smoothing subroutine removes most of the random fluctuations present in the spectra and secondly, the minimization subroutine approximates the smoothed data by a series of Cauchy functions. The final ^{234}Th doublet peak intensity is then calculated by mathematically integrating only the two Cauchy functions assigned to the doublet and subtracting a measured background intensity. To estimate the precision of the unfolding technique, several spectra were collected under identical conditions and the actual dispersion, S_6 , measured. The spectra in the set were then averaged. The reliability of the technique can then be checked by comparing the mean of the S_6 data set to the calculated intensity for the averaged spectra, x_{ave} . Tables 64-66 show the precision data accumulated for specimens containing 0.027%, 1.44% and 15.39% $^{235}\text{U}_3\text{O}_8$. Included in each table are the standard counting errors, S_N' , for each measurement calculated artificially as if the intensity data were obtained directly from the spectra. Table 67

Table 64

Precision data collected to determine the spectral
unfolding error at 0.027% $^{235}\text{U}_3\text{O}_8$.

$I \text{ } ^{234}\text{Th}$ (cts/20 min)	S_N $\pm(\%)$	$(x_i - \bar{x})$	$(x_i - \bar{x})^2 \times 10^5$
60775	0.44	+609	3.71
60690	0.44	+524	2.75
60439	0.45	+273	0.75
60359	0.45	+193	0.37
59654	0.45	-512	2.62
59409	0.45	-757	5.73
60040	0.45	-126	0.16
59044	0.45	-1122	12.59
60306	0.45	+135	0.18
60501	0.45	+335	1.12
60007	0.45	-159	0.25
60071	0.45	+605	3.66

$$\bar{x} = 60166$$

$$\Sigma = 33.89$$

$$S_N = \pm 0.45\%$$

$$S_6 = \pm 0.92\%$$

Table 65

Precision data collected to determine the spectral unfolding error at 1.44% $^{235}\text{U}_3\text{O}_8$.

I ^{234}Th (cts/20 min)	S_N $\pm(\%)$	$(x_1 - \bar{x})$	$(x_1 - \bar{x})^2 \times 10^{-5}$
61822	0.46	- 90.	0.08
61726	0.46	-186	0.35
61685	0.46	-227	0.52
61377	0.46	-535	2.86
61830	0.46	- 82	0.07
62543	0.46	+631	3.98
62558	0.46	+646	4.17
61581	0.46	-331	1.10
61667	0.46	-245	0.60
62642	0.46	+730	5.33
62133	0.46	+221	0.49
61389	0.46	-523	2.74

$$\bar{x} = 61912$$

$$S_N = +0.46\%$$

$$S_6 = \pm 0.73\%$$

$$\Sigma = 22.27$$

Table 66

Precision data collected to determine the spectral
unfolding error at 15.39% $^{235}\text{U}_3\text{O}_8$.

$I^{234}\text{Th}$ (cts/20 min)	S_N ±(%)	$(x_1 - \bar{x})$	$(x_1 - \bar{x})^2 \times 10^{-5}$
53859	0.64	+394	1.55
54268	0.64	+803	6.45
52530	0.65	+935	8.74
53843	0.64	+578	1.43
52889	0.65	-576	3.32
54528	0.63	+1063	11.30
52432	0.65	-1033	10.98
53697	0.64	+232	0.54
53722	0.64	+257	0.66
53277	0.65	-188	0.51
53691	0.64	+226	0.51
52845	0.65	-620	3.84

$$\bar{x} = 53465$$

$$\Sigma = 49.69$$

$$S_N' = 0.64\%$$

$$S_G = 1.26\%$$

Table 6/

Unfolding precision summary for the three concentration groups.

$\%^{235}\text{U}_3\text{O}_8$	\bar{x} (cts/20'min)	x_{ave} (cts/20 min)	S_N' $\pm(\%)$	S_6 $\pm(\%)$	S_6/S_N'
0.027	60166	60174	0.45	0.92	2.04
1.44 /	61912	61915	0.46	0.73	1.59
15.39	53465	53473	0.64	1.26	1.97

average 1.87

compares the mean intensity obtained for each data set, \bar{x} , and the intensity as calculated from the averaged spectra, x_{ave} . For the three concentration ranges, these values have a relative difference of only 0.01% or less and are essentially equivalent. Also in table 67, the magnitude of S_G and S_N' are compared for each concentration range. The measured precision, S_G , is consistently higher than the S_N' values by an average factor of 1.87. Due to its ease of calculation, the total precision of a peak intensity as obtained by the unfolding procedure was estimated by multiplying the S_N' values by this factor. This error, S_U , although it is not strictly the unfolding error because it incorporates the statistical counting errors, was taken to be the total precision achievable for a peak intensity measurement by the unfolding technique.

From appendix C, the instrumental error of the γ -ray spectrometer, produced by an operational variance, S_0^2 , amounts to $\pm 0.29\%$. Therefore, the total precision limits in tables 57-60 for a measured peak intensity consists of $\pm(S_N'^2 + S_0^2)^{\frac{1}{2}}$ and $\pm(S_0^2 + S_U^2)^{\frac{1}{2}}$ for the ^{235}U and ^{231}Th peaks respectively. The total error for the measured peak ratio is then given by:

$$S_T(\%) = [\sqrt{S_N'^2 + S_0^2} + \sqrt{S_0^2 + S_U^2}]^{\frac{1}{2}} \dots \dots \dots 4.37$$

5. CONCLUSIONS AND CONTRIBUTIONS TO KNOWLEDGE

5.1. The K X-ray experiment

An apparatus, consisting of a radioisotopic point source mounted on a one dimensional goniometer, was designed and manufactured to specifically analyze uranium using uranium K shell fluorescence. The specimens were partially thick powders of uranium bearing ore. The goniometer was used to find the optimum geometrical conditions for analysis. Scatter angles in excess of 130° were found to provide the most favourable background intensities. A secondary bismuth target was employed to measure the initial to transmitted intensity ratio which enabled the net specimen scattering intensities to be determined. A procedure was developed to measure the sample thickness from the net specimen Compton scattering intensity. By studying the X-ray absorption characteristics for an average uranium bearing granite and possessing a knowledge of the above ratios and thicknesses, assumptions were drawn which led to the conclusion that actual specimen mass absorption coefficients for energies of both the excitation and fluorescent radiation could be experimentally measured. The matrix and thickness factors, as contained in the fundamental excitation equation for partially thick specimens, could then be directly delineated. This unique approach for analyzing uranium in uranium bearing ores then constitutes measuring the uranium K shell fluorescent intensity and modifying it by the simultaneously determined matrix and thickness factors. The corrected uranium fluorescent intensity is then proportional to the uranium weight fraction present in the sample.

The performance of this technique was investigated on a total of

46 uranium ore samples originally from four major uranium mineral zones of Canada. Quantitative improvements in the accuracy of analysis were demonstrated in all cases. From the value of the mass absorption coefficient calculated for each specimen, additional information is obtained, e.g. it was deduced that in Key Lake and Elliot Lake ores, co-mineralization with uranium had occurred. Using the apparatus and procedure as described, the minimum detectable limit was 0.04% U_3O_8 with a sensitivity of 0.86 counts/sec/% U_3O_8 /mCi. It must be stressed that the apparatus for this experiment and the remaining X-ray experiments were designed to evaluate analytical approaches aimed towards satisfying the objectives of the thesis, rather than being practical analytical instruments as is. In this regard, large increases in sensitivity could easily be achieved by adopting a more compact design incorporating the desired optimum collimation and scatter angle configurations

Obviously, this technique is a prime candidate for application to on-stream industrial analysis. The attractive feature is that the matrix and thickness factors are simultaneously and experimentally determined without the need for comparative standards. Extensive changes in chemical composition will not affect the accuracy of analysis. Different specimen physical forms, such as solutions and slurries may also be analyzed effectively. Because the energies of excitation and fluorescence are very high, specimen homogeneity and surface feature requirements are not a salient restriction to accuracy. The technique is capable of analyzing the uranium content of a process stream directly through the walls of the containing vessel. Thicknesses of crushed rock, powdered ore, slurries and solutions up to several centimeters can be tolerated.

Due to high backgrounds, the technique appears more suitable for uranium analysis at a higher concentration range. Relative precisions of $\pm 1-2\%$ (S_N) were obtained from 1% U_3O_8 ore samples, however the precision deteriorates very rapidly at lower concentrations. It is probable that this approach may be of greatest benefit when employed in circuits processing highly concentrated uranium solutions.

5.2. The L X-ray experiment

A secondary excitation system, consisting of a radioisotopic source and target assembly, was designed and manufactured to selectively excite uranium L_{III} shell fluorescence. The apparatus was built to accommodate thick samples of uranium bearing ore in powdered form. The distinctive feature of the excitation system is that the energy of the primary Compton scattered excitation peak lies below the uranium L_{III} absorption edge. From the fundamental excitation equation for thick samples, only a matrix factor effects the intensity of the observed uranium fluorescence. A technique was developed to quantitatively analyze uranium by measuring the uranium L_{III} fluorescence to Compton scattering intensity ratio. By examining the X-ray absorption characteristics of an average uranium bearing granite at the appropriate energies, it was shown that this ratio would be independent of chemical composition for a wide range of expected matrix element concentrations. Surface texture and particle size effects are also minimized by the ratio technique chosen.

The technique exhibited a capacity to accurately analyze uranium over a wide range of concentrations. Application of the technique gave a calibration curve which is linear in concentration of U_3O_8 for four

orders of magnitude. The accuracy was checked by exchanging analyses with an external laboratory. The results presented are favourably compared with those obtained by a fluorimetric procedure. With the experiment as described, a minimum detectable limit of 0.02% U_3O_8 along with a sensitivity of 0.004 counts/sec/% U_3O_8 /mCi was achieved. The conversion of primary to secondary target excitation fluorescence is very inefficient and is responsible for the poor sensitivity. However, by employing a more efficient and stronger excitation source, the sensitivity can be readily improved by a factor of several hundred.

This technique may also be well suited to industrial on-stream uranium analysis. No comparative standards are required for matrix compensation or for specimen presentation corrections. Background levels are remarkably low. It is interesting to note that the minimum detectable limit was better than in the K X-ray case despite the much poorer sensitivities. The method is better suited to analyzing lower concentrations of uranium. It has the capability to span the concentration range typical of uranium extraction plant wastes to high grade ore material. The major significant difference concerning the utility of this and the K X-ray technique concerns the effective volume analyzed. In the latter case, homogeneity requirements were not severe since the K shell fluorescence can easily penetrate several centimeters of specimen. For the L X-ray situation, the depth of observation by the L_{III} shell fluorescence is approximately two millimeters. More stringent control on specimen homogeneity would be a mandatory requirement.

5.3. The M X-ray experiment

The principle motivation for investigating uranium analysis using M_V shell fluorescence is that this approach can potentially detect smaller quantities of uranium than can either K or L shell excitation. If no comparative standards are to be used, this can only be taken advantage of by analyzing thin specimens of uranium chemical precipitate. These thin specimens were prepared by electrodepositing the uranium onto a stainless steel cathode using a mixed chloride-oxalate electrolyte. An appropriate anode and cathode were fabricated for this purpose. The optimum electrodeposition time was determined for the apparatus as described. A primary radioisotopic excitation system was designed and manufactured to selectively excite the uranium M_V shell fluorescence.

It was found that if lanthanum was added to the electrolyte, the intensity of the lanthanum L_{III} shell fluorescence could be employed as an internal standard to correct for thickness effects. The calibration curve obtained was linear for at least two orders of magnitude. A further benefit from the addition of lanthanum to the electrodeposition cell revealed itself by a remarkable improvement in specimen preparation error. Several low grade Canadian ores were analyzed by this technique. A phase transfer catalyst was employed to separate the uranium from the ore prior to the electrodeposition. By assuming one gram ore or soil samples, a minimum detectable limit of 0.0001% U_3O_8 and a sensitivity of 300 counts/sec/% U_3O_8 /mCi was obtained. This quantity is three to five times less than the average global concentration of uranium. In addition to the higher intrinsic sensitivity of the analysis of the M_V shell fluorescence, further increments in sensitivity result from the very

compact radioisotopic excitation source designs possible with low energy sources and from the secondary enhancement effects from the specimen mounting material. In regard to the latter point, the chromium present in the stainless steel planchet acts as a target material producing secondary excitation fluorescence. In this case, uranium was deposited directly onto the target resulting in improved excitation efficiency.

The major drawback to the application of this technique is the lengthy procedure required to prepare sufficiently thin specimens of uranium chemical precipitate. It is likely that improvements in the anode and cathode designs would result in the creation of the proper diffusion layer in a significantly shorter electrodeposition time. In addition, when complex samples such as ores or soils are analyzed, a clean uranium separation is required. However, this approach could readily be applied to the situation where the required thin specimens can be conveniently prepared or already exist for some other purpose. The excitation technique is well suited to uranium analysis of specimens prepared for α -spectroscopy to determine electrodeposition yields for example. Sufficiently thin aerosol samples, taken from the uranium precipitation area in an industrial process could easily be prepared and rapidly analyzed by this approach.

5.4. The γ -ray spectroscopy experiment

The $^{235}\text{U}/^{238}\text{U}$ isotope ratio has been determined on thin specimens of uranium chemical precipitate by γ -ray spectroscopy. The ^{235}U and ^{238}U contents were analyzed by measuring the intensities of the 0.186 MeV ^{235}U and 0.0925 MeV ^{234}Th doublet γ -rays, respectively. Interferences

normally encountered by using the latter peak were removed by approximating the spectrum in the region of the ^{234}Th doublet by a series of Cauchy functions.

Intensity ratios varied linearly with isotope ratios for at least three orders of magnitude from highly depleted to highly enriched uranium in ^{235}U content. Statistical precisions for the measured intensity ratios of the order of $\pm 1\%$ were obtained with the technique as written. The uranium isotope ratio was measured on several high grade Canadian uranium ores. For industrial quality yellow cake, the technique appears to be independent of sample thickness.

Depending on the process used in the uranium extraction plant, radium may or may not be present in the finally processed yellow cake. If not, the technique may be directly applied to analyze the uranium isotope ratio on bulk samples or uranium chemical precipitates. The influence of radium activity must either be removed instrumentally or chemically if present in the yellow cake.

REFERENCES

1. J.H. Hubbell, *J. Physical and Chemical Reference Data* 4 (1975) 471.
2. J.H. Hubbell et al., *International Tables for X-ray Crystallography* 4 (1974) 47.
3. J.H. Hubbell, *Radiation Research* 70 (1977) 58.
4. J.H. Hubbell and W.J. Veigele, *Nat. Bur. Stand. (U.S.), Tech. Note*, (Apr. 1976).
5. J.D. Garcia, R.J. Fortner, T.M. Kavanagh, *Rev. Mod. Physics* 45 (1973) 111.
6. E. Storm and H.I. Israel, *Atomic Data and Nucl. Data Tables* A7 (1970) 565.
7. C.A. Ziegler, L.L. Bird and D.J. Chleck, *Anal. Chem.* 31 (1959) 1795.
8. R. Woldseth, X-ray Energy Spectrometry, Kevex Corporation, Burlingame, Calif., (1973) 1.16.
9. *Ibid.*, 1.4.
10. E.P. Berton, Principles and Practice of X-ray Spectrometric Analysis, Plenum, New York, (1975) 23.
11. S. Wieder, The Foundations of Quantum Theory, Academic Press, New York, (1973) 125.
12. J.A. Beardon, *Rev. Mod. Physics* 39 (1967) 78.
13. J.W. Colby, *Advan. X-ray Anal.* 11 (1968) 287.
14. J. Hower, *Amer. Mineral.* 44 (1959) 19.
15. R. Jenkins and J.L. deVries, Practical X-ray Spectrometry, Springer-Verlag, New York, (1969) 138.
16. W.D. Moak, *Anal. Chem.* 29 (1957) 1906.
17. A. Taylor, B.J. Kagle and E.W. Beiter, *Anal. Chem.* 33 (1961) 1699.
18. B.J. Mitchell, *Anal. Chem.* 30 (1958) 1894.
19. B.J. Mitchell, *Anal. Chem.* 32 (1960) 1652.
20. B.J. Mitchell, *Anal. Chem.* 33 (1961) 917.

21. J. Sherman, *Advan. X-ray Anal.* 1 (1958) 231.
22. W. Marti, *Spectrochim. Acta* 18 (1962) 1499.
23. R.J. Traill and G.R. Lachance, *Can. Spectrosc.* 11 (1966) 63.
24. H.J. Lucas-Tooth and E.C. Pyne, *Advan. X-ray Anal.* 3 (1964) 523.
25. S.D. Raspberry and K.F.J. Heinrich, *Anal. Chem.* 46 (1974) 81.
26. J.W. Criss and L.S. Birks, *Anal. Chem.* 40 (1968) 1080.
27. A.R. Hawthorne and R.P. Gardner, *Anal. Chem.* 48 (1976) 2130.
28. G. Anderman and J.W. Kemp, *Anal. Chem.* 30 (1958) 1306.
29. D.L. Taylor and G. Anderman, *Anal. Chem.* 43 (1971) 712.
30. K.B. Krauskopf, *Introduction to Geochemistry*, McGraw-Hill, New York, (1967) 639.
31. R. Woldseth, *X-ray Energy Spectrometry*, Kevex Corporation, Burlingame, Calif. (1973) 2.1.
32. E.P. Berton, *Principles and Practice of X-ray Spectrometric Analysis*, Plenum, New York, (1975) 89.
33. W.W. Bowman, K.W. McCurdo, *Atomic Data and Nucl. Tables*, 13 (1974) 89.
34. J.C. McCue, L.L. Byrd, C.A. Ziegler and J.J. O'Conner, *Anal. Chem.* 33 (1961) 41.
35. C.A. Ziegler and J.C. McCue, *Int. J. Appl. Rad. Isotopes* 12 (1961) 1.
36. L. Gorski, *Kernenergie* 6 (1963) 710.
37. S. Forberg and A.R. deRuvo, *Proc. Symp. IAEA, Salzburg, Oct. (1964)* 485.
38. S.A. Baldin and L.M. Ioannesyants, *Pribory i Teknika Eksperimental* 2 (1971) 84.
39. P.G. Burkhalter, *Applications of Low Energy X- and γ -rays*, Gordon and Brech, New York (1971) 147.
40. N. Bachvarov, T. Draznev, S. Georgiev, J. Karamonova, T. Ruskov and T. Tomov, *Radiochem. Radioanal. Lett.* 14 (1973) 1.
41. G.W. James, *Anal. Chem.* 49 (1977) 967.
42. N.H. Clark and J.G. Pyke, *Anal. Chim. Acta* 58 (1972) 234.

43. P. Voldet, Anal. Chim. Acta 62 (1972) 297.
44. J. Bacso and K. Balogh, J. Radioanal. Chem. 22 (1974) 157.
45. B. Holynska and L. Langer, Anal. Chim. Acta 40 (1968) 115.
46. N. Bialy, J. Kierzek and J. Parus, J. Radioanal. Chem. 34 (1976) 365.
47. J. Kierzek and J.L. Parus, J. Radioanal. Chem. 24 (1975) 73.
48. K.J.H. Mackay, J. Inorg. Nucl. Chem. 19 (1961) 171.
49. P.G. Burkhalter, Anal. Chem. 43 (1971) 10.
50. C. Shenburg, A.B. Haim, and S. Amiel, 45 (1973) 1804.
51. J.R. Rhodes, T.G. Ahier and J.S. Boyce, Proc. Symp., IAEA, Salzburg, Oct. (1965) 431.
52. C. Shenburg and S. Amiel, Anal. Chem. 43 (1971) 1025.
53. R.D. Giauque, Anal. Chem. 40 (1968) 2075.
54. A.G. Miller, Anal. Chem. 48 (1976) 176.
55. C.W. Sill, K.W. Puphal and F.D. Hindman, Anal. Chem. 46 (1974) 1725.
56. C.W. Sill and R.L. Williams, Anal. Chem. 41 (1969) 1624.
57. C.W. Sill, Anal. Chem. 49 (1977) 618.
58. A.H. Khan, Radiochim. Acta 18 (1972) 30.
59. N.A. Talvitie, Anal. Chem. 44 (1972) 280.
60. B.L. Rao, P.P. Parekh, G.R. Reddy and M. Sankar Das, Anal. Chim. Acta 64 (1973) 296.
61. B.L. Rao, P.P. Parekh and M. Sankar Das, J. Radioanal. Chem. 33 (1976) 67.
62. K.W. Puphal and D.R. Olsen, Anal. Chem. 44 (1972) 284.
63. A. Robert and P. Martinelli, Proc. Symp., IAEA, ~~Salzburg~~, Oct. (1964) 401.
64. D.G. Coles, J.W.T. Meadows and C.L. Lindeken, UCRL - 75619 (July 26, 1974).
65. L.A. Kull and R.O. Ginavan, BNL 50414 (March 1974).

66. G.R. Reddy and M. Sankar Das, B.A.R.C./I-241 (1973).
67. C.J. Umbarger, L.R. Cowder, Nucl. Instr. and Meth. 121 (1974) 491.
68. T.E. Sampson, Nucl. Instr. and Meth. 98 (1972) 37.
69. D.F. Urquhart, AAEC/TM634 (January 1973).
70. H.W. Taylor, Int. J. Appl. Radiat Isotop. 24 (1973) 593.
71. T.E. Sampson, Nucl. Instr. and Meth. 111 (1973) 209.
72. G.E. Goote, New Zealand J. Sci. 13 (1970) 610.
73. Y.A. Ellis, Nucl. Data Sheets 21 (1977) 493.
74. H.T. Matsuda and A. Abrao, IEA No. 288 (1973).
75. J.A.S. Adams and P. Gasparini, Gamma-Ray Spectroscopy of Rocks Elsevier, Amsterdam (1970) 115.
76. R.D.B. Fraser and E. Suzuki, Anal. Chem. 38 (1966) 1770.
77. A. Savitzky and M. Golay, Anal. Chem. 36 (1964) 1627.
78. S.D. Conte and C. deBoor, Elementary Numerical Analysis, McGraw-Hill, New York, Maidenhead, (1972) 260.
79. J.C. Ingles, Canadian Radioactive Ore Standards, Extraction Metallurgy Division, Mines Branch, Department of Energy, Mines and Resources, Ottawa, (1973).
80. K.E. Apt and E.A. Byrant, Saskatchewan Geological Society, Special Publication #3 (1976) 193.
81. M.A. Wakat, Atomic Data and Nucl. Tables, 7 (1971) 445.
82. E. Rabinowitch and R.L. Belford, Spectroscopy and Photochemistry of Uranyl Compounds, Pergamon Press, New York, N.Y. (1964) 91.
83. R. Fletcher and M.J.D. Powell, Comp. J. 6 (1963) 163.
84. R. Folch, Compt. Rend. 255 (1962) 1916.
85. Progress Report, AECL-1472, PR-P-52 (Atomic Energy of Canada Ltd., Chalk River, Ontario, October 1961) 26.

APPENDIX A

A.1. Data acquisition procedure

The acquisition of data in a useful form, suitable for computer analysis, required four basic steps. (i) transfer of paper tape to magnetic tape, (ii) conversion of the magnetic tape data density, (iii) translation from 7-bit to 8-bit character codes, and (iv) reorganization of the digital data.

For large volumes of paper tape data, such as obtained in this work, a fast paper tape reader is essential. Unfortunately, the computing services available at the University of Regina's XEROX SIGMA 9 system do not include this capability. This function was performed using the computing facilities of Sask Tel Corporation, 2350 Albert St., Regina. The seven track paper tapes were transferred to nine track magnetic tape in 100 data block format, i.e. each record on the magnetic tape contains 100 characters. The data density on the magnetic tape from their IBM system is 800 BPI (bits per inch). However, the XEROX computing system can only accept a data density of 1600 BPI on an input magnetic tape. It is therefore necessary to convert the data density from 800 to 1600 BPI. These data density conversions require a dual speed magnetic tape drive unit and were performed at Sask Comp Corp., System Centre, Legislative Grounds, Regina.

The programme written for this procedure is presented in listing A.1. As can be seen, it consists entirely of IBM JCL (job control language). Essentially, the IBM system instructs the dual speed tape drive to read input data from one magnetic tape at a particular speed

Listing A.1.

```
//US2500 JCB US25,TARROWSON
/*JOBPARM  TIME=5
/*RESOURCE TAPE=1,TAPEDD=1
/'DENSIT  PRCC  TAPEIN=999999,TAPEOUT=999999
//ONE EXEC PGM=IEBGENER
//SYSPRINT DD  SYSPUT=A
//SYSIN DD  DUMMY
//SYSUT1 DD  DSN=US25.IN,VOL=SER=&TAPEIN,
// UNIT=TAPEDD,DISP=(OLD,KEEP,KEEP),
// DCB=(RECFM=FB,LRECL=100,BLKSIZE=100),
// LABEL=(,NL)
//SYSUT2 DD  DSN=LS25.OUT,VOL=SER=&TAPEOUT,
// UNIT=TAPE,DISP=(NEW,KEEP,KEEP),
// DCB=(RECFM=FB,LRECL=100,BLKSIZE=100,DEN=3),
// LABEL=(,NL)
// PENC
//RUN EXEC PRCC=DENSIT,TAPEIN=C00938,TAPEOUT=000939
/*
```

and to output that data on another tape at half that speed. The data density, now is twice what it was initially at 1600 BPI. The data on the magnetic tape are then compatible with the XEROX system.

The initial characters punched on the seven track paper tapes were written in the 7-bit ASCII character codes. In order to obtain meaningful data from the nine track magnetic tape it is necessary to translate the 7-bit ASCII characters to the 8-bit EBCDIC character codes which are used by the XEROX system. A programme written for this purpose is available in this system's user library, the load module required is %ASCII.

The decoded data contain 100 characters per record, since the paper tapes were initially transferred to magnetic tape in 100 data block format. The records in the spectrum however are not all the same length and this results in the decoded data appearing completely disorganized. Included in each of the 100 character strings are channel numbers, contents of channel numbers as well as decoded teletype carriage return and line feed commands. The programme shown in listing A 2. was written to arrange the data in eleven vertical columns. The left most column contains the channel numbers in decades and the remaining columns list the numerical content of the channel numbers between the decades. The teletype commands were also deleted.

The programme, REORG, must be adapted for each particular experiment. As written, the programme reads enough characters into a linear array to contain a complete spectrum, it then reorganizes the data and deletes characters as described. When the spectrum is in its final form, it then reads in the next spectrum. The magnetic tape will

Listing A.2.

```
C
C
C          PROGRAMME REORG
C THIS PROGRAMME REORGANIZES THE DATA IN THE SPECTRUM
C INTO A FORM CONVENIENT FOR COMPUTER ANALYSIS.
C
C DIMENSION M(100),I(6600)
C INTEGER HEX6A,HEX4A,HEX4B
C
C INITIALIZE KEY CONSTANTS
C
C DATA HEX6A/8Z6A404C4C/
C DATA HEX4A/8Z4A40404C/
C DATA HEX4B/8Z4B404C4C/
C
C LOCATE BEGINNING OF SPECTRUM
C
10 READ(3,1000,END=100)(M(J),J=1,100)
   DO 20 J=1,100
   IF(M(J).NE.HEX6A)GO TO 30
20 CONTINUE
   GO TO 10
30 BACKSPACE 3
C
C READ IN ENTIRE SPECTRUM
C
   N=6600
   READ(3,1000)(I(K),K=1,N)
   K=1
40 IF(I(K).NE.HEX6A)GO TO 50
   K=K+1
   GO TO 40
50 IF(I(K).EQ.HEX4A)GO TO 60
   WRITE(100,3000)I(K),K
   STOP
C
```

Listing A.2. (continued)

```

C      DELETE TELETYPE COMMANDS AND INITIALIZE START OF
C      SPECTRUM
C
60     K=K+3
       JI=K
C
C      CHECK FOR END OF SPECTRUM AND END OF RECORD RESPECTIVELY
C
70     IF(I(K).EQ.HEX48)GO TO 80
       IF(I(K).EQ.HEX4A)GO TO 90
       IF(K.EQ.N)GO TO 110
       K=K+1
       GO TO 70
C
C      INITIALIZE END OF SPECTRUM AND OUTPUT COMPLETED RECORD
C
80     JF=K-1
       WRITE(4,4000)(I(L),L=JI,JF)
       GO TO 10
C
C      INITIALIZE END OF RECORD AND OUTPUT IN COMPLETED FORM
C
90     JF=K-1
       WRITE(4,4000)(I(L),L=JI,JF)
       GO TO 60
100    STOP'NORMAL END'
110    WRITE(108,2000)
       STOP
1000   FORMAT(100A1)
2000   FORMAT(1X,'SPECTRUM SIZE DIMENSIONED TOO SMALL')
3000   FORMAT('ERROR IN DATA OF SPECTRUM SIZE DIMENSIONED
5000   STOP LARGE',5X,'I(K) = ',A4,5X,'K = ',I5)
4000   FORMAT(80A1)
       END

```

generally contain hundreds of consecutive spectra, and it is necessary that the linear array be dimensioned so that it will read in only enough characters to include the entire spectrum but not any of the data belonging to the following spectrum. This has to be found by a 'trial and error' approach, because the dimension size required will depend upon the analyzer channel number output settings. Because of the 100 data block records, the array size will always be a multiple of 100. For example, in listing A.2., the spectrum is dimensioned as 6600 characters in length, i.e. 1(6600). To aid in locating the proper array length, the programme will tell the user when the array size is too small or too large. Once found, the dimension size required to contain the spectrum will not alter as long as the analyzer channel number output settings are not changed. Occasionally, the paper tape drive will miss-punch resulting in the appearance of alphanumerical characters in the spectrum. This programme also checks each character in the data to insure that the spectrum consists entirely of digits. If an alphanumerical character is found, the character and the column number it was located in are identified. The output from REORG is the final completed spectrum as shown in listing A.3. Channel number 0000 always contains the time of observation in seconds. From the listing, the output settings in channel numbers were from 3151 to 3959.

Listing A.3.

0000	000600										
3151	000596	000560	000595	000560	000572	000532	000506	000504	000526		
3160	000504	000537	000532	000572	000574	000625	000635	000682	000679	000691	
3170	000753	000740	000700	000675	000635	000693	000644	000621	000670	000626	
3180	000588	000563	000579	000560	000564	000592	000607	000680	000681	000746	
3190	000804	000898	001000	001000	000992	001030	000994	000955	000868	000839	
3200	000810	000801	000732	000697	000686	000667	000651	000603	000730	000676	
3210	000707	000813	000713	000762	000763	000741	000717	000733	000653	000651	
3220	000644	000541	000606	000583	000644	000632	000682	000792	000912	000994	
3230	001164	001157	001302	001399	001362	001317	001336	001208	001085	000964	
3240	000941	000940	000925	000983	001013	001023	001097	001100	001107	001060	
3250	001090	000968	000961	000854	000800	000743	000698	000662	000638	000604	
3260	000661	000576	000573	000578	000529	000573	000563	000582	000655	000672	
3270	000765	000911	000993	001123	001185	001243	001317	001281	001248	001077	
3280	001010	000915	000770	000760	000727	000666	000633	000635	000581	000574	
3290	000583	000574	000529	000513	000525	000513	000486	000480	000433	000428	
3300	000451	000426	000432	000410	000421	000430	000455	000463	000420	000421	
3310	000416	000423	000422	000407	000401	000386	000455	000414	000407	000401	
3320	000457	000434	000384	000413	000381	000423	000458	000396	000424	000427	
3330	000438	000381	000406	000383	000392	000379	000373	000385	000428	000424	
3340	000437	000427	000423	000407	000447	000429	000431	000403	000462	000455	
3350	000455	000457	000441	000443	000496	000419	000451	000480	000510	000483	
3360	000582	000533	000597	000577	000647	000648	000682	000754	000713	000694	
3370	000723	000716	000671	000702	000638	000609	000574	000568	000561	000559	
3380	000607	000547	000555	000493	000546	000524	000484	000517	000508	000514	
3390	000539	000562	000563	000531	000549	000512	000531	000524	000485	000473	
3400	000470	000445	000461	000430	000426	000444	000419	000447	000428	000410	
3410	000426	000410	000400	000399	000379	000361	000415	000358	000397	000365	
3420	000407	000365	000383	000349	000373	000385	000403	000390	000373	000365	
3430	000378	000411	000411	000396	000393	000371	000342	000408	000379	000381	
3440	000374	000419	000423	000394	000411	000420	000427	000446	000420	000453	
3450	000439	000385	000436	000389	000399	000413	000407	000381	000408	000402	
3460	000407	000392	000379	000402	000381	000409	000373	000377	000370	000375	
3470	000409	000382	000372	000396	000394	000389	000370	000371	000382	000393	
3480	000405	000405	000385	000385	000406	000406	000372	000396	000422	000349	

Listing A.3. (continued)

3490	000397	000374	000376	000417	000392	000407	000390	000405	000355	000348
3500	000369	000407	000366	000290	000352	000371	000406	000361	000400	000371
3510	000369	000398	000372	000401	000396	000368	000391	000416	000381	000368
3520	000399	000425	000373	000399	000385	000398	000396	000362	000400	000394
3530	000355	000368	000414	000354	000425	000398	000392	000403	000393	000401
3540	000356	000359	000417	000393	000364	000399	000379	000380	000417	000353
3550	000343	000391	000419	000379	000399	000367	000355	000397	000400	000378
3560	000364	000375	000402	000368	000395	000368	000370	000396	000360	000400
3570	000379	000407	000396	000393	000385	000404	000359	000406	000415	000392
3580	000396	000373	000394	000392	000409	000393	000420	000393	000384	000390
3590	000385	000403	000410	000400	000400	000398	000435	000358	000371	000468
3600	000474	000519	000505	000566	000556	000550	000570	000575	000572	000561
3610	000517	000544	000475	000496	000502	000467	000477	000434	000403	000471
3620	000401	000440	000414	000414	000391	000370	000389	000421	000436	000437
3630	000428	000424	000407	000413	000397	000403	000404	000421	000407	000397
3640	000410	000403	000393	000431	000391	000418	000433	000435	000430	000405
3650	000422	000400	000424	000409	000411	000430	000448	000440	000420	000416
3660	000405	000407	000465	000293	000426	000427	000410	000407	000406	000419
3670	000398	000416	000465	000403	000433	000406	000437	000464	000502	000461
3680	000468	000520	000501	000473	000427	000468	000492	000435	000462	000431
3690	000411	000429	000445	000415	000420	000430	000470	000438	000411	000431
3700	000440	000418	000397	000404	000400	000408	000405	000418	000401	000394
3710	000415	000399	000394	000406	000394	000401	000392	000423	000376	000407
3720	000412	000369	000390	000395	000403	000397	000377	000395	000377	000365
3730	000413	000392	000365	000275	000359	000406	000381	000404	000350	000366
3740	000366	000382	000388	000415	000421	000438	000417	000458	000446	000458
3750	000421	000474	000410	000421	000411	000383	000391	000386	000407	000414
3760	000393	000350	000378	000371	000352	000388	000340	000363	000358	000346
3770	000397	000360	000399	000365	000361	000418	000356	000387	000344	000366
3780	000368	000371	000415	000271	000331	000384	000357	000371	000332	000361
3790	000354	000364	000341	000364	000343	000358	000342	000374	000370	000379
3800	000385	000361	000350	000341	000363	000349	000358	000362	000353	000337
3810	000363	000364	000358	000345	000373	000353	000357	000341	000366	000340
3820	000367	000344	000374	000355	000321	000370	000334	000353	000329	000354
3830	000339	000329	000399	000316	000352	000340	000360	000352	000356	000345

Listing A.3. (continued)

3840 000337 000349 000373 000246 000346 000360 000338 000331 000346 000305
3850 000346 000347 000366 000243 000364 000340 000368 000382 000351 000347
3860 000348 000334 000367 000373 000385 000355 000333 000354 000356 000369
3870 000323 000372 000345 000382 000375 000340 000345 000365 000372 000336
3880 000369 000389 000378 000398 000363 000341 000355 000402 000388 000364
3890 000359 000370 000331 000381 000401 000405 000377 000371 000392 000400
3900 000426 000432 000412 000440 000521 000606 000729 000863 001035 001215
3910 001401 001553 001735 001840 001790 001837 001787 001625 001455 001191
3920 001139 000974 000945 000839 000802 000713 000696 000593 000580 000584
3930 000545 000507 000462 000453 000420 000430 000391 000385 000382 000361
3940 000361 000346 000365 000348 000364 000377 000315 000341 000341 000338
3950 000331 000318 000315 000364 000372 000336 000338 000338 000375 000347

APPENDIX B

B.1. Evaluation of peak areas and statistical precisions

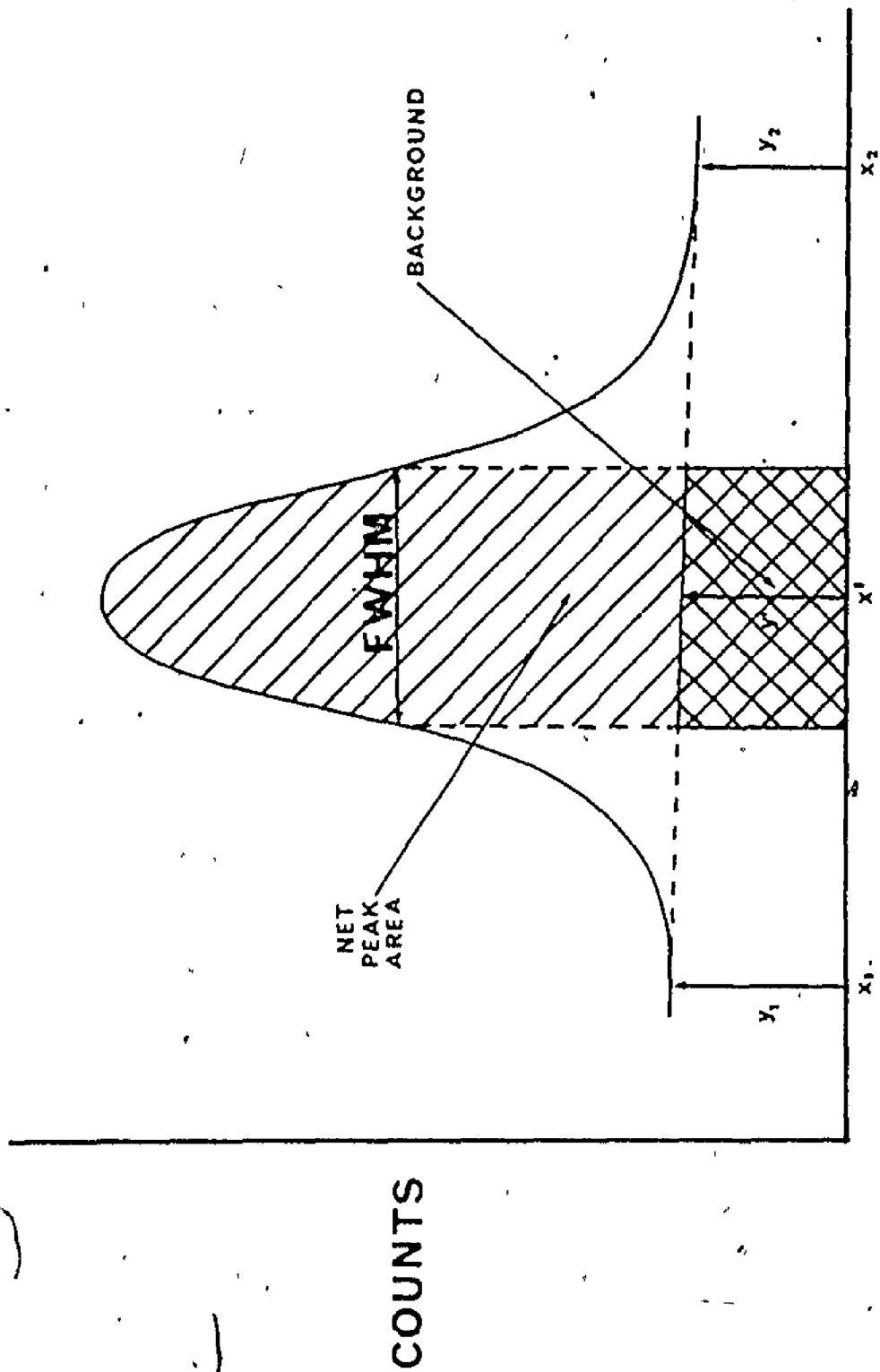
All peak intensities (except for the ^{234}Th 0.0925 MeV doublet intensity in the γ -ray spectroscopy experiment) were measured using the subroutines listed in this appendix. Peak intensities were evaluated by summing approximately between FWHM (full width half maximum) for the peaks and subtracting the appropriate trapezoidal backgrounds as shown in figure B.1. From this figure, the background y' for a particular channel number x' under the peak is estimated by the following equation.

$$y' = y_2 + \frac{(y_1 - y_2)}{(x_1 - x_2)}[x' - x_1] \quad \dots \dots \dots \text{B.1}$$

where x_1 and x_2 are channel numbers on the low and high energy side of the peak respectively, and y_1 and y_2 are the number of counts in channel numbers x_1 and x_2 . Four sequentially called subroutines were written to perform this function. The peak intensities to be measured are determined externally by a control file read in by the main programme.

The first subroutine called by the main programme is LOWBKGRD, listing B.1. This subroutine measured the average background intensity over a number of channels, as selected by the control file, on the low energy side of the desired peak. The value is assigned to y_1 .

Subroutine HIBKGRD, listing B.2, follows to measure in the same fashion the average background at channel number x_2 , that is y_2 . Since the multichannel analyzer can output a maximum of 1000 channels per spectrum, the main programmes in appendices D, E, F and G all initialize



CHANNEL NUMBER

Fig. B.1. Procedure for calculating the net peak area

Listing B.1.

```
      SUBROUTINE LOWBKCRD(NC,LCM1,NO1,SUM1,AVE1,NCNTS,NCHAN)
C
C   THIS SUBROUTINE CALCULATES THE AVERAGE BACKGROUND
C   ON THE LOW ENERGY SIDE OF A PEAK.  THE LOCATION
C   AND WIDTH IN CHANNEL NUMBERS OF THE AVERAGED BACKGROUND
C   ARE DESIGNATED BY AN EXTERNAL CONTROL FILE READ IN
C   DURING THE MAIN PROGRAMME.
C
      DIMENSION NCNTS(1)
      INDEX=NCHLN1-NCHAN+1
      NEND=INDEX+NO1-1
      SUM1=1
      DO 1 I=INDEX,NEND
1     SUM1=SUM1+NCNTS(I)
      AVE1=SUM1/NO1
      RETURN
      END
```

Listing B.2.

```
      SUBROUTINE HIBKGRD(NCHLN3,NO3,SUM3,AVE3,NCNTS,NCHAN)
C
C   THIS SUBROUTINE CALCULATES THE AVERAGE BACKGROUND ON
C   THE HIGH ENERGY SIDE OF A DESIGNATED PEAK. AN ERROR
C   MESSAGE IS ISSUED AS A PRECAUTION AGAINST PROCESSING
C   EXTRANEUS DATA.
C
      DIMENSION NCNTS(1)
      INDEX=NCHLN3-NCHAN+1
      NEND=INDEX+NO3-1
      SUM3=0
      DO 1 I=INDEX,NEND
      IF(NCNTS(I).LT.0)GO TO 2
1     SUM3=SUM3+NCNTS(I)
      AVE3=SUM3/NO3
      RETURN
2     WRITE(6,3)I
3     FORMAT(5X,'NCNTS(',I3,') *****')
      STOP
      END
```

the one dimensional array containing the spectrum to -1, as a precaution against processing data that were not originally present in the spectrum.

This subroutine warns the user when negative values are being encountered.

The total peak area is then found by subroutine PFAK, listing B.3, simply by summing up the content between two channel numbers as pre-determined in the external control file.

And finally, subroutine AREA, listing B.4, calculates the slope of the straight line between (y_1, x_1) and (y_2, x_2) . By using equation B.1 the trapezoidal background is determined and subtracted from the total peak area to give the net peak area. The statistical precision of the measured peak is evaluated from:

$$1 S_N(\%) = \frac{100 \sqrt{N_p + N_b}}{N_p - N_b} \dots \dots \dots B.2$$

where N_p and N_b are the total counts under a peak and the background under a peak respectively and $S_N(\%)$ is the relative standard counting error. Typical output from the four subroutines is given in listing B.5.

Listing B.3.

```
C      SUPROUTINE PEAK(NCHLN4,NCHLN5,SUM2,NCNTS,NCHAR)
C
C      THIS SUBROUTINE EVALUATES THE TOTAL AREA UNDER A
C      DESIGNATED PEAK.
C
C      DIMENSION NCNTS(1)
C      INDEX=NCHLN4-NCHAR+1
C      NEND=INDEX+(NCHLN5-NCHLN4)-1
C      SUM2=C
C      DO 1 I=INDEX,NEND
C      SUM2=SUM2+NCNTS(I)
C      RETURN
C      END
```

Listing B.4.

```

SUBROUTINE AREA(AVE1, SUM2, AVE3, NCHLN1, NCHLN3, NCHLN4, NCHLN5, NC2)
C
C THIS SUBROUTINE CALCULATES THE NET PEAK AREA AND
C THE STANDARD COUNTING ERROR FOR A DESIGNATED PEAK.
C
C SLOPE=(AVE3-AVE1)/(NCHLN3-NCHLN1)
C
C DETERMINATION OF TRAPEZOIDAL BACKGROUND
C
C Y1=AVE1+SLOPE*(NCHLN4-NCHLN1)
C Y2=AVE1+SLOPE*(NCHLN5-NCHLN1)
C IF((Y1-Y2).LE.0)GO TO 10
C DIFF=Y1-Y2
C TRAP2=(Y2+DIFF*0.5)*NC2
C GO TO 20
10 DIFF=Y2-Y1
C TRAP2=(Y1+DIFF*0.5)*NC2
20 NAREA=SUM2-TRAP2
C
C CALCULATION OF STATISTICAL COUNTING ERROR
C
C ERRCR=SGRT(SUM2+TRAP2)
C RRRCR=100*ERRCR/NAREA
C
C OUTPUT REQUIRED INFORMATION
C
C WRITE(6,2000)AVE1
C WRITE(6,3000)AVE3
C WRITE(6,4000)SUM2
C WRITE(6,5000)NAREA
C WRITE(6,6000)ERRCR
C WRITE(6,7000)RRRCR
2000 FORMAT(C40X,'L W SIDE AVERAGE BACKGROUND(COUNTS) = ',I6)
3000 FORMAT(C40X,'HIGH SIDE AVERAGE BACKGROUND(COUNTS) = ',I6)
4000 FORMAT(C40X,'TOTAL AREA UNDER PEAK(COUNTS) = ',I8)

```

Listing B.4. (continued)

```
5000  FORMAT(040X,1X,NET AREA UNDER PEAK(COUNTS) = ',I8)
6000  FORMAT(040X,1X,STATISTICAL COMPUTING ERROR = ',I6)
7000  FORMAT(040X,1X,COEFFICIENT OF VARIATION(Y) = ',F6.2)
      RETURN
      END
```

Listing B.5.

LOW SIDE AVERAGE BACKGROUND(COUNTS) = 23
HIGH SIDE AVERAGE BACKGROUND(COUNTS) = 4
TOTAL AREA UNDER PEAK(COUNTS) = 24424
NET AREA UNDER PEAK(COUNTS) = 23904
STATISTICAL COUNTING ERROR = 157
COEFFICIENT OF VARIATION(%) = 0.66

Appendix C

C.1. Precision evaluation procedure

As described by equation 3.7, the total variance of a measurement performed with the X-ray or γ -ray spectrometer is the sum of several terms. In this appendix, the variances resulting from errors related to the spectrometer are determined, i.e.,

$$S_T^2 = S_N^2 + S_I^2 + S_O^2 \dots \dots \dots C.1$$

The standard counting error, S_N , has twofold significance: (i) it represents the maximum precision attainable, and cannot be eliminated from a process based on counting photons as it depends only on the total accumulated count; and (ii) it can be accurately calculated and used as a standard against which to evaluate the precision actually attained. The method used throughout this work to evaluate S_N for a measured peak intensity is fully described in appendix B.

Instrumental errors generally consist of short-term and long-term variations. The former occur from moment to moment and/or over the duration of a series of analytical measurements and are caused by variations in: (i) ambient temperature, pressure and humidity of the laboratory, (ii) the ac power line, and (iii) the operation of the electronic detection, processing and output components. Long-term fluctuations occur over a period of several days to many months and are generally due to aging of instrumental components. Operational errors consist of slight non-reproducibilities in instrumental settings. It is essentially dependent on the amount of backlash in the controls and on the attentiveness of the operator.

The evaluation of long-term instrumental error, S_{IL} , is generally performed by simply loading a specimen onto the spectrometer and recording many consecutive measurements of a spectral line intensity over a period of several months, without disturbing the spectrometer settings or sample. The selection of a proper specimen is important as it must present a consistent surface to the source and detector over this extended period of time. A plane, smooth, thick rigid piece of homogeneous metal - preferably a pure element - is desirable. The standard deviation, S_1 , is calculated for the entire set of measurements and compared to the counting error, S_N , which is determined from the average number of counts accumulated during the counting duration. Any significant difference between these two values may be attributed to some type of long-term instrumental error. The variance for this instability is:

$$S_{IL}^2 = |S_1^2 - S_N^2| \dots \dots \dots C.2$$

if the data are collected in sets of 10-20 consecutive measurements, each set taken at regular intervals throughout the entire series, the short-term instrumental error, S_{IS} , is then calculated by determining the standard deviation, S_2 , of each of the individual sets and comparing them to S_N in the same manner as before. The variance for this instability is:

$$S_{IS}^2 = |S_2^2 - S_N^2| \dots \dots \dots C.3$$

To determine the operational error, S_0 , a series of measurements is made without disturbing the specimen; after each measurement, all instrumental controls are reset. The standard deviation of the series, S_3 , is calculated and the variance given by.

$$S_0^2 = |S_3^2 - S_7^2| \dots \dots \dots C.4$$

For this precision analysis of the X-ray and γ-ray spectrometer, a slightly different procedure was adopted. To perform the long-term instrumental analysis as described above, would inconveniently involve both spectrometers for many months since both units share a common data processing and storage facility. If one spectrometer was occupied with a precision analysis, it was desirable to utilize the other for supplementary work. Due to this fact, the analyzer settings were continually being changed and thus the long-term instrumental evaluation would also include the operational variance. To facilitate this, the short-term instrumental error was initially, tentatively assumed to be zero and the operational error evaluated first, i.e.

$$S_0^2 = |S_3^2 - S_N^2| \dots \dots \dots C.5$$

The operational variance was then subtracted from S_1^2 , to reveal the long-term variance.

$$S_{IL}^2 = |S_1^2 - S_N^2 - S_0^2| \dots \dots \dots C.6$$

For each set of 10 - 20 measurements, the instrumental settings were not changed so the short-term instrumental error was then calculated by equation C.3. The short-term error, if present, was then subtracted from the operational error.

C.2. X-ray spectrometer precision analysis

The precision analysis of the X-ray spectrometer was performed using the L X-ray source and holder described in section 3.4.2. The specimen consisted of a thick, lead plate whose surface was initially

machined flat and polished. Once in place, the specimen was not disturbed for the entire precision evaluation procedure. The spectral intensity measured was the Pb $L_{\alpha_1\alpha_2}$ peak at 10.6 keV⁽¹²⁾ in all cases.

C.2.1. Operational error precision analysis

Using an observation time of 3 minutes, 21 consecutive intensity measurements were recorded. Before each spectrum was taken, all the X-ray amplifier and ADC controls were turned to their opposite extremities and then reset to the values listed in table 9. The operational error precision data are presented in table C.1. The relative standard deviation about a mean value for the set of 21 measurements, S_3 , was calculated.

C.2.2. Instrumental error precision analysis

Using the same counting duration of 3 minutes, 10 sets of 15 spectra each were recorded. A two week interval followed each set of measured intensities so that the entire procedure required 20 weeks to perform and 150 spectra to complete. The data, divided into sets, are shown in table C.2. The coefficient of variation for the entire series of data, S_1 , was evaluated. In addition, the coefficient of variation for each set, S_2 , was determined.

C.2.3 Precision analysis summary

Before evaluating equations C.5, C.6 and C.3, the F ratio test was applied to determine if the differences between the measured standard deviations of the appropriate data sets (S_1 , S_2 and S_3) and the average

Table C.1
Data for operational precision analysis for
the X-ray spectrometer

Pb $\text{La}_{1\alpha_2}$ Intensity (x_i)	S_N ±(%)	($x_i - \bar{x}$)	($x_i - \bar{x}$) ² × 10 ⁻⁴
4240	7.08	-173	3.00
4800	6.65	+387	14.95
4540	6.75	+127	1.60
4480	6.79	+ 67	.44
4300	7.03	-113	1.28
4880	6.55	+467	21.78
4040	7.31	-373	13.94
3860	7.41	-553	30.62
4640	6.75	+227	5.14
4600	6.78	+187	3.48
4380	7.08	- 33	.11
4720	6.72	+307	9.41
4340	6.91	- 73	.54
4120	7.17	-293	8.60
4420	6.87	+ 7	.00
4760	6.66	+347	12.02
4280	7.05	-133	1.78
4360	7.01	- 53	.28
4580	6.75	+167	2.78
3960	7.38	-453	20.55
4380	6.99	- 33	.11

$\bar{x} = 4413$

$\Sigma = 152.43$

$S_3 = 6.26\%$

Table C.2

Data for long-term and short-term instrumental precision analysis for the X-ray spectrometer

Set Number	Pb $\text{La}_{1\alpha_2}$ Intensity (x_j)	S_N $\pm(\%)$	$(x_j - \bar{x})$		$(x_j - \bar{x})^2 \times 10^{-4}$	
			short-term	long-term	short-term	long-term
	5160	6.36	+589	+626	34.73	39.24
	4300	7.03	-271	-234	7.33	5.46
	4560	6.78	- 11	+ 26	.01	.07
	5000	6.47	+429	+466	18.43	21.75
	4100	7.21	-471	-434	22.15	18.80
	4080	7.19	-491	-454	24.08	20.57
	4540	6.89	- 31	+ 6	.09	.00
#1	4560	6.76	- 11	+ 26	.01	.07
	4600	6.68	+ 29	+ 66	.09	.44
	4600	6.73	+ 29	+ 66	.09	.44
	4380	6.88	-191	-154	3.64	2.36
	5220	6.37	+649	+686	42.16	47.11
	4560	6.76	- 11	+ 26	.01	.07
	4560	6.75	- 11	+ 26	.01	.07
	4340	6.90	-231	-194	5.32	3.75

$\bar{x} = 4571$
 $S_2 = 7.35\%$

$\Sigma = 158.15$

Table C.2 continued

Set Number	Pb $L_{\alpha_1\alpha_2}$ Intensity (x_i)	S_N ±(%)	$(x_i - \bar{x})$		$(x_i - \bar{x})^2 \times 10^{-4}$	
			short-term	long-term	short-term	long-term
	4000	7.27	-592	-534	35.05	28.47
	5200	6.29	+608	+666	36.97	44.41
	4700	6.63	+108	+166	1.17	2.77
	4600	6.78	+ 8	+ 66	.00	.44
	4700	6.66	+108	+166	1.17	2.77
	4460	6.81	-132	- 74	1.74	.54
	4860	6.56	+268	+326	7.18	10.65
2	4360	6.96	-232	-174	5.38	3.01
	4400	7.00	-192	-134	3.69	1.78
	4720	6.59	+128	+186	1.64	3.47
	4460	6.90	-132	- 74	1.74	.54
	4620	6.75	+ 28	+ 86	.08	.75
	4540	6.80	- 52	+ 6	.27	.00
	5000	6.56	+408	+466	16.65	21.75
	4260	6.97	-332	-274	11.02	7.49

$\bar{x} = 4592$
 $S_2 = 6.47\%$

$\Sigma = 123.74$

Table C.2 continued

Set Number	Pa La ₁ a ₂ Intensity (x ₁)	S _N ±(%)	(x ₁ - \bar{x})		(x ₁ - \bar{x}) ² × 10 ⁻⁴	
			short-term	long-term	short-term	long-term
	4960	6.47	+524	+426	27.46	18.18
	4460	6.92	+ 24	- 74	.06	.54
	4340	6.97	- 96	-194	.92	3.75
	4260	7.04	-176	-274	3.10	7.49
	4300	7.00	-136	-234	1.85	5.46
	4840	6.53	+404	+306	16.32	9.39
	3960	7.39	-476	-574	22.65	32.90
#3	4480	6.85	+ 44	- 54	.19	.29
	4640	6.75	+204	+106	4.16	1.13
	4480	6.77	+ 44	- 54	.19	.29
	3960	7.18	-476	-574	22.66	32.90
	4180	7.11	-256	-354	6.55	12.50
	4800	6.60	+364	+266	13.25	7.10
	4380	6.82	- 56	-154	.31	2.36
	4500	6.93	+ 64	- 34	.41	.11

$\bar{x} = .4936$

$\Sigma = 120.01$

$S_2 = 6.60\%$

Table C.2 continued

Set Number	Pa $\text{La}_{1\alpha_2}$ Intensity (x_1)	S_N $\pm(\%)$	$(x_1 - \bar{x})$		$(x_1 - \bar{x})^2 \times 10^{-4}$	
			short-term	long-term	short-term	long-term
	4280	7.08	-213	-254	4.55	6.43
	4640	6.76	+147	+106	2.15	1.13
	4380	6.87	-113	-154	1.28	2.36
	4840	6.63	+347	+306	12.02	9.39
	4580	6.74	+ 87	+ 46	.75	.22
	4180	7.11	-313	-354	9.82	12.50
	4480	6.85	- 13	- 54	.02	.29
	4480	6.85	- 13	- 54	.02	.29
	4460	7.01	- 33	- 74	.11	.54
	4480	6.80	- 13	- 54	.02	.29
	4680	6.69	+187	+146	3.48	2.14
	4900	6.53	+407	+366	16.54	13.43
	4760	6.69	+267	+266	7.11	5.13
	4000	7.40	-493	-534	24.34	28.47
	4260	7.15	-233	-274	5.44	7.49

$\bar{x} = 4493$
 $S_2 = 5.57\%$

$\Sigma = 87.65$

Table C.2 continued

Set Number	Pa $\text{La}_1\alpha_2$ Intensity (x_1)	S_N $\pm(\%)$	$(x_1 - \bar{x})$		$(x_1 - \bar{x})^2 \times 10^{-4}$	
			short-term	long-term	short-term	long-term
	4720	6.69	+181	+186	3.29	3.48
	4860	6.54	+321	+326	10.33	10.65
	4500	6.81	- 39	- 34	.15	.11
	4380	6.88	-159	-154	2.52	2.36
	4780	6.62	+241	+246	5.82	6.07
	4280	6.98	-259	-254	6.69	6.43
	4300	7.03	-239	-234	5.70	5.46
45	4720	6.69	+181	+186	3.29	3.47
	4160	7.21	-379	-374	14.34	13.96
	3780	7.57	-759	-754	57.56	56.79
	4460	6.87	- 79	- 74	.62	.54
	4360	6.98	-179	-174	3.19	3.01
	4620	6.71	+ 81	+ 86	.66	.75
	5140	6.35	+601	+606	36.16	36.77
	5020	6.50	+481	+486	23.17	23.66

$$\bar{x} = 4539$$

$$S_{2\sigma} = 7.76\%$$

$$\Sigma = 173.48$$

Table C.2 continued

Set Number	Pa $\alpha_1\alpha_2$ Intensity (x_1)	S_N $\pm(\%)$	$(x_i - \bar{x})$		$(x_i - \bar{x})^2 \times 10^{-4}$	
			short-term	long-term	short-term	long-term
	5000	6.37	+339	+466	15.86	21.75
	4740	6.67	-139	+206	1.92	4.26
	4280	7.01	-321	-254	10.35	6.43
	4680	6.72	+79	+146	.62	2.14
	4820	6.57	+219	+286	4.78	8.20
	4620	6.66	+19	+86	.03	.75
	4480	6.86	-121	-54	1.47	.29
6	4840	6.66	+239	+306	5.70	9.39
	4560	6.78	-41	+26	.17	.07
	4540	6.77	-61	+6	.38	.00
	4600	6.79	-1	+66	.00	.44
	4660	6.69	+58	+126	.34	1.60
	4400	6.89	-201	-134	4.05	1.78
	4320	7.04	-281	-214	7.91	4.56
	4480	6.79	-121	-54	1.47	.29
$\bar{x} = 4601$			$\Sigma = 55.08$			
$S_2 = 4.31\%$						

Table C.2 continued

Set Number	Pb $L_{\alpha_1\alpha_2}$ Intensity (x_j)	S_N $\pm(\%)$	$(x_j - \bar{x})$		$(x_j - \bar{x})^2 \times 10^{-4}$	
			short-term	long-term	short-term	long-term
	5160	6.37	+653	+625	42.69	39.24
	4720	6.71	+213	+186	4.55	3.47
	4440	6.97	- 67	- 94	.44	.88
	4520	6.94	+ 13	- 14	.02	.02
	4600	6.79	+ 93	+ 66	.87	.44
	4460	6.84	- 47	- 74	.22	.54
	4540	6.86	+ 33	+ 6	.11	.00
#7	4200	7.05	-307	-334	9.40	11.13
	4620	6.83	+113	+ 86	1.28	.75
	4620	6.76	+113	+ 86	1.28	.75
	4600	6.84	+ 93	+ 66	.87	.44
	4340	7.00	-167	-194	2.78	3.75
	4560	6.78	+ 53	+ 26	.28	.07
	3740	7.61	-767	-794	58.78	62.98
	4480	6.85	- 27	-54	.07	.29

$\bar{x} = 4507$
 $S_2 = 6.59\%$

$\Sigma = 123.65$

- 285 -

Table C.2 continued
J

Set Number	Pb $L_{\alpha_1\alpha_2}$ Intensity (x_i)	S_N ±(%)	$(x_i - \bar{x})$		$(x_i - \bar{x})^2 \times 10^{-4}$	
			short-term	long-term	short-term	long-term
	4880	6.55	+368	+346	13.54	12.00
	5020	6.51	+508	+486	25.81	23.66
	4160	7.25	-352	-374	12.39	13.96
	4920	6.52	+408	+386	16.65	14.93
	4100	7.25	-412	-434	16.97	18.80
	4400	6.91	-112	-134	1.25	1.78
	4620	6.79	+118	+86	1.17	.75
#8	4300	7.03	-212	-234	4.49	5.46
	4800	6.51	+288	+266	8.29	7.10
	4560	6.75	+48	+26	.23	.07
	4200	7.05	-312	-334	9.73	11.13
	4340	6.91	-172	-194	2.96	3.75
	4440	6.98	-72	-94	.52	.88
	4620	6.74	+108	+86	1.17	.75
	4320	6.96	-192	-213	3.69	4.56

$\bar{x} = 4512$

$S_2 = 6.46\%$

$\Sigma = 118.86$

Table C.2 continued

Set Number	Pb $L_{\alpha_1\alpha_2}$ Intensity (x_i)	S_N $\pm(\%)$	$(x_i - \bar{x})$		$(x_i - \bar{x})^2 \times 10^{-4}$	
			short-term	long-term	short-term	long-term
	4540	6.86	- 35	+ 6	.12	.00
	4780	6.65	+ 205	+ 246	4.22	6.07
	4580	6.93	+ 5	+ 46	.00	.22
	4640	6.81	+ 65	+ 106	.43	1.13
	4500	6.80	- 75	- 34	.56	.11
	3380	7.90	-1195	-1154	142.72	133.08
	4840	6.51	+ 265	+ 306	7.04	9.39
	4340	6.99	- 235	- 194	5.51	3.75
	4380	7.05	- 195	- 154	3.79	2.36
	4840	6.68	+ 265	+ 306	7.04	9.39
	4520	6.88	- 55	- 14	.30	.02
	5020	6.41	+ 445	+ 486	19.83	23.66
	4840	6.55	+ 265	+ 306	7.04	9.39
	4620	6.74	+ 45	+ 86	.21	.75
	4800	6.68	+ 225	+ 266	5.08	7.10

$\bar{x} = 4575$
 $S_2 = 8.34\%$

$\Sigma = 203.89$

- 287 -

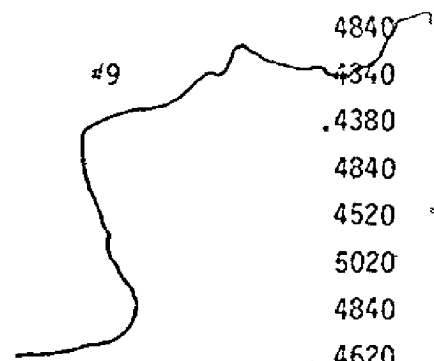


Table C.2 continued

Set Number	Pa La ₁ α ₂ Intensity (x ₁)	S _N ±(%)	(x ₁ - \bar{x})		(x ₁ - \bar{x}) ² x 10 ⁻⁴	
			short-term	long-term	short-term	long-term
	4760	6.72	+249	+226	6.21	5.13
	4220	7.13	-291	-314	8.45	9.83
	4820	6.61	+309	+286	9.57	8.21
	4600	6.78	+ 89	+ 66	7.98	.44
	4140	7.14	-371	-394	13.74	15.49
	4200	7.09	-311	-334	9.65	11.13
	4100	7.15	-411	-434	16.86	18.80
*10	4460	6.96	- 51	- 74	.26	.54
	4700	6.71	+189	+166	3.58	2.77
	4340	6.93	-171	-194	2.91	3.75
	4480	6.91	- 31	- 54	.09	.29
	4940	6.51	+429	+406	18.43	16.52
	4920	6.53	+409	+386	16.76	14.93
	4540	6.75	+ 29	+ 6	.09	.00
	4440	6.88	- 71	- 94	.50	.88

$\bar{x} = 4511$

$\Sigma = 107.91$

$S_2 = 6.15\%$

$\Sigma = 1308.41$

For total data, in table C.2. $\bar{x} = 4534$; $S_1 = 6.54\%$; $\bar{S}_N = 6.83\%$

Table C.3

Application of the F test for equality of variances resulting
from instrumental errors within the X-ray spectrometer

Dispersion Measured	Number of Determinations	Coefficient of Variation (%)	Average Relative Counting Error (%)	F _{cal}	F _{tab} @95%	F _{tab} @99%
S ₃	21	±6.26	±6.83	1.19	1.87	2.47
S ₁	150	±6.54	±6.83	1.09	1.29	1.43
S ₂ , set #1	15	±7.35	±6.83	1.16	2.16	3.06
S ₂ , set #2	15	±6.47	±6.83	1.11	2.16	3.06
S ₂ , set #3	15	±6.60	±6.83	1.07	2.16	3.06
S ₂ , set #4	15	±5.57	±6.83	1.50	2.16	3.06
S ₂ , set #5	15	±7.76	±6.83	1.29	2.16	3.06
S ₂ , set #6	15	±4.31	±6.83	2.50	2.16	3.06
S ₂ , set #7	15	±6.59	±6.83	1.07	2.16	3.06
S ₂ , set #8	15	±6.46	±6.83	1.18	2.16	3.06
S ₂ , set #9	15	±8.34	±6.83	1.49	2.16	3.06
S ₂ , set #10	15	±6.15	±6.83	1.23	2.16	3.06

counting error, S_N , were significantly different. The measured Pb $L_{\alpha_1\alpha_2}$ intensities are in units of counts/hour, however, the actual counting duration was only 3 minutes. The mean intensity for the entire series of 4534 counts/hour was established by an average population of 227 photons per peak. Therefore, when using the F test tables, the number of degrees of freedom for the average counting error, S_N , was taken as 200. The number of degrees of freedom for the appropriately measured standard deviation was one less than the number of measured intensities recorded in the set. The F ratio was calculated by:

$$F_{cal} = S_a^2/S_b^2 \dots \dots \dots C.7$$

where S_a^2 is larger than S_b^2 . F_{cal} was then compared to the values found in the tables, F_{tab} , at the 95% and 99% confidence level. If the calculated ratios are less than the tabulated values, then the two variances are not significantly different and it is not worthwhile to seek an assignable source of error in the instrument.

This comparison is presented in table C 3. All values of F_{cal} are less than F_{tab} at the 95% confidence limit except for S_2 , set #6, which is less than F_{tab} at a 99% confidence interval. The values of equations C.5, C.6 and C.3 are therefore zero and no source of instrumental error can be attributed to the X-ray spectrometer when operated under these conditions.

C.3. γ -spectrometer precision analysis

A radioisotope was employed to determine the instrumental variances in the γ -ray spectrometer. The specimen consisted of approximately 1 g of uranium metal foil, highly enriched in ^{235}U . Once in place, the

specimen was not disturbed throughout the entire precision determination schedule. The intensity of the most prominent γ -ray emitted from this nuclide, at 0.786 MeV⁽³³⁾, was measured.

C.3.1. Operational error precision analysis

To determine the variance due to operational errors, 24 consecutive spectra were taken. The observation time was 3 minutes for each measurement. The γ -ray amplifier and ADC controls were reset, to the values shown in table 12 before each intensity measurement was made, in the same manner as described for the X-ray spectrometer. Table C.4 lists the operational precision data. The relative standard deviation about the mean value for the set of 24 measurements, S_3 , was calculated.

C.3.2. Instrumental error precision analysis

A counting time of 3 minutes was used to record 108 spectra divided into 9 sets of 12 measurements each. The spectra were taken so that a time interval of one week elapsed between each set. The data, divided into sets, are shown in table C.5. The coefficients of variation for each set, S_2 , and for the whole series, S_1 , were evaluated.

C.3.3. Precision analysis summary

Similar to the X-ray spectrometer case, the F ratio test was applied to determine if the difference between the measured standard deviations of the appropriate data sets (S_1 , S_2 and S_3) and the average counting error, S_N , were significantly different. For this purpose, the number of degrees of freedom present in the variance due the statistical counting

error was taken as infinite since the average number of photons per peak was 296,471.

The appropriate variances are contrasted according to the F ratio test as shown in table C.6. As can be seen from this table, there is real source of operation error. The magnitude of the variance resulting from this error can be calculated from equation C.5.

$$\begin{aligned} S_0^2 &= |(.35)^2 - (0.19)^2| \\ &= .0864 \\ \text{or } S_0 &= +0.29\% \end{aligned}$$

The net long-term instrumental error is then evaluated from equation C.6. To determine if any significant difference exists between S_1^2 and $(S_N^2 + S_0^2)$ the F ratio test was again applied. From table C.6

$$\begin{aligned} S_1^2 &= (0.30)^2 \\ &= .0900 \\ \text{and } (S_N^2 + S_0^2) &= (0.19)^2 + (0.29)^2 \\ &= .1225 \\ \therefore F_{\text{cal}} &= .1225/.0900 \\ &= 1.36 \end{aligned}$$

The F_{tab} values are 1.82 and 2.37 for a confidence interval of 95% and 99% respectively. The calculated ratio is less than the tabulated values for 23 and 100 degrees of freedom and hence no significant long-term instrumental error exists. From table C.6, all of the values of F_{cal} are less than F_{tab} at the 95% confidence limit for the short-term error, S_2 ; hence the only significant source of instrumental error in the γ -ray spectrometer is the operational error.

Table C.4

Data for operational precision analysis for the γ -ray spectrometer

^{235}U Intensity (x_1)	S_N (%)	$-(x_1 - \bar{x})$	$(x_1 - \bar{x})^2 \times 10^{-5}$
298722	.19	-1687	28.47
297232	.19	- 197	.39
296798	.19	+ 236	.56
297153	.19	- 118	.14
297356	.19	- 321	1.03
297237	.19	- 202	.41
298654	.19	-1619	26.22
296690	.19	+ 344	1.19
294518	.19	+2516	63.34
297782	.19	- 747	5.58
296735	.19	+ 299	.90
296942	.19	+ 92	.09
296937	.19	+ 97	.10
297919	.19	- 884	7.82
297576	.19	-541	2.93
297593	.19	- 558	3.12
297324	.19	- 289	.84
293906	.19	+3128	97.89
296683	.19	+ 351	1.24
296752	.19	+ 282	.80
296633	.19	+ 401	1.61
296959	.19	+ 75	.06
297895	.19	- 860	7.40
296837	.19	+ 197	.39

$$\bar{x} = 297034$$

$$s = 252.60$$

$$S_3 = 0.35\%$$

Table C.5

Data for long-term and short-term instrumental precision analysis for the γ -ray spectrometer

Set Number	²³⁵ U Intensity (x_i)	S_N $\pm(\%)$	$-(x_i - \bar{x})$		$(x_i - \bar{x})^2 \times 10^{-5}$	
			short-term	long-term	short-term	long-term
	295685	.19	+ 610	+ 786	3.73	6.18
	297402	.19	-1106	- 930	12.24	8.66
	295697	.19	+ 598	+ 774	3.58	5.99
	296492	.19	- 196	- 20	.39	.00
	296428	.19	- 132	+ 43	.18	.02
#1	295789	.19	+ 506	+ 682	2.57	4.65
	297310	.19	-1014	- 838	10.29	7.04
	296933	.19	- 637	- 461	4.06	2.13
	296442	.19	- 146	+ 29	.21	.01
	295398	.19	+897	+1073	8.06	11.52
	295657	.19	+ 638	+ 814	4.08	6.63
	296313	.19	- 17	+ 158	.00	.25

$\bar{x} = 296295$
 $S_N = 0.23\%$

$\Sigma = 49.39$

-1,294 -

Table C.5 continued

Set Number	235U Intensity (x_1)	S_N ±(%)	$-(x_1 - \bar{x})$		$(x_1 - \bar{x})^2 \times 10^{-5}$	
			short-term	long-term	short-term	long-term
	296567	.19	- 123	- 95	.15	.09
	296636	.19	- 192	- 164	.37	.27
	296579	.19	- 135	- 107	.18	.12
	296973	.19	- 529	- 501	2.81	2.52
	296159	.19	+ 284	+ 312	.81	.98
	296118	.19	+ 325	+ 353	1.06	1.25
	294910	.19	+1533	+1561	23.51	24.38
	296034	.19	+ 409	+ 437	1.68	1.91
	296784	.19	- 340	- 312	1.16	.98
	297730	.19	-1286	-1258	16.56	15.85
	296613	.19	- 169	- 141	.29	.20
	296217	.19	+ 226	+ 254	.51	.65

$\bar{x} = 296443$

$S_2 = 0.23\%$

$\Sigma = 49.08$

- 295 -

#2

Table C.5 continued

Set Number	235U Intensity (x_i)	S_N $\pm(\%)$	$-(x_i - \bar{x})$		$(x_i - \bar{x})^2 \times 10^{-6}$	
			short-term	long-term	short-term	long-term
	296506	.19	- 657	- .34	4.32	.01
	296051	.19	- 202	+ 420	.41	1.77
	295404	.19	+ 444	+1067	1.98	11.39
	295750	.19	+ 98	+ 721	.10	5.20
	295308	.19	+ 540	+1163	2.92	13.53
	296502	.19	- 653	- 30	4.27	.01
	295230	.19	+ 618	+1241	3.85	15.41
	295987	.19	- 138	+ 484	.19	2.35
	295954	.19	- 105	+ 517	.11	2.68
	295300	.19	+ 548	+1171	3.01	13.72
	295292	.19	+ 556	+1179	3.10	13.91
	296902	.19	-1053	- 430	11.09	1.86

$\bar{x} = 295848$

$S_2 = 0.19\%$

$\Sigma = 35.33$

Table C.5 continued

Set Number	235U Intensity (x_i)	S_N $\pm(\%)$	$-(x_i - \bar{x})$		$(x_i - \bar{x})^2 \times 10^{-5}$	
			short-term	long-term	short-term	long-term
	295216	.19	- 192	+ 255	.37	.65
	295975	.19	+ 49	+ 496	.02	2.46
	296275	.19	- 251	+ 196	.63	.39
	296336	.19	- 312	+ 135	.97	.18
	296775	.19	- 751	- 303	5.64	.93
	296112	.19	- 88	+ 359	.08	1.29
	295930	.19	+ 94	+ 541	.09	2.93
	296305	.19	- 281	+ 166	.79	.28
	296125	.19	- 101	+ 346	.10	1.20
	294526	.19	+1498	+1945	22.44	37.84
	296193	.19	- 169	+ 278	.29	.77
	295520	.19	+ 504	+ 951	2.54	9.05

$\bar{x} = 296024$
 $S_2 = 0.19\%$

$\Sigma = 33.96$

#4

Table C.5 continued

Set Number	235U Intensity (x_1)	S_N ±(%)	$-(x_1 - \bar{x})$		$(\bar{x}_1 - \bar{x})^2 \times 10^{-5}$	
			short-term	long-term	short-term	long-term
	294930	.19	+ 246	+1541	7.16	23.76
	295203	.19	+ 573	+1268	3.29	16.09
	295447	.19	+ 329	+1024	1.08	10.49
	296029	.19	- 242	+ 452	.59	2.05
	295843	.19	- 66	+ 628	.04	3.95
	295585	.19	+ 191	+ 886	.37	7.85
	295676	.19	+ 100	+ 795	.10	6.32
	295698	.19	+ 78	+ 773	.06	5.98
	295980	.19	- 203	+ 491	.41	2.41
	295925	.19	- 148	+ 546	.22	2.98
	297145	.19	-1368	- 673	18.73	4.54
	295866	.19	- 89	+ 605	.08	3.66

$\bar{x} = 295776$

$S_2 = 0.18\%$

$\sigma = 32.15$

Table C.5 continued

Set Number	235U Intensity (x_i)	S_N ±(%)	$-(x_i - \bar{x})$		$(x_i - \bar{x})^2 \times 10^{-5}$	
			short-term	long-term	short-term	long-term
	294937	.19	+ 779	+1534	6.08	23.54
	295425	.19	+ 291	+1046	.85	10.95
	295215	.19	+ 501	+1256	2.51	15.78
	296944	.19	-1227	- 472	15.06	2.23
	295885	.19	- 168	+ 586	.28	3.44
#6	295661	.19	+ 55	+ 810	.03	6.57
	295195	.19	+ 521	+1276	2.72	16.29
	296631	.19	- 914	- 159	8.36	.26
	295561	.19	+ 155	+ 910	.24	8.29
	296008	.19	- 291	+ 463	.85	2.15
	295311	.19	+ 405	+1160	1.65	13.46
	295829	.19	- 112	+ 642	.13	4.12
$\bar{x} = 295716$					$\Sigma = 38.77$	
$S_2 = 0.20\%$						

Table C.5 continued

Set Number	235U Intensity (x_i)	S_N $\pm(\%)$	$-(x_i - \bar{x})$		$(x_i - \bar{x})^2 \times 10^{-5}$	
			short-term	long-term	short-term	long-term
	297476	.19	- 72	-1004	.05	10.10
	297434	.19	- 30	- 962	.01	9.27
	297507	.19	- 103	-1035	.11	10.73
	297918	.19	- 514	-1446	2.65	20.95
	297312	.19	+ 91	- 340	.08	7.07
	298215	.19	- 811	-1743	6.59	30.41
	298444	.19	-1040	-1972	10.84	38.92
	297058	.19	+345	- 586	1.19	3.44
	296450	.19	+ 953	+ 21	9.08	.00
	297317	.19	+ 86	- 845	.07	7.15
	296611	.19	+ 792	- 139	6.27	.20
	297095	.19	+ 308	- 623	.95	3.89
	$\bar{x} = 297403$				$\Sigma = 37.90$	
	$S_2 = 0.20\%$					

Table C.5 continued

Set. Number	235U Intensity (x_i)	S_N ±(%)	$-(x_i - \bar{x})$		$(x_i - \bar{x})^2 \times 10^{-5}$	
			short-term	long-term	short-term	long-term
	298748	.19	-1318	-2276	17.40	51.84
	297714	.19	- 284	-1242	.81	15.44
	297616	.19	- 186	-1144	.35	13.11
	298319	.19	- 889	-1847	7.92	34.14
	297720	.19	- 290	-1248	.85	15.59
	297121	.19	+ 308	- 649	.95	4.22
	297259	.19	+ 170	- 787	.29	6.21
	297295	.19	+ 134	- 823	.18	6.79
	297052	.19	+ 377	- 580	1.42	3.37
	296863	.19	+ 566	- 391	3.20	1.53
	297053	.19	+ 376	- 581	1.41	3.38
	296389	.19	+1040	+ 82	10.82	.01

$\bar{x} = 297429$

$\Sigma = 45.60$

$S_2 = 0.22\%$

Table C.5 continued

Set Number	235U Intensity (x_i)	S_N ±(%)	$-(x_i - \bar{x})$		$(x_i - \bar{x})^2 \times 10^{-5}$	
			short-term	long-term	short-term	long-term
	297757	.19	- 420	-1285	1.77	16.53
	298300	.19	- 963	-1828	9.28	33.44
	297539	.19	- 202	-1067	.41	11.40
	297476	.19	- 139	-1004	.19	10.10
	297059	.19	+ 277	- 587	.77	3.45
	296117	.19	+1219	+ 354	14.87	1.25
	296884	.19	+ 452	- 412	2.05	1.70
	297221	.19	+ 115	- 749	.13	5.62
	297874	.19	- 537	-1402	2.89	19.68
	296861	.19	+ 475	- 389	2.26	1.52
	297029	.19	+ 307	- 557	.95	3.11
	297921	.19	- 584	-1449	3.42	20.01

$\bar{x} = 297336$

$\Sigma = 38.99$

$S_2 = 0.20\%$

For total data in table C.5

$\bar{x} = 296471$

$\Sigma = 865.81$

$S_1 = 0.30\%$

$\overline{S_N} = 0.19\%$

Table C.6

Application of the F ratio test for equality of variances
resulting from instrumental errors within the γ -ray spectrometer

Dispersion Measured	Number of Determinations	Coefficient of Variation (%)	Average Relative Counting Error (%)	F_{cal}	F_{tab} @95%	F_{tab} @99%
S_3	24	± 0.35	± 0.19	3.39	1.76	2.26
S_1	108	± 0.30	± 0.19	2.49	1.28	1.43
S_2 , set #1	12	± 0.23	± 0.19	1.47	2.40	3.60
S_2 , set #2	12	± 0.23	± 0.19	1.47	2.40	3.60
S_2 , set #3	12	± 0.19	± 0.19	1.00	2.40	3.60
S_2 , set #4	12	± 0.19	± 0.19	1.00	2.40	3.60
S_2 , set #5	12	± 0.18	± 0.19	1.11	2.40	3.60
S_2 , set #6	12	± 0.20	± 0.19	1.11	2.40	3.60
S_2 , set #7	12	± 0.20	± 0.19	1.11	2.40	3.60
S_2 , set #8	12	± 0.22	± 0.19	1.34	2.40	3.60
S_2 , set #9	12	± 0.20	± 0.19	1.11	2.40	3.60

- APPENDIX D

D.1. Programme KXRAY

The main programmes listed in this appendix and in appendices E, F and G are all similar in design and purpose. The main functions are to read in data; calculate designated net peak areas and to organize output information.

The initial data read in must have the same structure as shown in listing A.3 produced from REORG. As noted from the main programmes, the contents of channel number 0000 and the first channel number appearing in the spectrum are assigned their own variables, RT (for real observation time in seconds) and NCHAN respectively. If desired, RT can then be used to convert the net peak areas to net intensities. NCHAN is used in the subroutines called to calculate the net peak areas, as described in appendix B. Two internal counters are employed, JCHK and ICHK. The former counts and labels each spectrum processed and the latter is a control counter indicating which peak in the spectrum is being measured.

An external control file is read into the main programme to locate and analyze appropriate peaks. For the K X-ray spectrum the file name is CONTOLK. From the main programme, listing D.1, each record of the control file contains the following integers:

NCHLN1 = channel number where the background on the low energy side of the peak is to be measured,

NCHLN3 = channel number where the background on the high energy side of the peak is to be measured,

Listing D.1.

```

C
C          PROGRAMME KXRAY
C
C
C      THIS PROGRAMME MEASURES THE NET INTENSITY OF THE MAJOR
C      URANIUM K SHELL FLUORESCENT PEAKS.
C
C      DIMENSION NCNTS(1000)
C      DATA NCNTS/1000*1/
C
C      SET SPECTRUM NUMBER AND PEAK NUMBER COUNTERS TO ZERO
C
C      JCHK=0
10    ICHK=0
C
C      READ IN ONE COMPLETE SPECTRUM
C
C      READ(5,1000,END=120)RT,NCNTS,(NCNTS(I),I=1,9)
C      DO 20 I=10,1000,10
C      K=I+9
C      READ(5,2000,END=30)IZ,(NCNTS(J),J=1,K)
C      IF (IZ.NE.0)GO TO 20
C      BACKSPACE 5
C      GO TO 30
20    CONTINUE
30    JCHK =JCHK+1
C      WRITE(6,3000)JCHK
40    ICHK=ICHK+1
C
C      DETERMINE WHICH PEAK IS TO BE ANALYZED
C
C      IF (ICHK.EQ.2)GO TO 50
C      IF (ICHK.EQ.3)GO TO 60
C      IF (ICHK.EQ.4)GO TO 70
C      IF (ICHK.EQ.5)GO TO 75

```

Listing D.1. (continued)

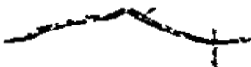
```

      IF (ICLK.EC.6)GO TO 80
      IF (ICLK.EC.7)GO TO 115
      WRITE(6,4000)
      GO TO 90
50    WRITE(6,4100)
      GO TO 90
60    WRITE(6,4200)
      GO TO 90
70    WRITE(6,4300)
      GO TO 90
75    WRITE(6,7000)
      GO TO 90
80    WRITE(6,4400)
      C
      C   READ IN CONTROL FILE
      C
90    READ(4,7100)NCHLN1,NCHLN3,NCHLN4,NCHLN5,N01,N02,N03
      C
      C   EVALUATE NET PEAK AREA AND THE STATISTICAL PRECISION
      C
      CALL LOWBKGRD(NCHLN1,N01,SUM1,AVE1,NCNTS,NCHAN)
      CALL PEAK(NCHLN4,NCHLN5,SUM2,NCNTS,NCHAN)
      CALL HIBKGRD(NCHLN3,N03,SUM3,AVE3,NCNTS,NCHAN)
      CALL AREA(AVE1,SUM2,AVE3,NCHLN1,NCHLN3,NCHLN4,NCHLN5,
      N02,NAPEA,ERROR)
      GO TO 90
115   REWIND 4
      C
      C   PROCESS NEXT SPECTRUM
      C
      GO TO 10
120   STOP
1000  FORMAT(5X,I6/I4,9(1X,I6))
2000  FORMAT(I4,10I7)
3000  FORMAT('1','SPECTRUM 4',I2)

```

Listing D.1. (continued)

```
4000  FORMAT(50X,'URANIUM K-ALPHA2 PEAK DATA',//)
4100  FORMAT(///50X,'URANIUM K-ALPHA1 PEAK DATA',//)
4200  FORMAT(///50X,'URANIUM K-BETA1 PEAK DATA',//)
4300  FORMAT(///50X,'URANIUM K-BETA2 PEAK DATA',//)
4400  FORMAT(///50X,'BISMUTH K-ALPHA1 PEAK DATA',//)
7000  FORMAT(///50X,'RAYLEIGH SCATTERED PEAK DATA',//)
7100  FORMAT(4I4,3I2)
      END
```



NCHLN4 = channel number where peak integration is to commence,
NCHLN5 = channel number where peak integration is to terminate,
N01 = number of channels the low energy background is to be
averaged over,
N02 = peak width in channel numbers,
N03 = number of channels the high energy background is to be
averaged over.

For the K X-ray case, the complete control file is:

3450356634603501106010

3450356635113555104510

3660381136853734105010

3660381137343780104710

3830390138473887104110

3151326032033240104410

As an example, the first record of CONTOLK contains all the control parameters for the U $K\alpha_2$ peak:

NCHLN1 = 3450

NCHLN3 = 3566

NCHLN4 = 3460

NCHLN5 = 3501

N01 = 10

N02 = 60

N03 = 10

The assignment of values to the control parameters was initially obtained by visually observing the spectrum on the analyzer oscilloscope. If the instrumental settings are not changed, table 8 for the K X-ray experiment,

then these control parameter values will remain constant for all the K X-ray work. The second record then contains these constants for the U $K\alpha_1$ peak and so on for the remaining peaks. Typical output from KXRAY is shown in listing D.2. All the initial peak intensities used in the K X-ray experiment were obtained from this programme. As stated earlier, the Compton scattering intensity was obtained from the total background intensity under the B₁ $K\alpha_1$ peak.

Listing D.2.

SPECTRUM # 1

URANIUM K-ALPHA2 PEAK DATA

LOW SIDE AVERAGE BACKGROUND(COUNTS) = 160
HIGH SIDE AVERAGE BACKGROUND(COUNTS) = 43
TOTAL AREA UNDER PEAK(COUNTS) = 7694
NET AREA UNDER PEAK(COUNTS) = 1996
STATISTICAL COUNTING ERROR = 124
COEFFICIENT OF VARIATION(%) = 6.46

URANIUM K-ALPHA1 PEAK DATA

LOW SIDE AVERAGE BACKGROUND(COUNTS) = 160
HIGH SIDE AVERAGE BACKGROUND(COUNTS) = 43
TOTAL AREA UNDER PEAK(COUNTS) = 7089
NET AREA UNDER PEAK(COUNTS) = 3629
STATISTICAL COUNTING ERROR = 102
COEFFICIENT OF VARIATION(%) = 2.83

URANIUM K-BETA1 PEAK DATA

LOW SIDE AVERAGE BACKGROUND(COUNTS) = 30
HIGH SIDE AVERAGE BACKGROUND(COUNTS) = 27
TOTAL AREA UNDER PEAK(COUNTS) = 3082
NET AREA UNDER PEAK(COUNTS) = 1616
STATISTICAL COUNTING ERROR = 67
COEFFICIENT OF VARIATION(%) = 4.17

URANIUM K-BETA2 PEAK DATA

Listing D.2. (continued)

LOW SIDE AVERAGE BACKGROUND(COUNTS) = 30
HIGH SIDE AVERAGE BACKGROUND(COUNTS) = 27
TOTAL AREA UNDER PEAK(COUNTS) = 1819
NET AREA UNDER PEAK(COUNTS) = 489
STATISTICAL COUNTING ERROR = 56
COEFFICIENT OF VARIATION(%) = 11.47

RAYLEIGH SCATTERED PEAK DATA

LOW SIDE AVERAGE BACKGROUND(COUNTS) = 27
HIGH SIDE AVERAGE BACKGROUND(COUNTS) = 23
TOTAL AREA UNDER PEAK(COUNTS) = 2607
NET AREA UNDER PEAK(COUNTS) = 1554
STATISTICAL COUNTING ERROR = 60
COEFFICIENT OF VARIATION(%) = 3.89

BISMUTH K-ALPHA1 PEAK DATA

LOW SIDE AVERAGE BACKGROUND(COUNTS) = 137
HIGH SIDE AVERAGE BACKGROUND(COUNTS) = 137
TOTAL AREA UNDER PEAK(COUNTS) = 10842
NET AREA UNDER PEAK(COUNTS) = 4785
STATISTICAL COUNTING ERROR = 129
COEFFICIENT OF VARIATION(%) = 2.72

APPENDIX E

E.1. Programme LXRAY

The main programme used to obtain the initial peak intensity data for the L X-ray experimental work, LXRAY, is presented in listing E.1. The general features of the programme routine have been previously outlined in appendix D. Both the U L α peak and the composite (U L β_2 + Mo K α Compton) peak areas are measured. With the instrumental settings for the L X-ray work, table 9, the appropriate control file, CONTOLL, is:

```
3250338032703380 20110 20
```

```
3450378034703780 20310 20
```

All control constants perform the same function as in program KXRAY.

Typical output from LXRAY is shown in listing E.2

Listing E.1. (continued)

```

50   GC TC 60
      WRITE(6,4100)
      GC TC 60
C
C   .READ IN CONTROL FILE
C
60   READ(4,7100)NCHLN1,NCHLN3,NCHLN4,NCHLN5,N01,N02,N03
C
C   EVALUATE NET PEAK AREA AND THE STATISTICAL PRECISION
C
      CALL LC*BGGRD(NCHLN1,N01,SUM1,AVE1,NCNTS,NCHAN)
      CALL PEAK(NCHLN4,NCHLN5,SUM2,NCNTS,NCHAN)
      CALL HIBKGRD(NCHLN3,N03,SUM3,AVE3,NCNTS,NCHAN)
      CALL AREA(AVE1,SUM2,AVE3,NCHLN1,NCHLN3,NCHLN4,NCHLN5,
      N02,NAREA,ERRCP)
      GC TC 40
70   REWIND 4
C
C   PROCESS NEXT SPECTRUM
C
      GC TC 10
80   STOP
1000  FORMAT(5X,I6/I4,9(1X,I6))
2000  FORMAT(14,10I7)
3000  FORMAT(11,'SPECTRUM ',I2)
4000  FORMAT(10,'50X','URANIUM L-ALPHA PEAK DATA',/)
4100  FORMAT(///38X,'URANIUM L-BETA2 + MOLYBDENUM K-ALPHA COMPTON PEAK
      & DATA',/)
7100  FORMAT(4I4,3I3)
      END

```

Listing E.2.

SPECTRUM # 1

- 315 -

URANIUM L-ALPHA PEAK DATA

LOW SIDE AVERAGE BACKGROUND(COUNTS) = 145
HIGH SIDE AVERAGE BACKGROUND(COUNTS) = 573
TOTAL AREA UNDER PEAK(COUNTS) = 30020
NET AREA UNDER PEAK(COUNTS) = 29627
STATISTICAL COUNTING ERROR = 174
COEFFICIENT OF VARIATION(%) = .59

URANIUM L-BETA2 + MOLYBDENUM K-ALPHA COMPTON PEAK DATA

LOW SIDE AVERAGE BACKGROUND(COUNTS) = 163
HIGH SIDE AVERAGE BACKGROUND(COUNTS) = 26
TOTAL AREA UNDER PEAK(COUNTS) = 23706
NET AREA UNDER PEAK(COUNTS) = 23433
STATISTICAL COUNTING ERROR = 154
COEFFICIENT OF VARIATION(%) = .66

APPENDIX F

F.1. Programme MXRAY

Programme MKRAY, listing F.1, was written to analyze the net U $M_{\alpha,\beta}$ and the La L_{α} peak areas as observed in the M X-ray spectrum. The basic routine is analogous to that previously described in programmes KXRAY and LXRAY. Using the instrumental settings listed in table 10, the control file, CONTROLM, is:

```
3151393132323369 30138 25
```

```
3151393136623727 30 66 25
```

For a description of the purpose of the control file, see appendix D. In the M X-ray case, it was observed that La L-shell fluorescence, probably mostly La L_1 , i.e. $L_{III} M_I$ transition, contributes to the measured U $M_{\alpha,\beta}$ peak area. This interference was measured and the total contribution to the uranium fluorescence amounted to 3.35% of the La L_{α} peak area. The main programme MXRAY also evaluates this correction. Listing F.2 contains the typical output from MXRAY showing both the measured data and the corrected data for the U $M_{\alpha,\beta}$ peak area.

Listing F.1.

```

C
C          PROGRAMME MXRAY
C
C
C   THIS PROGRAMME MEASURES THE INTENSITIES OF THE
C   URANIUM M-ALPHA, BETA AND THE LANTHANUM L-ALPHA
C   PEAKS AS REQUIRED BY THE M X-RAY EXPERIMENT.
C
C   DIMENSION NCNTS(1000)
C   DATA NCNTS/1000*1/
C
C   SET SPECTRUM NUMBER AND PEAK NUMBER COUNTERS TO ZERO
C
C   JCHK=0
10  ICHK=0
C
C   READ IN ONE COMPLETE SPECTRUM
C
C   READ(5,1000,END=80)PT,NCHAN,(NCNTS(I),I=1,9,
C   DO 20 I=10,1000,10
C   K=I+9
C   READ(5,2000,END=30)IZ,(NCNTS(J),J=I,K)
C   IF (IZ.NE.0)GO TO 20
C   BACKSPACE 5
C   GO TO 30
20  CONTINUE
30  JCHK =JCHK+1
C   WRITE(6,3000)JCHK
40  ICHK=ICHK+1
C
C   DETERMINE WHICH PEAK IS TO BE ANALYZED
C
C   IF (ICHK.EQ.2)GO TO 50
C   IF (ICHK.EQ.3)GO TO 70
C   WRITE(6,4000)

```

Listing F.1. (continued)

```

50      GO TO 60
        WRITE(6,4100)
        UMA1=NAREA
        UERR=ERROR
        GO TO 60
C
C      READ IN CONTROL FILE
C
60      READ(4,7100)NCHLN1,NCHLN3,NCHLN4,NCHLN5,N01,N02,N03
C
C      EVALUATE NET PEAK AREA AND THE STATISTICAL PRECISION
C
        CALL LBKGRD(NCHLN1,N01,SUM1,AVE1,NCNTS,NCHAN)
        CALL PEAK(NCHLN4,NCHLN5,SUM2,NCNTS,NCHAN)
        CALL HIBKGRD(NCHLN3,N03,SUM3,AVE3,NCNTS,NCHAN)
        CALL AREA(AVE1,SUM2,AVE3,NCHLN1,NCHLN3,NCHLN4,NCHLN5,
5N02,NAREA,ERROR)
        GO TO 40
C
C      CALCULATE CORRECTION FOR URANIUM PEAK
C
70      LALA1=NAREA
        LAERR=ERROR
        WRITE(6,4200)
        CERU=UMA1-0.0335*LALA1
        USTD=SQRT(UERR**2 + 0.0335*LALA1)
        RLSTD= 100*USTD/CERU
        WRITE(6,5000)CERU
        WRITE(6,5100)USTD
        WRITE(6,5200)RLSTD
        REWIND 4
C
C      PROCESS NEXT SPECTRUM
C
        GO TO 10

```

Listing F.1. (continued)

```
80   STCP
1000  FORMAT(5X,I6/I4,9(1X,I6))
2000  FORMAT(I4,10I7)
3000  FORMAT('1','SPECTRUM #',I2)
4000  FORMAT(5//50X,'URANIUM M-ALPHA,BETA PEAK DATA',/)
4100  FORMAT(///50X,'LANTHANUM L-ALPHA PEAK DATA',/)
4200  FORMAT(///50X,'CORRECTED URANIUM PEAK DATA',/)
5000  FORMAT(40X,'CORRECTED URANIUM M-ALPHA,BETA PEAK(COUNTS) = ',I6)
5100  FORMAT(40X,'STATISTICAL COUNTING ERROR(COUNTS) = ',I6)
5200  FORMAT(40X,'COEFFICIENT OF VARIATION(%) = ',F6.2)
7100  FORMAT(4I4,3I3)
      END
```

Listing F.2.

SPECTRUM # 1

URANIUM M-ALPHA, BETA PEAK DATA

LOW SIDE AVERAGE BACKGROUND(COUNTS) = 23
HIGH SIDE AVERAGE BACKGROUND(COUNTS) = 4
TOTAL AREA UNDER PEAK(COUNTS) = 14603
NET AREA UNDER PEAK(COUNTS) = 11855
STATISTICAL COUNTING ERROR = 131
COEFFICIENT OF VARIATION(%) = 1.11

LANTHANUM L-ALPHA PEAK DATA

LOW SIDE AVERAGE BACKGROUND(COUNTS) = 23
HIGH SIDE AVERAGE BACKGROUND(COUNTS) = 4
TOTAL AREA UNDER PEAK(COUNTS) = 38384
NET AREA UNDER PEAK(COUNTS) = 37717
STATISTICAL COUNTING ERROR = 197
COEFFICIENT OF VARIATION(%) = .52

CORRECTED URANIUM PEAK DATA

CORRECTED URANIUM M-ALPHA, BETA PEAK(COUNTS) = 10591
STATISTICAL COUNTING ERROR(COUNTS) = 136
COEFFICIENT OF VARIATION(%) = 1.29

APPENDIX G

G.1. Programme GAMARAY

The programme GAMARAY, listing G.1, measures the 0.186 MeV ^{235}U and the 0.0925 MeV doublet ^{234}Th peak areas as required by the γ -spectroscopy experiment. As written in the listing, the programme produced the data presented in tables 55-56. A total of six peaks were unfolded requiring 18 iteration parameters. The background was measured at a convenient location adjacent to the ^{234}Th peaks. Once shown, that Cauchy functions could approximate the spectrum, the number of iteration parameters were reduced to 10 by fixing all peak locations and some relative intensities to constant values. No changes are required for GAMARAY except that the number of initial iteration parameters read in must be reduced.

Because the ^{234}Th intensity is approximated by a series of Cauchy functions, the data are read in a different manner. In the previous three appendices, three spectra were taken from each specimen, analyzed and the results averaged. In this case, three spectra were taken from each specimen, averaged and then analyzed. Accordingly, two internal counters are employed, JCHK and JEND. JCHK, as before keeps count of the spectrum number and JEND labels each specimen. The programme analyzes the net ^{235}U area first in the fashion used for the X-ray experiments. The first record of the control file, ISOCTL, contains the required peak area calculation constants.

The averaged data are then smoothed by a nine point best least squares smoothing subroutine, SMOOTH, to remove much of the random

Listing G.1.

```

C
C          PROGRAMME G/M/RAY
C
C
C          THIS PROGRAMME MEASURES THE NET INTENSITIES OF THE
C          OF THE 0.186 MEV 235-URANIUM AND THE 0.0925 MEV DOUBLET
C          234-THORIUM GAMMA-RAYS AS DESCRIBED BY THE GAMMA
C          SPECTROSCOPY EXPERIMENT.
C
C          EXTERNAL FUNCT
C          INTEGER THBACK
C          DIMENSION NCNTS(1000),MCNTS(1000),MCHAN(1000),NARRAY(1000)
C          DIMENSION ARG(12),GRAD(12),H(225)
C          COMMON MCNTS,MCHAN,THBACK
C          DATA NCNTS/1000*-1/,NARRAY/1000*0/
C
C          INITIALIZE SPECIMEN NUMBER AND SPECTRUM NUMBER
C
C          JEND=0
10  JCHK=1
C          JEND=JEND+1
C
C          READ IN ONE COMPLETE SPECTRUM
C
15  READ(5,3000,END=90)RT,NCHAN,(NCNTS(I),I=1,9)
C          DO 20 I=10,1000,10
C          K=I+9
C          READ(5,3100,END=90)IZ,(MCNTS(J),J=I,K)
C          IF (IZ.NE.0100) GO TO 20
C          BACKSPACE 5
C          GO TO 30
20  CONTINUE
30  CONTINUE
C
C          TAKE THE AVERAGE OF THREE SPECTRA

```

Listing G.1. (continued)

```

C
C   DO 35 K=1,N
35  NARRAY(K)=NARRAY(K)+NCNTS(K)
C   IF (JCHK.EQ.3)GO TO 40
C   JCHK=JCHK+1
C   GO TO 15
40  DO 50 L=1,N
50  NCNTS(L)=NARRAY(L)/JCHK
C
C   READ IN CONTROL FILE FOR 235-U PEAK AREA DETERMINATION
C
C   READ(4,4000)NCHLN1,NCHLN3,NCHLN4,NCHLN5,N01,N02,N03
C
C   EVALUATE THE NET 235-U PEAK AREA AND ITS STATISTICAL PRECISION
C
C   WRITE(6,5000)
C   CALL LBKGRD(NCHLN1,N01,SUM1,AVE1,NCNTS,NCHAN)
C   CALL PEAK(NCHLN4,NCHLN5,SUM2,NCNTS,NCHAN)
C   CALL HBKGRD(NCHLN3,N03,SUM3,AVE3,NCNTS,NCHAN)
C   CALL AREA(AVE1,SUM2,AVE3,NCHLN1,NCHLN3,NCHLN4,NCHLN5,
C   SUM2,AREA,ERROR)
C
C   SMOOTH DATA PRIOR TO MINIMIZING FUNCTION
C
C   READ(4,1000)N
C   CALL SMOOTH(N,NCNTS,M,MCNTS)
C
C   READ IN INITIAL ITERATION ARGUMENTS AND DEFINE
C   REQUIRED CONTROL CONSTANTS.
C
C   READ(4,6000)(ARG(I),I=1,18)
C   EST=0
C   EPS=10**(-6)
C   LIMIT=50
C   NARG=18

```

Listing G.1. (continued)

```

C
C   CREATE LINEAR ARRAY OF CHANNEL NUMBERS
C
C   MCHAN(1)=0
C   DO 60 I=2,130
60  MCHAN(I)=MCHAN(I-1)+1
C
C   ESTIMATE BACKGROUND IN THE VICINITY OF THE 234-TH PEAKS
C
C   CALL BACK(N02)
C
C   MINIMIZE FUNCTION AND OUTPUT CONVERGENCE INFORMATION
C
C   CALL FMFP(FUNCT,NARG,ARG,VAL,GRAD,EST,EPS,LIMIT,IER,H)
C   IF(IER.NE.C)OUTPUT IER
C   WRITE(6,6210)(ARC(I),I=1,18)
C   WRITE(6,6220)VAL
C
C   EVALUATE THE NET 234-TH DOUBLET PEAK AREA BY INTEGRATION
C   OF THE TWO ASSIGNED CAUCHY FUNCTIONS
C
C   CALL GAMMA1(ARG,NINTE)
C
C   EVALUATE THE PRECISION OF THE 234-TH PEAKS
C
C   U238=NAREA
C   U238=NINTE*50*THBACK
C   E1NTE=SQRT(NINTE)
C   RINTE=100*E1NTE/U238
C
C   OUTPUT UNFOLDED PEAK AREAS AND PRECISION
C
C   WRITE(6,6100)
C   WRITE(6,6110)THBACK
C   TBACK=50*THBACK

```

Listing G.1. (continued)

```

WRITE(6,6120)TBACK
WRITE(6,6130)L238
WRITE(6,6140)EINTEN
WRITE(6,6150)PINTEN
REWIND 4
DC 70 L=1,N
70 NARRAY(L)=0
C
C PROCESS NEXT SPECIMEN
C
GO TO 1C
90 STOP
1000 FORMAT(I3)
3000 FORMAT(5X,I6/I4,9(1X,I6))
3100 FORMAT(I4,10I7)
4000 FORMAT(4I4,3I3)
5000 FORMAT('1',50X,'L-235 PEAK DATA(AT 185 KEV)',//)
6000 FORMAT(10F/8F)
6100 FORMAT(/////50X,'TH-234 PEAK DATA(AT 92.25 AND 92.70 KEV)',//)
6110 FORMAT(40X,'BACKGROUND COUNTS PER CHANNEL = ',I4)
6120 FORMAT(40X,'TOTAL BACKGROUND UNDER PEAKS = ',I6)
6130 FORMAT(40X,'NET PEAK AREA = ',I6)
6140 FORMAT(40X,'STATISTICAL PRECISION(CTS) = ',I6)
6150 FORMAT(40X,'RELATIVE STATISTICAL ERROR(%) = ',F6.2)
6210 FORMAT('1',40X,'ITERATION PARAMETERS ARE: ',/(52X,F10.3))
6220 FORMAT(////////,40X,'FUNCTION VALUE IS: ',F9.4)
END

```

statistical fluctuations present in the spectrum data. The background in the vicinity of the 0.0925 MeV ^{234}Th peaks was estimated using the subroutine BACK, listing G.2. The portion of the spectrum neighbouring the Th doublet was then subjected to the function minimization subroutine FMFP. Appendix H contains a listing and description of both SMOOTH and FMFP. Subroutine GAMMA1, listing G.3. evaluates the net ^{234}Th peak area by numerically integrating the two Cauchy functions assigned to the doublet.

The starting iteration parameters were read in through the same control file as the peak area calculation constants. The second record contains the number of points to be smoothed and the following records contain the initial 18 iteration parameters. The complete control file is as follows:

```
3870394038903929 10 40 10
809
158.,55.6,6.6,1950.,78 4,612,282.,80.2;5.,1908.,
74.4,5.3,483.,91.7,6.8,834.,119.,7.1,
```

Listing G.4 presents typical output from GAMARAY. The statistical precision data listed for the ^{234}Th peaks are the S_N values discussed in the gamma ray results and discussions section

Listing G.2.

```
C      SUBROUTINE BACK(NC2)
C
C      THIS PROGRAMME ESTIMATES THE BACKGROUND IN THE VICINITY
C      OF THE 234-THORIUM PEAKS.
C
      INTEGER THBACK
      DIMENSION MCNTS(1000),MCHAN(1000)
      COMMON MCNTS,MCHAN,THBACK
      TOTAL=0
      DO 10 I=139,158
10     TOTAL=TOTAL+MCNTS(I)
      THBACK=TOTAL/NC2+.5
      RETURN
      END
```

Listing G.3.

```
C
  SUBROUTINE GAMMA1(ARG,NINTEN)
C
C   THIS SUBROUTINE EVALUATES THE NET 234-THORIUM PEAK
C   AREA BY INTEGRATION OF THE TWO ASSIGNED CAUCHY FUNCTIONS.
C
  INTEGER THBACK
  DIMENSION MCNTS(1000),MCHAN(1000),ARG(1)
  COMMON MCNTS,MCHAN,THBACK
  NINTEN=0
  DO 10 I=50,100
    NINTEN=NINTEN+ARG(4)/(1+(2*(MCHAN(I)-ARG(5))/ARG(6)
    5)**2)+ARG(10)/(1+(2*(MCHAN(I)-ARG(11))/ARG(12)
    5)**2)+THBACK
  10 CONTINUE
  RETURN
  END
```

Listing G.4.

ITERATION PARAMETERS ARE:

2256.801
56.505
4.690
3365.373
78.427
5.233
2538.722
81.138
4.731
3266.694
75.127
5.566
7838.730
92.790
6.096
15114.250
119.742
6.965

FUNCTION VALUE IS: 1212.7390

Listing G.4. (continued)

U-235 PEAK DATA(AT 185 KEV)

LOW SIDE TOTAL BACKGROUND(COUNTS) = 9665
HIGH SIDE TOTAL BACKGROUND(COUNTS) = 2539
TOTAL AREA UNDER PEAK (COUNTS) = 853474
NET AREA UNDER PEAK(COUNTS) = 830221
STATISTICAL ERROR(COUNTS) = 924
RELATIVE STATISTICAL ERROR(%) = .11

TH-234 PEAK DATA(AT 92.25 AND 92.70 KEV)

BACKGROUND COUNTS PER CHANNEL = 1292
TOTAL BACKGROUND UNDER PEAKS = 64600
NET PEAK AREA = 53473
STATISTICAL PRECISION(CTS) = 343
RELATIVE STATISTICAL ERROR(%) = .64

APPENDIX H

H.1. Spectrum approximation by Cauchy functions

Three basic steps are required to fit a series of Cauchy functions to the spectrum (i) the data must be smoothed to remove random statistical fluctuations, (ii) a function must be designed such that its minimum value will yield the best fit of the Cauchy functions to the smoothed data, and (iii) minimization of this function.

The first step was performed using the nine point best least squares cubic polynomial smoothing subroutine, SMOOTH, as shown in listing H.1. Best results are obtained if several spectra are taken and the results averaged prior to smoothing. The averaged spectrum can then be subjected to consecutive smoothing operations if desirable. The smoother the data, the easier and faster the function can be minimized

The function to be minimized was defined by equation 3.11 such that the sum of the squares of the differences between the initial data and the series of Cauchy functions be a minimum, i.e.

$$M(P_1, P_2, P_3, \dots, P_{3m}, b) = \sum_{i=1}^m \left\{ \sum_{j=1}^m (c_{ij} + b) - y_i \right\}^2$$

All parameters are defined in section 3.6.2. The minimization procedure requires a subroutine to evaluate this function and the gradients of this function with respect to each one of the iteration parameters in order to find the function minimum. The gradient calculations required are: (1) with respect to the P_{3j-2} parameter,

Listing H.1.

```

C      SUBROUTINE SMOOTH(N,NCNTS,M,PCNTS)
C
C      THIS SUBROUTINE SMOOTHS RAW DATA USING A NINE POINT
C      CUBIC BEST SQUARES ROUTINE
C
C      DIMENSION NCNTS(1000),PCNTS(1000),NP(9)
C      COMMON PCNTS MCHAN,THBACK
C      M=N*8
C      DO 10 I=2,9
C      J=I-1
C      NP(I)=NCNTS(J)
C      DO 200 I=1,M
C      J=I+8
C      DO 11 K=1,8
C      KA=K+1
C      NP(K)=NP(KA)
C      NP(9)=NCNTS(J)
C      NSUM=59*NP(5)+54*(NP(4)+NP(6))+39*(NP(3)+NP(7))+
C      514*(NP(2)+NP(8))+21*(NP(1)+NP(9))
C      PCNTS(I)=NSUM/231
C      CONTINUE
C      RETURN
C      END
200

```

$$\frac{\partial M}{\partial P_{3j-2}} = \frac{\partial}{\partial P_{3j-2}} \sum_{i=1}^n \sum_{j=1}^m (c_{ij} + b) - y_i^2$$

$$= 2 \sum_{i=1}^n \sum_{j=1}^m \frac{(c_{ij} + b - y_i)}{(1 + [2(x_i - P_{3j-1})/P_{3j}]^2)} \dots \dots \dots \text{H.1}$$

(ii) with respect to the P_{3j-1} parameter,

$$\frac{\partial M}{\partial P_{3j-1}} = \frac{\partial}{\partial P_{3j-1}} \sum_{i=1}^n \sum_{j=1}^m (c_{ij} + b) - y_i^2$$

$$= 16 \sum_{i=1}^n \sum_{j=1}^m \frac{(c_{ij} + b - y_i)(x_i - P_{3j-1})P_{3j-2}}{P_{3j}^2(1 + [2(x_i - P_{3j-1})/P_{3j}]^2)^2} \dots \dots \dots \text{H.2}$$

(iii) with respect to the P_{3j} parameter,

$$\frac{\partial M}{\partial P_{3j}} = \frac{\partial}{\partial P_{3j}} \sum_{i=1}^n \sum_{j=1}^m (c_{ij} + b) - y_i^2$$

$$= 16 \sum_{i=1}^n \sum_{j=1}^m \frac{(c_{ij} + b - y_i)(x_i - P_{3j-1})^2 P_{3j-2}}{P_{3j}^3(1 + [2(x_i - P_{3j-1})/P_{3j}]^2)^2} \dots \dots \dots \text{H.3}$$

and (iv) with respect to the background parameter, b.

$$\frac{\partial M}{\partial b} = 2 \sum_{i=1}^n \sum_{j=1}^m (c_{ij} + b - y_i) \dots \dots \dots \text{H.4}$$

Subroutine FUNCT, listing H.2, evaluates the function and the gradients necessary to approximate six peaks by Cauchy functions. The background parameter was replaced by a constant hence only eighteen gradients are included. Generally it is wise to use as few iteration parameters as

Listing H.2.

```

C
SUBROUTINE FUNCT(NARG,ARG,VAL,GRAD)
C
C THIS SUBROUTINE CALCULATES THE FUNCTION VALUE AND THE
C GRADIENT VALUE WITH RESPECT TO EACH OF THE ITERATION
C PARAMETERS FOR THE MINIMIZATION FUNCTION AS DESCRIBED
C FOR THE GAMMA RAY SPECTROSCOPY EXPERIMENT.
C
INTEGER THBACK
DIMENSION MCNTS(1000),ARG(18),GRAD(18)
DIMENSION MCHAN(1000)
COMMON MCNTS,MCHAN,THBACK
DO 10 K=1,NARG
GRAD(K)=0
10 CONTINUE
VAL=0
DO 30 I=45,130
X=0
LEXP=NARG
C
C CALCULATE THE FUNCTION VALUE
C
DO 20 J=3,LEXP,3
K=J-2
ASUM=ARG(K)/((1+(2*(MCHAN(I)-ARG(K+1)))/ARG(K+2))**2)
20 X=X+ASUM
F=X+THBACK
DEV=F-MCNTS(I)
VAL=VAL+(DEV**2)*10**(-5)
C
C CALCULATE THE GRADIENT VALUES
C
DEN1=1/((1+(2*(MCHAN(I)-ARG(2)))/ARG(3))**2)
DEN2=1/((1+(2*(MCHAN(I)-ARG(5)))/ARG(6))**2)
DEN3=1/((1+(2*(MCHAN(I)-ARG(8)))/ARG(9))**2)

```

Listing H.2. (continued)

```

DEN4=1/(1+(2*(MCHAN(I)-ARG(11))/ARG(12))**2)
DEN5=1/(1+(2*(MCHAN(I)-ARG(14))/ARG(15))**2)
DEN6=1/(1+(2*(MCHAN(I)-ARG(17))/ARG(18))**2)
Z=16*DEV
GRAD(1)=GRAD(1)+2*DEV*(DEN1)
GRAD(2)=GRAD(2)+Z*ARG(1)*(MCHAN(I)-ARG(2))*(DEN1)**2/(ARG(3))**2
GRAD(3)=GRAD(3)+Z*ARG(1)*(MCHAN(I)-ARG(2))**2*(DEN1)**2/
5(ARG(3))**3
GRAD(4)=GRAD(4)+2*DEV*(DEN2)
GRAD(5)=GRAD(5)+Z*ARG(4)*(MCHAN(I)-ARG(5))*(DEN2)**2/(ARG(6))**2
GRAD(6)=GRAD(6)+Z*ARG(4)*(MCHAN(I)-ARG(5))**2*(DEN2)**2/
5(ARG(6))**3
GRAD(7)=GRAD(7)+2*DEV*(DEN3)
GRAD(8)=GRAD(8)+Z*ARG(7)*(MCHAN(I)-ARG(8))*(DEN3)**2/(ARG(9))**2
GRAD(9)=GRAD(9)+Z*ARG(7)*(MCHAN(I)-ARG(8))**2*(DEN3)**2/
5(ARG(9))**3
GRAD(10)=GRAD(10)+2*DEV*(DEN4)
GRAD(11)=GRAD(11)+Z*ARG(10)*(MCHAN(I)-ARG(11))*(DEN4)**2/
5(ARG(12))**2
W1=(MCHAN(I)-ARG(11))**2
GRAD(12)=GRAD(12)+Z*ARG(10)*W1*(DEN4)**2/(ARG(12))**3
GRAD(12)=GRAD(12)+Z*ARG(10)*W1*(DEN4)**2/(ARG(12))**3
GRAD(13)=GRAD(13)+2*DEV*(DEN5)
GRAD(14)=GRAD(14)+Z*ARG(13)*(MCHAN(I)-ARG(14))*(DEN5)**2/
5(ARG(15))**2
W2=(MCHAN(I)-ARG(14))**2
GRAD(15)=GRAD(15)+Z*ARG(13)*W2*(DEN5)**2/(ARG(15))**3
GRAD(16)=GRAD(16)+2*DEV*(DEN6)
GRAD(17)=GRAD(17)+Z*ARG(16)*(MCHAN(I)-ARG(17))*(DEN6)**2/
5(ARG(18))**2
W3=(MCHAN(I)-ARG(17))**2
GRAD(18)=GRAD(18)+Z*ARG(16)*W3*(DEN6)**2/(ARG(18))**3
CONTINUE
RETURN
END

```

possible. If any of the iteration parameters can be replaced by known constants, then convergence is considerably more rapid and less expensive. Major changes in the programming are required only for the subroutine FUNCT.

The minimization subroutine used is shown in listing H.3. A complete description of the routine can be found in reference (83).

Listing H.3.

```

C
C .....
C
C   SUBROUTINE FMFF
C
C   PURPOSE
C       TO FIND A LOCAL MINIMUM OF A FUNCTION OF SEVERAL VARIABLES
C       BY THE METHOD OF FLETCHER AND POWELL
C
C   USAGE
C       CALL FMFF(FUNCT,N,X,F,G,EST,EPS,LIMIT,IER,H)
C
C   DESCRIPTION OF PARAMETERS
C       FUNCT - USER-WRITTEN SUBROUTINE CONCERNING THE FUNCTION TO
C               BE MINIMIZED. IT MUST BE OF THE FORM
C               SUBROUTINE FUNCT(N,ARG,VAL,GRAD)
C               AND MUST SERVE THE FOLLOWING PURPOSE
C               FOR EACH N-DIMENSIONAL ARGUMENT VECTOR ARG,
C               FUNCTION VALUE AND GRADIENT VECTOR MUST BE COMPUTED
C               AND, ON RETURN, STORED IN VAL AND GRAD RESPECTIVELY
C
C       N     - NUMBER OF VARIABLES
C       X     - VECTOR OF DIMENSION N CONTAINING THE INITIAL
C               ARGUMENT WHERE THE ITERATION STARTS. ON RETURN,
C               X HOLDS THE ARGUMENT CORRESPONDING TO THE
C               COMPUTED MINIMUM FUNCTION VALUE
C       F     - SINGLE VARIABLE CONTAINING THE MINIMUM FUNCTION
C               VALUE ON RETURN, I.E. F=F(X).
C       G     - VECTOR OF DIMENSION N CONTAINING THE GRADIENT
C               VECTOR CORRESPONDING TO THE MINIMUM ON RETURN,
C               I.E. G=G(X).
C       EST  - IS AN ESTIMATE OF THE MINIMUM FUNCTION VALUE.
C       EPS  - TESTVALUE REPRESENTING THE EXPECTED ABSOLUTE ERROR.
C               A REASONABLE CHOICE IS 10**(-6), I.E.
C               SOMEWHAT GREATER THAN 10**(-D), WHERE D IS THE
C               NUMBER OF SIGNIFICANT DIGITS IN FLOATING POINT
C

```

Listing H.3. (continued)

```

C      REPRESENTATION.
C      . LIMIT - MAXIMUM NUMBER OF ITERATIONS.
C      IER    - ERROR PARAMETER
C              IER = 0 MEANS CONVERGENCE WAS OBTAINED
C              IER = 1 MEANS NO CONVERGENCE IN LIMIT ITERATIONS
C              IER = -1 MEANS ERRORS IN GRADIENT CALCULATION
C              IER = 2 MEANS LINEAR SEARCH TECHNIQUE INDICATES
C              . IT IS LIKELY THAT THERE EXISTS NO MINIMUM.
C              .
C              . - WORKING STORAGE OF DIMENSION N*(N+7)/2.
C
C      REMARKS
C      I) THE SUBROUTINE NAME REPLACING THE DUMMY ARGUMENT FUNCT
C         MUST BE DECLARED AS EXTERNAL IN THE CALLING PROGRAM.
C      II) IER IS SET TO 2 IF, STEPPING IN ONE OF THE COMPUTED
C          DIRECTIONS, THE FUNCTION WILL NEVER INCREASE WITHIN
C          A TOLERABLE RANGE OF ARGUMENT.
C          IER = 2 MAY OCCUR ALSO IF THE INTERVAL WHERE F
C          INCREASES IS SMALL AND THE INITIAL ARGUMENT WAS
C          RELATIVELY FAR AWAY FROM THE MINIMUM SUCH THAT THE
C          MINIMUM WAS OVERLEAPED. THIS IS DUE TO THE SEARCH
C          TECHNIQUE WHICH DOUBLES THE STEPSIZE UNTIL A POINT
C          IS FOUND WHERE THE FUNCTION INCREASES.
C
C      SUBROUTINES AND FUNCTION SUBPROGRAMS REQUIRED
C      FUNCT
C
C      METHOD
C      THE METHOD IS DESCRIBED IN THE FOLLOWING ARTICLE
C      R. FLETCHER AND M.J.D. POWELL, A RAPID DESCENT METHOD FOR
C      MINIMIZATION)
C      COMPUTER JOURNAL VOL.6, ISS. 2, 1963, PP.163-168.
C
C      .....
C
C      SUBROUTINE FMFP(FUNCT,N,X,F,G,FST,EPS,LIMIT,IER,H)

```

Listing H.3. (continued)

```

C
C      DIMENSIONED DUMMY VARIABLES
      DIMENSION H(1),X(1),G(1)
C
C      COMPUTE FUNCTION VALUE AND GRADIENT VECTOR FOR INITIAL ARGUMENT
      CALL FUNCT(N,X,F,G)
C
C      RESET ITERATION COUNTER AND GENERATE IDENTITY MATRIX
      IER=0.
      KCUNT=0
      N2=N+N
      N3=N2+N
      N31=N3+1
1     K=N31
      DO 4 J=1,N
      F(K)=1.
      NJ=N-J
      IF(NJ)5,5,2
2     DO 3 L=1,NJ
      KL=K+L
3     F(KL)=C.
4     K=KL+1
C
C      START ITERATION LOOP
5     KCUNT=KCUNT +1
C
C      SAVE FUNCTION VALUE, ARGUMENT VECTOR AND GRADIENT VECTOR
      ELDF=F
      DO 9 J=1,N
      K=N+J
      F(K)=G(J)
      K=K+N
      F(K)=X(J)
C
C      DETERMINE DIRECTION VECTOR H

```

Listing H.3. (continued)

```

      K=J+N3
      T=0.
      DO 8 L=1,N
      T=T-G(L)*H(K)
      IF(L=J)6,7,7
6     K=K+N-L
      GO TO 8
7     K=K+1
8     CONTINUE
9     H(J)=T
C
C     CHECK WHETHER FUNCTION WILL DECREASE STEPPING ALONG H.
      DY=0.
      HNRM=0.
      GNRM=0.
C
C     CALCULATE DIRECTIONAL DERIVATIVE AND TEST VALUES FOR DIRECTION
C     VECTOR H AND GRADIENT VECTOR G.
      DO 10 J=1,N
      HNRM=HNRM+ABS(H(J))
      GNRM=GNRM+ABS(G(J))
10    DY=DY+H(J)*G(J)
C
C     REPEAT SEARCH IN DIRECTION OF STEEPEST DESCENT IF DIRECTIONAL
C     DERIVATIVE APPEARS TO BE POSITIVE OR ZERO.
      IF(DY)11,51,51
C
C     REPEAT SEARCH IN DIRECTION OF STEEPEST DESCENT IF DIRECTION
C     VECTOR H IS SMALL COMPARED TO GRADIENT VECTOR G.
11   IF(HNRM/GNRM=EPS)51,51,12
C
C     SEARCH MINIMUM ALONG DIRECTION H
C
C     SEARCH ALONG H FOR POSITIVE DIRECTIONAL DERIVATIVE
12   FY=F

```

Listing H.3. (continued)

```

        ALFA=2.*(EST-F)/DY
        AMBDA=1.
C
C     USE ESTIMATE FOR STEPSIZE ONLY IF IT IS POSITIVE AND LESS THAN
C     1. OTHERWISE TAKE 1. AS STEPSIZE
        IF(ALFA)15,15,13
13 IF(ALFA=AMBDA)14,15,15
14 AMBDA=ALFA
15 ALFA=C.
C
C     SAVE FUNCTION AND DERIVATIVE VALUES FOR OLD ARGUMENT
16 FX=FY
    DX=DY
C
C     STEP ARGUMENT ALONG H
    DO 17 I=1,N
17 X(I)=Y(I)+AMBDA*H(I)
C
C     COMPUTE FUNCTION VALUE AND GRADIENT FOR NEW ARGUMENT
    CALL FUNCT(N,X,F,G)
    FY=F
C
C     COMPUTE DIRECTIONAL DERIVATIVE DY FOR NEW ARGUMENT. TERMINATE
C     SEARCH, IF DY IS POSITIVE. IF DY IS ZERO THE MINIMUM IS FOUND
    DY=C.
    DO 18 I=1,N
18 DY=DY+G(I)*H(I)
    IF(DY)19,36,22
C
C     TERMINATE SEARCH ALSO IF THE FUNCTION VALUE INDICATES THAT
C     A MINIMUM HAS BEEN PASSED
19 IF(FY=FX)20,22,22
C
C     REPEAT SEARCH AND DOUBLE STEPSIZE FOR FURTHER SEARCHES
20 AMBDA=AMBDA+ALFA

```

Listing H.3. (continued)

```

        ALFA=AMBDA
C         END OF SEARCH LOOP
C
C         TERMINATE IF THE CHANGE IN ARGUMENT GETS VERY LARGE
        IF(HNRM*AMBDA-1.E10)15,16,21
C
C         LINEAR SEARCH TECHNIQUE INDICATES THAT NO MINIMUM EXISTS
21 IER=2
        RETURN
C
C         INTERPOLATE CUBICALLY IN THE INTERVAL DEFINED BY THE SEARCH
C         ABOVE AND COMPUTE THE ARGUMENT X FOR WHICH THE INTERPOLATION
C         POLYNOMIAL IS MINIMIZED
22 T=0.
23 IF(AMBDA)24,36,24
24 Z=3.*(FX-FY)/AMBDA+DX+DY
        ALFA=AMAX1(ABS(Z),ABS(DX),ABS(DY))
        DALFA=Z/ALFA
        DALFA=DALFA+DALFA-DX/ALFA+DY/ALFA
        IF(DALFA)51,25,25
25 W=ALFA*SQRT(DALFA)
        ALFA=DY-DX+W+W
        IF(ALFA) 250,251,250
250 ALFA=(DY-Z+W)/ALFA
        GO TO 252
251 ALFA=(Z+DY-W)/(Z+DX+Z+DY)
252 ALFA=ALFA*AMBDA
        DO 26 I=1,N
26 X(I)=X(I)+(T-ALFA)*H(I)
C
C         TERMINATE, IF THE VALUE OF THE ACTUAL FUNCTION AT X IS LESS
C         THAN THE FUNCTION VALUES AT THE INTERVAL ENDS. OTHERWISE REDUCE
C         THE INTERVAL BY CHOOSING ONE END-POINT EQUAL TO X AND REPEAT
C         THE INTERPOLATION. WHICH END-POINT IS CHOSEN DEPENDS ON THE
C         VALUE OF THE FUNCTION AND ITS GRADIENT AT X

```

Listing H.3. (continued)

```

C
  CALL FUNCT(N,X,F,G)
  IF(F=FX)27,27,28
27 IF(F=FY)36,36,28
28 DALFA=C.
  DO 29 I=1,N
29 DALFA=DALFA+G(I)*H(I)
  IF(DALFA)30,33,33
30 IF(F=FX)32,31,33
31 IF(DX=DALFA)32,36,32
32 FX=F
  DX=DALFA
  T=ALFA
  AMBDA=ALFA
  GO TO 23
33 IF(FY=F)35,34,35
34 IF(DY=DALFA)35,36,35
35 FY=F
  DY=DALFA
  AMBDA=AMBDA-ALFA
  GO TO 22

C
C   TERMINATE, IF FUNCTION HAS NOT DECREASED DURING LAST ITERATION
36 IF(ELDF=F+EPS)51,38,38

C
C   COMPUTE DIFFERENCE VECTORS OF ARGUMENT AND GRADIENT FROM
C   TWO CONSECUTIVE ITERATIONS
38 DO 37 J=1,N
  K=N+J
  H(K)=G(J)-H(K)
  K=N+K
37 H(K)=X(J)-H(K)

C
C   TEST LENGTH OF ARGUMENT DIFFERENCE VECTOR AND DIRECTION VECTOR
C   IF AT LEAST N ITERATIONS HAVE BEEN EXECUTED. TERMINATE, IF

```

Listing H.3. (continued)

```

C      BOTH ARE LESS THAN EPS
      IER=0
      IF(KCUNT=N)42,39,39
39  T=0.
      Z=0.
      DO 40 J=1,N
      K=N+J
      W=H(K)
      K=K+N
      T=T+ABS(H(K))
40  Z=Z+W*H(K)
      IF(WARM-EPS)41,41,42
41  IF(T-EPS)56,56,42

C
C      TERMINATE, IF NUMBER OF ITERATIONS WOULD EXCEED LIMIT
42  IF(KCUNT=LIMIT)43,50,50

C
C      PREPARE UPDATING OF MATRIX H
43  ALFA=0.
      DO 47 J=1,N
      K=J+N3
      W=0.
      DO 46 L=1,N
      KL=N+L
      W=W+H(KL)*H(K)
      IF(L=J)44,45,45
44  K=K+N-L
      GO TO 46
45  K=K+1
46  CONTINUE
      K=N+J
      ALFA=ALFA+W*H(K)
47  H(J)=W

C
C      REPEAT SEARCH IN DIRECTION OF STEEPEST DESCENT IF RESULTS

```

Listing H.3. (continued)

```

C      ARE NOT SATISFACTORY
      IF(Z*ALFA)48,1,48
C
C      UPDATE MATRIX H
48  K=N31
      DO 49 L=1,N
      KL=N2+L
      DO 49 J=L,N
      NJ=N2+J
      H(K)=H(K)+H(KL)*H(NJ)/Z-H(L)*H(J)/ALFA
49  K=K+1
      GO TO 5
C      END OF ITERATION LOOP
C
C      NO CONVERGENCE AFTER LIMIT ITERATIONS
50  IER=1
      RETURN
C
C      RESTORE OLD VALUES OF FUNCTION AND ARGUMENTS
51  DO 52 J=1,N
      K=N2+J
52  X(J)=F(K)
      CALL FUNCT(N,X,F,G)
C
C      REPEAT SEARCH IN DIRECTION OF STEEPEST DESCENT IF DERIVATIVE
C      FAILS TO BE SUFFICIENTLY SMALL
      IF(GNRM=EPS)55,55,53
C
C      TEST FOR REPEATED FAILURE OF ITERATION
53  IF(IER)56,54,54
54  IER=-1
      GO TO 1
55  IER=0
56  RETURN
      END

```